

AD-A262 549



AN INVESTIGATION OF GRAPHITE PEEK
COMPOSITE UNDER COMPRESSION
WITH A CENTRALLY LOCATED
CIRCULAR DISCONTINUITY

THESIS

Benjamin Wham II, Captain, USAF

AFIT/GA/93M-01

DISTRIBUTION STATEMENT A

Approved for public release;
Distribution Unlimited

DEPARTMENT OF THE AIR FORCE
AIR UNIVERSITY

AIR FORCE INSTITUTE OF TECHNOLOGY

Wright-Patterson Air Force Base, Ohio

93 4 02 146

DTIC
SELECTED
APR 05 1993
S B D

AFIT/GA/93M-01

AN INVESTIGATION OF GRAPHITE PEEK
COMPOSITE UNDER COMPRESSION
WITH A CENTRALLY LOCATED
CIRCULAR DISCONTINUITY

THESIS

Benjamin Wham II, Captain, USAF

^{2/14}
AFIT/GA/93M-01

Approved for public release; distribution unlimited

93 4 02 146

93-06997



25/01

DISCLAIMER NOTICE



THIS DOCUMENT IS BEST QUALITY AVAILABLE. THE COPY FURNISHED TO DTIC CONTAINED A SIGNIFICANT NUMBER OF COLOR PAGES WHICH DO NOT REPRODUCE LEGIBLY ON BLACK AND WHITE MICROFICHE.

AFIT/GA/93M-01

AN INVESTIGATION OF GRAPHITE PEEK COMPOSITE UNDER COMPRESSION WITH A CENTRALLY LOCATED CIRCULAR DISCONTINUITY

THESIS

Presented to the Faculty of the School of Engineering
of the Air Force Institute of Technology

Air University

**In Partial Fulfillment of the
Requirements for the Degree of
Master of Science in Astronautical Engineering**

Benjamin Wham II, B.S.C.E., E.I.T.

Captain, USAF

DTIC QUALITY INSPECTED

March 1993

Approved for public release; distribution unlimited

Accession For

NTIS

DTIC

Unass

Jan

A-1

Acknowledgments

This thesis would not have been completed had it not been for the support of many individuals and organizations throughout Wright-Patterson AFB. First, I would like to thank Dr. Anthony Palazatto, my thesis Advisor, for all his assistance, support, and criticism in making this project a reality. Dr. Palazotto was always willing to help me work through any problems or concerns which I had as well to provide excellent moral support on academic and personal matters. Second, I would like to state my indebtedness to Dr. R.S. Sandhu, my thesis sponsor. Dr. Sandhu is truly one of the top engineering minds in the field of composites and in the nation. He has taught me all the various aspects of composite materials from the theoretical to the structural applications. In addition, he has taught me much about the world outside my own and I am a much better man for having known him.

I would like to thank everyone in FIBCA including Dr. Greg Schoeppner for all his assistance in providing computational support, excellent engineering advice, and a good game of racquetball to remove the thesis tension; Mr. Chuck Ramsey for allowing me access to all his equipment and to bother his personnel whenever I had a problem; finally, Mr. Forrest Sandow for his computational expertise as well as refreshing outlook on life.

I am also indebted to :

Mr. Wayne Yarcho for being the point man for all the experimental work conducted for this thesis; Mr. Jack Smith for his highly valuable technical advice and leg work; Mr. Doug Dolvin for providing good engineering direction and advise on my experimental work as well as the assistance of shop personnel when needed.

Mr. Larry Mack, Mr. Rick Zimmerman, and all the people at Beta Industries for their work in constructing the composites I used for my experiment and modifying the Boeing fixture for experimentation.

Mr. Bill Yoskul, Mr. Larry Marchum, Mr. Cliff Hitchcock and Mr. Jim Weiher for their intricate work in placing gages on the Boeing compression specimens.

Mr. Don Cook and Mr. Larry Bates for their support in the testing of many composite samples, as well as a good laugh each day I showed up.

Mr. Mark Blodgett, of WL/MA, for his valuable time and expertise in the ultrasonic investigation of the failed specimens.

Capt. Steve Creaghan for all his support and words of encouragement, until he graduated.

Finally, I would like to thank the three most important people in my life. My mother, Dr. Betty Breyer, for putting me here on Earth to go through all this stuff as well as proofreading this document (told you that Ph D. in English would come in handy.). My daughter, Jennifer, who was always there for a smile at the end of a long day and missed her Dad even though she did not know where he went. Lastly, my wife Ellen for her patience, support, and love. Without her support this task would have been infinitely more difficult. Thank you all and ONE.

TABLE OF CONTENTS

<u>TITLE</u>	<u>PAGE</u>
Acknowledgments	ii
List of Figures	viii
List of Tables	x
Abstract	xi
I. Introduction	1-1
A. Purpose	1-2
B. Background	1-2
II. Theory	2-1
A. Mechanics of Composite Materials	2-1
(1) Micromechanical Behavior of Composite Materials	2-1
(2) Macromechanical Behavior of Composite Materials	2-7
(3) Compressive Mechanics	2-15
B. Linear Finite Element Theory	2-28
C. Nonlinear Constitutive Relationships	2-33
D. Strain Energy Failure Theory	2-39
III Analysis	3-1
A. Finite Element Modeling	3-1
B. Comparison of the Meshes	3-5
C. Boundary Conditions	3-6
D. Executing a Nonlinear Analysis	3-8

IV. Experimentation	4-1
A. Specimen Description	4-2
B. Specimen Instrumentation	4-5
C. Instrumented Specimen Testing	4-10
D. Mounting Fixture	4-12
E. Post Failure Analysis	4-16
(1) Scanning Electron Microscope	4-16
(2) Ultrasonic Scanning	4-17
V. Results and Discussion	5-1
A. Basic Properties Tests.	5-2
B. Boeing Open Hole Compressive Fixture	5-8
(1) Initial Testing in Boeing Fixture	5-8
(2) Ultimate Strength Compression Testing in the Boeing Fixture	5-12
(a) $[0^\circ]_{16}$ Unidirectional Specimens	5-12
(b) $[90^\circ]_{16}$ Unidirectional Specimens	5-23
(c) $[0^\circ/90^\circ]_{4S}$ Crossply Specimens	5-29
(d) $[\pm 45^\circ]_{4S}$ Shear Specimens	5-36
(e) $[0^\circ/\pm 45^\circ/90^\circ]_{2S}$ Quasi-isotropic Specimens	5-42
(3) Progression of Failure Testing in the Boeing Fixture	5-51
(a) $[0^\circ]_{16}$ Unidirectional Specimen	5-52
(b) $[90^\circ]_{16}$ Unidirectional Specimen	5-55
(c) $[0^\circ/90^\circ]_{4S}$ Crossply Specimen	5-55
(d) $[\pm 45^\circ]_{4S}$ Shear Specimen	5-58
(e) $[0^\circ/\pm 45^\circ/90^\circ]_{2S}$ Quasi-isotropic Specimen	5-59
C. Analytical Comparison	5-61
(1) $[0^\circ]_{16}$ Unidirectional Model	5-62
(2) $[90^\circ]_{16}$ Unidirectional Model	5-69
(3) $[0^\circ/90^\circ]_{4S}$ Crossply Model	5-74
(4) $[\pm 45^\circ]_{4S}$ Shear Model	5-81
(5) $[0^\circ/\pm 45^\circ/90^\circ]_{2S}$ Quasi-isotropic Model	5-87
(6) Complex Variable Analysis	5-99

VI. Conclusions	6-1
A. Experimental versus Analytical Failure Predictions	6-1
(1) $[0^0]_{16}$ Unidirectional Laminates	6-1
(2) $[90^0]_{16}$ Unidirectional Laminates	6-2
(3) $[0^0/90^0]_{4S}$ Crossply Laminates	6-2
(4) $[\pm 45^0]_{4S}$ Shear Laminates	6-2
(5) $[0^0/\pm 45^0/90^0]_{2S}$ Quasi-isotropic Laminates	6-3
B. Compression Testing	6-4
C. General Conclusions	6-5
(1) Nonlinear Finite Element Program (PLNRS)	6-5
(2) Macromechanical versus Micromechanical	6-6
(3) Closing	6-7
Appendix A: Material Properties Curves	A-1
Appendix B: Test Plan	B-1
Appendix C: Representative Data for Experimental Results	C-1
Bibliography	R-1
Vita	V-1

LIST OF FIGURES

FIGURE		PAGE
Figure 1-1	Types of Failures Around Holes	1-4
Figure 2-1	Typical Matrix-Fiber Construction	2-3
Figure 2-2	Effects of a Broken Fiber	2-4
Figure 2-3	Coordinate Transformation	2-13
Figure 2-4	Interlamina Forces	2-15
Figure 2-5	Fiber Waviness Effects	2-19
Figure 2-6	Tension and Shear/Fiber Failure Modes	2-21
Figure 2-7	Free Body Diagram of Fiber	2-24
Figure 2-8	Modeling of Composite as Springs	2-25
Figure 2-9	Constant Strain Triangle	2-29
Figure 2-10	Area of Triangle	2-30
Figure 2-11	Nodal Locations	2-32
Figure 2-12	Biaxial State of Stress	2-35
Figure 2-13	Comparison of Failure Criterion	2-42
Figure 2-14	Option 1 Unloading Scheme	2-44
Figure 2-15	Option 2 Unloading Scheme	2-45
Figure 3-1	Half Mesh	3-2
Figure 3-2	Quarter Mesh	3-2
Figure 3-3	Modeling of the Ply Thicknesses	3-4
Figure 3-4	Martin/Fisher Meshes	3-5
Figure 3-5	Boundary Conditions on the Model	3-7
Figure 4-1	Materials Property Specimens	4-3
Figure 4-2	Boeing Specimens	4-4
Figure 4-3	Placement of Strain Gages on Material Properties Specimens	4-5

Figure 4-4	Placement of Gages on Boeing Specimen	4-6
Figure 4-5	Location of Hole Gage with Respect to Finite Element Mesh	4-8
Figure 4-6	Strain Gage at Hole	4-7
Figure 4-7	Material Properties Instron Machine	4-11
Figure 4-8	Compression Testing Instron Machine	4-11
Figure 4-9	Boeing Device with Stability Plates	4-13
Figure 4-10	End Loading Configuration	4-14
Figure 4-11	Modification to Boeing Specimen	4-15
Figure 4-12	Cutting Pattern to View Failed Ends	4-16
Figure 5-1	Basic Material Properties Specimens (Tension)	5-2
Figure 5-2	Basic Material Properties Specimens (Compression)	5-4
Figure 5-3	Failure Modes Encountered During Initial Tests	5-9
Figure 5-4	0° Specimen Exhibiting Longitudinal Splitting	5-13
Figure 5-5	Graph of Far Field and Hole Strain for 0°	5-14
Figure 5-6	Location of Split Gages	5-17
Figure 5-7	Ultrasonic Images of 0° With Split	5-18
Figure 5-8	SEM Photographs of 0°	5-19
Figure 5-9	Graph of Far Field and Hole Strain for 90°	5-24
Figure 5-10	SEM Photographs of 90°	5-25
Figure 5-11	Graph of Far Field and Hole Strain for 0°/90°	5-30
Figure 5-12	SEM Photographs of 0°/90°	5-31
Figure 5-13	Scissoring of the Fibers of a Shear Specimen	5-37
Figure 5-14	Graph of Far Field and Hole Strain for ±45°	5-39
Figure 5-15	Ultrasonic Images of ±45°	5-40
Figure 5-16	Graph of Far Field and Hole Strain for 0°/±45°/90°	5-43

Figure 5-17	SEM Photographs of $0^{\circ}/\pm 45^{\circ}/90^{\circ}$	5-45
Figure 5-18	Ultrasonic Images of 0°	5-53
Figure 5-19	Ply-by-Ply Analysis of Specimen #10	5-54
Figure 5-20	Ultrasonic Images of 90° Specimen	5-55
Figure 5-21	Ultrasonic Images of $0^{\circ}/90^{\circ}$ Specimen	5-56
Figure 5-22	Ply-by-Ply Analysis of Specimen #12	5-57
Figure 5-23	Ultrasonic Images of $\pm 45^{\circ}$ Specimen	5-58
Figure 5-24	Ply-by-Ply Analysis of Specimen #11	5-60
Figure 5-25	Comparison of Analytical and Experimental Data for 0° (Split)	5-63
Figure 5-26	Progression of Failure for 0° Model	5-65
Figure 5-27	Contour Plots of 0° Model	5-66
Figure 5-28	Analytical-Experimental Comparison of 90°	5-69
Figure 5-29	Progression of Failure for 90° Model	5-71
Figure 5-30	Contour Plots of 90° Model	5-72
Figure 5-31	Analytical-Experimental Comparison of $0^{\circ}/90^{\circ}$	5-75
Figure 5-32	Progression of Failure for $0^{\circ}/90^{\circ}$ Model	5-77
Figure 5-33	Contour Plots of $0^{\circ}/90^{\circ}$ Model	5-79
Figure 5-34	Analytical-Experimental Comparison of $\pm 45^{\circ}$	5-82
Figure 5-35	Progression of Failure for $\pm 45^{\circ}$ Model	5-84
Figure 5-36	Contour Plots of $\pm 45^{\circ}$ Model	5-86
Figure 5-37	Analytical-Experimental Comparison of $0^{\circ}/\pm 45^{\circ}/90^{\circ}$	5-88
Figure 5-38	Progression of Failure for $0^{\circ}/\pm 45^{\circ}/90^{\circ}$ Model	5-90
Figure 5-39	Contour Plots of $0^{\circ}/\pm 45^{\circ}/90^{\circ}$ Model	5-94
Figure 5-40	Location of Elements for Delamination Check	5-98
Figure B-1	Loading Conditions for Savin's Calculation	B-1

LIST OF TABLES

TABLE		PAGE
Table 4-1	List of Boeing Specimens and Their Uses	4-8
Table 5-1	Comparison of Material Properties	5-6
Table 5-2	Ultimate Strength of 0° Specimens	5-12
Table 5-3	Ultimate Strength of 90° Specimens	5-23
Table 5-4	Ultimate Strength of Crossply Specimens	5-29
Table 5-5	Maximum Strength for Shear Specimens	5-38
Table 5-6	Ultimate Strength of Quasi-isotropic Specimens	5-41
Table 5-7	Comparison of Complex Variable to FEM	5-99

Abstract

The purpose of this thesis was to determine (both experimentally and analytically) the initiation and progression of failure, stress-strain response, and the failure loads of Graphite/Polyetheretherketone (Gr/PEEK) laminates, incorporating a 0.5" circular discontinuity, loaded in axial compression at room temperature. The ply lay-ups of these specimens were $[0^0]_{16}$, $[90^0]_{16}$, $[\pm 45^0]_{4S}$, $[0^0/90^0]_{4S}$, and $[0^0/\pm 45^0/90^0]_{2S}$. The specimens were loaded using a Boeing Open Hole Compression fixture. The specimens were tested and then evaluated using a Scanning Electron Microscope to locate any micromechanical failure characteristics. In addition, specimens of each lay-up were loaded to 90% and 95% of their expected ultimate strength and were then scanned using ultrasonic techniques to determine the progression of failure.

Analytically, a nonlinear material finite element program was used to predict the initiation and progression of failure, stress-strain response, and the failure loads of the Gr/PEEK laminates. The specimens were modeled using a quarter symmetry mesh and the load was applied in the form of constant displacement at the end nodes. The state of strain within the meshes was plotted to determine the location of strain concentrations and the corresponding stress concentrations. Finally, the "gross" stress states of the Gr/PEEK laminates were considered in the analytical portion of the thesis.

In the experimentation, $[90^0]_{16}$, $[0^0/90^0]_{4S}$, and $[0^0/\pm 45^0/90^0]_{2S}$ laminates, as well as three of the $[0^0]_{16}$, failed as the result of a crack that was normal to the loading direction and initiated from the edge of the hole progressing to the outer edges of the specimen. Scanning Electron Microscope images were taken of a representative sample of the failed specimens. While there was evidence of micromechanical failures, there is no indication of a dominate mode of failure of the composite. Ultrasonic imaging was made of specimens that did not fail by a horizontal crack and of all specimens used in the

progression of failure testing. The $[\pm 45^\circ]_{4S}$ specimens failed internally due to a crack that originated from the hole at the outer edge and then travelled at an angle of about 45% to the direction of loading. The $[0^\circ]_{16}$ specimens the failed due to a vertical split showed little or no indication that a horizontal crack was forming.

The experimental and analytical results were then compared. The initiation and progression of failure and stress-strain response compared well for the $[\pm 45^\circ]_{4S}$, $[0^\circ/90^\circ]_{4S}$, and $[0^\circ/\pm 45^\circ/90^\circ]_{2S}$ laminates. The value of the ultimate analytical stress is of some debate. The curves modeled the sudden increase in strain that was observed to precede the total failure of the composite in the experimental testing. The $[0^\circ]_{16}$ laminate failed in a catastrophic manner in the analytical portion of the thesis, but the manner of the failure did not model either the vertical split or the horizontal crack that was observed during the experimental testing. The $[90^\circ]_{16}$ failed at a much higher analytical load than was obtained during the experimental testing. There existed a slight change in the slope similar to the type that was experienced with each of the multidirectional laminates occurring at a lower stress.

Overall the finite element method used to analytically model the failure of Gr/PEEK did a good job of modeling the response of the specimens tested experimentally. While there was no clear indication of where the analytical model failed in compression, there is a portion of the stress-strain response which models the sudden increase in strain that a specimen experiences experimentally before it fails. If this characteristic is chosen as the point in which the analytical model fails then the ultimate failure stress in the analysis agrees with the experimental ultimate stress by 5 to 25%, depending on the laminate.

The use of Dr. Sandhu's Nonlinear Finite Element technique is superior to any micromechanical methods used to determine the ultimate strength of the composite since it incorporates the true time history of a composite and models the nonlinear material characteristics of the composite material. Included within the material properties curves

are many of the different types of failure mechanisms that are present within the specimens tested experimentally. For this reason and based on the results of this thesis, one can draw the conclusion that this type of analytical modeling using strain energy best approximates the true failure characteristics of a nonlinear composite material system.

AN INVESTIGATION OF GRAPHITE PEEK COMPOSITE UNDER COMPRESSION WITH A CENTRALLY LOCATED CIRCULAR DISCONTINUITY

I. Introduction

Composite materials have become the next major structural material of scientists and engineers because of their low weight and high strength. Because of its use in many different applications, the ability to predict a composite's ultimate strength and its failure characteristics are of the utmost importance.

Composites excel over conventional structural materials in their higher strength to weight ratio, increased toughness, and higher stiffness to weight ratio. These characteristics are extremely important in aircraft frames and space structures where large increases in weight result in significant reduction in performance. The problem with many composites is that they are extremely labor intensive and difficult to manufacture. To make the manufacturing process easier ICI Fiberite developed the composite Graphite Polyetheretherketone, Gr/PEEK, that has many advantages over existing thermoset composites. These advantages include high impact toughness and damage tolerance; rapid, automated, economical fabrication processes; excellent hot-wet performance; low moisture absorption and excellent solvent resistance; superior tribological properties; outstanding fire resistance; and ease of repair [1].

A large body of research conducted on Gr/PEEK exists and includes the investigation of Gr/PEEK under both tension and compression with a centrally located cutout. Some of this research has discussed a need to include the nonlinear stress-strain behavior of the materials in the evaluation of the composite. This research will investigate the nonlinear properties of Gr/PEEK using the nonlinear finite element program, PLNRS, and validate the results both with a complex variable analysis and actual experimentation.

A. Purpose

The purpose of this thesis is to determine (using both experimental and analytical methods) the basic material properties of Gr/PEEK, the initiation and progression of compressive failure, the stress-strain response of the material, and the ultimate failure load of Gr/PEEK with a centrally located 0.5" circular cutout. The Gr/PEEK specimens were end loaded both analytically and experimentally with a Boeing Open Hole Compression Apparatus, BSS-7260. The composite was loaded at room temperature. The ply layups used for the investigation were $[0^{\circ}_{16}]$, $[90^{\circ}_{16}]$, $[\pm 45^{\circ}]_{4s}$, $[(0^{\circ}/90^{\circ})_{4s}]$, and $[0^{\circ}/\pm 45^{\circ}/90^{\circ}]_{2s}$.

The objectives of this study are to:

- 1) Investigate the initiation and progression of compressive failure and the ultimate strength of each laminate. The final failure load will be predicted with finite element techniques and the failure modes will be verified using ultrasonic analysis and fractographic methods.
- 2) Determine the "gross" state of stress and strain that occurs within the various layups.
- 3) Compare the experimental results with the analytical results. Further correlation of results will be obtained with a complex variable point stress analysis program developed by the author.

B. Background

Composite materials are almost as old as recorded history itself. The first major composite material was developed by incorporating straw into mud to make bricks for buildings. Laminated sheets of wood or plywood were used by the early Egyptians in their construction of homes and temples [2]. In the modern age, reinforced concrete

made possible the construction of the skyscraper and completely revolutionized the building industry throughout the world. Using reinforced concrete buildings were constructed to heights never possible with conventional masonry construction, due to the dramatic increase in the strength to weight ratio. Now once again the use of "advanced composite materials" has revolutionized all industries where the products are weight and performance sensitive. Advanced composites have the advantages of a very high strength, high modulus, and high stiffness due to the incorporation of fibers into a matrix material. The composite can be made of ceramics, metals, or plastics.

The ability of a composite to be tailored to a specific loading condition makes it ideal for use in the aerospace industry. Composite components are used in many types of aircraft including the F-16 Fighting Falcon, F-15 Strike Eagle, and the F-111 Aardvark. The best known use of composites in aerospace is the F-117A Stealth fighter and the B-2 Stealth bomber. These aircrafts are constructed of composites to make maximum use of their high strength and low radar visibility. The use of composites is not restricted to aircraft. In NASA's design for the Space Station Freedom, composite materials will be used in the racks needed to hold experimental equipment. Their incorporation into the design will save thousands of dollars in payload costs [3]. Composites have also been used in the sporting goods industry. Composites were used extensively by many nations during the 1992 Summer Olympics in Barcelona, Spain. Athletic equipment manufactured with composite materials is much lighter and higher in strength than conventional equipment, giving an athlete that slight advantage that would be needed to win [4].

Composite components are connected to other components with the use of adhesive bonds, mechanical fasteners, or a combination of both. With the use of mechanical fasteners, holes must be introduced between the components which necessitates the ability to predict correctly the stress distribution around the hole from normal service loads. The ability to predict this stress distribution is of critical

importance because a hole can fail when the stress concentration around it exceeds the ultimate strength of the composite. This failure could be one of the types shown in Figure 1-1 [5]. To predict these stresses both experimental and analytical methods can be

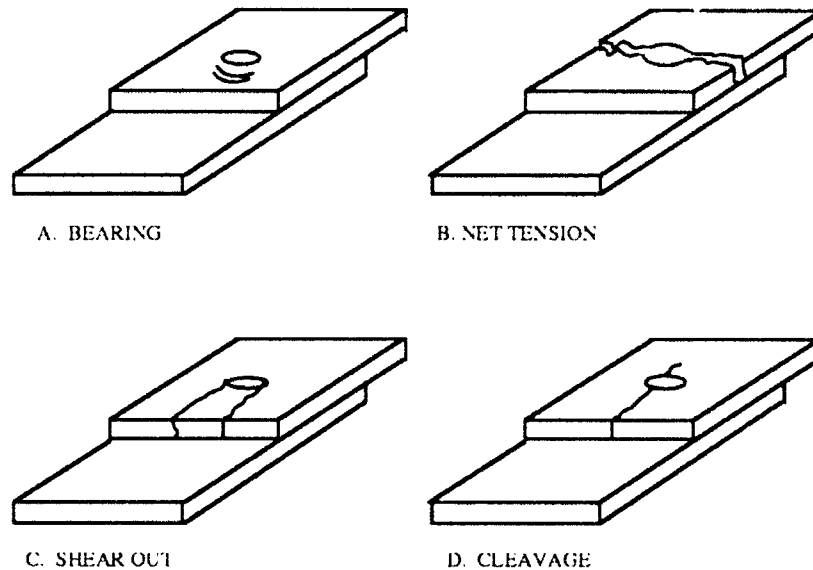


Figure 1-1: Types of Failures Around Holes

used. Analytical methods are preferable because of the of time and cost savings. Unfortunately, it is very difficult to predict a composite's strength analytically because of the mathematics involved and the uncertainties that exist. Compressive failure is even more difficult to predict because of the many types of uncertainties that can arise in compression.

There are currently two techniques used to predict the state of stress and the ultimate strength of a composite. The first is the fracture mechanics approach and the second is the finite element approach. Both methods are used extensively in the existing literature for the testing of Gr/PEEK specimens in both tension and compression. Because so many techniques now exist there is truly no accepted way to predict the strength of Gr/PEEK using analytical methods.

A comprehensive review of analytical fracture mechanics methods was published by Awerbuch in 1985. This study investigated the mechanics of metal-metal composites and thermoset composites. At the time of the study Gr/PEEK was just coming into use throughout the industry and only a cursory glance was given to it by Awerbuch. He concluded from the review that there are serious questions raised as to the applicability of classical fracture mechanics to composite materials. This problem centers around the fact that semi-empirical fracture mechanics models do not address the micromechanical and macromechanical factors that can be associated with the extension of a crack within the composite. In addition, many of these models make use of correlation factors that are usually derived from experimental results specific to a type of composite and are frequently subject to question [6].

In this investigation a nonlinear finite element program, PLNRS, developed by Dr. R. S. Sandhu of Wright Laboratories, Wright-Patterson AFB, Ohio was used for the analytical portion. Because of the non-linearity of Gr/PEEK laminates, the stress-strain response was modeled with the use of a piece-wise cubic spline interpolation function. These functions are applicable to this type of usage since they maintain continuity over the first derivative and provide a smooth surface over the entire length of the curve. Because the material is not isotropic, its response to tension will not be the same as its response to compression and Dr. Sandhu's method does an extremely good job of modeling these differences [7,8].

The finite element programs will also be used to model the progression of failure from its initiation to the final ultimate strength of the composite. Existing fracture mechanics methods do not allow for this load-history response picture and thus can only be used to check the finite element results. The geometry of the specimen and the boundary conditions it is subjected to can be modeled fairly well using the finite element technique. The analytical portion of this thesis will be discussed in detail in Chapter III.

In addition to the analytical study, experiments were conducted to verify the stress-strain response, the initiation and progression of failure, the "gross" state of stress for the laminates, and the ultimate failure loads of the composites. The experimental portion of this study will be described in Chapter IV.

Finally, a comparison of the results will be addressed in Chapter V and conclusions that can be drawn from this thesis will be presented in Chapter VI.

II. Theory

This thesis will make use of the following theories: mechanics of composite materials, linear finite element theory, nonlinear constitutive relationships, and strain energy failure theory for composite laminates.

The mechanics of composite materials will include both micromechanics and macromechanics, as well as a discussion of compressive mechanics. While the main interest of this thesis is the macromechanical behavior of the laminates, it will take a look at the micromechanical response as well. Compressive response is not as well understood as the response to tension, and therefore some of the existing compressive failure criteria will be discussed.

This investigation uses a finite element program that incorporates the nonlinear nature of the material, but much of the mathematics within the program is based on linear finite element theory. For this reason, linear finite element theory will be discussed so that the complete nature of the program can be understood. The incorporation of the nonlinear response of Gr/PEEK into the finite element code will be discussed. Finally, the failure criteria and the various unloading options used within the code will be explained.

A. Mechanics of Composite Materials

1) Micromechanical Behavior of Composite Materials.

Micromechanics is defined by R.M. Cook as:

The study of composite material behavior wherein the interaction of the *constituent* materials (are) examined in detail as part of the definition of the behavior of the *heterogeneous* composite material. [5]

Micromechanical behavior differs from macromechanical behavior where the composite material is considered to be a homogeneous material or "smeared" in nature. What is

important in micromechanics is properties of the fiber and matrix and what their individual contribution is to supporting an imposed load.

Gr/PEEK is classified as an Aromatic Polymer Composite consisting of a polyaromatic resin containing continuous Hercules AS-4 fibers. The matrix is composed of linear polymers that have been cross-linked. The composite is constructed in such a way that the crystalline chains remain parallel throughout the consolidation process when the composite is cooling down. The fiber-matrix interface is of critical importance since it is required to support an applied load. In a composite, the matrix serves three major purposes. First and foremost, it is what transfers the load from one fiber to surrounding fibers. Second, the matrix provides stability to fibers when a load is applied. Finally, the matrix serves to protect the fibers from environmental conditions that could degrade the fibers as well as providing some protection against damaging loads, such as a dropped wrench [9].

While this fiber-matrix interface is of critical importance to a composite, the fiber-matrix interface in Gr/PEEK is not very well understood. Tension tests where the fibers were pulled out of the matrix have shown that Gr/PEEK has a good fiber-matrix interface. It was shown that those fibers still have some of the matrix adhering to the fiber surface. This is an excellent indicator that there is a good fiber-matrix interface since when they failed they failed as a unit. Tests have shown that this is the case in such loading conditions as creep, impact, shear, fatigue, or tension and this has been one of the major reasons Gr/PEEK was so quickly accepted by the composite materials industry. However, many of the tests meant to determine why the fiber-matrix interface is so good have produced strange and conflicting results. For this reason it is felt that to understand the interface, the chemistry and morphology at the surface must be understood [10].

A typical fiber-matrix lamina construction is shown in Figure 2-1. While there are other types of fiber matrix arrangements such as two dimensional weaves, three

dimensional weaves, and a random whiskers arrangement, only the unidirectional fiber arrangement will be studied.

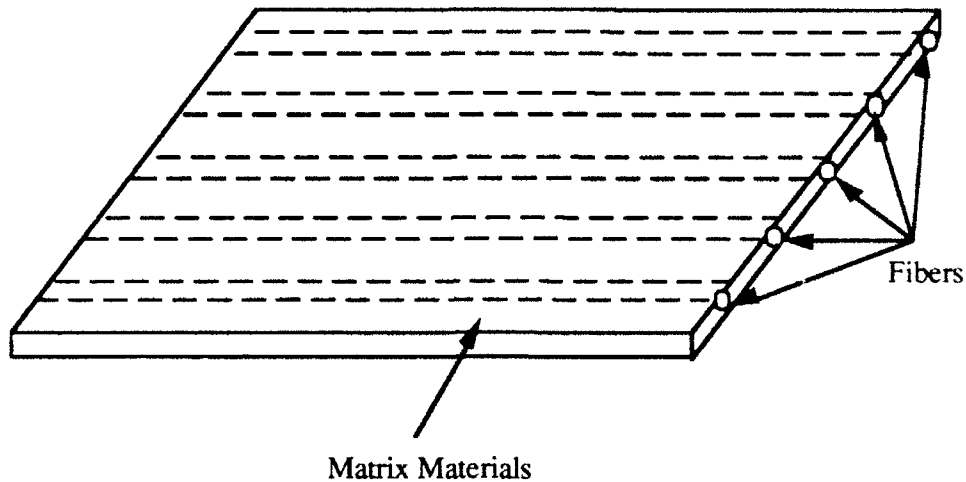


Figure 2-1: Typical Matrix-Fiber Construction

If a fiber fails, the matrix has the ability to transfer the load from the failed fiber to the adjacent fibers. A possible depiction of this load transference is shown in Figure 2-2 [5]. The load from the broken fiber is transferred to the adjacent fibers through the resulting increase in shearing stresses within the matrix material. This fiber-matrix interface is considered a weak link between the two components since environmental conditions such as an increase in temperature or the introduction of chemicals like solvents can cause the shear strength to decrease.

There are seven major material properties that will be used extensively during this study. These properties are 0° tension modulus, E_{11} ; the 0° compressive modulus; the 90° tension modulus, E_{22} ; the 90° compressive modulus; the shear modulus, G_{12} ; and the Poissons ratios in tension and compression, ν_{12T} and ν_{12C} . In micromechanical theory, the most common way of computing these properties is to use the rule of mixtures as shown below [5]:

$$E_l = E_f \cdot v_f + E_m \cdot v_m \quad (1)$$

where: E_f = the modulus of the fiber

v_f = the Possions ratio of the fiber

E_m = the modulus of the matrix

v_m = the Possions ratio of the matrix.

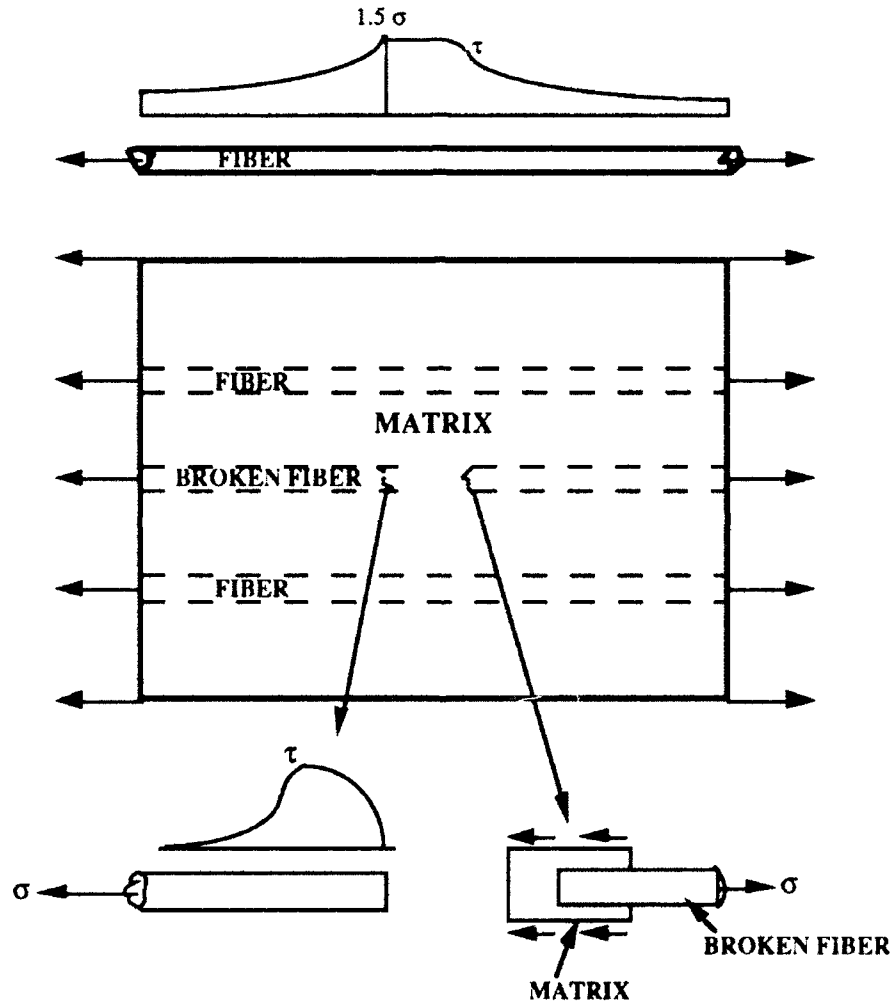


Figure 2-2: Effects of a Broken Fiber

This method is used extensively when the properties of both materials are well known, but it has very limited applicability to Gr/PEEK since the modulus of the matrix or E_m can vary over the history of an applied load. To get an accurate picture of the

performance of a nonlinear material, one would have to have a time history of the E_m modulus and recompute E_1 at the various times in the loading process. Another micromechanical method of calculating the strength of a composite material was proposed by Fan and Knapp in 1987. Their approach used the Second Law of Thermodynamics to derive the work from internal energy equations. From there, using Gauss's theorem, an equation for the energy of the respective components was derived [11]. Once again the final equations were predicated on the initial modulus of the components and would give a higher than actual strength when analyzing a nonlinear matrix. Many of the micromechanical theories suffer from the assumption that the initial modulus of a composite material and its components are constant throughout their loading history, and thus do not produce an accurate picture of the strength of nonlinear composites.

The nonlinear behavior of the matrix can be classified as a micromechanical response. Many of the present approaches to composite mechanics, both micromechanical and macromechanical, have chosen to ignore the nonlinear behavior of some composite materials. There have been some attempts to incorporate this behavior and a quick summary of these methods was conducted by Mahmoud N. Nahas [12]. One of the theories for incorporating nonlinear material behavior was set forth by Petit and Waddoups. This approach attempts to model the experimental material properties curves using a corrector technique. The problem with this method is that it fails to accurately model the curve. It also assumes that the failure of the lamina occurs when any other of the strain components relative to the material axis reaches a limiting value established by experimentation. This method assumes that the strain along one axis is not influenced by the presence of stresses along another axis, which is not the case. The resulting failure stresses predicted by this method are higher than the actual failure stress.

The second method was proposed by Hahn and Tsai and attempts to model the nonlinear behavior of the material with the use of the equation shown:

$$\epsilon_6 = S_{66}\sigma_6 + S_{6666}\sigma_6^3 \quad (2)$$

where ϵ_6 = shear strain

σ_6 = shear stress

S_{66} = compliance term

S_{6666} = nonlinearity constant.

While many composites display nonlinear behavior in shear tests, some composites, including Gr/PEEK, display nonlinear behavior in other loading directions [13]. This makes the Hahn-Tsai approach ineffective since the actual strain conditions are not accurately modeled.

The nonlinear method used in this study was developed by Dr. R.S. Sandhu. This method utilizes a piece-wise cubic-spline interpolation function to represent the stress-strain response of a composite. In addition, the theory incorporates the premise that the stress state of a composite is dependent on the stress-strain response in any other direction by the use of an equivalent strain equation. This method will be discussed in depth in part C of this section [7,8].

While the micromechanical approach is important for understanding exactly what a composite's components are and how they interact, for the purposes of this thesis the macromechanical approach will be used. Many of the micromechanical methods used in predicting the ultimate strength of a composite will be discussed in the Compressive Mechanics section of this chapter. While they are useful in some types of applications, including providing the engineer a prediction of the ultimate strength of a composite structure, they are not as accurate as Dr. Sandhu's method. Throughout this thesis the author will illustrate why the macromechanical approach using Dr. Sandhu's program, PLNRS, is better than the micromechanical approach.

B. Macromechanical Behavior of Composite Materials

Macromechanical behavior is defined by R.M. Jones as:

The study of composite material behavior wherein the materials [are] presumed *homogenous* and the effects of the constituent materials are detected only as averaged apparent properties of the composite. [5]

While a composite cannot be exactly represented by only one material, its response can be well approximated with macromechanical methods. For this reason a composite is treated as "smeared matter" with one set of material properties and the material is considered to be anisotropic.

A composite laminate is composed of individual laminae bonded together to form a single element. A composite is constructed so that it is able to resist loading in more than one direction, since unidirectional loading is a rather uncommon structural occurrence. However, one of the problems with constructing a composite with multidirectional laminae is that each lamina will respond differently to an applied load. Since all the laminae are bonded together to form a laminate, the laminate will deform as a unit. This deformation results in the creation of shear stresses between the laminae. These stresses, called interlamina forces, will be dependent on the material properties of each lamina and will be greatest at the edges of the structural member. If these interlamina forces exceed the bonding strength between the laminae then delamination can occur resulting in the failure of the composite structure. Both transverse and longitudinal stresses can contribute to the interlamina forces causing delamination to occur earlier in the loading.

For the purpose of this macromechanical approach, linear elasticity is assumed. Because the nonlinear behavior of Gr/PEEK is modeled incrementally, it is acceptable to utilize a macromechanical approach [14]. In linear elastic theory, the basic principle that is utilized is Hooke's Law:

$$\sigma_i = C_{ij} \epsilon_j \quad i,j=1,2,\dots,6 \quad (3)$$

where σ_i = stress
 C_{ij} = stiffness term
 ϵ_j = strain.

In order to simplify the equation writing in this thesis a contracted notation similar to that utilized by Jones and others will be utilized. The contracted notation is shown below [5]:

<u>TENSOR NOTATION</u>	<u>CONTRACTED NOTATION</u>
σ_{11}	σ_1
σ_{22}	σ_2
σ_{66}	σ_3
τ_{26}	σ_4
τ_{61}	σ_5
τ_{12}	σ_6
ϵ_{11}	ϵ_1
ϵ_{22}	ϵ_2
ϵ_{33}	ϵ_3
$\gamma_{26}=2\epsilon_{23}$	ϵ_4
$\gamma_{61}=2\epsilon_{61}$	ϵ_5
$\gamma_{12}=2\epsilon_{12}$	ϵ_6

where γ_{ij} = engineering shearing strain
 ϵ_{ij} = tensorial shearing stress.

Using linear elastic theory we can represent the strain-displacement relationship in contracted notation as:

$$\epsilon_1 = \frac{\partial w}{\partial x} \quad \epsilon_2 = \frac{\partial v}{\partial y} \quad \epsilon_3 = \frac{\partial w}{\partial z} \quad (4)$$

$$\gamma_{26} = \frac{\partial v}{\partial z} + \frac{\partial w}{\partial y} \quad \gamma_{63} = \frac{\partial w}{\partial x} + \frac{\partial v}{\partial z} \quad \gamma_{16} = \frac{\partial v}{\partial x} + \frac{\partial u}{\partial y}$$

where u, v, w represent displacements in the x, y, z directions respectively.

Representing Hooke's Law in matrix form, we have a stiffness matrix (C_{ij}) which consists of 36 constants. This matrix is a real symmetric matrix so only 21 of the 36 constants are independent. The stress-strain relationship for an anisotropic material in real symmetric form can be written as:

$$\begin{Bmatrix} \sigma_1 \\ \sigma_2 \\ \sigma_3 \\ \sigma_4 \\ \sigma_5 \\ \sigma_6 \end{Bmatrix} = \begin{bmatrix} C_{11} & C_{12} & C_{13} & C_{14} & C_{15} & C_{16} \\ C_{21} & C_{22} & C_{23} & C_{24} & C_{25} & C_{26} \\ C_{31} & C_{32} & C_{33} & C_{34} & C_{35} & C_{36} \\ C_{41} & C_{42} & C_{43} & C_{44} & C_{45} & C_{46} \\ C_{51} & C_{52} & C_{53} & C_{54} & C_{55} & C_{56} \\ C_{61} & C_{62} & C_{63} & C_{64} & C_{65} & C_{66} \end{bmatrix} \begin{Bmatrix} \epsilon_1 \\ \epsilon_2 \\ \epsilon_3 \\ \epsilon_4 \\ \epsilon_5 \\ \epsilon_6 \end{Bmatrix} \quad (5)$$

This equation is the most general form of the stress-strain relationship for an anisotropic material with planes of material symmetry. However, in a composite material there are usually at least two planes of symmetry. In orthotropic materials there are three orthogonal planes of symmetry. This simplifies equation (5) into the form:

$$\begin{Bmatrix} \sigma_1 \\ \sigma_2 \\ \sigma_3 \\ \sigma_4 \\ \sigma_5 \\ \sigma_6 \end{Bmatrix} = \begin{bmatrix} C_{11} & C_{12} & C_{13} & 0 & 0 & 0 \\ C_{21} & C_{22} & C_{23} & 0 & 0 & 0 \\ C_{31} & C_{32} & C_{33} & 0 & 0 & 0 \\ 0 & 0 & 0 & C_{44} & 0 & 0 \\ 0 & 0 & 0 & 0 & C_{55} & 0 \\ 0 & 0 & 0 & 0 & 0 & C_{66} \end{bmatrix} \begin{Bmatrix} \epsilon_1 \\ \epsilon_2 \\ \epsilon_3 \\ \epsilon_4 \\ \epsilon_5 \\ \epsilon_6 \end{Bmatrix} \quad (6)$$

This reduces the number of independent constants from 21 to 9 and shows a decoupling of the shearing stresses from the normal strains and the normal stresses from the shearing strains.

Hooke's Law can now be written to solve for strains:

$$\epsilon_i = S_{ij} \sigma_j \quad i,j=1,2,\dots,6 \quad (7)$$

where S_{ij} = compliance matrix.

In most composite responses, it is easier to represent the terms of the compliance matrix than those of the stiffness matrix since these values can be determined from a set of simple tests performed with a single loading direction. Equation (7) (assuming the composite is an orthotropic material) can be rewritten in matrix form as:

$$\begin{Bmatrix} \epsilon_1 \\ \epsilon_2 \\ \epsilon_3 \\ \epsilon_4 \\ \epsilon_5 \\ \epsilon_6 \end{Bmatrix} = \begin{bmatrix} S_{11} & S_{12} & S_{13} & 0 & 0 & 0 \\ S_{21} & S_{22} & S_{23} & 0 & 0 & 0 \\ S_{31} & S_{32} & S_{33} & 0 & 0 & 0 \\ 0 & 0 & 0 & S_{44} & 0 & 0 \\ 0 & 0 & 0 & 0 & S_{55} & 0 \\ 0 & 0 & 0 & 0 & 0 & S_{66} \end{bmatrix} \begin{Bmatrix} \sigma_1 \\ \sigma_2 \\ \sigma_3 \\ \sigma_4 \\ \sigma_5 \\ \sigma_6 \end{Bmatrix} \quad (8)$$

Each of the terms of the compliance matrix (S_{ij}) can be written in terms of the engineering constants that have been determined from tests. The tests consist of a uniaxial tension and compression test conducted on both 0° and 90° laminates and a shear test conducted on $\pm 45^\circ$ laminates [15]. We can then rewrite the equation in the form of these constants:

$$[S_{ij}] = \begin{bmatrix} \frac{1}{E_1} & \frac{-\nu_{21}}{E_2} & \frac{-\nu_{31}}{E_3} & 0 & 0 & 0 \\ \frac{\nu_{12}}{E_1} & \frac{1}{E_2} & \frac{-\nu_{32}}{E_3} & 0 & 0 & 0 \\ \frac{-\nu_{13}}{E_1} & \frac{-\nu_{23}}{E_2} & \frac{1}{E_3} & 0 & 0 & 0 \\ 0 & 0 & 0 & \frac{1}{G_{23}} & 0 & 0 \\ 0 & 0 & 0 & 0 & \frac{1}{G_{31}} & 0 \\ 0 & 0 & 0 & 0 & 0 & \frac{1}{G_{12}} \end{bmatrix} \quad (9)$$

In this study the laminates are treated as thin plates, thus a plane stress assumption can be used. This assumption is based on the theory that the through-the-thickness stress can be neglected and thus allows us to model the composite using a two dimensional finite element analysis. It may not be valid where through-the-thickness stresses are generated with certain types of ply layups.

In the plane stress assumption, it is assumed that $\sigma_3=\sigma_4=\sigma_5=0$ and equation (9) can be simplified to:

$$\begin{Bmatrix} \epsilon_1 \\ \epsilon_2 \\ \epsilon_6 \end{Bmatrix} = \begin{bmatrix} \frac{1}{E_1} & \frac{-\nu_{21}}{E_2} & 0 \\ \frac{\nu_{12}}{E_1} & \frac{1}{E_2} & 0 \\ 0 & 0 & \frac{1}{G_{12}} \end{bmatrix} \begin{Bmatrix} \sigma_1 \\ \sigma_2 \\ \sigma_6 \end{Bmatrix} \quad (10)$$

The S_{ij} matrix can be inverted to solve for the stresses so that the equation has the form:

$$\begin{Bmatrix} \sigma_1 \\ \sigma_2 \\ \sigma_6 \end{Bmatrix} = \begin{bmatrix} Q_{11} & Q_{12} & 0 \\ Q_{21} & Q_{22} & 0 \\ 0 & 0 & Q_{66} \end{bmatrix} \begin{Bmatrix} \epsilon_1 \\ \epsilon_2 \\ \epsilon_6 \end{Bmatrix} \quad (11)$$

$$\text{where } Q_{11} = \frac{S_{22}}{S_{11} S_{22} - S_{12}^2} = \frac{E_1}{1 - \nu_{12} \nu_{21}}$$

$$Q_{12} = Q_{21} = -\frac{S_{12}}{S_{11} S_{22} - S_{12}^2} = \frac{\nu_{12} E_2}{1 - \nu_{12} \nu_{21}} = \frac{\nu_{21} E_1}{1 - \nu_{12} \nu_{21}}$$

$$Q_{22} = \frac{S_{11}}{S_{11} S_{22} - S_{12}^2} = \frac{E_2}{1 - \nu_{12} \nu_{21}}$$

$$Q_{66} = \frac{1}{S_{66}} = \frac{\nu_{12}}{E_1} = \frac{\nu_{21}}{E_2} = G_{12}$$

For an orthotropic lamina subjected to inplane forces the equations (9 through 11) are the basis for the stiffness and stress calculations that will be utilized in the finite element analysis [5].

Normally the principal axes of a laminate do not coincide with a given coordinate axis as shown in Figure 2-3. When the principal axes do not coincide, a transformation is required so that both the stresses and strains imposed on one coordinate system can be interpreted and utilized in another coordinate system. In this thesis the plane stress assumption allows for a coordinate transformation based on the angle θ which is the angle between the material fiber axis 1 and the x coordinate axis. Had the plane stress assumption not been valid a three-dimensional transformation would be required.

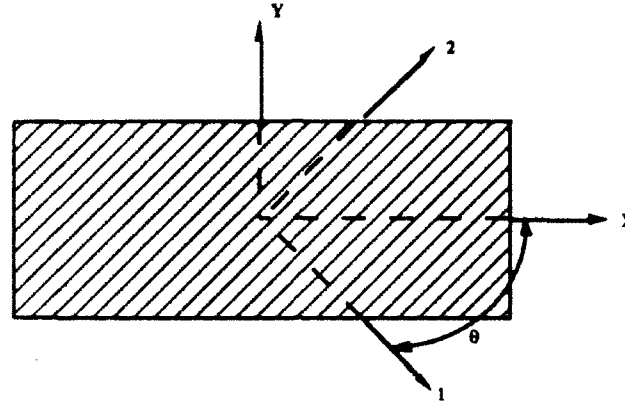


Figure 2-3: Coordinate Transformation

The two dimensional transformation can be expressed:

$$\begin{Bmatrix} \sigma_x \\ \sigma_y \\ \tau_{xy} \end{Bmatrix} = \begin{bmatrix} m^2 & n^2 & -2nm \\ n^2 & m^2 & 2nm \\ nm & -nm & m^2 - n^2 \end{bmatrix} \begin{Bmatrix} \sigma_1 \\ \sigma_2 \\ \tau_{12} \end{Bmatrix} \quad (12)$$

where $m = \cos \theta$ and $n = \sin \theta$.

Finally, both the stiffness matrix in equation (11) and the transformation matrix in equation (12) can be combined to give an equation for the relationship of stress to strain in which the material axis is not aligned with the structural or global coordinate axis. This expression is known as the transformed reduced stiffness matrix and equals:

$$\begin{Bmatrix} \sigma_1 \\ \sigma_2 \\ \sigma_6 \end{Bmatrix} = \begin{bmatrix} \bar{Q}_{11} & \bar{Q}_{12} & \bar{Q}_{16} \\ \bar{Q}_{21} & \bar{Q}_{22} & \bar{Q}_{26} \\ \bar{Q}_{16} & \bar{Q}_{26} & \bar{Q}_{66} \end{bmatrix} \begin{Bmatrix} \epsilon_1 \\ \epsilon_2 \\ \epsilon_6 \end{Bmatrix} \quad (13)$$

where $\bar{Q}_{11} = Q_{11} m^4 + 2(Q_{12} + 2Q_{66}) n^2 m^2 + Q_{22} n^4$

$\bar{Q}_{12} = \bar{Q}_{21} = (Q_{11} - Q_{12} - 4Q_{66}) n^2 m^2 + Q_{12} (n^4 + m^4)$

$$\overline{Q}_{22} = Q_{11}n^4 + 2(Q_{12} + 2Q_{66})n^2m^2 + Q_{22}m^4$$

$$\overline{Q}_{16} = \overline{Q}_{16} = (Q_{11} - Q_{12} - 2Q_{66})n^3m + (Q_{12} - Q_{22} + 2Q_{66})n^3m$$

$$\overline{Q}_{26} = \overline{Q}_{26} = (Q_{11} - Q_{12} - 2Q_{66})n^3m + (Q_{12} - Q_{22} + 2Q_{66})n^3m$$

$$\overline{Q}_{66} = (Q_{11} + Q_{22} - 2Q_{12} - 2Q_{66})n^2m^2 + Q_{66}(n^4 + m^4)$$

The most notable feature about the transformed reduced stiffness matrix is that the shear strains are coupled to the normal stresses and the normal strains are coupled to the shear stresses. Only when the material axis and coordinate axis are aligned are these terms uncoupled. What is not considered in this equation is the effect of interlamina forces that can result in planes of different orientations due to specific loading conditions.

Many times these interlamina stresses can result in delamination of a composite. Formula (13) does not take into account the through-the-thickness stresses, σ_z , σ_{xz} , and σ_{yx} , thus neglecting the force that contributes to the delamination of the composite. The stresses affecting a composite material are shown in Figure 2-4. D.H. Woolstencroft, et. al. in 1981 showed in a study on unidirectional composites that σ_z is much less than σ_x or σ_y and thus can be neglected [16]. As a result, this analysis does not take into account any through-the-thickness stresses and the plane stress assumption is assumed valid.

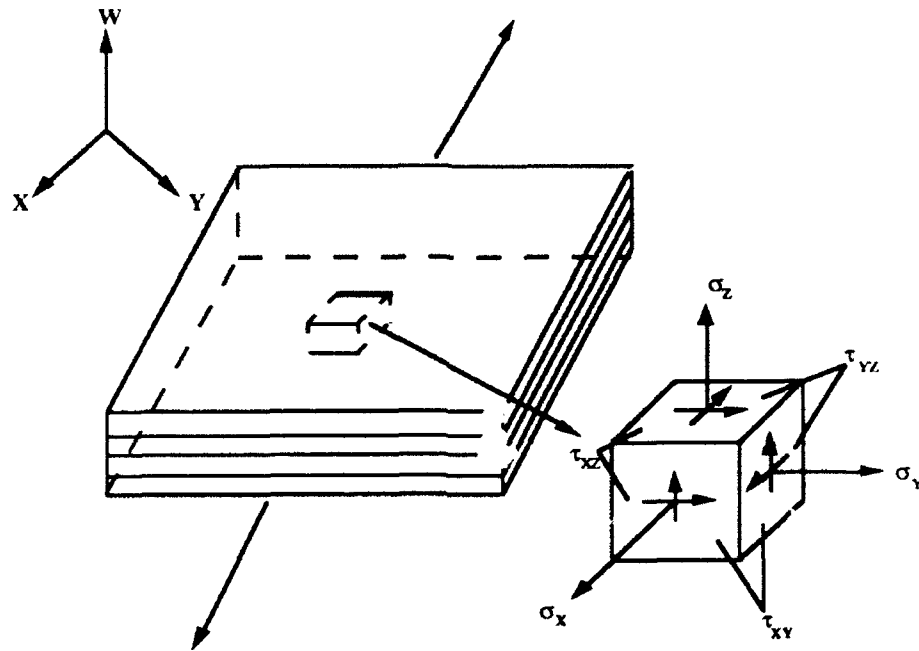


Figure 2-4: Interlamina Forces

Since a laminate may consist of various laminas oriented at different angles, equation (13) can be rewritten for each individual lamina. Therefore the behavior of a given laminate is the sum of the behaviors of each independent lamina.

$$\begin{Bmatrix} \sigma_x \\ \sigma_y \\ \sigma_{xy} \end{Bmatrix}_k = \begin{bmatrix} \bar{Q}_{11} & \bar{Q}_{12} & \bar{Q}_{16} \\ \bar{Q}_{21} & \bar{Q}_{22} & \bar{Q}_{26} \\ \bar{Q}_{16} & \bar{Q}_{26} & \bar{Q}_{66} \end{bmatrix} \begin{Bmatrix} \epsilon_x \\ \epsilon_y \\ \epsilon_{xy} \end{Bmatrix}_k \quad (14)$$

(3) Compressive Mechanics

This thesis will try to show that the use of Dr. Sandhu's two dimensional plane stress analysis to predict the compressive failure of Gr/PEEK is a proper application of the criterion. In compression, most isotropic materials behave as they would in tension. This is not the case for composite materials. Because of the orthotropic nature of composite

materials, the response is quite different in compression than it is in tension. This effect has been recognized by many who have sought to model the composite at both the micromechanical and macromechanical levels. In all the various attempts at modeling a composite, one thing is constant throughout; compression is treated differently than tension. Several methods that have been devised and utilized to predict the compressive strength of composite materials will be discussed. Since these methods are both on the micromechanical and macromechanical levels, an assortment of these criteria will be covered.

The first recognized look at compression in a material was performed by Euler who tried to model the buckling of a column. This column buckling is one way in which both the micromechanical and macromechanical ultimate strength of a composite can be roughly approximated. For the length of a given column the formula as derived by Euler is:

$$P_c = \frac{\pi E I}{L^2} \quad (15)$$

where E = the modulus of the column
 I = the moment of inertia of the column
 L = length of the simply supported column.

If the column is fixed at both ends then $L/2$ is substituted for L . In the case of composite materials, shearing forces become very important and the equation in (15) must be modified to:

$$P_{c,corr} = \frac{P_c}{1 + \frac{a P_c}{G A}} \quad (16)$$

where P_c = the previous column strength
 G = shear modulus of the composite
 a = a constant, 1.2 for rectangular cross-sections
 A = cross-sectional area of the column.

This formula shows that composites have a lower Euler buckling load because of the shear modulus. These equations are good estimates, but assume that the material is isotropic in nature, and thus do not take the true nature of composites into account. These formulas also assume that the column that is being compressed is straight to start with which is usually not the case [17].

Many different studies which take into account the material characteristics and physical characteristics of a composite material have been conducted in order to properly model the compressive strength of a composite. In 1979 Nuismer and Labor attempted to apply the Whitney and Nuismer point stress criterion to compressive responses in a composite to predict a composite's strength and state of stress [18]. In 1986, S.C. Tan utilized a complex variable analysis in order to compute the stress around a hole when a composite is under compression [19]. The problem with many of these semi-empirical techniques which were first introduced to predict the ultimate strengths is that they make the assumption that all composites are perfect. The process of constructing a composite material is full of steps that can introduce errors and imperfections. Any method that treats a composite as a perfect materials will produce results that are higher than the actual value. In addition, if constants are used to represent the material's properties then they ignore the load-history response of the material. In a truly nonlinear material the use of constant material properties is not a true representation of the material and can provide an incorrectly high ultimate strength.

When a Gr/PEEK specimen is manufactured, it is done using a unidirectional fiber tape with the matrix material impregnated into the tape. A combination of these tapes are laid out in the required stacking sequence, fused under the pressure of an autoclave, and allowed to cool under carefully controlled conditions. The process of constructing the specimens used for the experimental portion of this test research will be discussed in depth in Chapter 4 of this thesis. The important thing to keep in mind is that since this process

involves numerous steps, some of them done by hand, it is almost impossible to have a completely perfect composite where the fibers are perfectly straight in all directions, there are no voids, and all plies are at the exact angle specified by the stacking sequence. Resulting imperfections can lower the compressive strength of the composite.

One of the first places to look when trying to determine a cause of failure in a composite under compression is the straightness of the fibers. While great pains are taken in the manufacturing process to ensure that the fibers stay aligned, frequently they are not. Instead the fibers frequently take the appearance of a sinusoidal function that can be approximated using a Fourier series as shown in equation (17):

$$V = \sum_{n=1}^{\infty} a_n \sin \left(\frac{n \pi x}{l} \right) \quad (17)$$

where a = amplitude of fiber deflection
 n = wave number
 x = axial coordinate
 l = composite length.

When the composite is put under tension, the fibers that are in the loading direction tend to straighten out as shown in Figure 2-5. However, when compressive forces are applied in the fiber direction the fibers compress and the existing fiber waviness is compounded by the strain introduced by compression. As the compressive strain increases so does the fiber waviness as shown in Figure 2-5. If the matrix is sufficiently weak, it will not provide adequate side support for the fiber, and the fiber will buckle just as an Euler column might.

Because of the nature of composite materials, many different methods have been developed to characterize a composite's response to compression and the final compressive failure mode. Many of these methods attempt to incorporate the imperfections present in a

composite under compression. Because of the many varied lay-ups with which a composite can be constructed, many of these approaches are micromechanical.

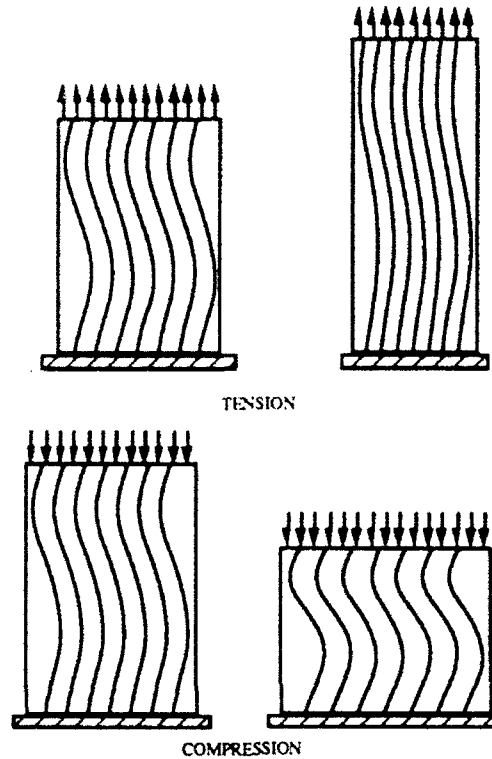


Figure 2-5: Fiber Waviness Effects

One of the ways of characterizing the compressive responses of a composite material is the use of a total energy formulation. Timoshenko and Gere determined a total energy criterion based on the Fourier series formulation of fiber waviness. Frost [20] modified equation (18) to determine the approximate fiber shape at any time during the loading procedure until failure starts to occur. The difference between the initial fiber displacement and subsequent fiber displacements gives us the amount of change in fiber displacement:

$$v = V - V_0 = \sum_{n=1}^{\infty} (a_n - a_{n0}) \sin \left(\frac{n \pi x}{l} \right) \quad (18)$$

where V_o = initial deflection

a_{no} = initial fiber amplitude.

The work or energy from the initial and present deflection of the fiber as shown in equation (19):

$$\text{Work Done (WD)} = \frac{\sigma_c}{h} \int_0^l \left(\left(\frac{dV}{dX} \right)^2 - \left(\frac{dV_o}{dX} \right)^2 \right) dx \quad (19)$$

where σ_c = the compressive stress

h = the fiber diameter.

From equations (18) and (19) an expression can be obtained for the work done with respect to the fiber amplitude:

$$WD = \frac{\sigma_c h l}{4} \sum_0^{\infty} \left(\frac{n \pi}{l} \right)^2 (a_n^2 - a_{no}^2) \quad (20)$$

Taking the first variation of this with respect to compressive stress yields several relationships which can be used to model various failure modes that can occur in a composite material under compression. These models include the tensile failure mode, shear and fiber failure mode and the fiber compressive mode.

The tension failure mode occurs when the fiber deforms out of phase with the fibers next to it as demonstrated in Figure 2-6.

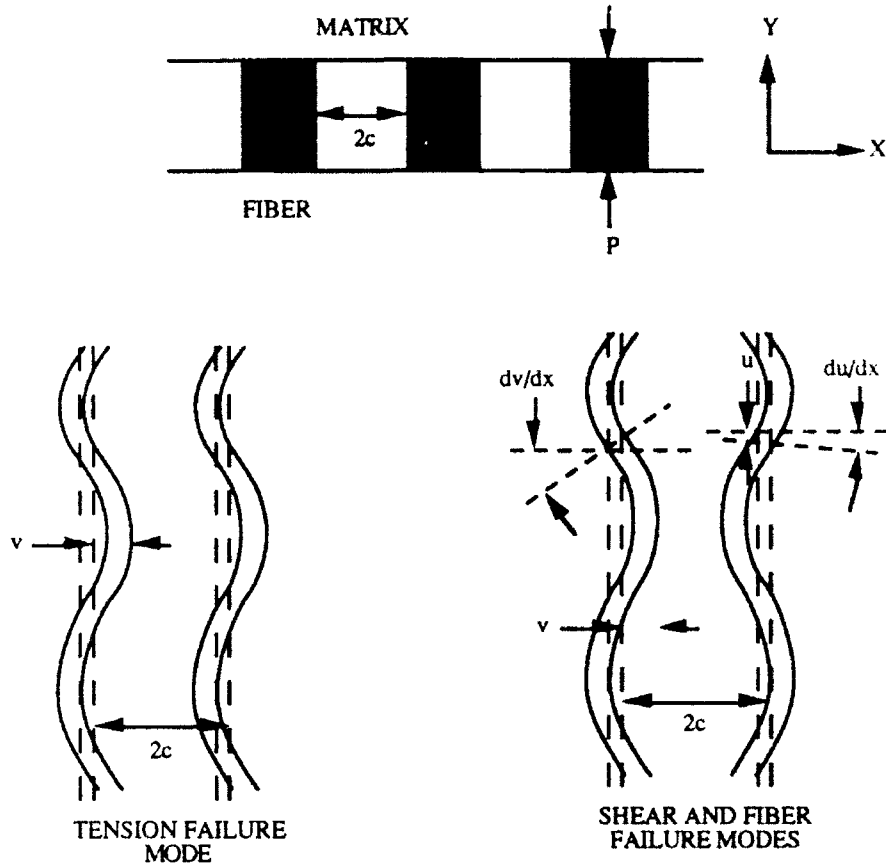


Figure 2-6: Tension and Shear/Fiber Failure Modes

In this representation, strain in the y direction is characterized by:

$$\epsilon_y = \frac{v}{c} \quad (21)$$

where c = one half the matrix width.

The strain energy absorbed by the fiber is in the form:

$$WD_f = \frac{E_f I}{2} \int_0^l \left(\frac{dv}{dX} \right)^2 dX \quad (22)$$

Using the relationships in equations (20), (21), and (22) a compressive stress function can be determined:

$$\sigma_{\text{comp}} = \left(\phi_f + \phi_m \frac{E_m}{E_f} \right) \left[\frac{2E_m}{ch} + \frac{E_f h^2}{12} \right] \left(\frac{n \pi^2}{l} \right) \left[\frac{a_n - a_{n0}}{a_n + a_{n0}} \right] \quad (23)$$

where ϕ_f = the fiber volume fraction

ϕ_m = the matrix volume fraction

E_m = the modulus of the matrix.

For the shear and fiber failure modes the fiber deflections are in phase as shown in Figure 2-6. In these modes the shear strain is assumed to be independent of y . Axial displacement can be determined by:

$$u = \frac{h}{2} \left(\frac{dv}{dx} - \Gamma_f \right) \text{ and } \frac{\partial u}{\partial y} = \frac{u}{c} \quad (24)$$

where Γ_f = the shear stress $\frac{\partial u}{\partial y} + \frac{\partial v}{\partial x}$.

Using the relationships for Γ_f and Γ_m , the matrix and fiber shearing stresses can be determined by substituting equation (20) and (24) into the relationship

$$G_m \Gamma_m = G_f \Gamma_f \quad (25)$$

where G_m = the shear modulus of the matrix

G_f = the shear modulus of the fiber.

The resulting equation is

$$\Gamma_{m,max} = (a_n - a_{no}) \left(\frac{n \pi}{l} \left(\frac{1 + h/2c}{1 + hG_m/2c G_f} \right) \right) \quad (26)$$

$$\Gamma_{f,max} = (a_n - a_{no}) \left(\frac{n \pi}{l} \left(\frac{1 + h/2c}{h/2c + G_f/G_m} \right) \right) = \frac{\tau_{f fail}}{G_f}$$

where $\tau_{f fail}$ = the ultimate shear strength of the matrix.

The fiber compressive failure mode occurs when fiber compressive strain is less than the compressive stress divided by the fiber's compressive modulus. This mode differs from the other two failure modes in that the fiber axial compressive strain to failure is greater than the composite's axial strain at the onset of fiber bending. This is not the case with the other two modes [20].

Hahn and Williams proposed a model of possible failure modes in a unidirectional laminate based on the equilibrium equations produced by forces on a single fiber, assuming small deflection. The equations are:

$$\begin{aligned} q + \frac{dQ}{dx} + P \frac{dw}{dx} &= 0 \\ p + \frac{dP}{dx} + Q \frac{dw}{dx} &= 0 \\ \frac{dM}{dx} - Q + m &= 0 \end{aligned} \quad (27)$$

where P = axial compressive force
 Q = transverse shear
 M = bending moment
 p = applied distributed axial force
 q = applied distributed transverse force
 m = applied distributed bending moment.

These forces are shown in Figure 2-7.

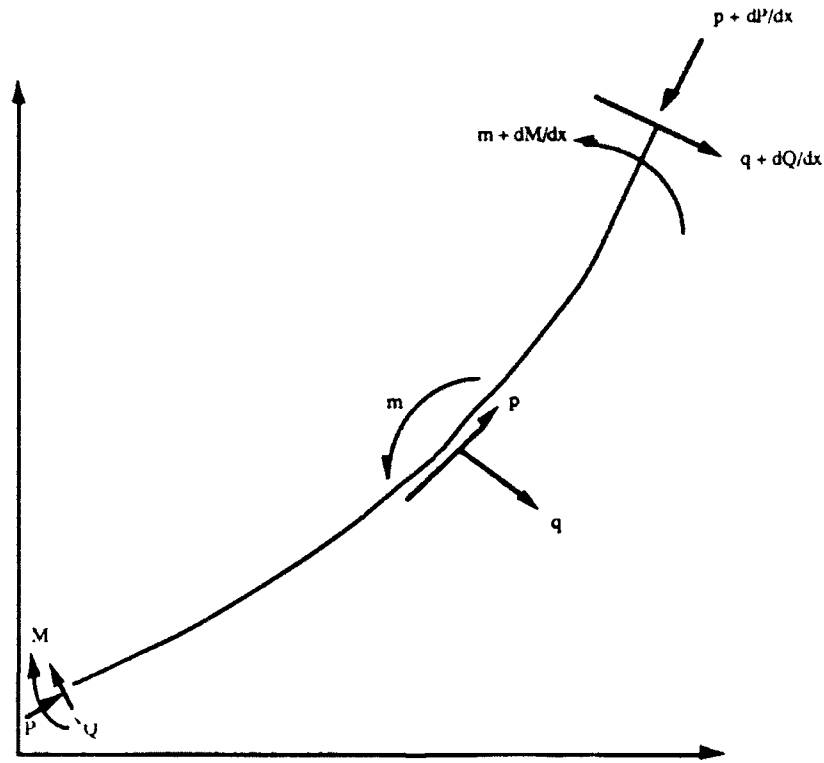


Figure 2-7: Free Body Diagram of Fiber

From these equations, the composite's buckling stress can be determined:

$$\sigma_c = \frac{G_m}{1 + \nu_f} + \nu_f \frac{E_f I_f}{h_f} \left(\frac{\pi}{l} \right)^2 \quad (28)$$

where h_f = thickness of the fiber layer.

An expression, including fiber curvature and the matrix material nonlinearity, can be developed using the distributed moment [21]:

$$\sigma_c = \nu_f \left[GLT + \sqrt{\frac{4E_m E_f}{h_m \pi}} \right] \frac{\gamma LT}{\gamma LT + \pi a_o/l} \quad (29)$$

where G_{LT} = the composite shear modulus
 γ_{LT} = the average shear strain.

A recent study conducted by Lessard [22,23,24] at Stanford University attempted to model the composite as a series of simply supported beams connected by springs as shown in Figure 2-8:

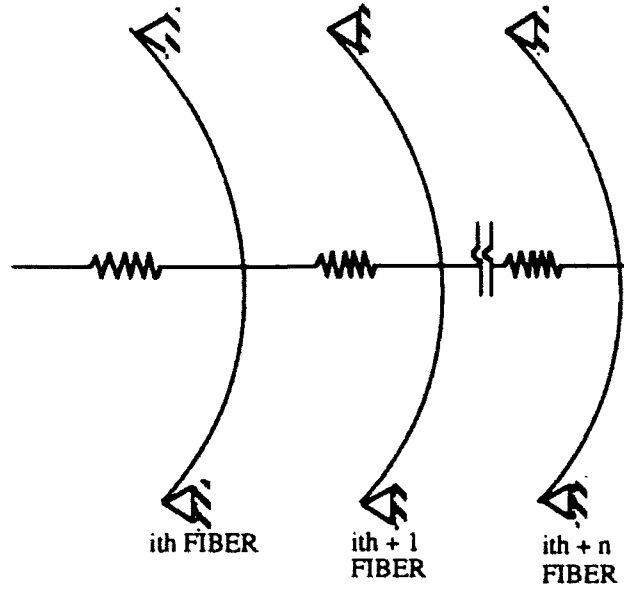


Figure 2-8: Modeling of Composite as Springs

The theory uses a strain energy method which incorporated the strain energy of the fiber bending, matrix extension, and matrix shearing as well as the work done by any applied load to produce an expression containing the total energy of a composite. The strain energy of loading is presented as

$$\Pi_i^f = \frac{1}{2} \int_0^l E_f I_f \left(\frac{d \bar{w}_i}{dx} \right)^2 dx \quad (30)$$

where \bar{w}_i = the total axial displacement of the fiber relative to a initial point.

Since \overline{w}_i is similar to V in equation (18), then V will be used from now on in the place of \overline{w}_i . The strain energy due to matrix extension is the tension in the matrix resulting from the relative lateral displacement of the adjacent fibers. The expression is:

$$\Pi^{\epsilon}_{i, i+1} = \frac{2 c E_m t_m}{2} \int_0^l \left(\epsilon_{i, i+1} \right)^2 dx \quad (31)$$

where t_m = the matrix thickness

$\epsilon_{i, i+1}$ = the strain of the i th fiber with respect to the $i+1$ fiber.

The strain energy due to matrix shearing is approximately expressed by:

$$\Pi^{\gamma}_{i, i+1} = \frac{2 c E_m t_m}{2} \int_0^l \left(\gamma_{i, i+1} \right)^2 dx \quad (32)$$

where $\gamma_{i, i+1}$ = the strain of the i th fiber with respect to the $i+1$ fiber.

Finally, the work done by the load is

$$\Pi^P_i = -\frac{P_i}{2} \int_0^l \left(\frac{dV}{dX} \right)^2 - \left(\frac{dV_o}{dX} \right)^2 dx \quad (33)$$

where P_i = the load applied to the i th fiber.

The total energy of the system can be written as the summation of all the individual energies:

$$\Pi = \sum_{i=1}^N \Pi^p_i + \sum_{i=1}^N \Pi^f_i + \sum_{i=1}^{N-1} \Pi^e_{i \ i+1} + \sum_{i=1}^{N-1} \Pi^y_{i \ i+1} \quad (34)$$

Taking the variations of this equation with respect to a given loading condition (i.e. shear stress, normal stress, transverse stress, or applied load) will lead to an equilibrium equation for the system and a critical load that can be isolated in the resulting expression. With this analysis Lessard took into account fiber imperfections, material nonlinearity (using the Hahn-Tsai equation), and non-uniform loading conditions which can result from constant displacement or uneven loading of a composite. From these equations critical stresses could be obtained and failure modes determined. The failure modes which Lessard intended to model include matrix tensile cracking, matrix compression failure, fiber buckling failure, and compression-shearing failure [22,23,24].

For the work herein, in addition to finite element analysis and experimentation, a complex variable analysis was used to determine the point stresses at a given location of a composite with a circular hole. The technique was presented by Gurdal and Haftka [25] and is based on a system of equations developed by Savin [36] of the former Soviet Union. A discussion of the results obtained from the experimental, computational, and the complex variable analysis's is presented in Section V. A FORTRAN code was developed by the writer to incorporate the equations for computing the point stresses. The equations, the code, and a discussion of the development of the code are presented in Appendix B of this thesis.

The compressive theories represented in this section are not the only compressive theories in existence. Indeed, many of the references listed contained proposed methods that are compressive modeling techniques or can be modified for compressive failure. These theories illustrate the diversity in the methods with which engineers and scientists try to model the characteristics of compressive failure. The common thread throughout each of

these recent theories is that the composite is never perfect. These small eccentricities in the straightness of the fiber can result in a substantially lower compressive strength. In order to understand the true nature of compression in a composite material one must understand how each fiber is interacting with the matrix around it and the other fibers near it. This is neither practical nor possible at the present time. What can be done is to accurately model the response of the composite while keeping the cost associated with this modeling to a minimum.

B. Linear Finite Element Theory

To understand Dr. Sandhu's theory one must first have a good understanding of what finite element theory is and how it can be properly used. The Finite Element Method (FEM) is a numerical procedure for analyzing structures and continua. Problems addressed by FEM are usually too complicated to be solved using a closed analytical form. The FEM depends upon the use of computers to perform the numerical calculations and very rarely produces an exact solution. The program used in this thesis, PLNRS, is a finite element modeling program developed by Dr. R. S. Sandhu and is used for modeling the failure initiation, progression, and strain contour plotting. The technique uses a grouped ply analysis and incorporates the number and orientation of the different plies throughout the composite material. While the program models nonlinear material behavior, it uses constant strain triangles as elements in the model.

The constant strain triangle is shown in Figure 2-9 [26]. The element is two dimensional and has six separate degrees of freedom.

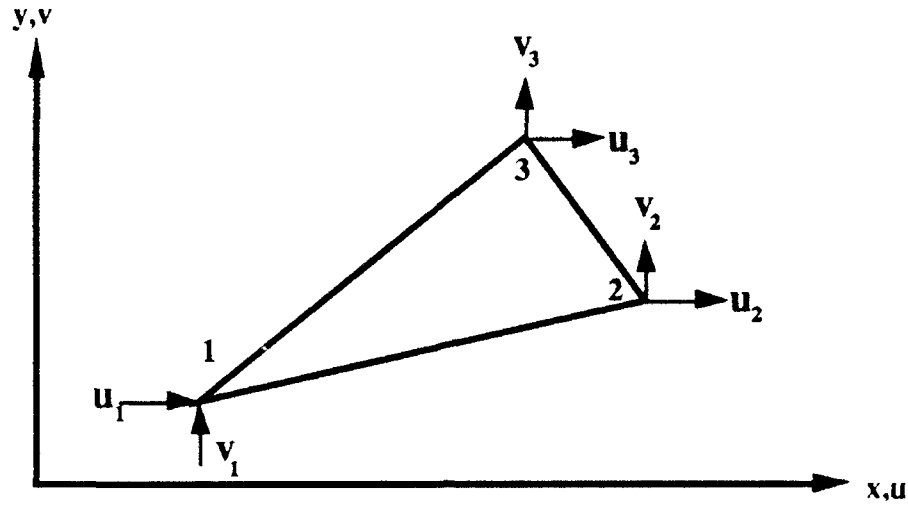


Figure 2-9: Constant Strain Triangle

It is one of the earliest finite elements and is based on a polynomial that is complete in both x and y direction displacement:

$$u = a_1 + a_2x + a_3y \text{ and } v = a_4 + a_5x + a_6y \quad (35)$$

where u, v = displacement in the x,y direction respectively.

The triangle can be subdivided into three separate triangles, each having its own area as shown in Figure 2-10. The area for each section can be computed using simple trigonometry. The formula to compute areas is shown below:

$$A_1 = \frac{y + y_3}{2} (x_3 - x) + \frac{y_2 + y_3}{2} (x_2 - x_3) - \frac{y + y_2}{2} (x_2 - x) \quad (36)$$

Taking the first partial derivative of A_1 with respect to x and y yields:

$$\frac{\partial A_1}{\partial x} = -\frac{y + y_3}{2} + \frac{y + y_2}{2} = \frac{y_2 + y_3}{2} \quad (37)$$

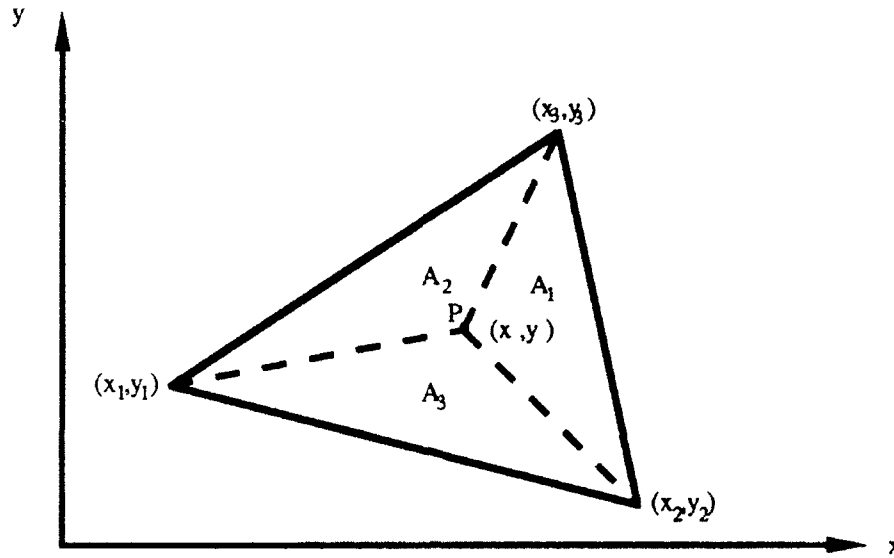


Figure 2-10: Area of Triangle

$$\frac{\partial A_1}{\partial y} = -\frac{x_3 - x}{2} - \frac{x_2 - x}{2} = \frac{x_3 + x_2}{2}$$

The same can be performed on A_2 and A_3 to produce:

$$\frac{\partial A_2}{\partial x} = \frac{y_3 + y_1}{2} \quad \frac{\partial A_2}{\partial y} = \frac{x_1 + x_3}{2} \quad (38)$$

$$\frac{\partial A_3}{\partial x} = \frac{y_1 + y_2}{2} \quad \frac{\partial A_3}{\partial y} = \frac{x_2 + x_1}{2}$$

Next the area is normalized so that the formulation is done in a natural coordinate system.

The expressions are each divided by the total area, thus allowing us to rewrite the displacement equations for the individual displacements of each node:

$$u = \eta_1 u_1 + \eta_2 u_2 + \eta_3 u_3 \quad (39)$$

$$v = \eta_1 v_1 + \eta_2 v_2 + \eta_3 v_3$$

where $\eta_i = \frac{A_i}{A}$.

This expression can be rewritten in matrix form after taking the partial derivative with respect to the x,y coordinate system as:

$$\epsilon_x = \frac{\partial u}{\partial x} = \left[\frac{\partial \eta_1}{\partial x} \quad \frac{\partial \eta_2}{\partial x} \quad \frac{\partial \eta_3}{\partial x} \right] \begin{bmatrix} u_1 \\ u_2 \\ u_3 \end{bmatrix} \quad (40)$$

$$\epsilon_y = \frac{\partial v}{\partial y} = \left[\frac{\partial \eta_1}{\partial y} \quad \frac{\partial \eta_2}{\partial y} \quad \frac{\partial \eta_3}{\partial y} \right] \begin{bmatrix} v_1 \\ v_2 \\ v_3 \end{bmatrix}$$

This can be combined together in matrix form so that an equation exists which is the relationship between strain and displacement. That relation is:

$$\begin{Bmatrix} \epsilon_x \\ \epsilon_y \\ \epsilon_{xy} \end{Bmatrix} = \begin{bmatrix} y_2 - y_3 & 0 & y_3 - y_1 & 0 & y_1 - y_2 & 0 \\ 0 & x_3 - x_2 & 0 & x_1 - x_3 & 0 & x_2 - x_1 \\ x_3 - x_2 & y_2 - y_3 & x_1 - x_3 & y_3 - y_1 & x_3 - x_2 & y_1 - y_2 \end{bmatrix} \begin{Bmatrix} u_1 \\ u_2 \\ u_3 \\ v_1 \\ v_2 \\ v_3 \end{Bmatrix} \quad (41)$$

where $\epsilon_{xy} = \frac{\partial u}{\partial y} + \frac{\partial v}{\partial x}$.

The 3 x 6 matrix is designated as the B matrix [27,26]. Now the element stiffness matrix, $[k]_e$, can be formulated using the [B] matrix:

$$[k]_e = \int_A [B]^T [E] [B] t \, da = [B]^T [E] [B] t A \quad (42)$$

where t = the element thickness

E = the constitutive equations for the plane stress assumption =

$$\frac{E}{1-\nu^2} \begin{bmatrix} 1 & \nu & 0 \\ \nu & 1 & 0 \\ 0 & 0 & \frac{1-\nu}{2} \end{bmatrix}$$

The above equation for $[k]$ can be compared to the generalized stress-strain relationship in equation (13) to form a general element stiffness matrix for an orthotropic material. [5]

$$[k] = \int_A [B]^T [\bar{Q}] [B] t \, da = [B]^T [\bar{Q}] [B] t A \quad (43)$$

What the program PLNRS does is take a four noded quadrilateral element and break it into four constant strain triangles to be analyzed by the program. The model can be entered as a quadrilateral mesh, thus saving time and computer memory. The decomposition of the element is shown in Figure 2-11.

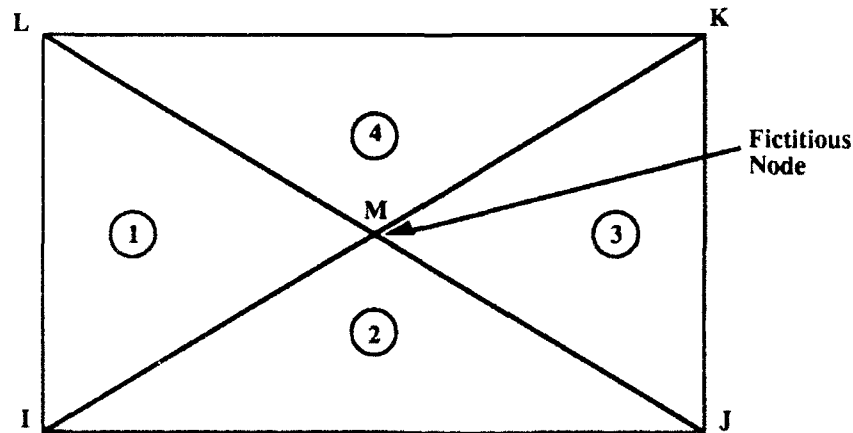


Figure 2-11: Nodal Locations

This decomposition produces a five-noded element resulting in a stiffness matrix that is 10×10 instead of 8×8 and a $[B]$ matrix that is 3×10 instead of 3×8 . Two of these rows are attributed to the fictitious node "M" shown in Figure 2-11, thus the matrices can be

reduced to form the 8 x 8 stiffness and 3 x 8 [B] matrix. This is accomplished by assuming that:

$$u_M = \frac{u_I + u_J + u_K + u_L}{4} \quad (44)$$

$$v_M = \frac{v_I + v_J + v_K + v_L}{4}$$

and then the value of U_m and V_m can be produced by this formulation and can be composed in this manner when required by the program. In order to account for the different orientations of the plies, the stiffness matrix can be formulated by summing up the individual stiffness matrices for each ply as shown below [14]:

$$[k_{eq}] = A \sum_{i=1}^n \int_A [B]^T [\bar{Q}_i] [B] t_i \quad (45)$$

where i = the i th laminate
 n = number of plies
 t_i = thickness of the i th ply.

C. Nonlinear Constitutive Relationships

As mentioned previously there have been several attempts at incorporating material nonlinearity into an analysis of a composite's strength. However, both the Petit-Waddoups and the Hahn-Tsai have shortcomings in modeling the material's response. Dr. Sandhu's program is very versatile because it predicts the initiation of damage in a composite material, the progression of damage, and the ultimate load of the composite. The program

allows for various finite elements, numerous different loading conditions, ply failure criteria, boundary conditions, and post failure element unloading options [14].

Gr/PEEK exhibits nonlinear properties in almost every unloading condition. The use of an incremental form of the constitutive law models the response of the composite well, but two assumptions must be made:

- (1) Increments of strain depend upon the strain state and the increments of stress.
- (2) The increment of strain is proportional to the increment of stress.

Because of these assumptions, Hooke's Law must be rewritten in an incremental constitutive law form for an anisotropic material as:

$$d\epsilon_i = S_{ij} d\sigma \quad (i,j = 1,2,6) \quad (46)$$

or

$$[d\epsilon] = [S][d\sigma]$$

where $d\epsilon_1$ = normal strain increment in the fiber direction
 $d\epsilon_2$ = normal strain increment in the transverse direction
 $d\epsilon_6$ = shear strain increment
 $d\sigma_1$ = normal stress increment in the fiber direction
 $d\sigma_2$ = normal stress increment in the transverse direction
 $d\sigma_6$ = shear stress increment.

For an orthotropic laminate we can simplify the expression by letting $S_{16} = S_{26} = 0$. The rest of the terms of the compliance matrix are defined by the same terms as in equation (10). Combining equations (46) and (10) we can rewrite the incremental stress-strain relationships for a given lamina.

$$d\epsilon_1 = \frac{d\sigma_1}{E_{11}} (1 - \nu_{12}R) \quad (47)$$

$$d\epsilon_2 = \frac{d\sigma_2}{E_{22}} (1 - \frac{\nu_{21}}{R})$$

$$d\epsilon_6 = \frac{d\sigma_6}{G_{12}}$$

where $R = \frac{d\sigma_2}{d\sigma_1}$ assuming $d\sigma_1 \neq 0$.

It is impossible to determine properly the incremental elastic constants (E_{11} and E_{22}) using $d\epsilon_1$ and $d\epsilon_2$ for the stress-strain curves under simple loading conditions. Under simple uniaxial loading on an anisotropic material, the resulting stress state is not the same as under biaxial loading conditions. This is best explained by an example presented by Dr. Sandhu in pictorial form in Figure 2-12.

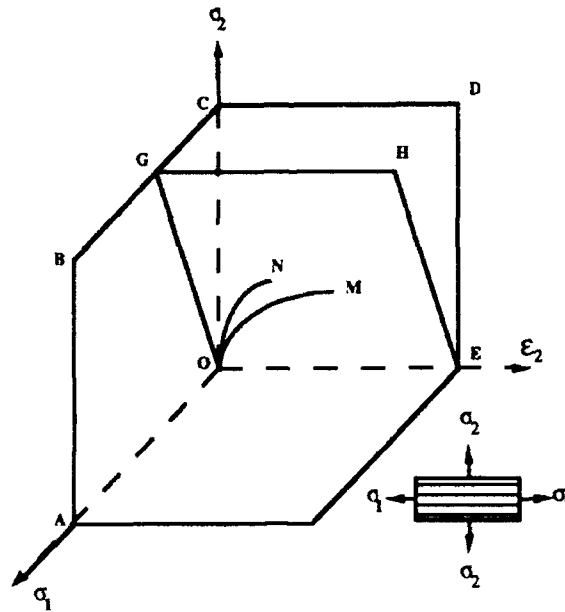


Figure 2-12: Biaxial State of Stress

For example, ϵ_2 is under a biaxial stress, (σ_1, σ_2) corresponds to the curve ON on the plane OEHG, whereas the simple stress-strain curve OM lies on the plane OEDC [7,8].

Therefore the curve ON has components of σ_1 as well as σ_2 . If ON is assumed to have only σ_2 components then the state of stress assumed is lower than the stress. This biaxial equivalent strain is one of the major attributes of this technique and enhances its ability to predict failure in a composite.

Because it would be extremely difficult and costly to produce experimental data on the biaxial state of stress, we calculate the biaxial state of stress based on uniaxial data. Dr. Sandhu used equation (42) to calculate an equivalent strain by defining:

$$d\epsilon_1|_{eq} = \frac{d\sigma_1}{E_{11}} = \frac{d\epsilon_1}{(1 - \nu_{12} R)} \quad (48)$$

$$d\epsilon_2|_{eq} = \frac{d\sigma_2}{E_{22}} = \frac{d\epsilon_2}{(1 - \frac{\nu_{21}}{R})}$$

where $d\epsilon_1|_{eq}$ and $d\epsilon_2|_{eq}$ = the equivalent strains in the 1 and 2 directions, respectively.

Using equation (46) we can invert the $[S_{ij}]$ matrix and get an expression that will give us the incremental stress value for a given incremental strain value and a calculated stiffness matrix:

$$[d\sigma]_k = [Q]_k [\epsilon]_k \quad (49)$$

where $[C]_k$ = the incremental stiffness matrix for the kth ply

$[d\sigma]_k$ = the incremental stress for a given ply relative to the material axis

$[d\epsilon]_k$ = the incremental strain for a given ply relative to the material axis.

We can use a ply by ply version of equation (10), where the θ_k is the angle for the k th ply, to transform the stiffness matrix and stress and strain vectors from the materials axis 1, 2 to the coordinate axis x, y. The transformations are represented as:

$$[d\bar{\sigma}]_k = [T]_k^{-1} [d\sigma]_k \quad (50)$$

$$[d\bar{\epsilon}]_k = [T]_k^{-1} [d\epsilon]_k$$

$$[\bar{Q}]_k = [T]_k^{-1} [Q]_k [T]_k$$

where $[T]$ = the axis transformation matrix equation (12)

Because of the stacked ply configuration, we can assume that the stresses are distributed uniformly throughout the thickness of each ply. This assumption allows us to calculate the stress resultant increments $[dN]$ in x, y coordinates as:

$$[N] = \sum_{k=1}^p [d\bar{\sigma}]_k t_k \quad (51)$$

where t_k = the thickness of the k th ply

p = the number of plies.

Using equation (50) we can rewrite equation (51) as

$$[dN] = \sum_{k=1}^p [\bar{Q}]_k [d\bar{\epsilon}]_k t_k \quad (52)$$

As mentioned before, the assumption is that all plies will deform in the same manner. This leads to the feature that each element of a through-the-thickness stack will have the same location. This allows us to assume that:

$$[d\bar{\epsilon}]_k = [\epsilon^0] \quad (53)$$

where $[\epsilon^0]$ = the strain of a given stack of elements.

Therefore, we can rewrite equation (53) as

$$[dN] = [A] [\epsilon^0] \quad (54)$$

$$\text{where } [A] = \sum_{k=1}^p [\bar{Q}]_k t_k$$

This allows us to solve for strain by inverting the $[A]$ matrix so that:

$$[\epsilon^0] = [A]^{-1} [dN] \quad (55)$$

In this equation $[A]^{-1}$ represents the average compliance properties for the laminate during the $n+1$ th load increment, which is not known when the $n+1$ th load increment is applied. To solve this, the elastic properties at the end of the n th load increment are used to compute the laminate strain increments $[\epsilon^0]$ and stress increments $[d\sigma]_k$ in the plies. This method is known as the "predictor-corrector" technique where:

$$[\epsilon^o]_{n+1} = [A]_n^{-1} [dN]_{n+1} \quad (56)$$

This equation is used by PLNRS in the incremental scheme to solve a given problem. Once $[\epsilon^o]_{n+1}$ has been calculated from equation (56) then $[d\sigma]_k$, $[d\epsilon]_k$, and $d\epsilon_i|_{eq}$ can be obtained. The stress and strain increments can be added to the summation of incremental stress and strains to calculate the average elastic properties of each of the plies and a new $[A]_n^{-1}$ is formed by the summation of the incremental elemental stiffness matrices. This incremental scheme is performed in each iteration of the program until the values of $[\epsilon]_{n+1}$ and $[\epsilon]_n$ have converged to a given tolerance [7,8]:

$$\frac{[\epsilon^{norm}]_{n+1} - [\epsilon^{norm}]_n}{[\epsilon^{norm}]_{n+1}} < 0.001 \quad (57)$$

where ϵ^{norm} = the norm of the strain vector = $\sqrt{\epsilon_x^2 + \epsilon_y^2 + \gamma_{xy}^2}$

To affect this stress-strain relationship the mechanical properties are inputted in the file in the form of tabular data at the end of the PLNRS data file. The properties are determined for this study through five separate uniaxial loading tests conducted on Gr/PEEK specimens. The procedures for obtaining this data will be discussed in Section IV of this thesis.

D. Strain Energy Failure Theory

There comes a point where a composite subjected to incremental compressive loading can no longer sustain a given load. At this point a composite reaches its ultimate

strength and fails. This ultimate load can be established under a general stress state by a criterion developed by Sandhu [7,8]. This criterion is a function of the stress, strain, and material characteristics and is represented by the scalar function:

$$f(\sigma, \epsilon, k) = 1 \quad (58)$$

where σ = the stress state

ϵ = the strain state

k = the material characteristics.

This equation can be written explicitly, using the strain energy of the materials to represent the nonlinear behavior. In the case of an orthotropic material, strain energies are independent of each other so they characterize all of these various effects of the material under a biaxial stress state. A linear combination of the different energies is written as:

$$\sum_{i=1}^3 \sum_{j=1}^3 k_{ij} \left[\int_{\epsilon_{ij}} \sigma_{ij} d\epsilon_{ij} \right]^{m_{ij}} = 1 \quad (59)$$

where ϵ_{ij} = current strain components

m_{ij} = the parameter defining the failure surface in strain-energy space.

The equation can be expanded to represent the plane stress condition:

$$k_1 \left[\int_{\epsilon_1} \sigma_1 d\epsilon_1 \right]^{m_1} + k_2 \left[\int_{\epsilon_2} \sigma_2 d\epsilon_2 \right]^{m_2} + k_6 \left[\int_{\epsilon_6} \sigma_6 d\epsilon_6 \right]^{m_6} = 1 \quad (60)$$

where k_1, k_2, k_6 = total area under the stress-strain curve in the 1, 2, 6 direction.

This equation assumes that the failure criterion is based upon the premise that the strain energies in the transverse, longitudinal, and shear directions are independent terms. This consideration requires that the ratio of each strain energy to the total maximum strain energy must be determined. The terms m_1 , m_2 , and m_6 are the shape factors representing the shape of the failure surface in strain energy space. The possible values for this parameter are $m_1=m_2=m_6=2$ for a spherical shape and $m_1=m_2=m_6=1$ for a pyramidal surface. This failure criterion is compared for different values of m to various other failure criteria in Figure 2-13.

This comparison was conducted by Sandhu on a boron-epoxy material system. The comparison was confined to the first quadrant of the stress state. One of the problems with the use of the m parameter is that the biaxial stress state data must be acquired to determine suitable values of m_1 , m_2 , and m_6 . As mentioned this is a very difficult task to do, so for this thesis the value of m_i will be taken to be unity.

Since a composite material is constructed of two separate components, one of the questions that must be determined is whether the failure is a fiber failure or matrix failure. The answer to this question will have a bearing on how the element is unloaded and how the failed element affects surrounding elements. The constituent component that fails first can be determined using the following relationship (60):

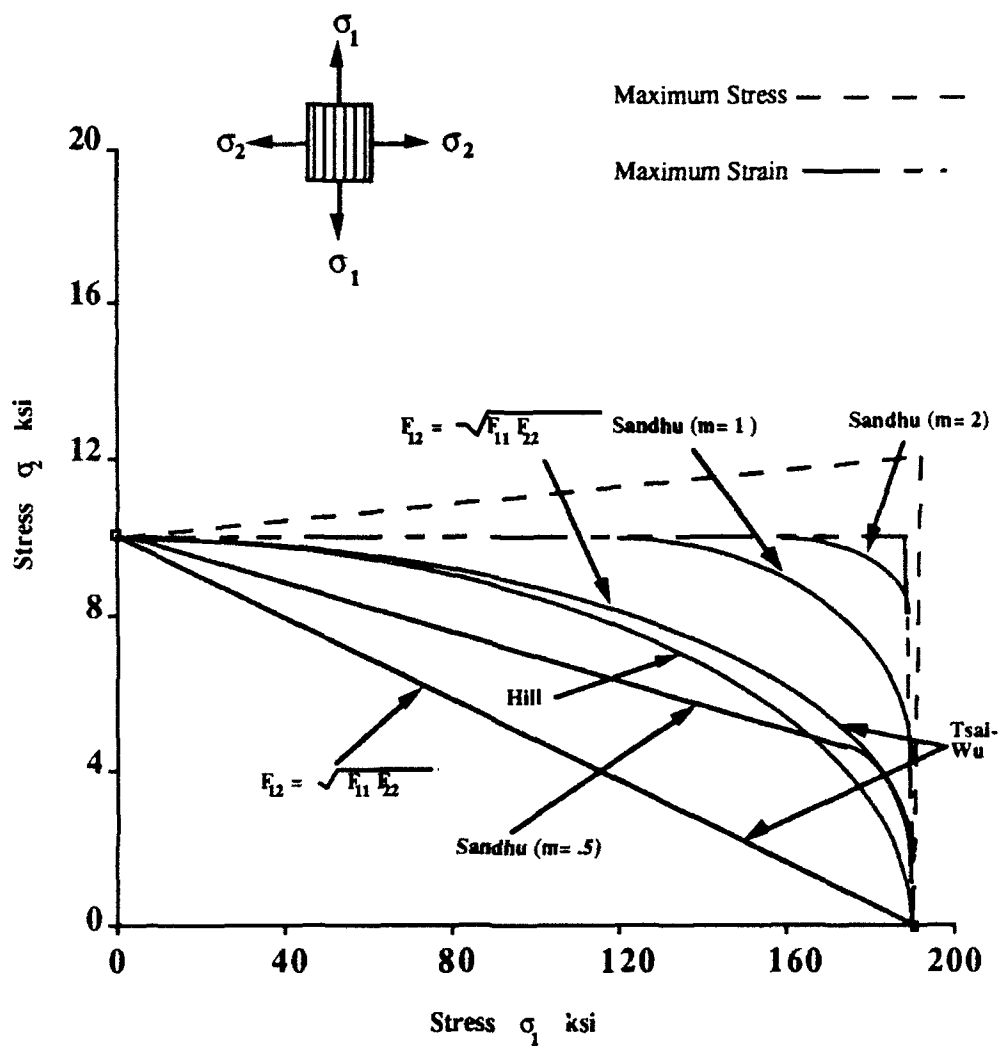


Figure 2-13: Comparison of Failure Criteria

$$\frac{k_1 \left[\int_{\epsilon_1} \sigma_1 d\epsilon_1 \right]}{\sum_{i=(1,2,3)} k_i \left[\int_{\epsilon_i} \sigma_i d\epsilon_i \right]} = \text{Check} \quad (61)$$

In a composite, if the matrix should fail the structure can still carry part of the load using the fibers. A load can be carried parallel to the fibers but will not be supported in the transverse or shear directions. If the fiber fails, the lamina will not be able to carry any significant loads and the load will be transferred to adjacent laminas and their elements. If the value of the ratio of equation (61) is greater than or equal to 0.1, then fiber failure occurs. If the element has met the criterion for failure but value of the ratio is less than 0.1 then matrix has failed instead of the fiber [7,8]. The criterion can be modified depending on the relationship between fiber and matrix materials. This value is determined using fracture testing experience with several different types of composites and has been found to yield accurate results.

Once an element in a given ply has failed it can no longer support the load imposed and the load must then be redistributed to adjacent elements within the model. There are two options within PLNRS that can be used to unload the failed elements.

Option one is a process of gradual unloading in which a failed element will not carry a load so the adjacent elements must carry the load. This unloading scheme is done by negating the affected elements modulus once the element meets the criteria for failure. This procedure will result in a gradual, incremental unloading of the element. When the stresses within the failed element have been reduced to zero the moduli are set to the nominal value of 100 psi [14]. This unloading scheme is shown in Figure 2-14.

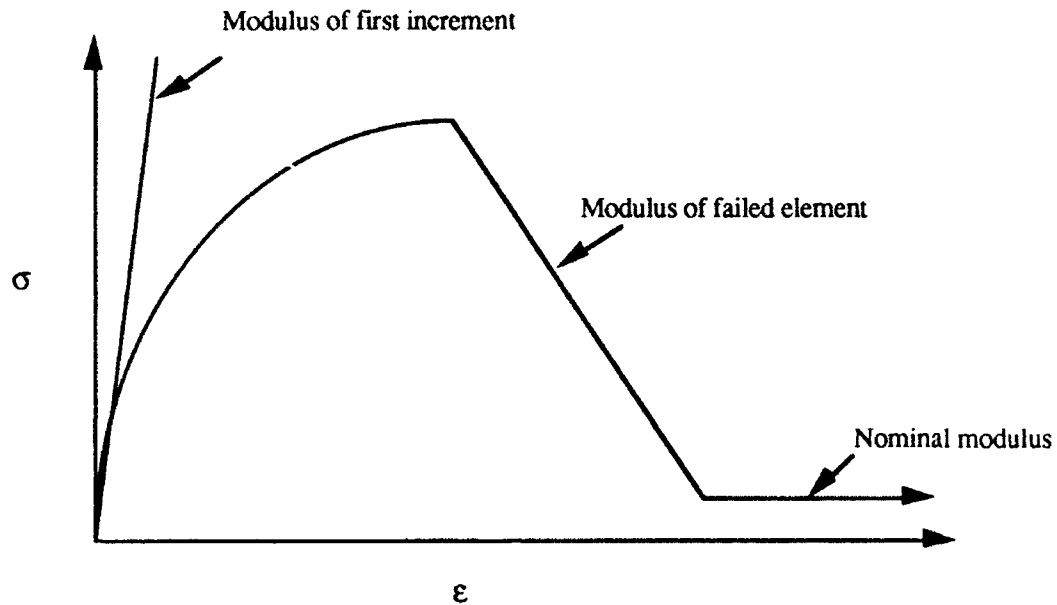


Figure 2-14: Option 1 Unloading Scheme

Option two is more conducive to a compressive type failure because it redistributes the nodal forces from a failure element to those of the elements around it. When an element reaches the maximum allowed strain energy for a given loading condition it is recorded as failed by PLNRS and its nodal forces are redistributed to the adjacent elements. This load distribution is shown in Figure 2-15. The nodal forces of the failed elements are

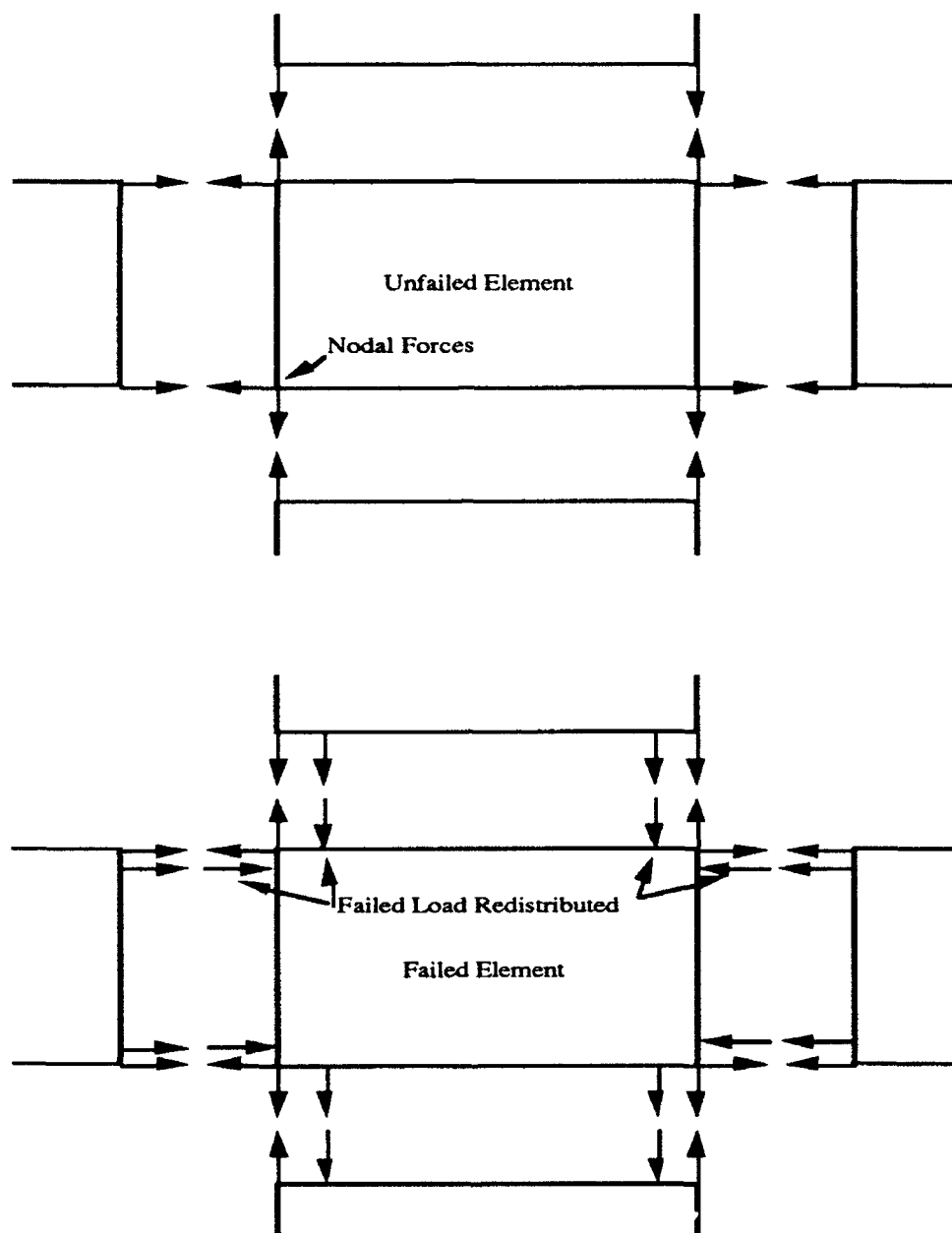


Figure 2-15: Option 2 Unloading

negated so that the sum of the nodal forces on each of the nodes of a failed element is equal to zero. The nodal forces are calculated by equation (62). This causes the nodal forces of

$$\{r_n\} = \int_{V_e} [B]^T [E] \{\epsilon_o\} dV \quad (62)$$

where E = the constitutive equations for the plane stress assumption

ϵ_o = the strain vector for the element

B is the matrix defined in equation (41)

the surrounding nonfailed elements to increase by the amount of the failed element. The model is then tested by PLNRS to ensure that no other elements fail because of the balancing of the node forces. This can result in a cascading failure where a large amount of elements will fail at once. This type of cascade failure is similar to the type of failures experienced during experimenting, where the specimen seems to failure almost instantaneously.

III. Analysis

Before composites can be applied to the various applications mentioned in Chapter I, we must be able to model the composites responses and failure characteristics. Because the use of fasteners in a composite are required for joining various composite components, it is essential that the geometry at the hole in a finite width plate be modeled. Dr. Sandhu's finite element method described in Chapter II is used to analyze the five separate Gr/PEEK laminates, each one with a centrally located 0.5" hole. This chapter will discuss the modeling techniques used in developing the finite element model, a comparison of the finite element model to models implemented in earlier analyses, and the procedures required to execute a nonlinear analysis program.

A. Finite Element Modeling

A finite element model should be able to depict the state of stress within the model, the existing boundary conditions, and the existing displacements and strains throughout the specimen. The model should also be refined in areas of interest so the stresses and displacements are adequately depicted.

The dimensions of the Boeing specimen that was used in this study are rather large so that the modeling of the entire specimen is impractical from a computational point of view. What is more practical is to model either a half or a quarter of the mesh. First the specimen was modeled using a half mesh shown in Figure 3-1. The mesh constructed was similar to the meshes used by Martin, Fisher, and Daniels [2,14,28]. This mesh has several advantages including simplicity of design and the fact that the centerline of the specimen shown in the figure lies along the centroid of the center elements. These advantages facilitate the comparison of the experimental data with the analytical results since the strain gage can also be located at the centroid of the element allowing the results to be compared with no interpolation required. However, this mesh

is rather coarse and a finer mesh would provide a more detailed picture of the progression of failure.

HALF SYMMETRY MESH

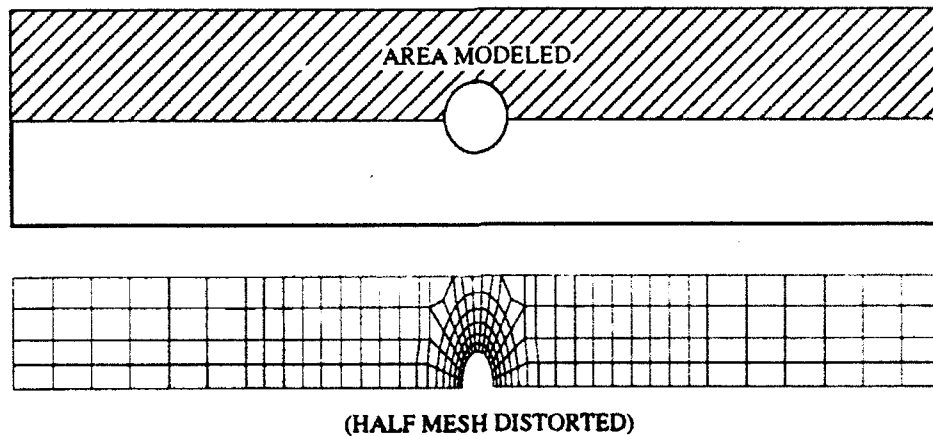


Figure 3-1: Half Mesh

When a quarter mesh is used instead of a half symmetry mesh, the model must be made fine enough to provide an accurate picture of the progression of failure. As a result, a quarter of the specimen was modeled as shown in Figure 3-2. The model was generated

QUARTER SYMMETRY MESH

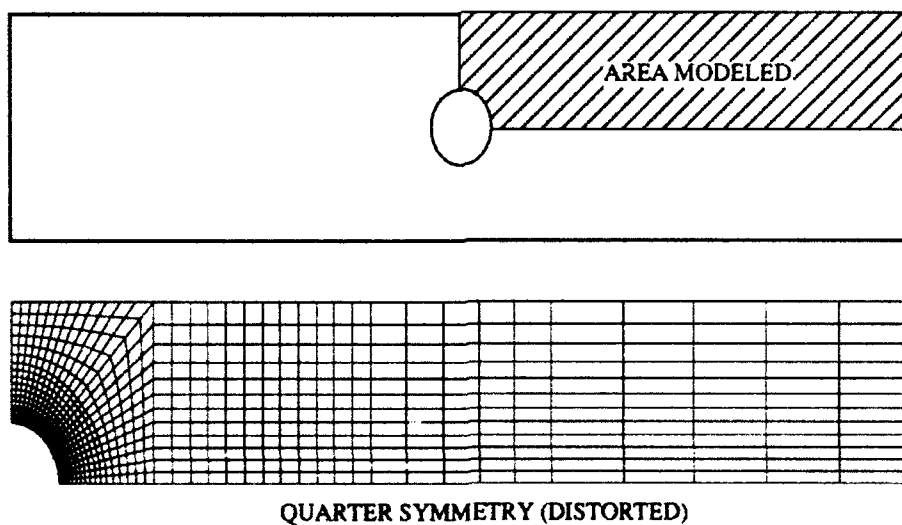


Figure 3-2: Quarter Mesh

using a mesh generation algorithm, called GENCIR, which was developed by Dr. Sandhu. The program generates a quarter symmetry mesh for a specimen containing a hole when the geometry of the model is inputted. The program requests the user to define the number of elements around the hole and the external geometry of the specimen, then it generates the mesh of 0° plies with an aspect ratio of 1-1 for the element around the hole and an aspect ratio specified by the user away from the hole. The mesh was constructed as to be so fine that the interpolation of the stress from the centroid of the elements to the edges of the model will not produce any appreciable change in the results. In this mesh the aspect ratio was 1-1 around the hole and within the first third of the far field, going to a 2-1 then 4-1 aspect ratio as the distance away from the hole increases.

Once the mesh was generated, it had to be adapted for each of the five different ply layups. When the mesh is generated it is only one ply thick. Each of the laminates used for this thesis has 16 separate plies. The layups are modeled in a stacked configuration that is shown in Figure 3-3. The 0° and 90° laminates are modeled with a one ply element that is 16 plies thick or 0.084". The $[0^\circ/90^\circ]_{4s}$ and $[\pm 45^\circ]_{4s}$ laminates are modeled as two through-the-thickness plies of 0.042" thick. The $[0^\circ/\pm 45^\circ/90^\circ]_{2s}$ laminate is modeled as four through-the-thickness elements each of 0.021" [14]. Since the plies are modeled as one ply of a specified thickness, the interlamina stresses discussed in Chapter II are neglected. The result of neglecting these forces will be discussed in Chapter V.

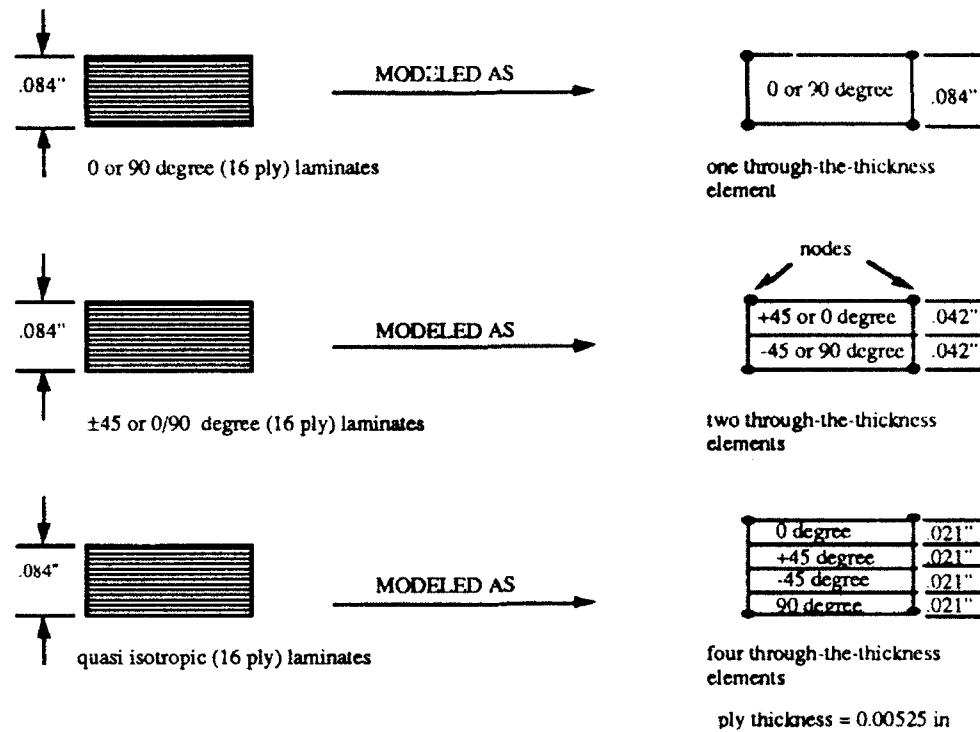


Figure 3-3: Modeling of the Ply Thicknesses

The elements within a through-the-thickness finite element model share the same nodes so the number of nodes remains constant from model to model. However, the number of elements per a layup change as the number of plies changes. The total number of elements is

$[0^0]_{16}, [90^0]_{16}$	672 elements
$[0^0/90^0]_{4s}, [\pm 45^0]_{4s}$	1344 elements
$[0^0/\pm 45^0/90^0]_{2s}$	2688 elements

Dr. Sandhu's program, GENCIR, was modified by the author to allow the generation of meshes with multiple directional layups.

B. Comparison of the Meshes

The concern with this modeling is whether the stresses and strains are being accurately predicted by the model. Martin created four different meshes, each one of a progressively finer construction as shown Figure 3-4. Stress concentration was calculated around the hole and the values were compared to values predicted by R.E. Peterson [29].

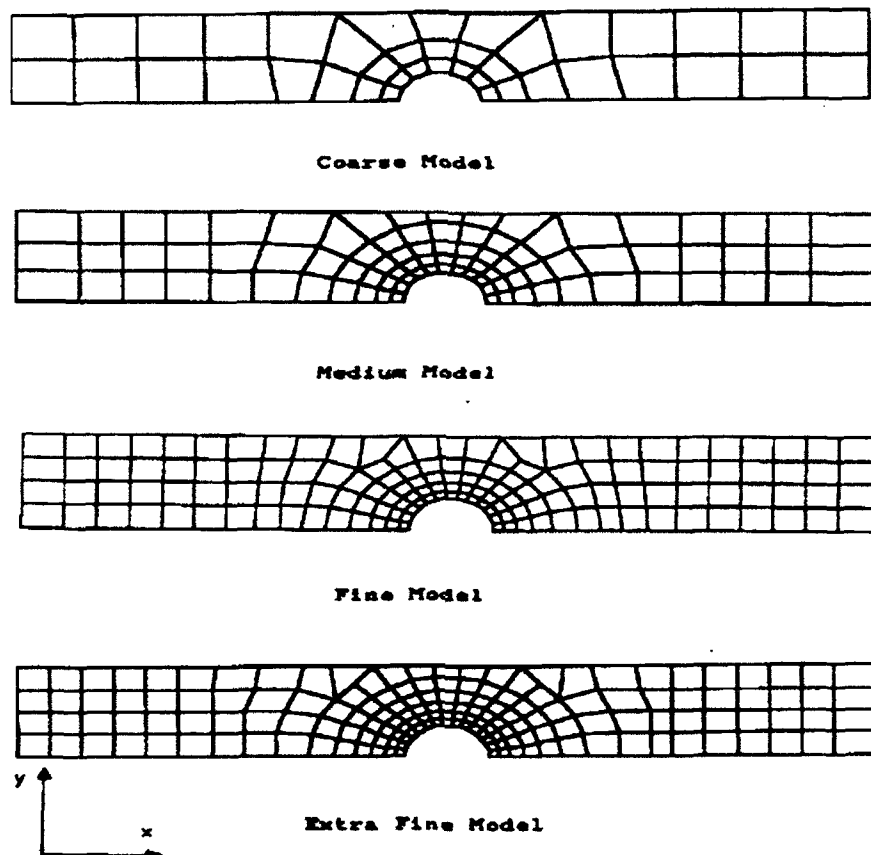


Figure 3-4: Martin/Fisher's Meshes

Fisher and Daniels also performed this analysis and discovered that the value of the stress concentration converges monotonically towards the value of 3.27 [2,28]. This compared favorably to the value of 3.46 obtained by Peterson . The same analysis was conducted

on the quarter mesh generated for this analysis. A linear analysis was performed on the mesh using PLNRS. The analysis was run by treating the composite as an isotropic material with $E_{11} = E_{22} = 19,600,000$ psi, $\nu = 0.30$, and the shear modulus was computed using the formula:

$$G = \frac{E_{11}}{2(1 - \nu)} \quad (63)$$

The shear modulus obtained was 14,000,000 psi. The stress concentration was found by dividing the stress at the hole by the stress at the far field. (The far field is defined as the stresses greater than 2 diameters away from the hole.) The value of the stress at the edge of the hole was extrapolated using a Lagrange Interpolation Function. The stress concentration obtained was 3.275 which shows an increase towards the 3.46 value obtained by Peterson. The analysis was run again using the modulus of steel, which Peterson used in his analysis, and a value of 3.40 was found. This result agrees favorably with the Peterson value of 3.46. Thus, the finer mesh is a better representation of the stresses and strains obtained than the coarser meshes used before.

C. Boundary Conditions

Once the finite element model has been developed for each of the layups, the boundary conditions that the specimen is subjected to must be incorporated in the model. The Boeing Open Hole compression fixture is an end loaded device so the boundary conditions are fairly easy to model. The boundary conditions are shown in Figure 3-5 and are as follows:

- a. Nodes in the area designated as A were given a prescribed displacement by the data file and all nodes in this location were displaced by that prescribed amount at the

start of execution of this program. They were constrained in the y direction and displaced by the prescribed amount in the x direction.

b. Nodes in area B were not allowed to displace in the y direction since it is the centerline of the actual specimen in the x direction and the centerline would not be displaced if the loading was not eccentric in nature.

c. Nodes in area C are constrained in the x direction since this is the centerline of the specimen in the y direction and the same conditions hold true as in 'b' above.

d. Nodes in all other areas within the model are allowed to displace freely in both the x and y directions.

BOUNDARY CONDITIONS OF QUARTER SYMMETRY MESH

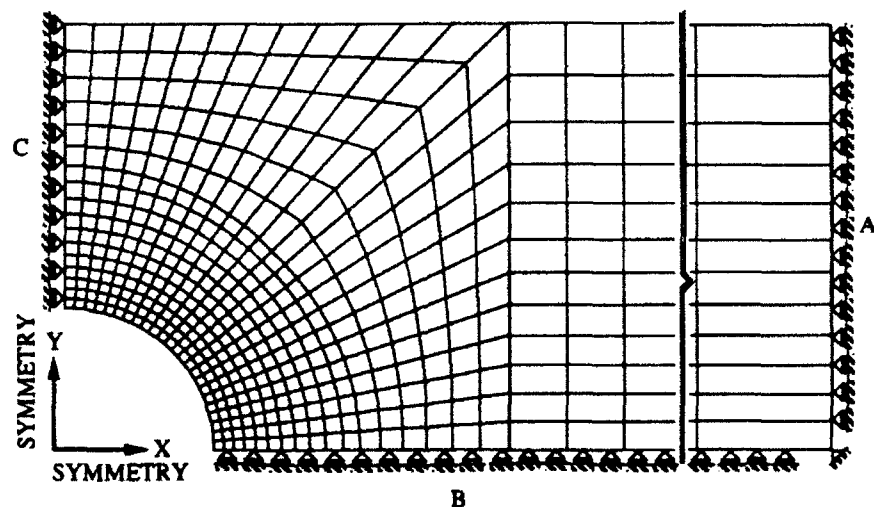


Figure 3-5: Boundary Conditions on the Model

Because the device is relatively easy to model in two dimensions, the boundary conditions can be easily modeled. There are, however, some possible complications with the device that may be difficult to model. This will be discussed in depth in Chapter V.

D. Executing a Nonlinear Analysis

Data is entered into PLNRS from a formatted datafile. The program is sent to a CRAY computer and then submitted to the computer's processors in the form of a batch file. The results of execution are written in an output file (an example of the datafile and output file are shown in Appendix A in Fisher's thesis [28].) In addition to an output file being produced, three other files are written during the program's execution. The first file, FORT.3, writes the current program information and the time at which the operation of the program was terminated. This feature allows the program to restart at the point of termination with all the existing conditions at the time of termination being applied. The next file, FORT.7, writes the stresses, strains, and centroid of each element at the end of each one of the increments during execution. The final file, FORT.9, writes the displacement data from each of the nodes at the end of each increment. The second and third files can be used with existing plotting programs to produce a graphical representation of the model at any instance during the execution. At the end of each increment, PLNRS will write to FORT.7 the current centroid, stresses, strains, and energies of each of the models' elements. The file is written in a format that can be read as a standard data file. The data file, which is written by the CRAY computer during execution is transferred to the VAX system.

Dr. Sandhu developed a software plotting package within the VAX system that will read the contents of the FORT.7 file and will create a contour plot using one of the ten quantities written to the data file. These quantities, when plotted, will show bands of constant value thus showing areas where concentrations of the quantities are present. This technique is extremely useful in determining the locations of stress concentrations within the model as well as the overall state of stress or strain.

This program is restricted to execution on the VAX system because it incorporates graphics subroutines located within Wright Laboratories' FDLENG VAX system. In addition, the plotting routines only function on a terminal with a Techtronics

T1404 emulator. To incorporate the plots within the thesis, the Versaterm program was utilized and the plots were captured in PICT format.

IV. Experimentation

The purpose of the experimental work conducted during this thesis was to determine the material properties, the ultimate strength, the composite failure modes, and the stress strain response of Gr/PEEK laminates under compression containing a 0.5" circular discontinuity. There were four separate sets of experiments conducted. The first set was conducted to determine the basic properties of a Gr/PEEK composite. Second, the applicability and limitations of the Boeing fixture were tested with one of each type of layup. The next set of tests were compression tests conducted on Gr/PEEK specimens placed inside a Boeing Open Hole compression device. These tests were to determine the stress-strain responses under compression as well as the final mode of failure. The final set was conducted using the Boeing Open Hole Compression device. Specimens from each type of layup were loaded to 90% and 95% of the expected ultimate load to determine the onset of failure within a composite and to verify the results obtained using the *Finite Element Method*. The laminates tested consisted of five different ply configurations: $[0^\circ]_{16}$, $[90^\circ]_{16}$, $[\pm 45^\circ]_{4S}$, $[0^\circ/90^\circ]_{4S}$, and $[0^\circ/\pm 45^\circ/90^\circ]_{2S}$.

Experimentation was conducted at the Structures Division of Wright Laboratories (Wright-Patterson AFB, OH). A total of eighty-four specimens were fabricated from panels laid up by Beta Industries, a USAF contractor, of Dayton, OH. Seven specimens, one each of $[0^\circ]_{16}$, $[90^\circ]_{16}$, $[0^\circ/90^\circ]_{4S}$, and $[0^\circ/\pm 45^\circ/90^\circ]_{2S}$ and three $[\pm 45^\circ]_{4S}$, were initially tested in the Boeing fixture. Twenty-five specimens were used in the basic material properties testing. Thirty specimens were instrumented with strain gages for use in a Boeing Open Hole Compression Apparatus. The last twenty-two specimens were used in the Boeing apparatus to determine the initiation and progression of failure at 90% and 95% of the ultimate compressive strength. All testing was conducted at room temperature using a 100 kips Instron Universal Testing Machine. The objective of the experimental portion of the thesis was:

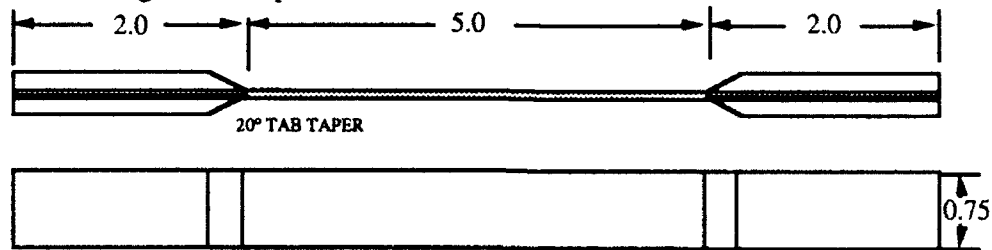
- a. To determine the basic material properties and representative stress-strain response curves for use in the analytical portion of this thesis.
- b. To determine the ultimate strength, type of failure modes, the compressive stress-strain responses, and the boundary condition effects on Gr/PEEK laminates containing a centrally located discontinuity.
- c. To determine the micromechanical mode of failure using a Scanning Electron Microscope (SEM) for each of the five layups.
- d. To determine the propagation of failure in partially failed specimens using Ultrasonic imaging.

A. Specimen Description

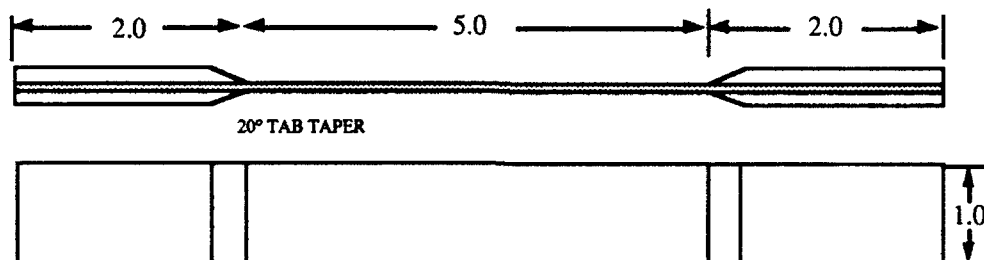
The specimens used in this thesis were fabricated from panels consisting of Gr/PEEK. They were constructed using a continuous pre-preg tape, 12 inches in width. The $\pm 45^\circ$ were measured by hand and laid into the proper stacking order, forming a "book". The book was then welded using a handheld iron that melted the matrix material together to act as a fastener. The book was then placed on a flat autoclaving surface and was bagged so that any air entrapped in and around the composite could be evacuated by the autoclave. The composite was then subjected to a temperature of $735^\circ \pm 15^\circ$ degree Fahrenheit for 20 ± 10 minutes and allowed to cool under controlled conditions so that the matrix did not consolidate unevenly over the composite panel. All the fabrication procedures were performed in accordance with ICI Fibrite specification for the fabrication of a Gr/PEEK composite component [1].

Once the fabrication procedure was complete, all the panels were subjected to a C-Scan evaluation to ensure that there were no major defects such as entrained air, resin starved areas, and fiber bunching. The C-scan was conducted by the Non-Destructive Branch of the Materials Laboratory (WL, WPAFB).

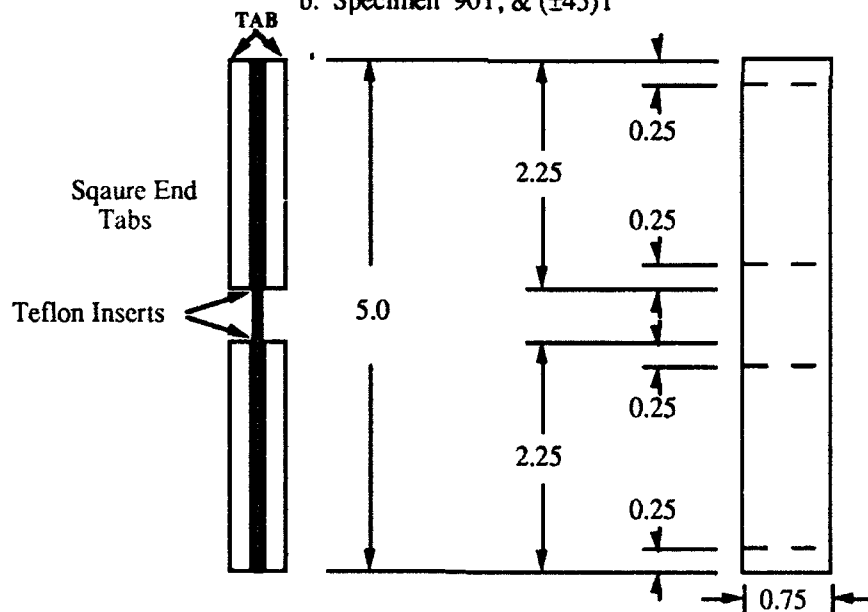
A complete cutting pattern for each of the panels is include in the Test Plan in Appendix D. Specimens fabricated from panels A and B were used for the basic material properties testing. These specimens each were fitted with tabs constructed of G-10 Glass



a. Specimen 0T



b. Specimen 90T, & (±45)T



c. Compression Specimens

Figure 4-1 Materials Property Specimens

Epoxy. These tabs provided for a uniform transfer of load from the testing machine to the specimens as well as a contact area for the hydraulic mounting grips used by the

Instron Machine. The tabs also prevented damage to the composite from the grips of the testing machine.

Panels C through G, shown in the Test Plan in Appendix D, were used for compressive testing within the Boeing Open Hole Compression apparatus. The specimens were constructed to specifications written by the Boeing Corporation in BSS -7260 and shown in Figure 4-2.

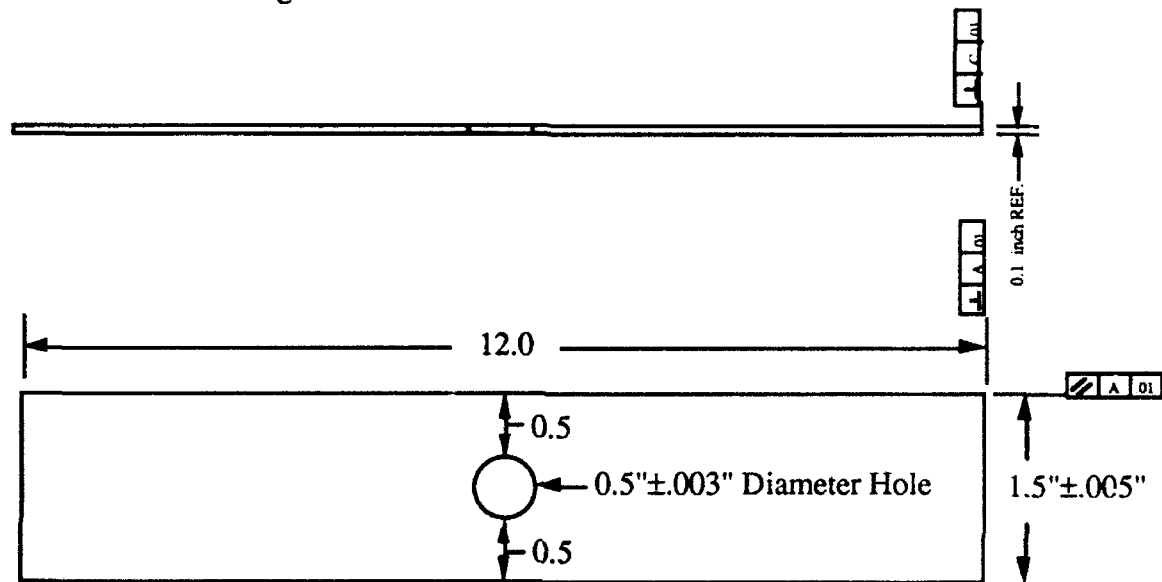


Figure 4-2: Boeing Specimens

The dimensions of the specimens were verified using mechanical measuring devices to check parallelism and to ensure that no eccentric loading conditions were introduced. The measurements of each specimen's width and thickness were taken to ensure that any specimen with a highly variable width or thickness was eliminated. The thicknesses and widths were then averaged to obtain an average area of the loading edge of the specimen so that a gross stress state of the specimen could be calculated given a load value using the formula:

$$\sigma = \frac{\text{LOAD}}{\text{WIDTH} \times \text{THICKNESS}} \quad (66)$$

The holes in the Boeing specimens were introduced by drilling a small initial hole in the center of the specimen, then expanding the hole by gradually increasing the bit size until the desired diameter was obtained. The incremental increase of the bit had to be very slight so that the drilling process did not introduce any failures or delamination around the hole.

B. Specimen Instrumentation

A total of fifty-five specimens was instrumented with strain gages. The material properties specimens were instrumented as shown in Figure 4-3.

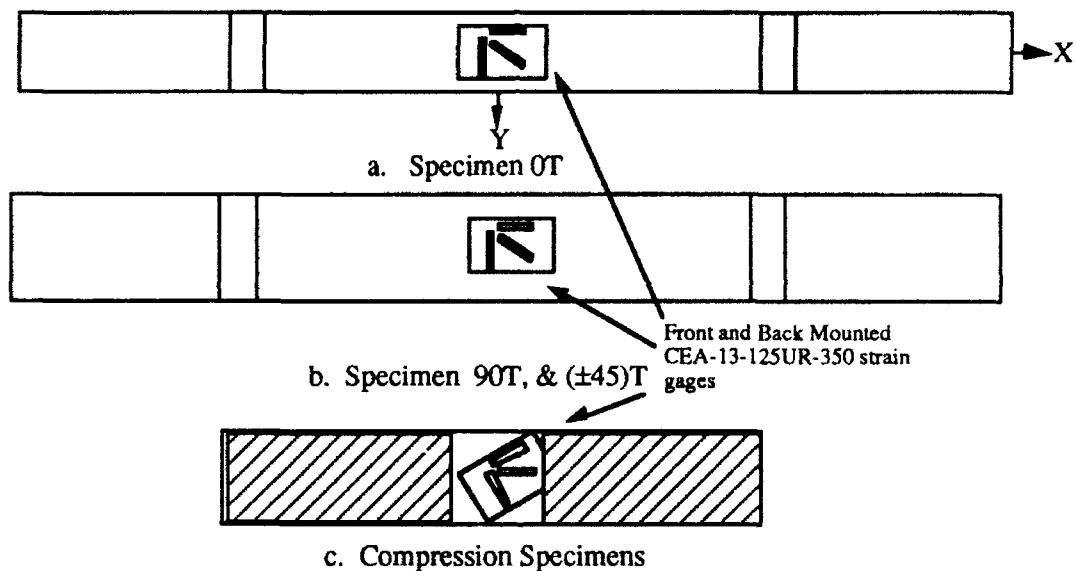


Figure 4-3: Placement of Strain Gages on Material Properties Specimens

The gages were located so that the longitudinal gage of the rosette was located at the center of the specimen and was bonded back-to-back on each specimen.

Thirty of the Boeing Specimens had four rosette strain gages, two stacked and two area gages. The locations of the gages are shown on Figure 4-4. The gages located at the hole were stacked rosettes intended to determine what the state of stress is at the hole and to detect if there were any three dimensional effects occurring at the hole. The gages

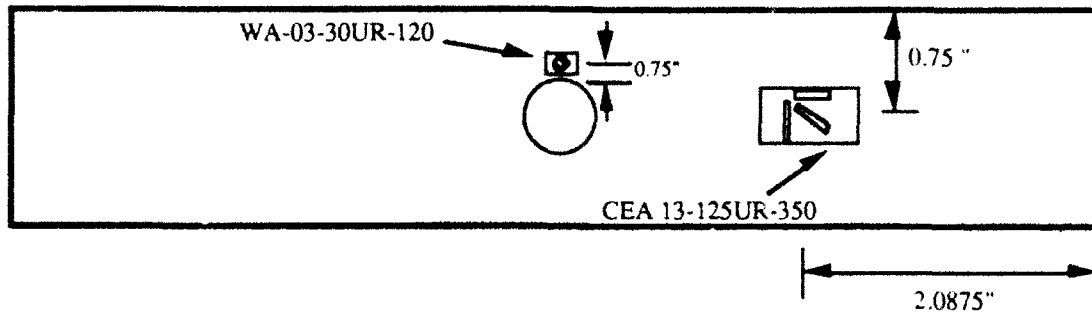


Figure 4-4: Placement of Gages on Boeing Specimen

were measured so that their location with respect a specific finite element was known. The location of the hole gage with respect to the finite element mesh is shown in Figure 4-5.

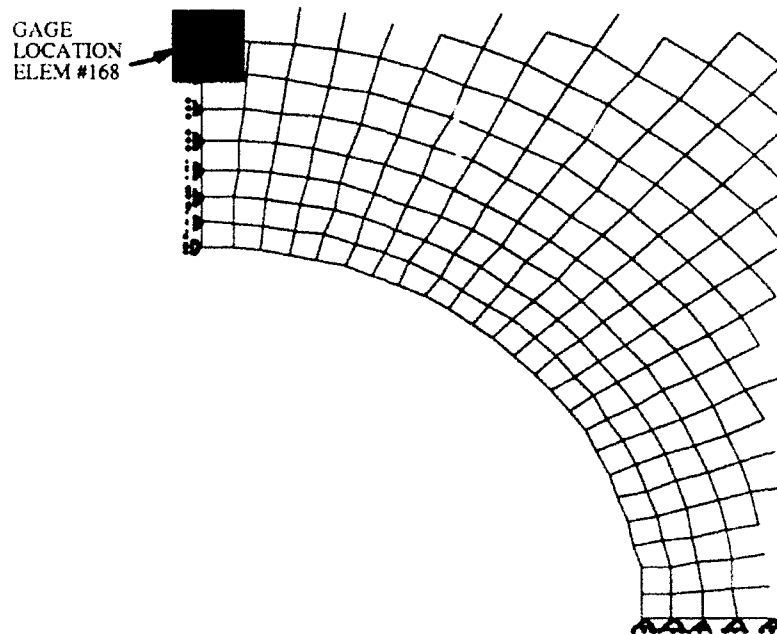


Figure 4-5: Location of Hole Gage with respect to Finite Element Mesh

The placement of the gage was important since if the center of the gage was located at the centroid of the element then a direct comparison can be drawn between the model and the actual specimen. Because of the small area of the elements it is possible that the gages could not be located at the centroid of the element so that some interpolation of the data might be required to get the exact state of stress of the model in relation to the strain.

The far field gages were used for determining if the stress field was uniform, as well as ensuring that there were no three dimensional effects occurring away from the hole. The location for the far field gages was equidistant between the centroid of the hole

and the end of the specimen. Both of the far field gages were of a configuration that measured longitudinal, transverse, and shear stress as shown in Figures 4-3 and 4-4 .

There are three reasons the back-to-back configuration for the gages was used. First, if one or more of the legs were to fail then the other gage could be used to obtain the required data. Second, if there were any three dimensional effects during the loading process they could be determined by an abrupt change in strain from one gage to another. This determination gives an excellent indication of the load level at which damage occurs at the hole. Finally, the values of the back-to-back gages can be averaged so that a stress-strain response of the material can be determined throughout the loading procedure.

For the near field or hole gages the orientation of the gages is shown in Figure 4-6. Only the transverse gage, leg A, coincides with the transverse or y coordinates of the specimen. A transformation of the data from the B and C legs must be performed to obtain the longitudinal and shear strains.

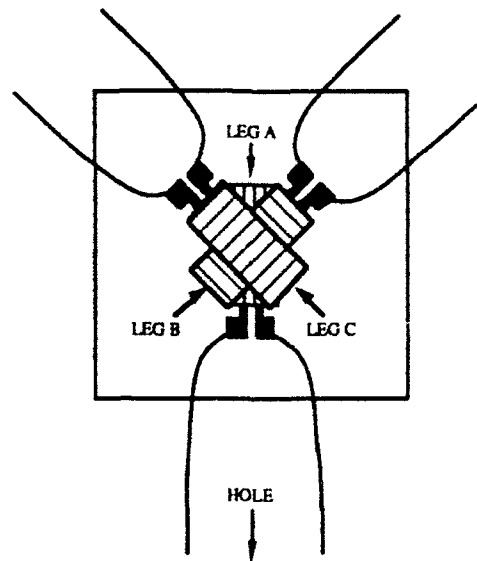


Figure 4-6: Strain Gage at Hole

For this transformation, equation (12) can be used this where θ equals 45 degrees so that the transformation looks like:

$$\begin{Bmatrix} \epsilon_x \\ \epsilon_y \\ \epsilon_{xy} \end{Bmatrix} = \begin{bmatrix} 0.5 & 0.5 & -1 \\ 0.5 & 0.5 & 1 \\ 0.5 & -0.5 & 0 \end{bmatrix} \begin{Bmatrix} \epsilon_1 \\ \epsilon_2 \\ \epsilon_{12} \end{Bmatrix} \quad (64)$$

The value for ϵ_y , ϵ_2 , and ϵ_1 is known so that the value of ϵ_{12} can be determined and then ϵ_x and ϵ_{xy} can be determined from the rest of the transformation.

The number of each specimen, as well as its cross sectional area (c/s area) and the type of test for which it will be used, is listed in Table 4-1. Some of the tests were unable to be conducted because of the failure of the specimen before a specified load was reached. The results of the experimental testing will be discussed in depth in Chapter V.

[0]_{16S}

PANEL #	SPECIMEN #	CROSS-SECTION (C/S) AREA(IN ²)	INITIAL TEST	STRAIN GAGES	PROGRESSIVE TEST
RS13992-1	1	0.1270		X	
	2	0.1270		X	
	3	0.1255		X	
	4	0.1260		X	
	5	0.1255		X	
	6	0.1261		X	
	7	0.1261			90% (F)
	8	0.1261			90%
	9	0.1286			95%
	10	0.1265			95% (F)
	11	0.1254			95%
	12	0.1264	X		

(F) DENOTES SPECIMEN FAILED BEFORE SPECIFIED LOAD WAS REACHED

Table 4-1: List of Boeing Specimens and Their Uses

[90]_{16S}

PANEL #	SPECIMEN #	C/S AREA (IN ²)	INITIAL TEST	STRAIN GAGES	PROGRESSIVE TEST
RS13992-2	1	0.1346		X	
	2	0.1311		X	
	3	0.1280		X	
	4	0.1270		X	
	5	0.1315		X	
	6	0.1300		X	
	7	0.1288	X		
	8	0.1322			90% (F)
	9	0.1338			90% (F)
	10	0.1327			90%

(F) DENOTES SPECIMEN FAILED BEFORE SPECIFIED LOAD WAS REACHED

[±45]_{4S}

PANEL #	SPECIMEN #	C/S AREA (IN ²)	INITIAL TEST	STRAIN GAGES	PROGRESSIVE TEST
RS17092-3	1	0.1331		X	
	2	0.1303		X	
	3	0.1296		X	
	4	0.1308		X	
	5	0.1318		X	
	6	0.1321		X	
	7	0.1378			90%
	8	0.1316	X		
	9	0.1318	X		
	10	0.1308	X		

[0/90]_{4S}

PANEL #	SPECIMEN #	C/S AREA (IN ²)	INITIAL TEST	STRAIN GAGES	PROGRESSIVE TEST
RS14092-2	1	0.1269		X	
	2	0.1296		X	
	3	0.1288		X	
	4	0.1312		X	
	5	0.1314		X	
	6	0.1320		X	
	7	0.1330			90% (F)
	8	0.1290			90%
	9	0.1283			90%
	10	0.1286			95% (F)
	11	0.1283	X		
	12	0.1290			95%

(F) DENOTES SPECIMEN FAILED BEFORE SPECIFIED LOAD WAS REACHED

Table 4-1: List of Boeing Specimens and Their Uses (cont)

$$[0/\pm 45/90]_{2s}$$

PANEL #	SPECIMEN #	C/S AREA (IN ²)	INITIAL TEST	STRAIN GAGES	PROGRESSIVE TEST
RS17092-2	1	0.1270		X	
	2	0.1285		X	
	3	0.1335		X	
	4	0.1346		X	
	5	0.1331		X	
	6	0.1340		X	
	7	0.1334	X		
	8	0.1339			90%
	9	0.1329			90%
	10	0.1339			95%
	11	0.1334			95%
	12	0.1329			95%

Table 4-1: List of Boeing Specimens and Their Uses (cont)

C. Instrumented Specimen Testing

All fifty-five of the instrumented specimens were tested to their ultimate strength. The Instron Machine shown in Figure 4-7 was used to determine the material properties in both tension and compression. The machine shown in Figure 4-8 was used to determine the ultimate compressive strength using the Boeing apparatus at room temperature. The load was applied at a constant crosshead velocity of 0.05 inches per second in accordance with the Boeing specification.

During the experiment, loading was determined as a function of time by the use of a strip chart connected to the Instron Machine. The chart provided valuable information because it plotted the response of the entire specimen, while the gages recorded only the response for a small area. The chart was useful in situations where the specimen might experience a momentary fluctuation in the loading process that the strain gages would not record. The gage data provided by this system included the load applied as well as the strain from each leg of the four strain gages, for a total of 13 data channels.

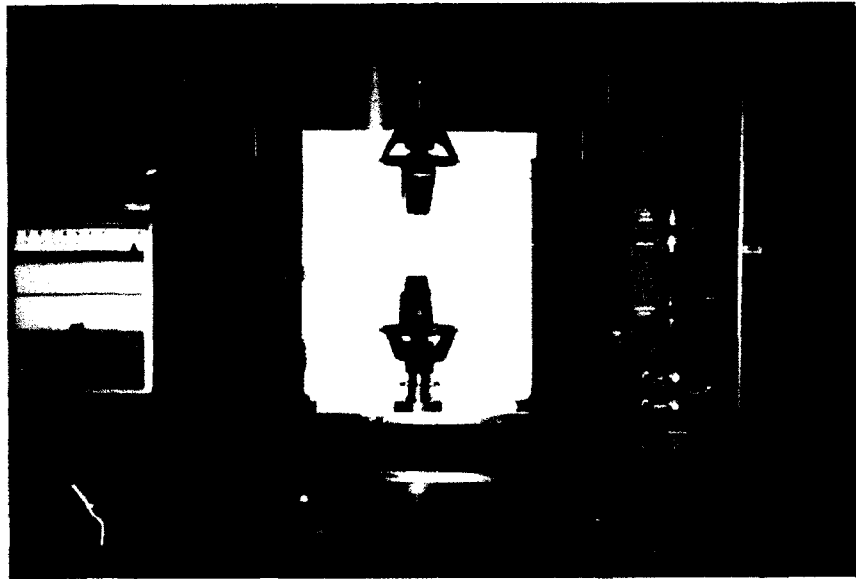


Figure 4-7: Material Properties Instron Machine

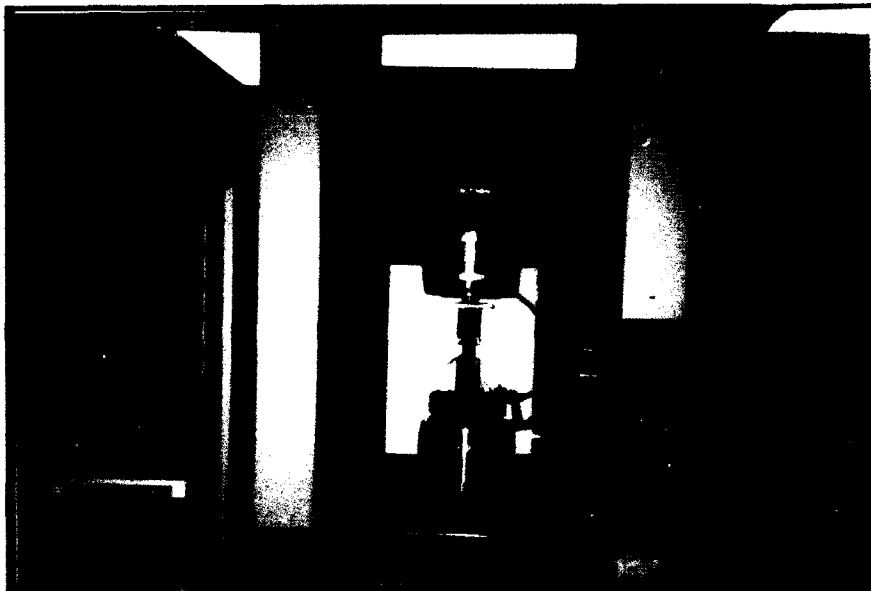


Figure 4-8: Compression Testing Instron Machine

To receive the strain gage data, a load was first applied to the specimen. A current was then sent across the gage to measure change in resistance and the strain was calculated with equation (65) [30].

$$\varepsilon = \frac{1}{S_g} \left(\frac{\Delta R}{R} \right) \quad (65)$$

where ϵ = the gage factor, set by the manufacturer
R = the resistance across the gage.

Wires were soldered to each lead of the gage and then connected to a terminal strip mounted to the Instron Machine. After the change in resistance was measured, the data was conditioned, amplified, and multiplexed into one signal. The data signal was sent to a VAX computer system for the calculation of strain and the writing of the data into a file. The file was downloaded from the VAX system to a Zenith personal computer on a 3.5" high density floppy disk. The files were converted to a Macintosh format and the data was stripped from the files and placed in a tabular format. The tabular files were then loaded into the Macintosh program, Cricket Graph, for analysis and plotting.

Different data collection rates were used depending on the type of experiment being conducted. For the material properties data, the rate was 1 sample/sec for 0° tension, 0° compression, and ±45° tension; 2 samples/sec for 90° compression; and 4 samples/sec for 90° tension. For all the Boeing fixture testing, the rate used was 2 samples/sec for 0°, 90°, 0°/±45°/90°, and 0°/90° and 1 sample/sec for ±45°. The reduced rate for the ±45° specimen was due to the high degree of elasticity that these specimens demonstrated. If the rate had not been reduced an enormous amount of data would have been produced.

D. Mounting Fixture

The used of different devices for compression testing has been debated in recent years. There have been many claims by engineers and scientist that they have designed a test fixture for compressive testing, but after careful analysis none has proven trustworthy. A device had to be chosen to study the boundary conditions effecting the failure of the composite as well as the ultimate strength of the Gr/PEEK specimens.

Since these tests were under compression, it was essential that a two dimensional load be approximated in the experimentation. Additionally, in compressive failure there were several modes that we did not wish to incur in the testing such as end brooming and out-of-plane buckling. To avoid such modes, the Boeing fixture was chosen for this task because it restrains the specimen on both the front and the back face with the use of stability plates shown on Figure 4-9. The fixture was constructed of 4340 Heat Treatable Steel by Beta Industries.

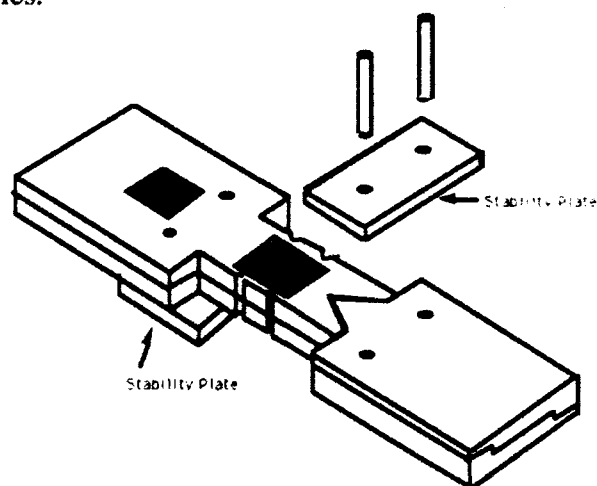


Figure 4-9: Boeing Device with Stability Plates.

While the merits and demerits of this device will be discussed later in Chapter V, it is important to note here that the fixture is not being loaded according to its original specifications. The fixture was originally designed Mr. Ron Zambora of the Boeing Corp., but has since been modified many times [31]. Originally the fixture was to have been mounted in the hydraulic grips of the Instron machine, but has been modified so that it can be end loaded. This procedure was done in accordance with the Suppliers of Advanced Composite Materials Association's Recommended Method 3-88 (SACMA RM 3-88) which recommends that the fixture be end loaded [32]. The end loading setup is shown in Figure 4-10. The plate on the top of the fixture is constructed of stainless steel, is 0.5" thick, and is placed there to provide an extremely smooth, flat loading surface.

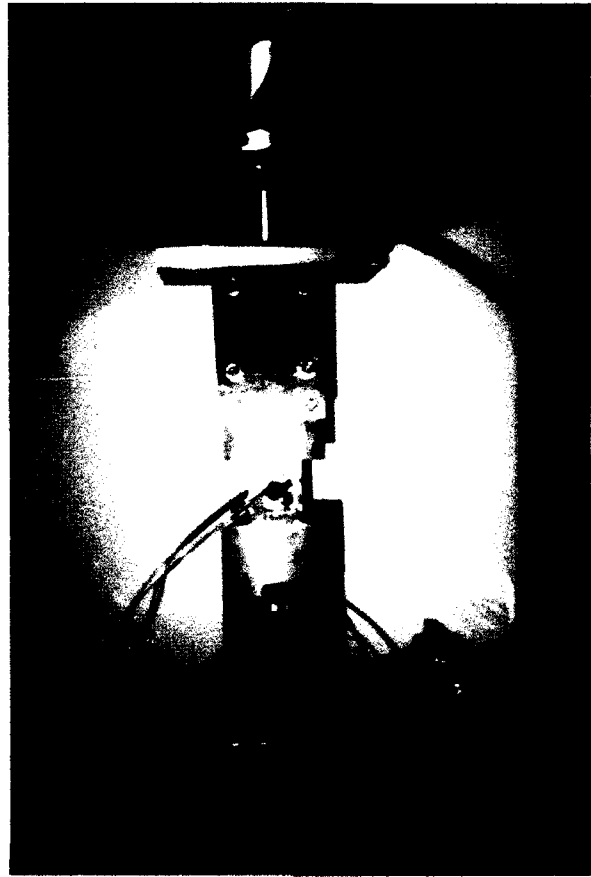


Figure 4-10: End Loading Configuration

The fixture was also modified to include the use of strain gages, both at the hole and in the far field as shown in Figure 4-11. The open cut into the steel was measured to ensure that it would not allow the specimen to buckle in the unsupported areas. In addition, for the testing of the $\pm 45^\circ$ specimens approximately 0.125" was removed from it so that the fixture would not close before the specimens failed. Once again, care was taken to ensure that the area removed from the specimen did not allow out-of-plane failure.

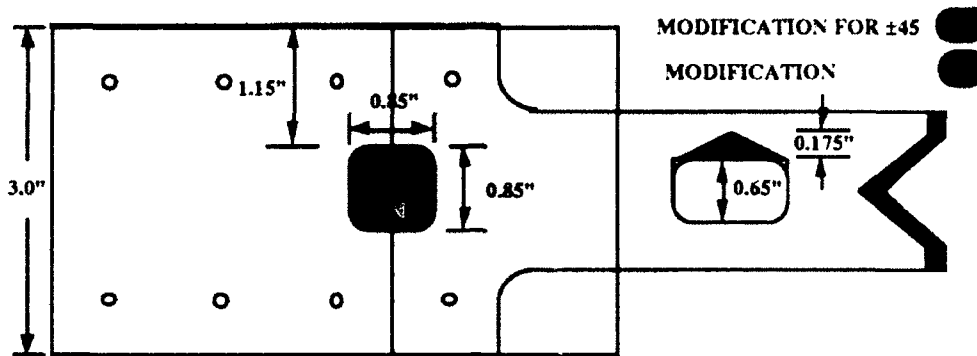


Figure 4-11: Modification to Boeing Specimen

To mount the specimen within the fixture, the fixture was completely disassembled and the specimen placed inside so that the strain gages were inside the cutout areas of the specimen shown in Figure 4-11. The wires for the strain gages were passed through the opening and the Allen head bolts were tightened by hand. The assembly was then stood on one of the ends and placed on a steel plate to ensure that the end specimen was flush with the end of the fixture. The bolts were then torqued to 5 in-lb. and the procedure was repeated for the other end of the fixture. Great care had to be taken to ensure that the fixture did not slide over the gage thus separating the wires from the gage leads or causing the gage to separate from the specimen.

Once the specimen was inside the fixture, the assembly was placed on the loading platen of the Instron machine. The wires were connected to the terminal strips and the bolts were checked to ensure that the 5 in-lb. was still present. Finally, the fixture was centered on the lower head of the loading platen and the steel loading block was placed on top of the fixture. The specimen was then loaded. The strip chart was started in motion with the crossheads. The data acquisition system started once the strip chart indicated that the specimen was beginning to take load.

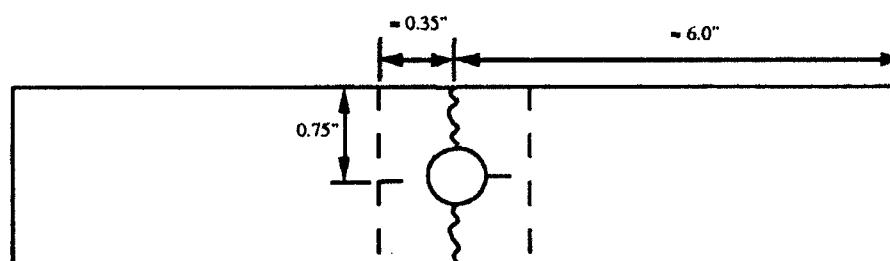
E. Post Failure Analysis

Once the specimen had failed, the data was imported from the VAX system to the Macintosh System and analyzed with the Cricket Graph Program. However after the stress-strain response of the specimens was determined, the failure surface needed to be examined to determine what the failure mechanisms were and how they contributed to the overall failure of the specimen. In addition, those composites that did not fail within the fixture or were loaded to 90 and 95% of ultimate load needed to be examined in order to determine the existing progression of failure. For this post loading analysis two techniques were used to examine the specimens that were loaded in the Boeing Open Hole Compression Device: a Scanning Electron Microscope (SEM) and an Ultrasound Analysis.

(1) Scanning Electron Microscope

The Scanning Electron Microscope allowed the author to perform a survey of the failure surface at the failed ends of the Boeing specimens. The microscope delivers resolution so fine that the end of a failed fiber can be viewed close enough to determine how it failed.

To perform this procedure the specimens tested in the Boeing device had to be cut down to fit within the evacuation chamber. The cutting pattern is shown in Figure 4-12.



All dashed areas have been cut using a band saw.
Care must be taken to ensure no delamination around the hole as well as no damage to the failure surface.

Figure 4-12: Cutting Pattern to View Failed Ends

Before the specimens were cut, the portions of the specimen 90° from the failure plane on the hole were examined to ensure that there was no damage in these areas. Next the specimens were placed in a specifically designed template and the areas were cut using a fine tooth bandsaw. The specimens were again examined to ensure that no major damage was inflicted on the cut surfaces and on the failure plane.

Then, all the remnants of the strain gages at the hole were removed and the cut portions were coated with carbon in a SPI Carbon Coating Device. The carbon coating was done to ensure that as little of the electron beam of the microscope as possible was disrupted while scanning the surface. The coated ends were then carefully placed in the evacuation chamber of the microscope. The failed surfaces were scanned and those that displayed areas of interest were photographed using a type of Polaroid camera built into the device and Polaroid 55 Professional Black and White Prints and Negative Film. The film was developed and the results are presented in Chapter V.

(2) Ultrasonic Scanning

Ultrasonic Scanning is a nondestructive procedure which allows one to investigate a specimen with a through-the-thickness or a grouped ply-by-ply inspection depending on what is desirable. There is no surface preparation for the specimen. Five specimens were submerged in a tank of distilled water and the ultrasonic transponder was centered over the specimen. A glass plate was placed underneath the specimens to reflect the signal. Once the specimens are in the tank and centered within the target area the ultrasonic transponder is lowered into the water to a depth of 1.0". A squarewave is sent from the data acquisition system to the transponder which emits the signal as a sinusoid. The signal passes through the specimen and is reflected by the glass and returns to the transponder. The signal that the transponder receives will consist of a sinusoidal function which will indicate the density of the specimen through which it passed.

When the signal returns to the transponder it is an analog signal. It is then digitized by the data acquisition system and recorded as a datafile which contains the strength of the signal which corresponds to a pixel on a computer generated image. The data file is generated on the Material Laboratories VAX system and then uploaded onto a DEC workstation. Once in the workstation the data is converted to a picture. The colors of the pictures can be modified, enhanced, and darkened to fit the users specifications. The images are printed on a color printer and then can be compared to the finite element model.

V. Results and Discussion

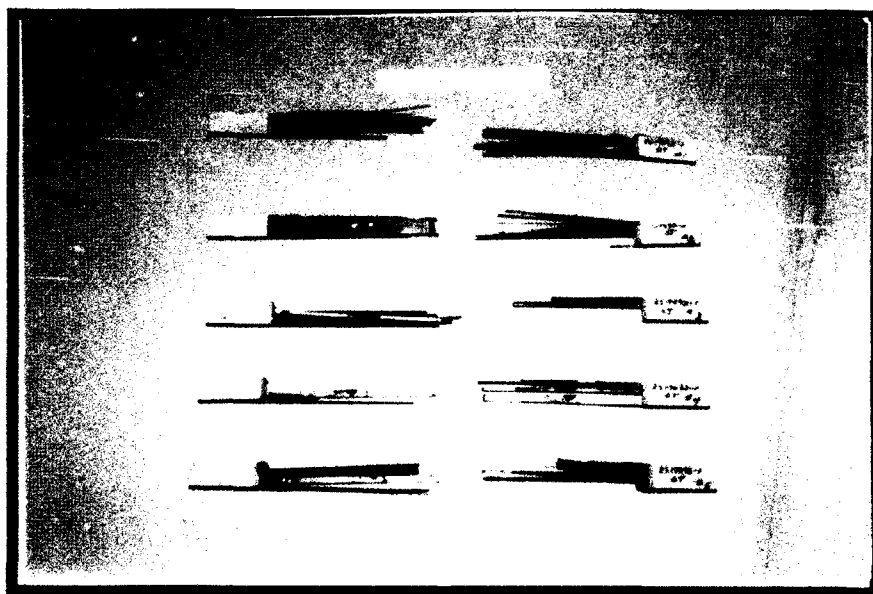
The purpose of this chapter is to present, discuss, and compare the experimental and analytical results of the investigation. The discussion will be presented in three separate sections: the results of the basic properties tests; the results of the Open Hole Compression testing and all post damage analysis techniques performed; and a comparison of the progression of failure studies and of the analytical results to the experimental results. The results of the basic properties tests contain the basic properties curves for Gr/PEEK as well as any notable items that occurred during this testing. The Open Hole Compression testing discussion contains ultimate strengths obtained for each layup, the stress-strain curves from the strain gages on the specimens, and the post damage analysis procedures conducted on the failed specimens. The stress-strain curves obtained from this section will also be used in comparing the experimental results with the analytical results. All experimental stress-strain curves were obtained from the data recorded during the loading of the specimen. The load recorded by the data acquisition system was converted to stress by dividing the loaded end area of each specimen. The global strain of the specimen was transformed from the strain data obtained from each of the strain gages, as described in Chapter 4.

For the analytical results, all the stresses were obtained from the output generated by PLNRS. The global stresses were obtained by summing all the incremental forces at the end nodes for the prescribed displacement. The sum of the forces was then divided by the model's end area, in this case $0.75'' \times 0.084''$, to produce a global stress. The global stress provided a common parameter with which to compare the analytical and the experimental. The analytical section will also include a comparison of the experimental and analytical progression of failure studies. This analysis will include comparing the ultrasonic images obtained from experimentation to the progression of failure within the analytical model.

A. Basic Properties Tests.

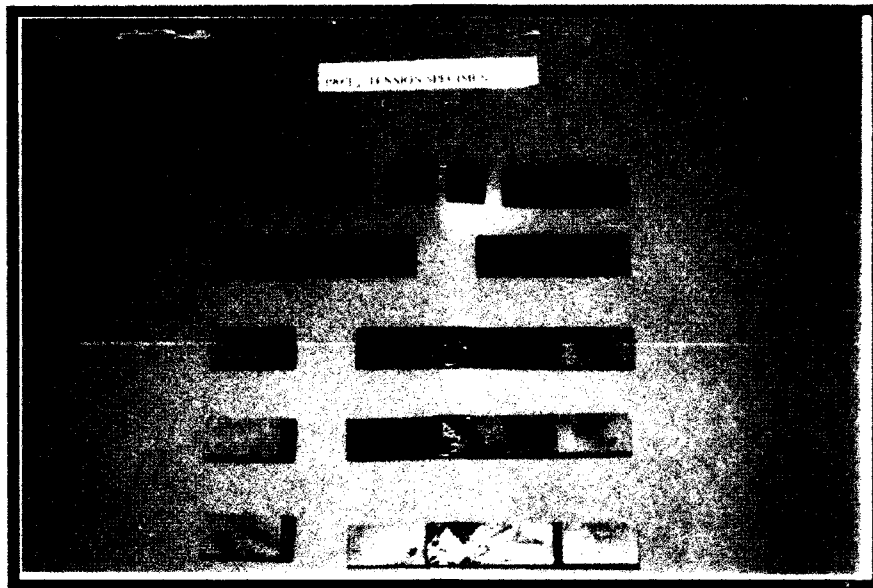
The nonlinear material properties were determined from the panels constructed by Beta Industries. When this investigation started, the author considered using the Basic Material Properties determined by Martin [2] in his thesis dealing with Gr/PEEK. However, the panels used by Martin, Fisher, Daniels, and others were manufactured by ICI Fibrite in Great Britain and shipped to the United States. The panel used for this investigation were constructed at Wright-Patterson AFB, OH. It was felt that the material properties results might differ from those obtained by Martin because the location, method, and material batches differed.

The specimens were constructed in accordance with the Test Plan in Appendix C and were tested in the Instron Machine shown in Figure 4-7. The results were recorded by the data acquisition system and were compared to the strip chart of load versus displacement that was generated by the machine. Figure 5-1 shows the specimens after each of the tension tests. Since each group failed in the same manner, the only point

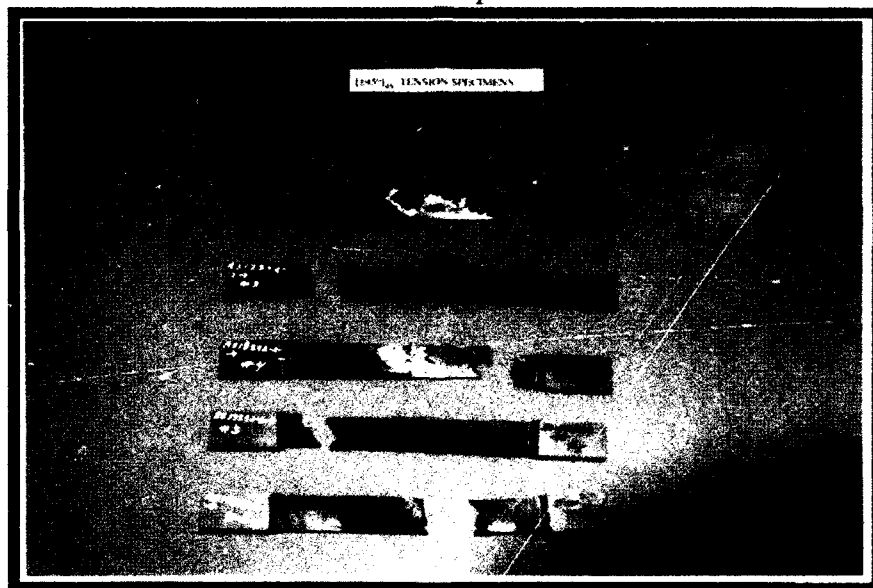


0° Tension Specimens

Figure 5-1: Basic Material Properties Specimens in Tension



90° Tension Specimens



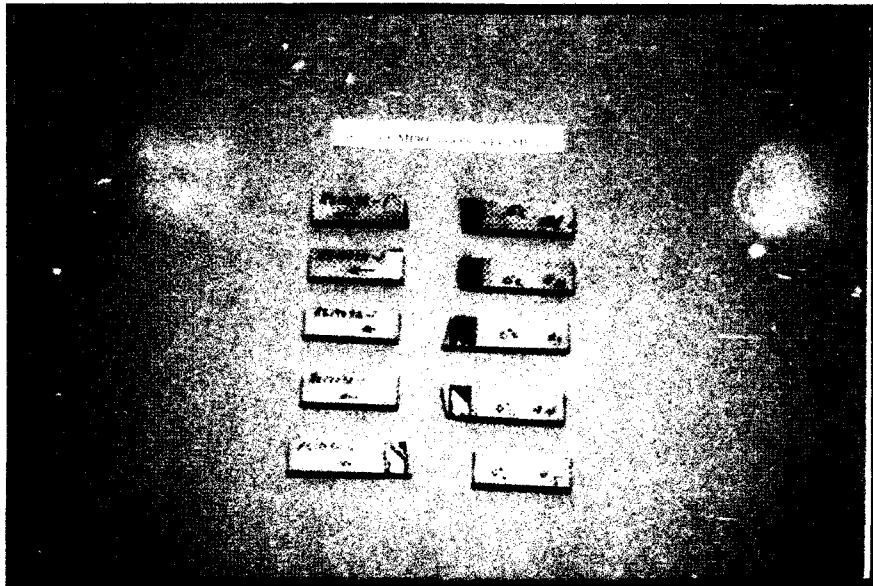
±45° Tension Specimens

Figure 5-1: Basic Material Properties Specimens in Tension (cont)

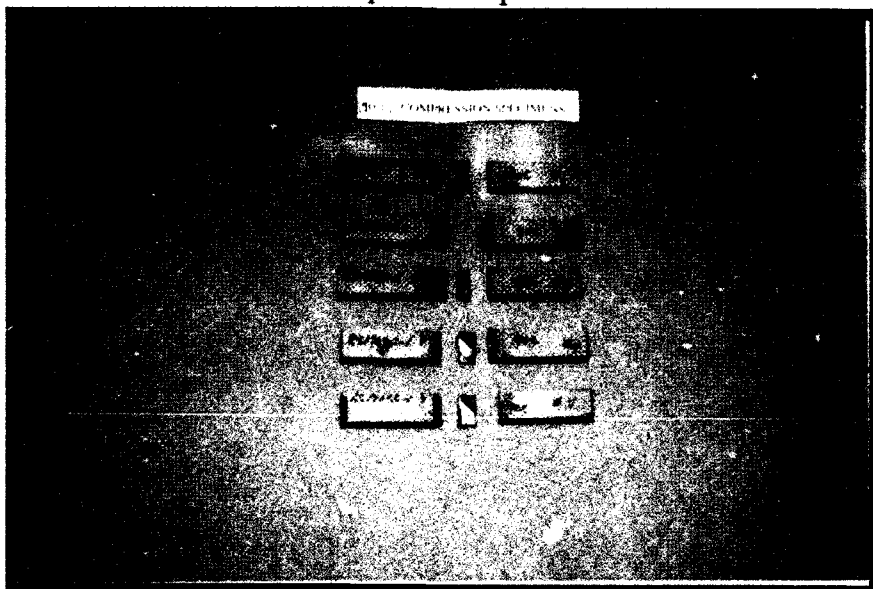
of interest is that none of the specimens failed at the center. They all failed towards the end of the specimen near the tabs. There was no pattern since in one instance the failure occurred towards the top tab, and on the next test the failure occurred towards the bottom tab. This fact is of some importance since the failures occurred away from the gage and

thus the results obtained do not represent the point of maximum stress for the specimen and could result in less than accurate properties.

The compression tests were also performed on the Instron Machine in Figure 4-7 using the Rolfes-Sendeckyj Compression Device. The specimens that were tested in the Rolfes Sendeckyj Device are shown in Figure 5-2.



0° Compression Specimens



90° Compression Specimens

Figure 5-2: Basic Material Properties Specimens in Compression

All of the 90° compression specimens failed at the center so the gages were able to record maximum strain. All but one of the 0° compression specimens failed within the tabs indicating that the maximum strain was within the tabs. This result could indicate that there may have been some eccentricity in the application of the load.

The Rolfes-Sendeckyj Device was recommended for compression materials property testing in an investigation by Daniels and Sandhu [35] of compression fixtures. Their findings demonstrated that the device produced the most uniform state of stress of all of the compression test devices by using strips of Teflon under the tabs. This eliminates areas of high stress concentration within the specimens that could result in erroneous data. The failure of the material properties specimens occurred beyond the Teflon strips.

Once the data was collected by the laboratories VAX computer, it was transferred to an IBM compatible system, and then converted to a Macintosh computer. Within the Macintosh, the data was striped from the large data file and placed in a tabular format. From there the data was transferred to Wright Laboratory's FDLENG VAX computer. The files contained the longitudinal stress, longitudinal strain, and the transverse strain. Because these curves are monotonic in nature, it was felt that a piece-wise cubic spline could be used to represent the data. The cubic spline is an excellent way of representing the data since it provides a smooth curve over its entirety and displays continuity of the first derivative. The first derivative of the curve represents the modulus of the material at any instance on the curve and is continuous. The five data files were combined into one curve by running a spline through each one of the specimen's material curves. The created splines were each feed a descretized set of strains, and the descretized stresses returned by the program were averaged and a spline was run through the average curve. The average spline curve is the material properties curve for each one of the uniaxial tests. The modulus for each property was determined by placing an appropriate curve fit

through the line, and the first derivative was taken to determine the initial modulus at the beginning of the loading cycle. The Poisson's ratio was obtained by the formula:

$$v_{12} = \frac{\epsilon_1}{\epsilon_2} \quad \text{and} \quad v_{21} = \frac{\epsilon_2}{\epsilon_1} \quad (66)$$

where v_{12} and v_{21} = the Poisson's ratio.

The piece-wise cubic spline is the best way to represent the material properties curves, and the spline coincides with the cubic spline method used in PLNRS.

The values for the moduli obtained were very close to the values recommended by ICI Fibrite. A comparison of these values is shown in Table 5-1. These values also compared favorable with the values obtained by Martin in his thesis. [2]

PROPERTY	ICI (PSI)	EXPERIMENTAL (PSI)	% DIFF
E11T	20000000.	19619000.	1.94%
E11C	18700000.	18325000.	2.05%
E22C	1480000.	1449400.	2.11%
G12	820000.	754970.	8.61%
v_{12}	0.30	0.34	11.76%

Table 5-1: Comparison of Material Properties

The material properties stress-strain curves and representative data points for each of the curves are shown in Appendix A. The 90° tension and 90° compression specimens illustrate why Gr/PEEK is considered a nonlinear material. This is also a good argument why the Hahn-Tsai method (of a nonlinear material response) is not a valid assumption for analyzing Gr/PEEK. The ±45° shear tension also provides an illustration of the nonlinear behavior of the composite. There was even some nonlinear behavior in the 0° tensile loading. In the 0° tension specimen, when the fiber is put in tension, it is possible

that fiber waviness is present and the fiber is straightening out as the strain increases, as shown in Figure 2-5.

Most of the gages functioned throughout the loading cycle; only the $\pm 45^\circ$ gages saturated about two thirds of the way into the loading cycle. When this saturation occurred the data was interpolated to the end of the loading cycle. Part of the reason for this saturation occurred was that a rosette was used in which the longitudinal, $+45^\circ$, and transverse gages were all located on one grid. The longitudinal and transverse gages are not allowed to function as independent units. It is also possible that the gage's matrix material could be inducing additional stresses on the gages as the $\pm 45^\circ$ undergoes a process known as scissoring. Scissoring occurs when off axis fibers are subjected to a uniaxial load. The fibers will align themselves parallel or normal to the loading depending on whether the loading is tensile or compressive in nature. Since the matrix material of the gage does not have the same material properties as the composites to which it is affixed, then shear stresses will be generated between the two. In a $\pm 45^\circ$ specimen, where the specimen undergoes a large amount of displacement, the forces between the gage and specimen may be so high that saturation of gage occurs and the gage eventually separates. Fisher discussed this concept of scissoring in his paper. [39] One solution to this problem would be the mounting of two linear strain gages on the front and two on the back of the specimen. The gages would be mounted so that they are orthogonal to each other and stresses between the gages and the specimen might be greatly reduced. This method, however, will not truly measure longitudinal strain; instead the gage will rotate when the specimen starts to scissor and the data may need to be transformed at the end of the loading cycle. Another possibility is the use of an extensometer to measure strain, but this would be an area measurement and not a point source measurement like that produced by a strain gage.

B. Boeing Open Hole Compressive Fixture

As stated earlier in chapter 4, we were attempting to induce a plane stress compressive loading on the Boeing specimens. There were five different types of specimens tested in the device. Three separate types of tests were conducted in the Boeing fixture: a test for possible failure modes; tests of the ultimate compressive strength of Gr/PEEK specimens; and a progressive failure study that included the compression of each layup to 90% or 95% of its average ultimate load. The results of each test will be discussed individually.

(1) Initial Testing in Boeing Fixture

The first set of tests were conducted to determine the possible failure modes, an idea of what the ultimate strength of each layup might be, and any possible problems that could arise from the use of the Boeing device. A procedure for loading the specimens into the device was developed. The modifications made to the fixture were validated to insure that the gages would fit within the cutout areas.

The Boeing fixture contains a total of 42 parts, each of which must be perfectly aligned to insure that the loading applied is not eccentric in nature. The first thing that had to be completed before the device could be modified as shown in Figure 4-11 was to insure the composite material would not buckle out of the device. The modification was validated by modeling the open areas as a simply supported column and using the modified Euler Buckling Formula (16). The value of the Euler compressive stress was checked against the ultimate strength of the composite. Since the ultimate strength of the composite was lower than the Euler Buckling load, it was assumed that modifications would not induce any instability into the device or any undesirable failure modes, such as those mentioned in Chapter 2.

The 0° , 90° , $0^\circ/90^\circ$, $\pm 45^\circ$, and $0^\circ/\pm 45^\circ/90^\circ$ specimens were all tested in the Boeing Device. No end brooming was observed in any of the specimens. All the specimens failed by a horizontal crack that formed at the edge of the hole perpendicular to the loading direction. The possible failure modes are each shown in Figure 5-3.

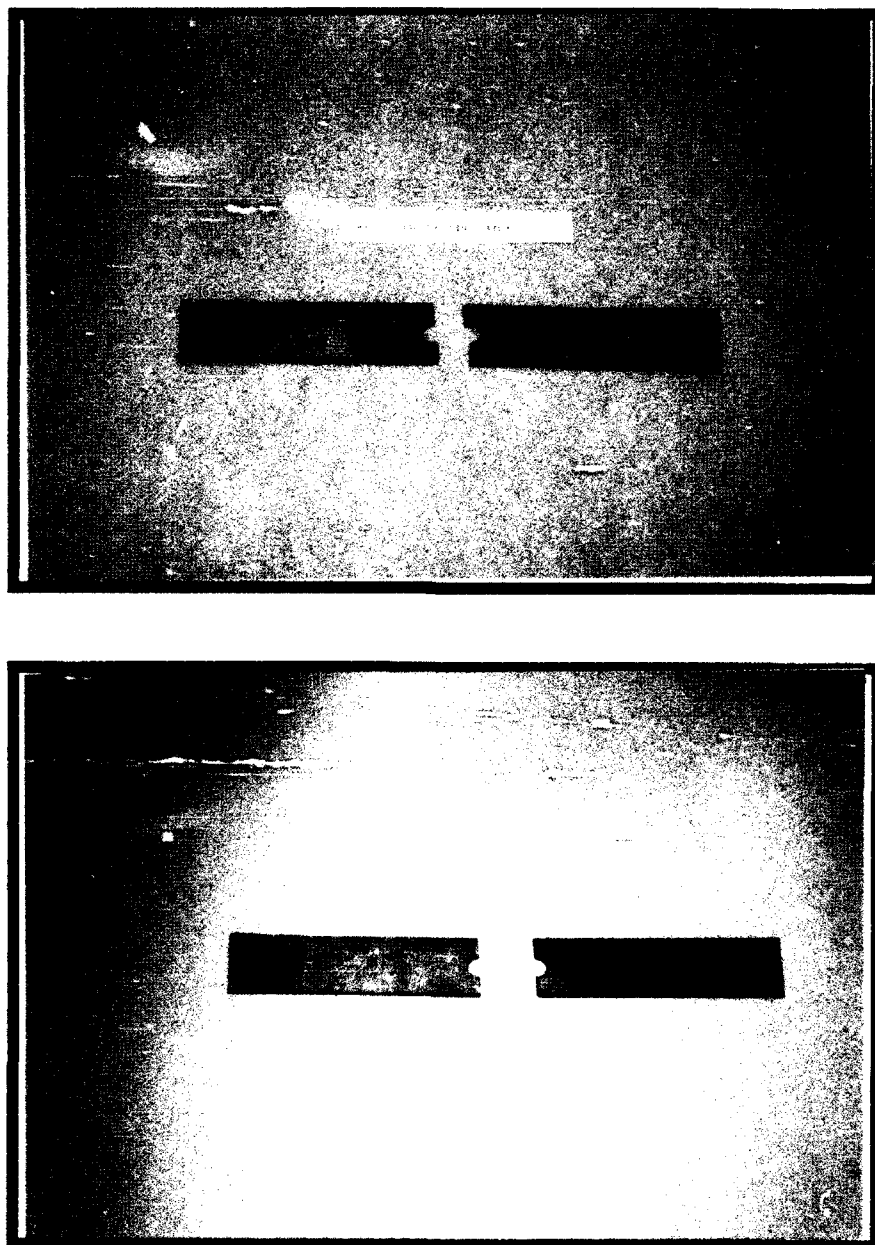


Figure 5-3: Failure Modes Encountered During Initial Tests

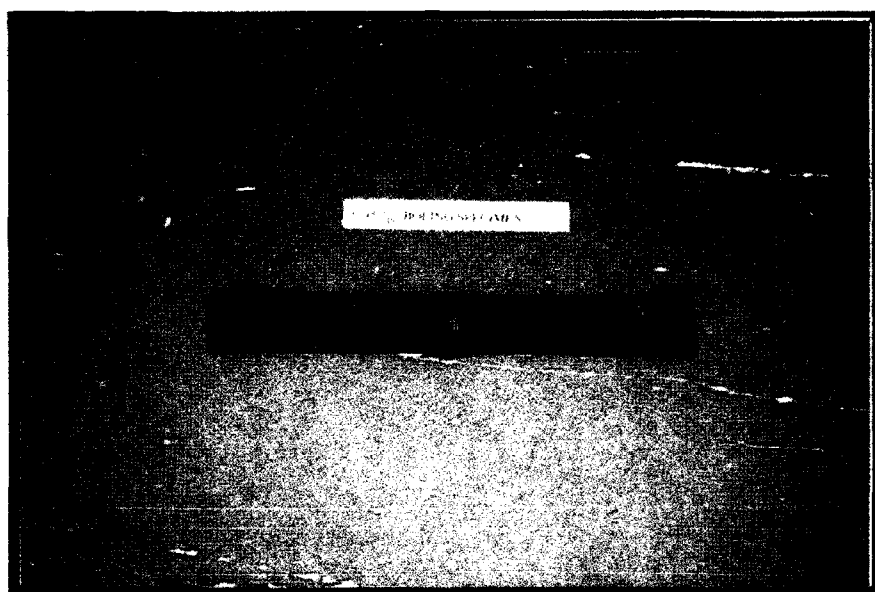
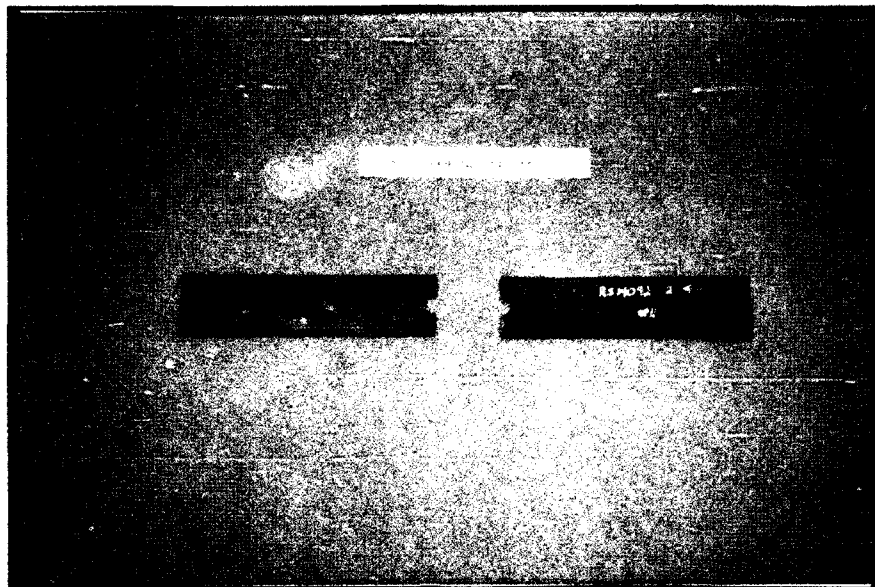


Figure 5-3: Failure Modes Encountered During Initial Tests (cont)

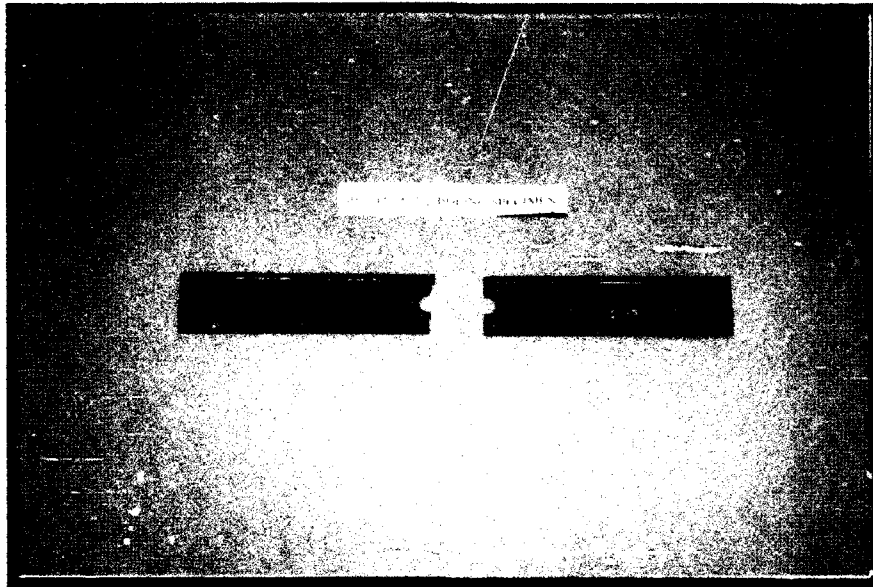


Figure 5-3: Failure Modes Encountered During Initial Tests (cont)

The $\pm 45^\circ$ specimen did not fail within the device. Instead, the gap between the two halves of the Boeing fixture closed before the specimen failed. The device was modified by cutting down the gap by 0.0625". Another $\pm 45^\circ$ specimen was tested in the same manner and again the specimen did not fail even though some closed form approximations indicated that the specimen would fail. These results are probably due to the fact that these methods do not take into account the nonlinear behavior of the material. The device was modified once again, removing 0.0625" from the gap. The results of this modification will be discussed when the results of the $\pm 45^\circ$ ultimate strength tests are addressed in Section 2. The second series of tests were conducted within the Boeing fixture as well, and were intended to determine the ultimate strength of a Gr/PEEK specimen with a centrally located discontinuity.

(2) Ultimate Strength Compression Testing in the Boeing Fixture

As previously stated in Chapter 4, the Boeing Open Hole Compression fixture was adopted by SACMA as the recommended device of open hole compression testing. [32] There exist several disadvantages to this device. For one thing, it requires a large amount of material and at \$400 a pound for Gr/PEEK the amount of material required could cause financial hardships. A complete analysis of the Boeing fixture and its performance will be included the conclusions in Chapter VI.

(a) $[0^0]_{16}$ Unidirectional Specimens

Six tests were conducted to determine the ultimate strength of 0^0 unidirectional specimens. The results of these tests are listed in Table 5-2. There were significant

$[0]_{16}$

SPECIMEN #	LOAD (LOAD)	EXPERIMENTAL STRESS (PSI)	TYPE OF FAILURE
1	5990.02	47135.82	CRACK
2	5965.81	46985.98	CRACK
3	7005.74	55822.63	SPLIT
4	6412.52	50893.02	SPLIT
5	6534.38	52066.77	SPLIT
6	5862.24	46496.19	CRACK
AVERAGE	6295.12	49900.07	
STD DEVIATION	439.30	3700.72	
AVG CRACK	5939.36	46872.66	
STD DEV	67.87	334.53	
AVG SPLIT	6650.09	52967.47	
STD DEV	313.30	2575.05	

Table 5-2: Ultimate Strength of 0^0 Specimens

occurrences in these tests. Three of the specimens displayed a crack at the hole similar to the failure modes shown in Figure 5-3. The other three specimens exhibited a longitudinal split at the edge of the hole traveling in a direction parallel to the load, as

shown in Figure 5-4. The splitting occurred at a higher ultimate load than the transverse cracking. The time versus load curves, produced by the Instron Machine (Figure 4-8)

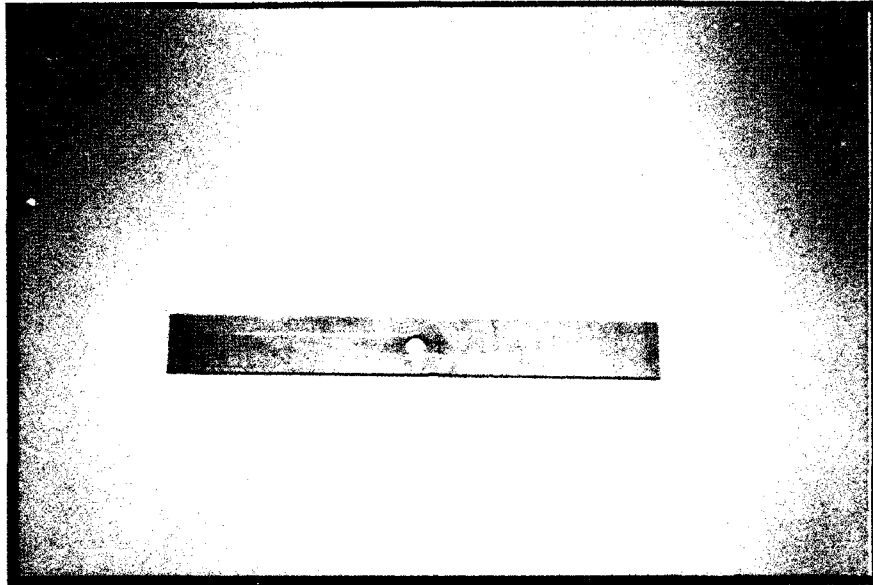
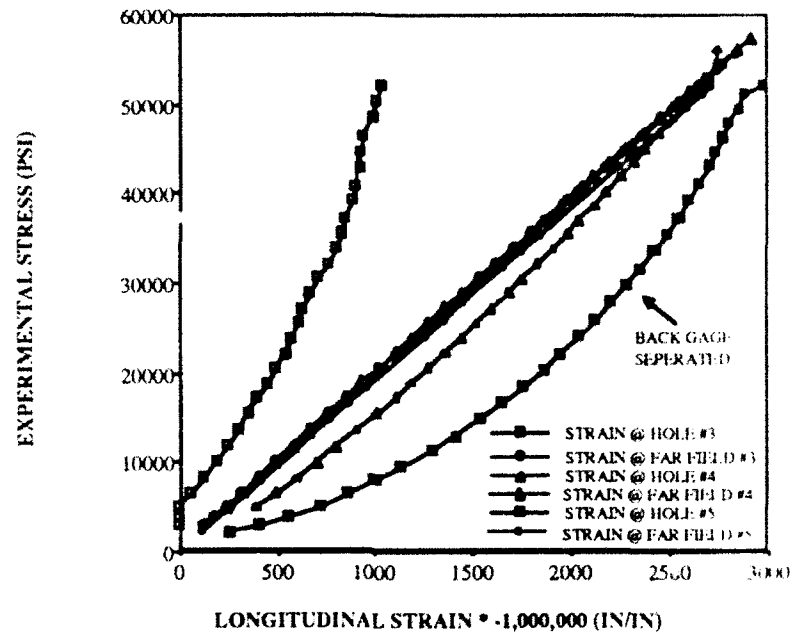


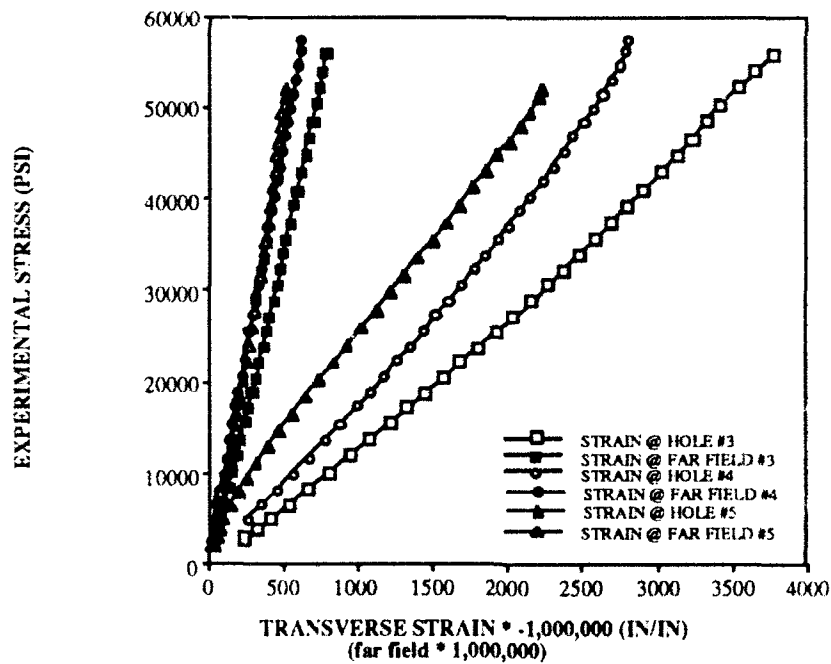
Figure 5-4: 0° Specimen Exhibiting Longitudinal Splitting

did not display any difference in the shape or the slope of the curve between the cracked and split specimens except that split specimens failed at a higher load. Both of the failure modes exhibited dynamic behavior. The failure was instantaneous, with the load dropping off by 1000 lb. on average and then leveling off for approximately 2 seconds until the test was stopped. The tests were stopped to preserve the end of the specimen so that it could be examined with a Scanning Electron Microscope. Graphs of the hole strain versus far field strain for both the transverse and longitudinal data are shown in Figure 5-5. Because of the two failure modes the specimens have been graphed by failure. For reasons of continuity, each specimen's data points are graphed with a line passing through the points and each test has been specified in the legend.

HOLE AND FARFIELD LONGITUDINAL STRAIN [0] (SPLIT)

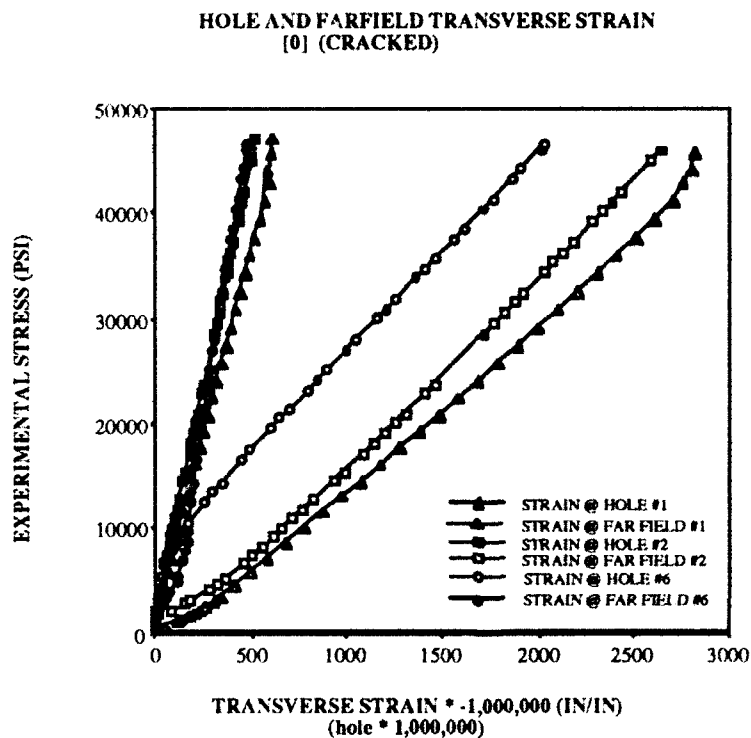
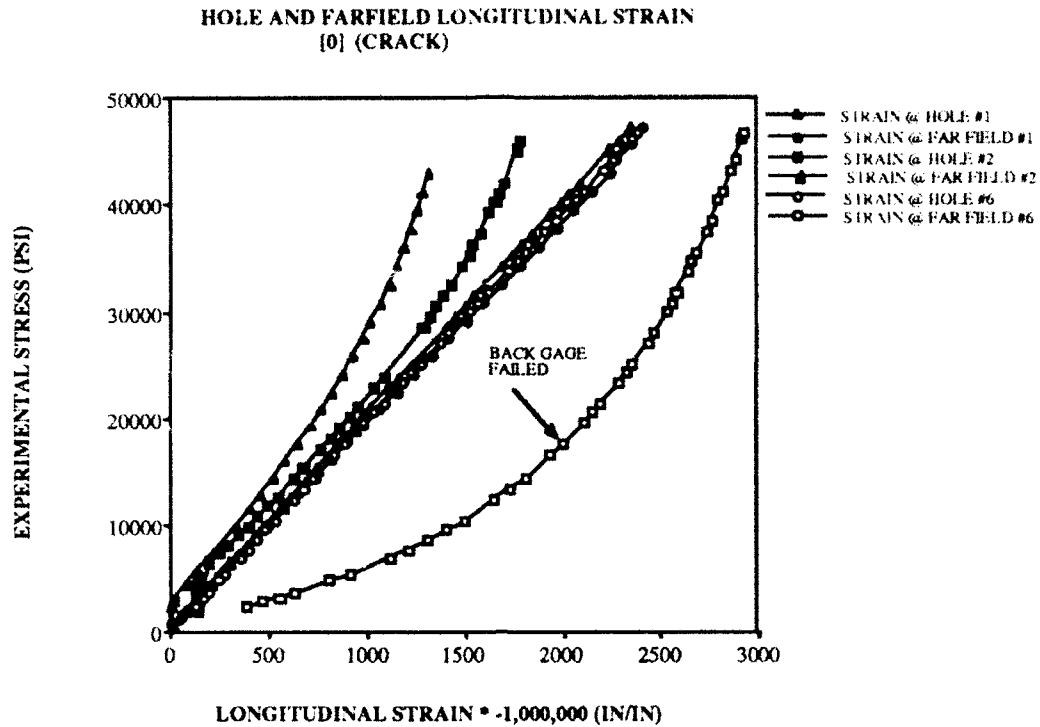


HOLE AND FARFIELD TRANSVERSE STRAIN [0] (SPLIT)



EXPERIMENTAL STRESS = LOAD / CROSS-SECTIONAL AREA

Figure 5-5: Graph of Far Field and Hole Strain for 0°



EXPERIMENTAL STRESS = LOAD / CROSS-SECTIONAL AREA

Figure 5-5: Graph of Far Field and Hole Strain for 0° (cont)

The author's first consideration was whether the fixture was inducing an eccentric loading on the specimen which might cause the specimen to separate into two distinct 0.5" wide plates with an unloaded 0.5" wide segment in the center. Since all the other specimen testing in the initial test exhibited horizontal cracks, it was felt at the time that the split was the result of an eccentric loading pattern. However, since the ultimate load was higher for the splits, the author investigated the possibility that this was a valid failure mode. The cracking is probably manifested by the formation of a kink band in the specimen that collapses into the hole. The inherent waviness of the fibers within the composite can exacerbate the compressive loading. The specimens, where splitting occurs, transform from one specimen with a centrally located discontinuity into two separate loaded plates that are 0.5" in width. If the specimen was eccentrically loaded in compression, and one of these two panels was subjected to the load then is it quite possible that this failure mode would have resulted. As odd as it seems, it is probable that the eccentrically loaded composite panel would fail at a higher load. After discussing this failure mode with several engineers, including Mr. Zambora of Boeing and Dr. Mark Shuart of NASA Langley, it was concluded that this failure mode was valid and possible for these loading conditions.

The splitting phenomenon was observed by Martin [2] in his work dealing with tension. While the results of his thesis were inconclusive as regards to the longitudinal splits, Sandhu continued his research and discovered that the splitting could be the result of a shear stress around the hole. To check this theory, he placed gages on two specimens with a hole as shown in Figure 5-6. Then his specimens were loaded to failure in tension the splitting occurred and the changes in strain were recorded. The gages in Figure 5-6 recorded the results of the testing. Those gages normal to the loading direction displayed a marked increase in strain when the splitting occurred. Those gages parallel to the loading direction recorded much different strain values as the specimen approached failure. As the splitting occurred, the gage above the split in Figure 5-6 showed an

increase in strain, while the gage at the bottom of the split showed a rapid decrease in strain to the point that it was almost unloaded before the test was stopped. The "two-plate" theory could have been tested, if the loading had been allowed to proceed after the splitting occurred. However with the obstructions of gages and restraint plate within the Boeing fixture it was extremely difficult to determine the failure mode until the specimen was removed from the apparatus. The removal procedure usually resulted in the debonding of the strain gage, thus obtaining more strain information was impossible.

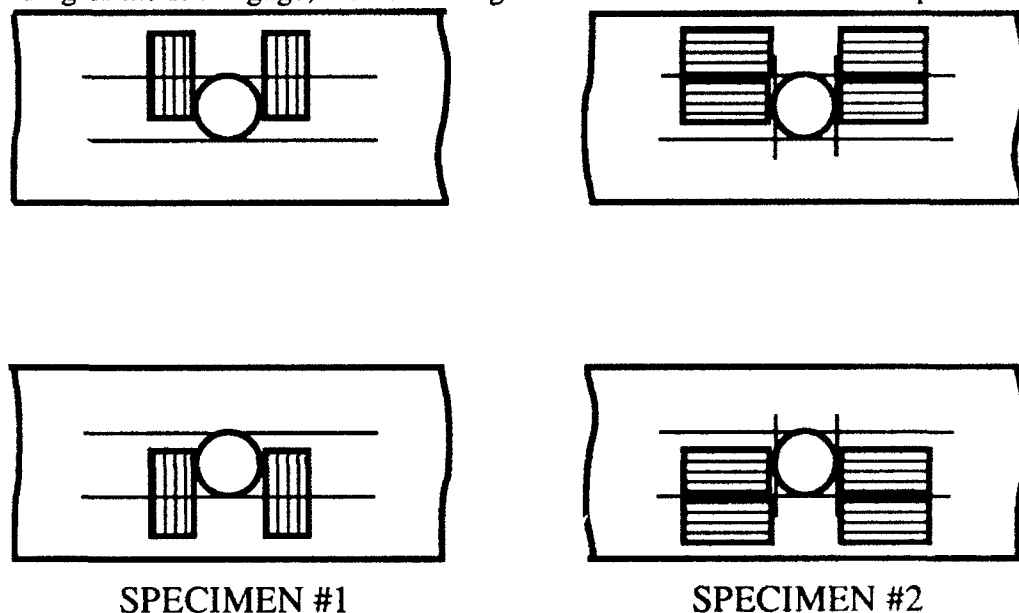


Figure 5-6: Location of Split Gages

It is the author's opinion that when the shear stresses exceed those of the matrix, the split forms at the hole edge and quickly propagates up the length of the specimen towards the loaded ends. Since the specimen was not broken into two separate pieces during the procedure it could not be surveyed by the electron microscope, without destroying the failure areas. The failed specimens were investigated using an ultrasonic analysis. The results of the specimens tested is shown in Figure 5-7. The examination failed to detect even traces of the initiation of a horizontal crack in the specimen. As seen from specimen #5 the crack formation was not always symmetric in nature and as a result could not be predicted.

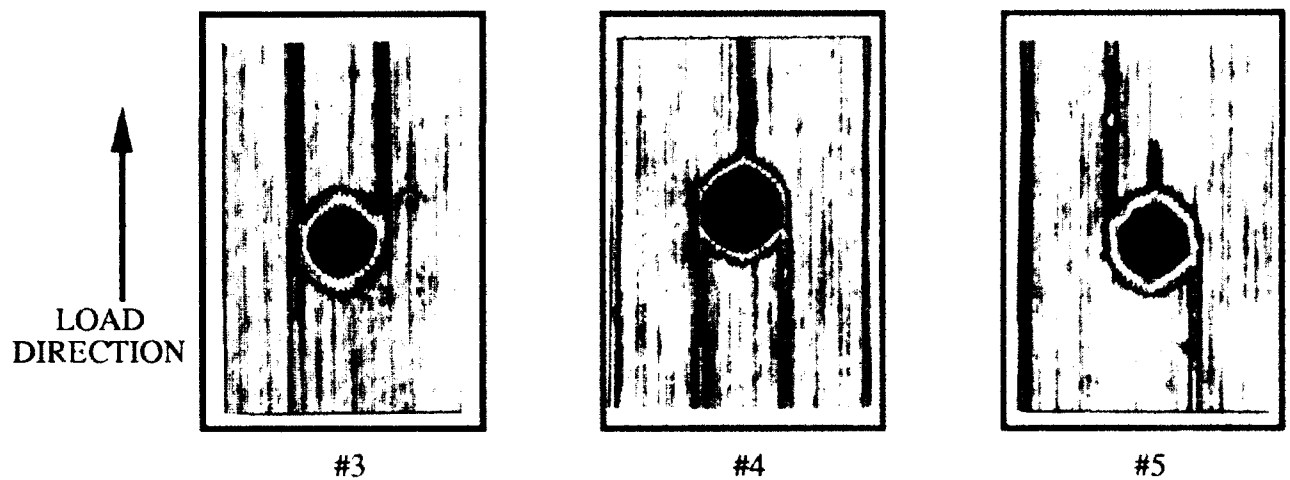
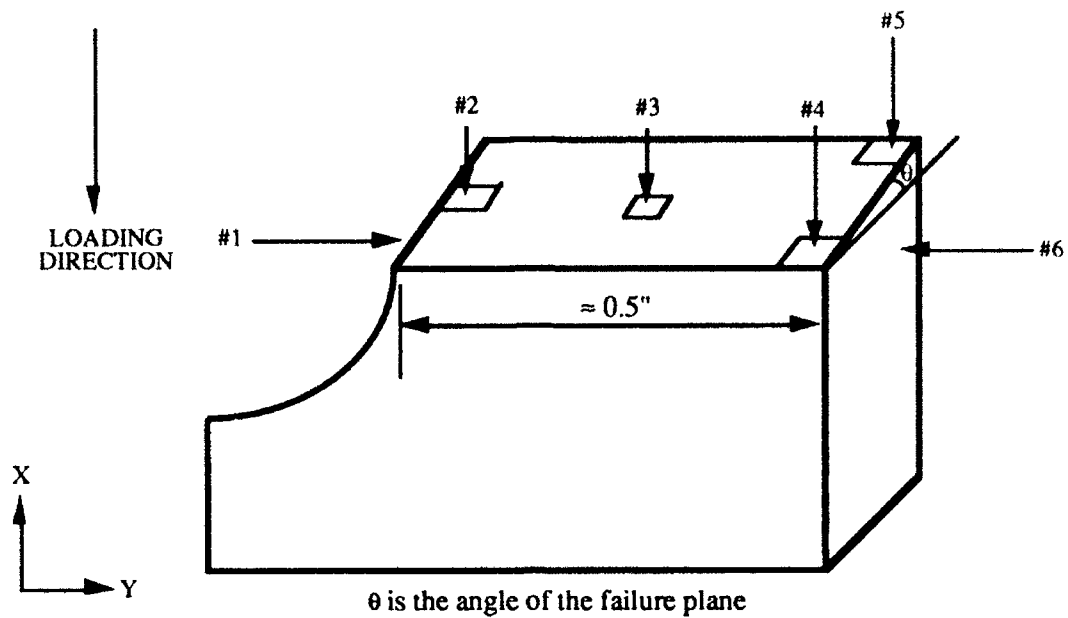


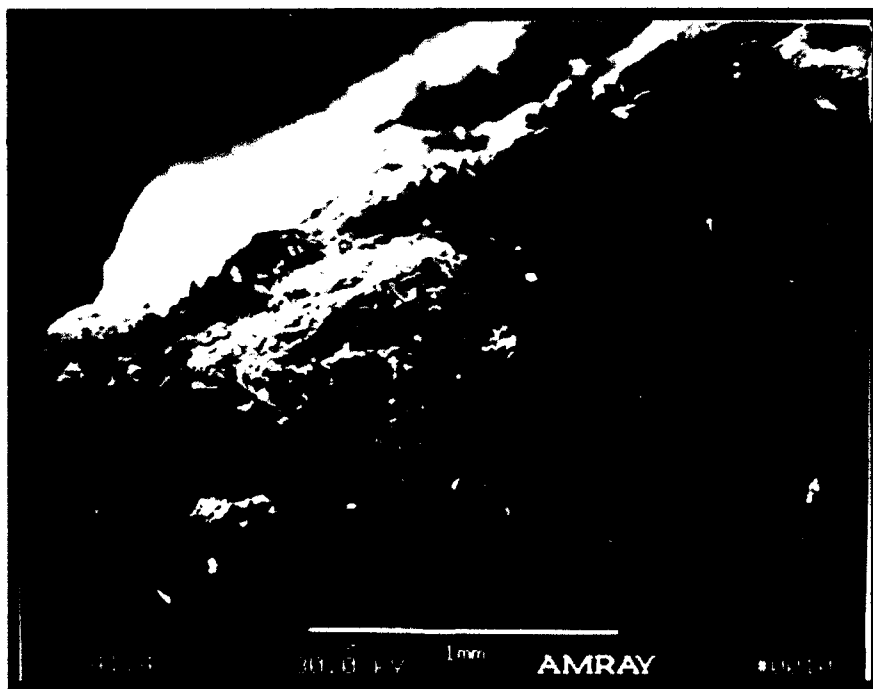
Figure 5-7: Ultrasonic Images of 0° With Split

The formation of the crack is an entirely different type of failure phenomenon. Like the split, the failure of the specimen is almost an instantaneous occurrence. However, horizontal cracking seemed to have more audible popping occurring before failure. The specimens that cracked normal to the load were examined with the electron microscope. There were several features of note.

The locations of the scans of the 0° and the photographs are shown in Figure 5-8. The first view was taken on the end of the specimen looking into the edge of the hole. This photo, #5, shows that the failure occurred by the formation of a shear plane. The angle of the plane is estimated from the photos to be approximately 65° from the loading direction. This type of failure feature was observed by Purslow [33] in his fractographic study of Gr/PEEK. The fibers at the center of the failure plane seem to have been bent at an angle of 30° from the normal, roughly perpendicular to the shear plane. A close-up view of the region, #6, indicates that part of the composite failed into the hole during the initiation of failure.

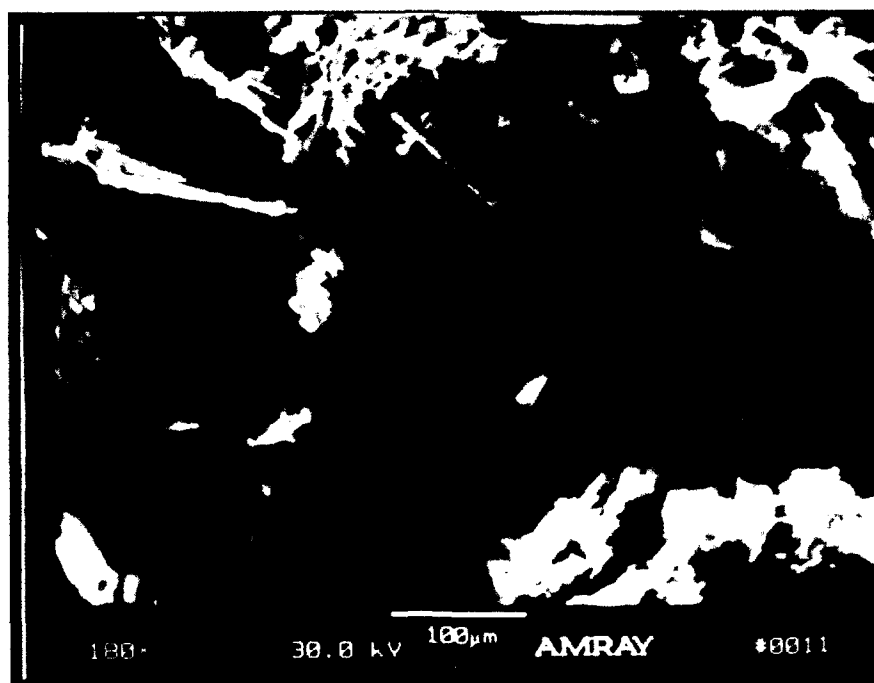


Location of SEM Photographs

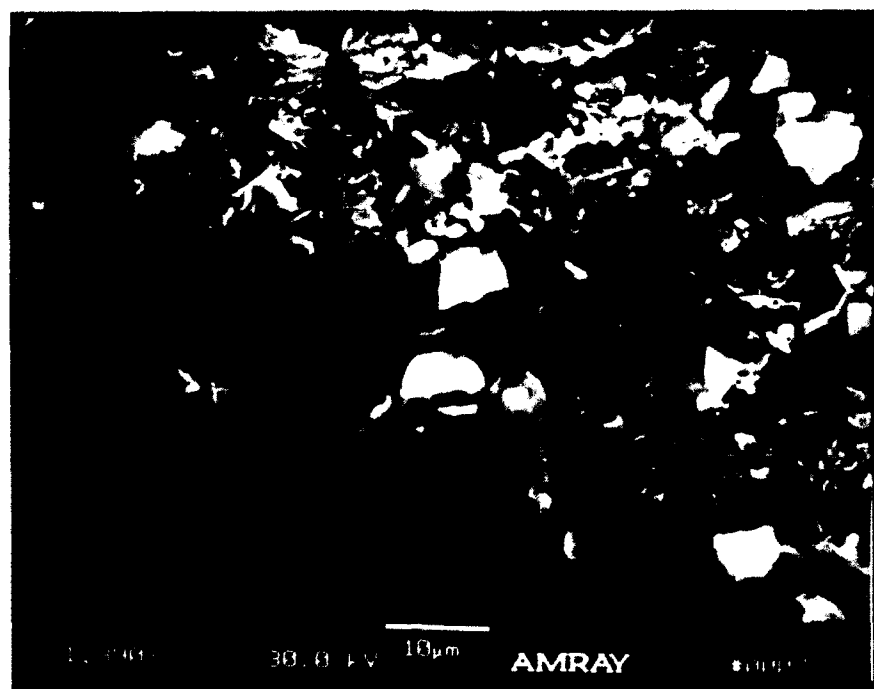


#5

Figure 5-8: SEM Photographs of 0°

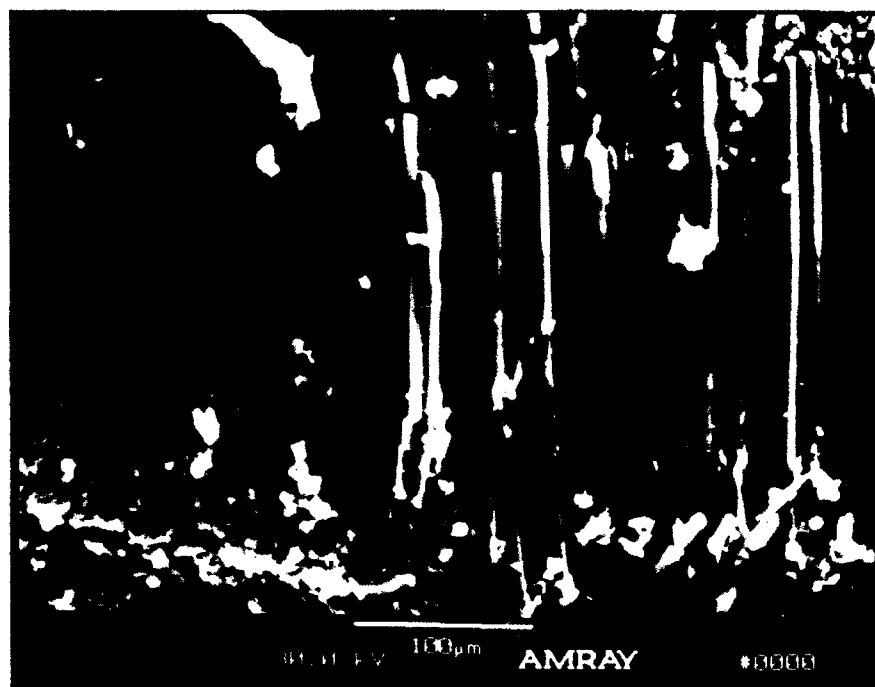


#6

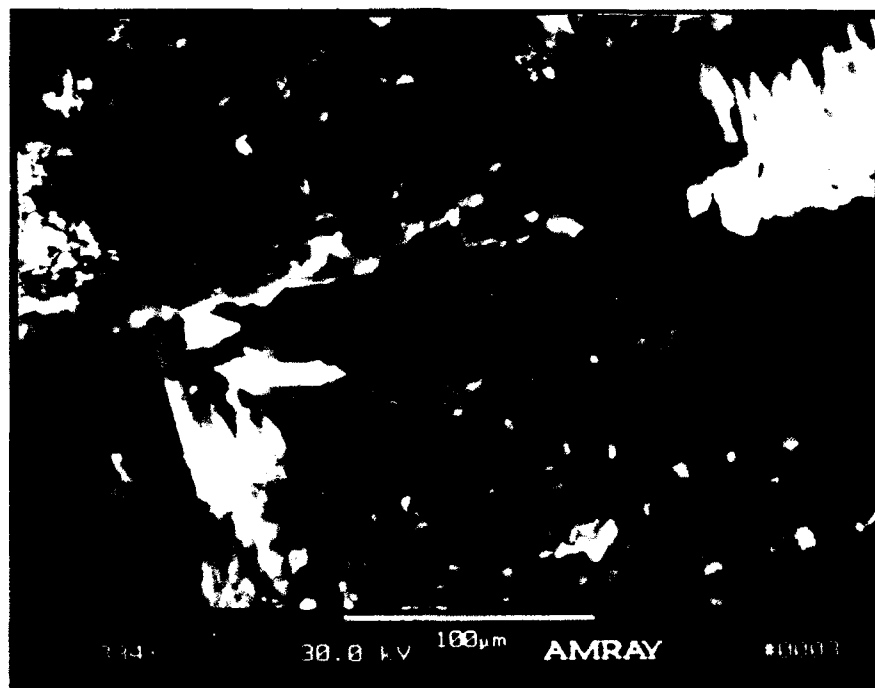


#4

Figure 5-8: SEM Photographs of 0^0 (cont)

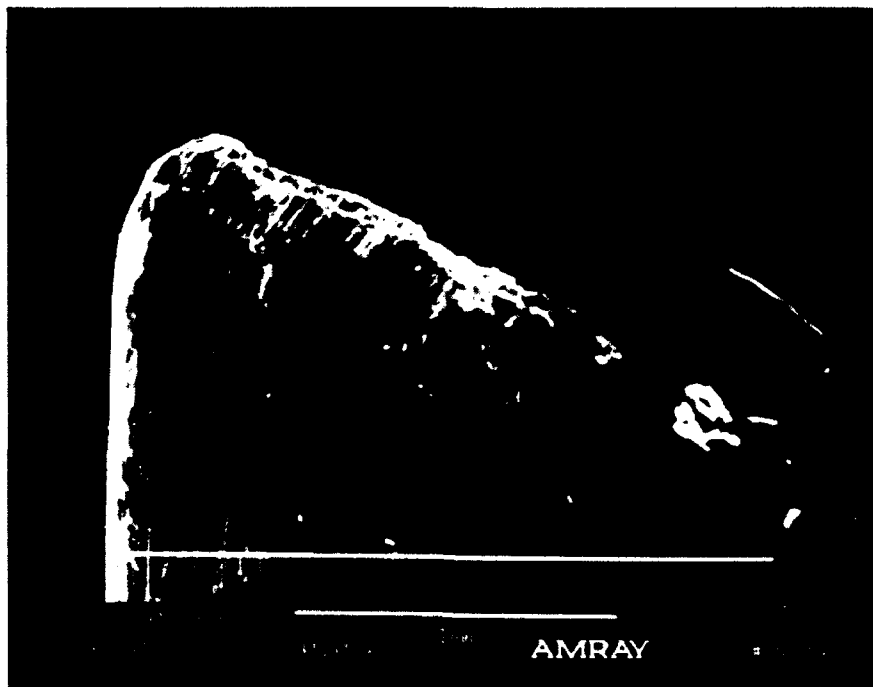


#1



#2

Figure 5-8: SEM Photographs of 0° (cont)



#3

Figure 5-8: SEM Photographs of 0° (cont)

The failure seems to start at the edge of the hole and then progress towards the edge of the specimen. This is evidenced by photo #4 that clearly shows a compressive failure of the fiber followed by a tensile failure of the matrix. The small spikes of matrix material show the tensile failure of the matrix and the direction of the spikes, toward the outer edge, indicate the direction of failure. A close examination of the fiber ends shows a compressive-tensile failure at the surface indicating that the shear plane created flexure in the fibers resulting in their breakage. Photo #1 is also interesting because it shows a type of failure where a layer of fibers has broken away from a ply and is bent over onto the failure surface. Fibers oriented at 0° are visible at the bottom of the picture showing the true direction of the fibers.

There is also some delamination present in photo #2 that shows the other end of the failed specimen. This could be due to the concentration of stress towards the end of the specimen right before the specimen breaks into two parts. At the end of the specimen the angle of the failure plane can still be measure at approximately 65° for the loading

direction as seen in photo #2. The fibers at the end of the specimen appear to be bent over approximately 25° from the loading direction and appear almost perpendicular to the failure plane.

Of all the specimens tested only the 0° specimens exhibited any inconsistency in the final failure mode. The 90° showed a consistent failure surface in each one of the specimens tested.

(b) $[90^\circ]_{16}$ Unidirectional Specimens

All six of the 90° specimens displayed the same type of failure surface. The specimens however did exhibit some deviation in the ultimate strength. The results of these tests are listed in Table 5-3

$[90]_{16}$

SPECIMEN #	LOAD (LB.)	EXPERIMENTAL STRESS (PSI)
1	2448.41	18190.27
2	2357.72	17984.13
3	2569.11	20071.17
4	2554.61	20115.04
5	2327.13	17696.81
6	2382.65	18328.08
AVERAGE	2439.93	18730.92
STD DEVIATION	102.64	1076.45

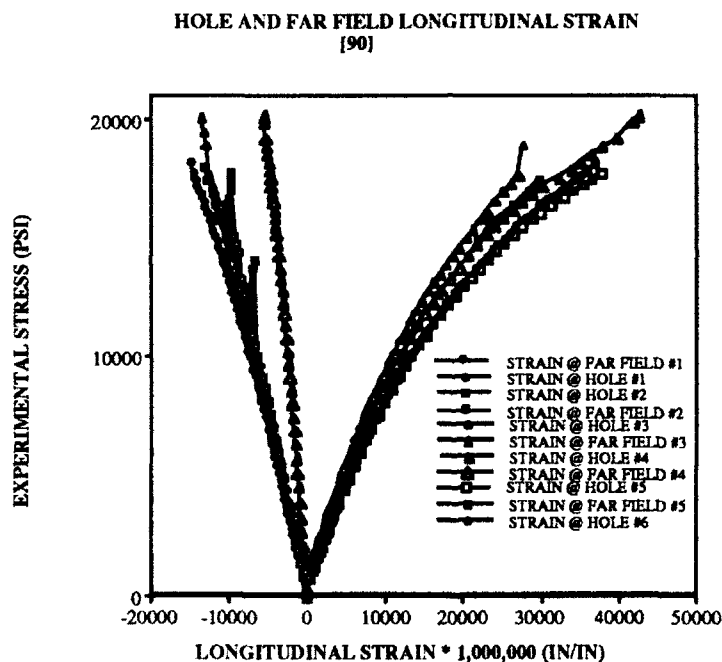
Table 5-3: Ultimate Strength of 90°

As seen in the material properties tests, in compression testing 90° specimens have a much lower compressive strength than the 0° specimens. When the fibers are normal to the loading direction, the matrix is the component that is resisting the applied load. Since the PEEK matrix material is not an extremely brittle material and exhibits extensive material nonlinearity, the stress-strain response of the specimens is nonlinear.

The Instron strip chart shows good continuity between each of the six specimens. However specimens # 1,3,4 display an odd increase in the slope of the line approximately

95% - 98% of the ultimate recorded strength. Also the load data obtained by the data acquisition system showed a large increase in load before failure in the last four seconds of the test. It is possible that the compressive displacement of around 0.20011" of the fixture may have been so great that the gap within the fixture closed. The initial gap of the fixture before modification was 0.22" and there may have been more displacement than recorded by the strain gages. The difference between the point where the slope changes and the ultimate strength is only 75 lb., but it is possible that this difference effected the ultimate strength of the specimens.

The longitudinal stress-strain responses for the hole and far field are shown in Figure 5-9.

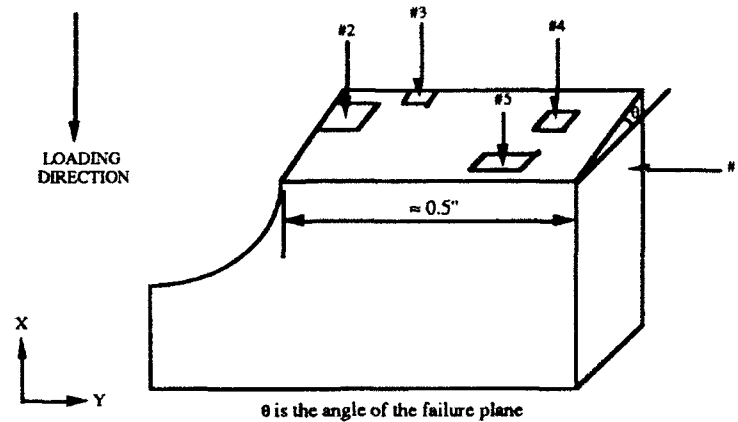


EXPERIMENTAL STRESS = LOAD / CROSS-SECTIONAL AREA

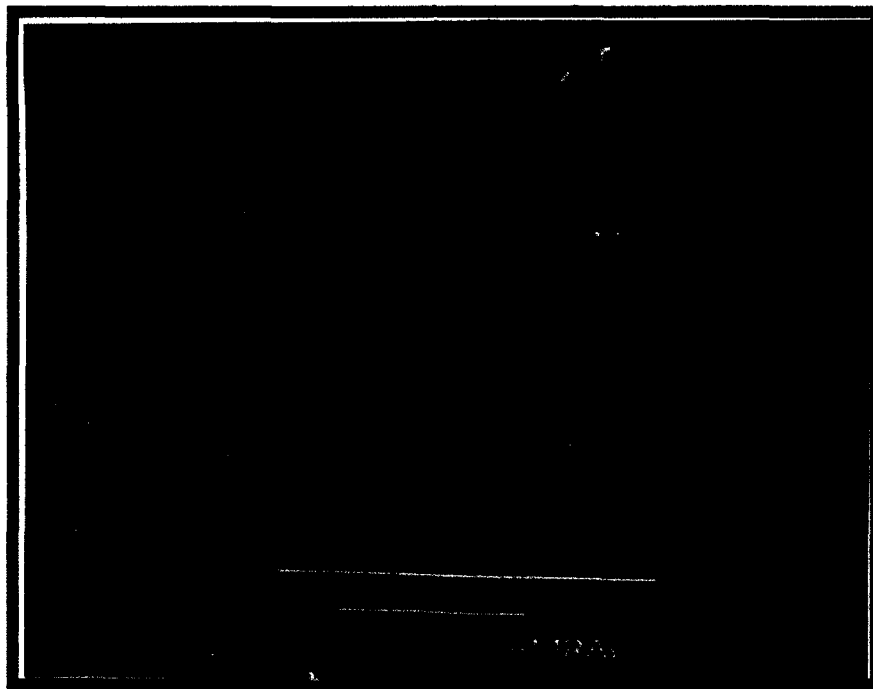
Figure 5-9: Graph of Far Field and Hole Strain for 90°

There are several interesting points of note in both graphs. In the longitudinal graph, the specimens that exhibited the jump in load at the end of the loading cycle also exhibited a jump in the strain data. The far field gages in specimen #3 seem to have failed by separating towards the end of the loading cycle.

All specimens were visually inspected and checked under a conventional microscope to determine if there were any differences in the failure surfaces. The specimen selected seemed to best display the various failure modes formed within the 90° specimens. The pictures were taken while looking down at the specimen as shown in Figure 5-10.



Location of SEM Photographs

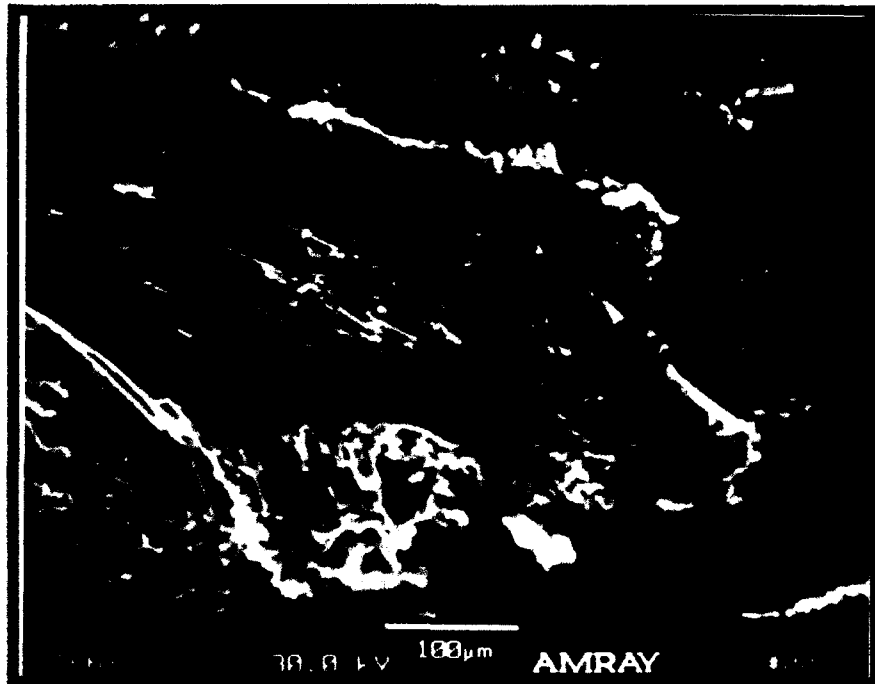


#1

Figure 5-10: SEM Photographs of 90°

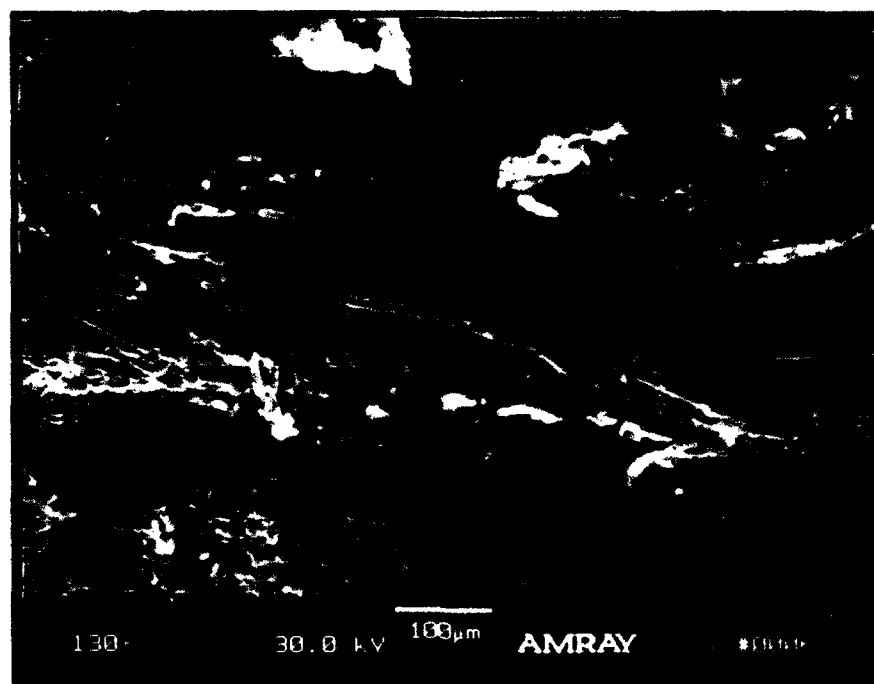


#2

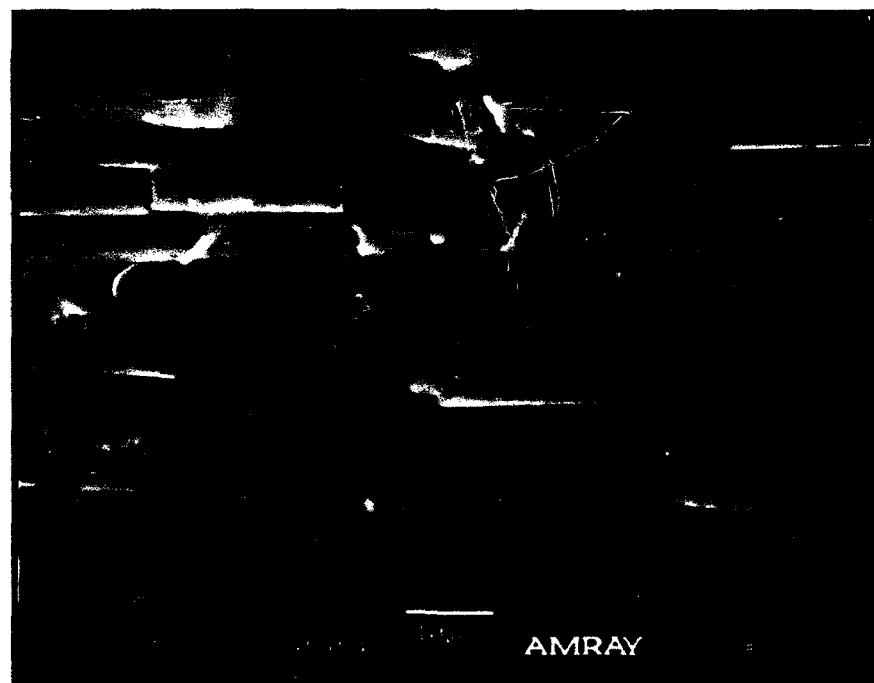


#3

Figure 5-10: SEM Photographs of 90° (cont)



#4



#5

Figure 5-10: SEM Photographs of 90° (cont)

The first photo, #1, shows a side view of the failed area indicating the formation of a clean shear plane that was formed during the failure of the specimen. The angle of the shear plane is approximately 25° for the loading direction. The cracked portion at the tip of the specimen is not a result of the quasi-isotropic loading of the specimen, but rather a post damage effect of its dynamic failure. The next photo, #2, shows that, unlike the 0° specimen, the failure was not precipitated by collapsing into the hole. The photo shows a small lip of matrix material and crushed fibers away from the edge, but for the most part there is continuity of the fibers.

There were several areas of interest in the composites that were not part of the normal shear plane. In photo #3 there seems to be a bundle of fibers that separated from the rest of the surface and is bent down. This condition may either be a post damage effect or a case where there was a little delamination in a ply that was subsequently bent down when failure occurred. The bundle has a width of around 0.0105" which is extremely close to the thickness of two plies. There is also evidence in photo #4 of disarray of the fibers. This effect may either be an imperfection in the composite at the location or a post damage effect.

Photo #5 shows the type of failure surface that was seen over most of the surface. At the top of the picture there is an indication that some fibers were crushed during the loading. The picture also demonstrates that the matrix adheres to the fiber during and after failure. This adherence is an indication of the good fiber-matrix interface mentioned in Chapter 1 and provides validity to the macromechanical approach. This pictures also reveals some of the character of a "slow-ductile" failure that was observed by Purslow in his look at shear failures. [34]

These photographs exhibit the type of material failure that could be expected from any composite that is dependent on the nonlinear properties in its matrix. The types of failures that were present in the 0° and 90° would probably be present in a composite that is constructed with plies of these orientations.

(c) $[0^0/90^0]_{4s}$ Crossply Specimens

All six of the crossply specimens exhibited a horizontal crack created at the hole which seems to be the dominate failure mode for most of the specimens. There was also some deviation in the failure values from the mean as shown in Table 5-4.

$[0/90]_{4S}$

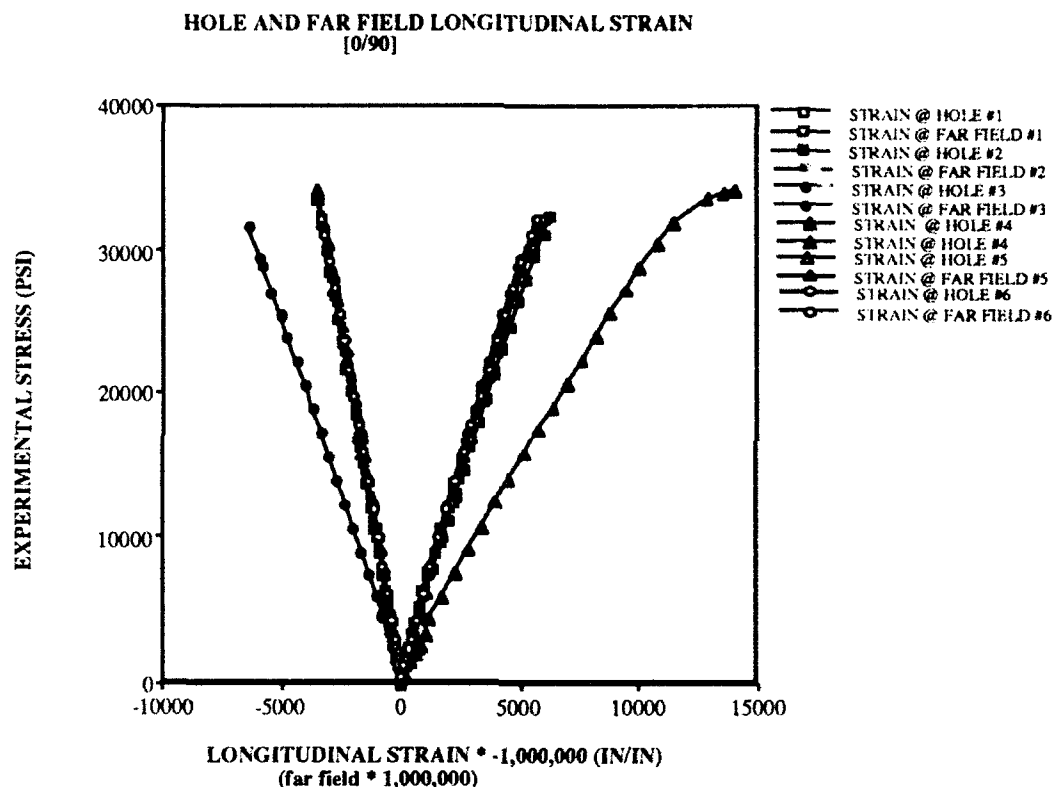
SPECIMEN #	LOAD (LB.)	EXPERIMENTAL STRESS (PSI)
1	4117.35	32445.63
2	4249.50	32789.35
3	4064.80	31559.01
4	4484.96	34184.15
5	4050.21	30823.52
6	4272.07	32364.17
AVERAGE	4206.48	32362.26
STD DEVIATION	165.01	1142.71

Table 5-4: Ultimate Strength of Crossply Specimens

The $[0^0/90^0]_{4s}$ specimens exhibited an extremely linear behavior as shown by the strip charts produced by the Instron Machine. All of the tested specimens exhibited a strange discontinuity at approximately 300 lb. into the loading cycle. There seems to be no logical reason to assume that the discontinuity is related to something within the specimen. Instead the author feels that it may be some sort of a settling effect within the fixture since the fixture is secured to the specimen by torquing the bolts that hold it together.

The stress-strain data was checked to insure that the discontinuity was not recorded during the collection. There is no evidence that this anomaly was related to the specimen. The linearity of the data was clearly evident in the graphs comparing the stress-strain response in Figure 5-11. Only the transverse strain at the hole exhibited any

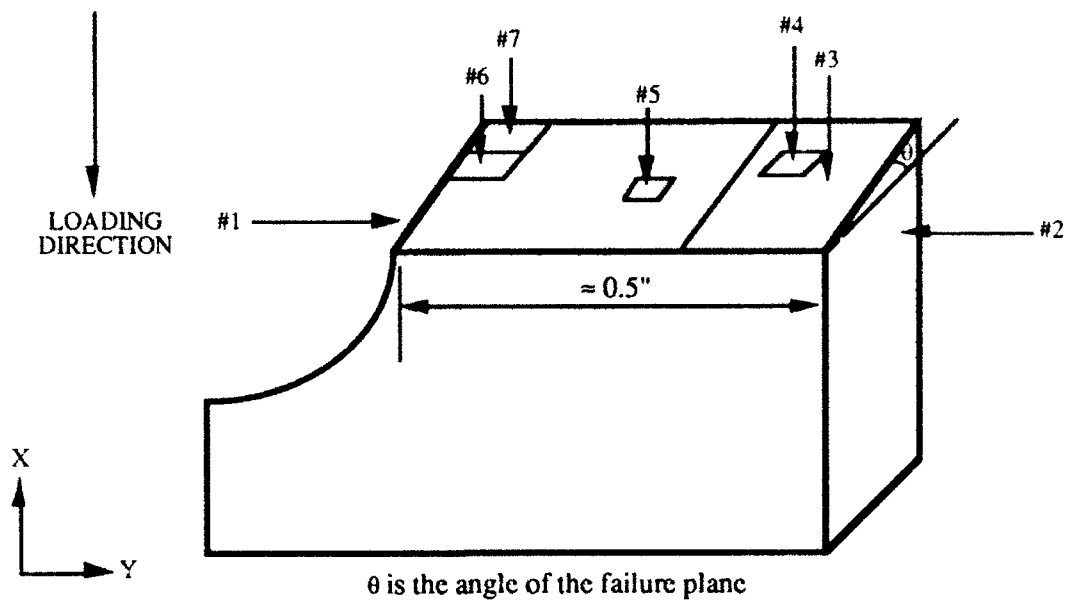
behavior that was nonlinear in nature. Another point of interest within these curves is that the transverse data is of much lower order in magnitude than the longitudinal data. This behavior is more in line with the response of the 90° specimens than the 0° specimens. Both the #3 and #4 specimens displayed more nonlinear behavior at the hole than did the others. There is no real explanation for the anomaly, but by studying the raw data it appears that one of the gages may have been malfunctioning due to a discrepancy in the two gages at the end of the loading.



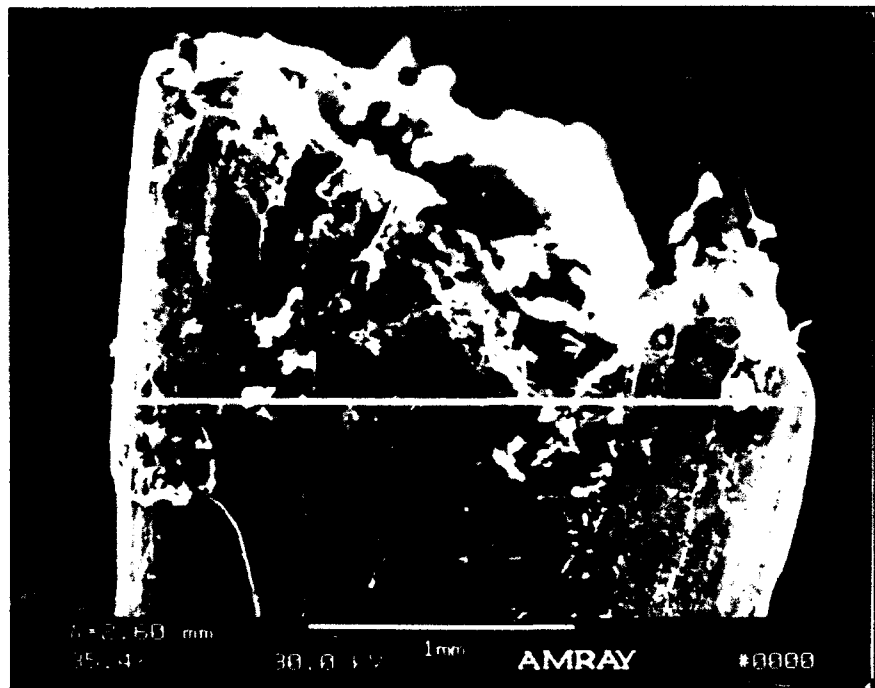
$$\text{EXPERIMENTAL STRESS} = \text{LOAD} / \text{CROSS-SECTIONAL AREA}$$

Figure 5-11: Graph of Far Field and Hole Strain for $0^\circ/90^\circ$

All of the failure ends were examined and four of the six specimens exhibited a dual planed failure surface. The locations of the photographs are shown in Figure 5-12.

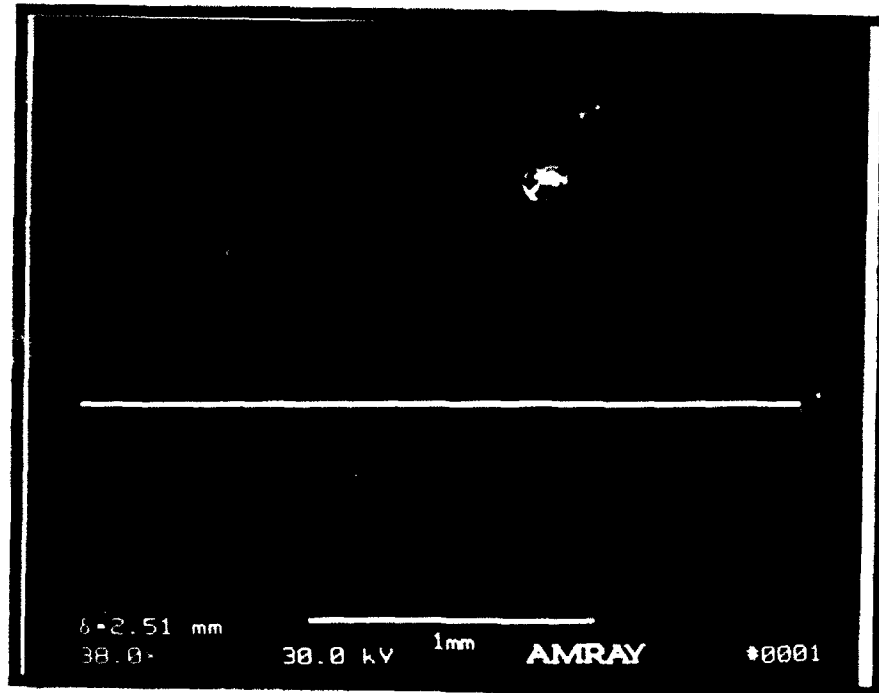


Location of SEM Photographs

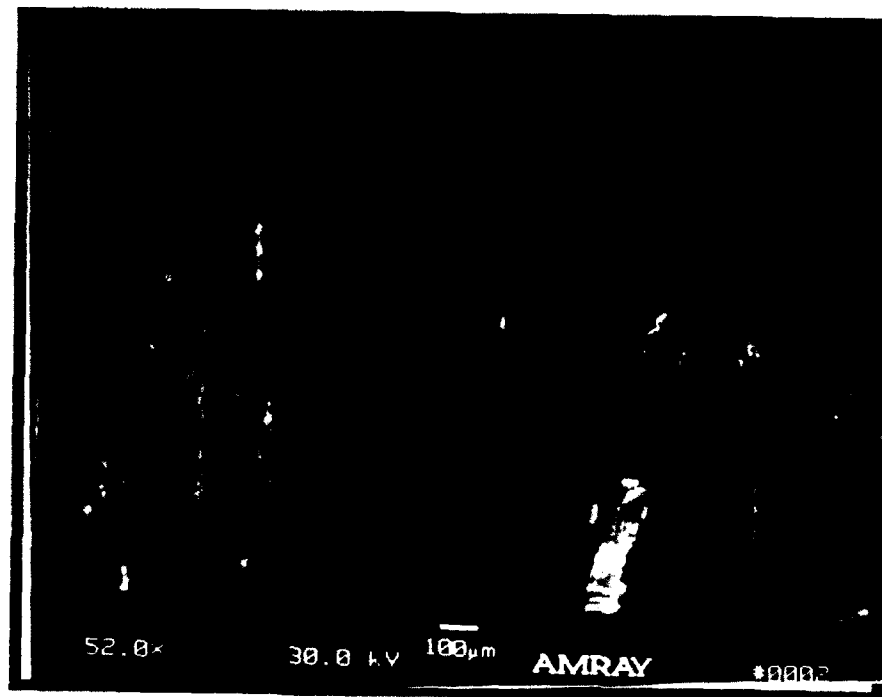


#1

Figure 5-12: Crossply SEM Photographs

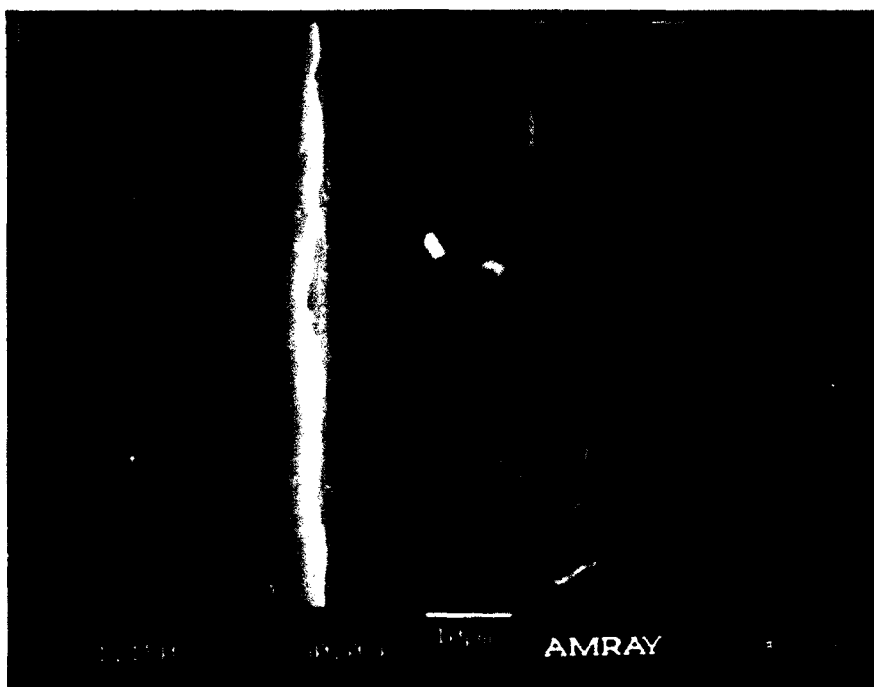


#2

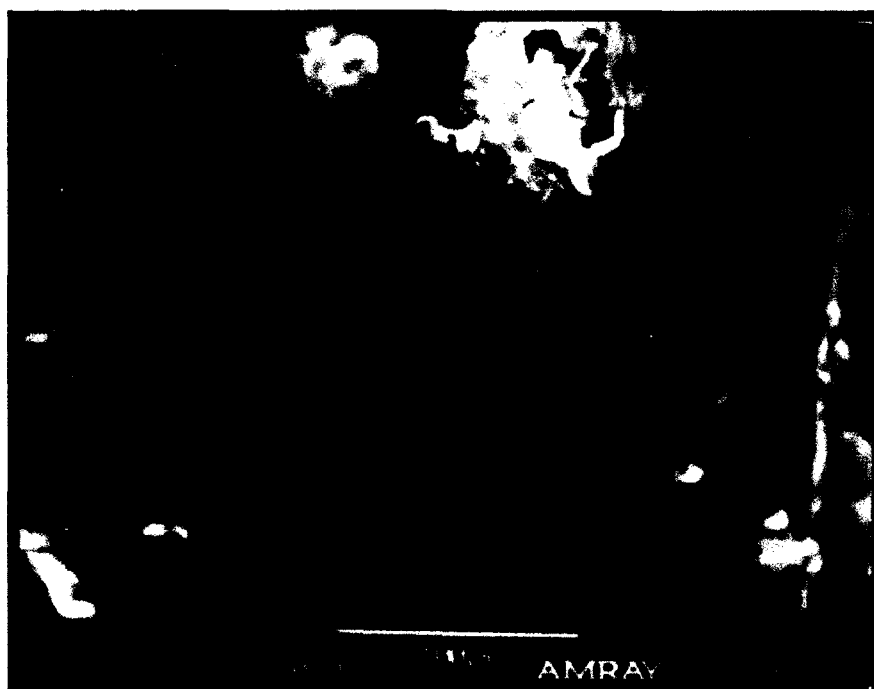


#3

Figure 5-12: Crossply SEM Photographs (cont)



#4

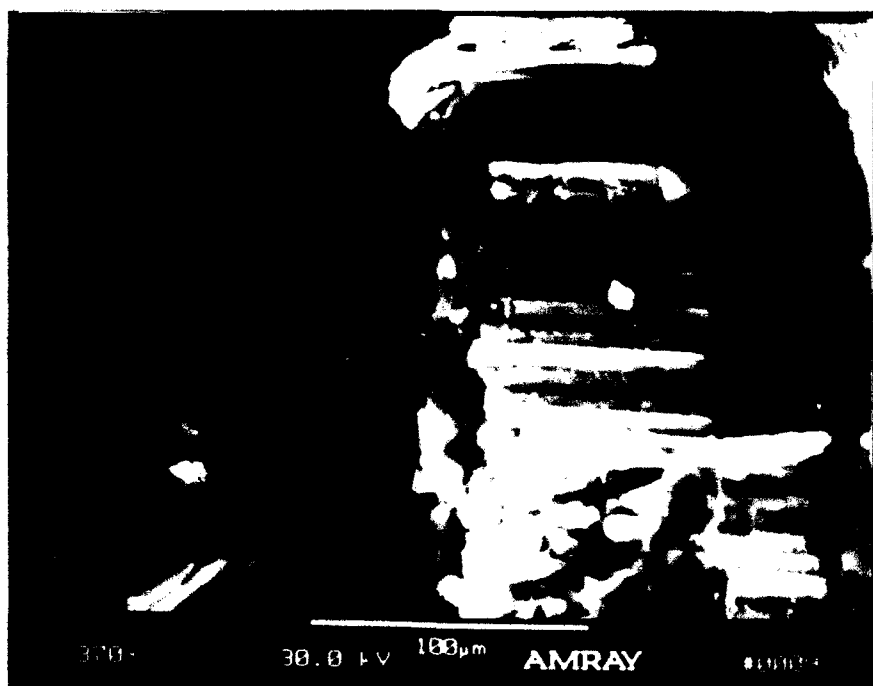


#5

Figure 5-12: Crossply SEM Photographs (cont)



#6



#7

Figure 5-12: Crossply SEM Photographs (cont)

The view in photo #1 shows a large amount of catastrophic failure at the hole as evidenced by the delamination at the edges of the hole. The white lines along the edge of the specimen shown in photo #1, and seen more clearly in photo #2 at the end of the specimen, indicated that delamination did occur within the specimen. The failure in #1 appears to have been precipitated by the failure of 0^0 plies into the hole and the edge of the hole seems to have expanded by 0.0184" in the horizontal direction. The sections between the white lines have a thickness of approximately 0.0105" or two plies of thickness. This delamination only occurred in the left half of photo #2. It appears by the depth of each crack that there was some bending taking place in the left half that caused this delamination. The delamination occurs at the meeting of a 0^0 ply on the right with a 90^0 ply on the left. It is possible that as the failure plane on the right formed it caught the failure plane on the left side causing the left portion to bend resulting in the delamination and the fracturing of the center section.

The next photo, #3, shows a view of the entire end of the specimen. Of note is the center section that seems to have separated from the rest of the specimen. Also clearly visible are the different types of plies of the specimen. The failure surface seems to be oriented in the direction of the left side of photo #2. There are several areas, visible in both photos, where portions of a 0^0 ply have been snapped off and have slid down the failure surface. The 90^0 plies seem to be in the best shape. In photo #4 an interesting phenomenon is present. The failure surface seems to have been driven through a layer of 90^0 plies preserving the matrix and protecting the fibers. This result also demonstrates the slow ductile failure that was observed by Purslow [34]. The direction of the failure can be determined by the direction of the ripples in the matrix. This failure could be expected since PEEK tends to be a ductile material and the loading was quasi-static in nature.

Photo #5 is a close view of the failure that occurred at the mid-field of the failure surface. The 0^0 fibers seem to have been broken and displaced in clumps. At the same

time the 90° fibers seem to be intact and a substantial amount of PEEK is still present on the fiber's surface. The next two photographs show the failure effects at the edge of the hole. Photo #6 show the occurrence of a shear failure on the left of the photograph. The sharpness of the spikes of the PEEK that have pulled away from the surface of the 90° fibers indicates that this is not a "slow-ductile" failure. These spiking waves would seem to indicate that the shear wave traverses the specimen at a much faster rate in this area. The waves may be the initiation point of failure since the 0° fibers that are visible to the right of the 90° ply seem to be crushed and unable to support any type of load.

The final photo, #7, is at the very edge of the surface of the hole and shows the same compression-tension failure that was observed in the 0° specimens. The fibers were crushed and shifted away from the failure surface. The 90° layer next to this 0° layer has been bent down towards the edge of the hole.

The linearity of the curves demonstrates that this type of lay-up is not as nonlinear as the 90° layup. The nonlinear behavior of the 90° layers seems to be counteracted by the 0° layers resulting in this linear behavior. The delamination that is visible is probably due the dynamic failure of the composite and is a post damage effect.

(d) $[\pm 45^{\circ}]_{4S}$ Shear Specimens

The $\pm 45^{\circ}$ specimens were the most difficult of all the composite layups to test. Because the fibers were neither parallel nor perpendicular to the loading direction, they did not support the load directly; instead it was transmitted from fiber to fiber and to the matrix by shear forces. In addition, as the load increased and the specimens were compressed, the fibers tended to move towards an alignment that was perpendicular to the direction of the loading as shown in Figure 5-13.

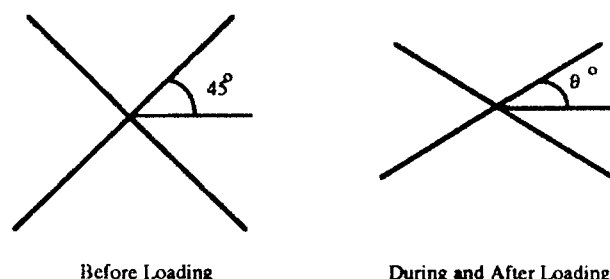


Figure 5-13: Scissoring of the Fibers of a Shear Specimen

The dynamic effect results in some of the energy introduced into the composite being dissipated by the rotation of the fibers. This effect occurs in just about any composite where the fibers are oriented off of the loading direction [39]. This dynamic effect is not accounted for in any of the closed form solutions discussed in the Compressive Mechanics section of Chapter 2, but could account for a large amount of energy introduced into the composite.

Because the scissoring results in a substantial amount of displacement of the specimen, the concern of the author was that the fixture would close before the specimen failed. The device was modified by removing 0.0625" from the gap to increase the amount of displacement the specimen should experience. After the initial test another 0.0625" was removed from the gap and another shear specimen was tested. The load on the specimen increased to 2300 lb. and dropped off, but then continued to increase until the fixture closed. (Closure of the device is determined to the point at which the graph transitions from the material curve to a curve with an extremely steep slope.) The specimen did not fracture into two pieces so it was assumed that failure did not take place.

The scissoring effect was observed by Fisher in his investigation of tension [28,39]. This effect also lead to difficulties in collecting data because it causes saturation of the hole gages at approximately 65% of the maximum load obtained from the device. The results of the testing are shown in Table 5-5, but this may not represent the ultimate strength of the composite.

[±45]_{4S}

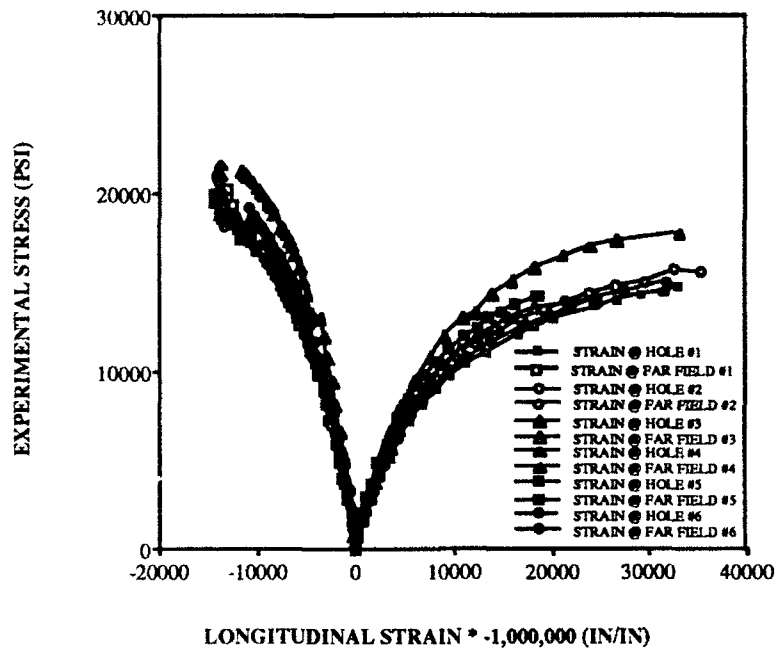
SPECIMEN #	LOAD (LB.)	EXPERIMENTAL STRESS (PSI)
1	2858.93	21463.44
2	2685.25	20608.21
3	2804.38	21632.06
4	2793.01	21353.29
5	2642.58	20049.92
6	2566.78	19430.58
AVERAGE	2725.16	20756.25
STD DEVIATION	111.60	883.38

Table 5-5: Maximum Strength for Shear Specimens

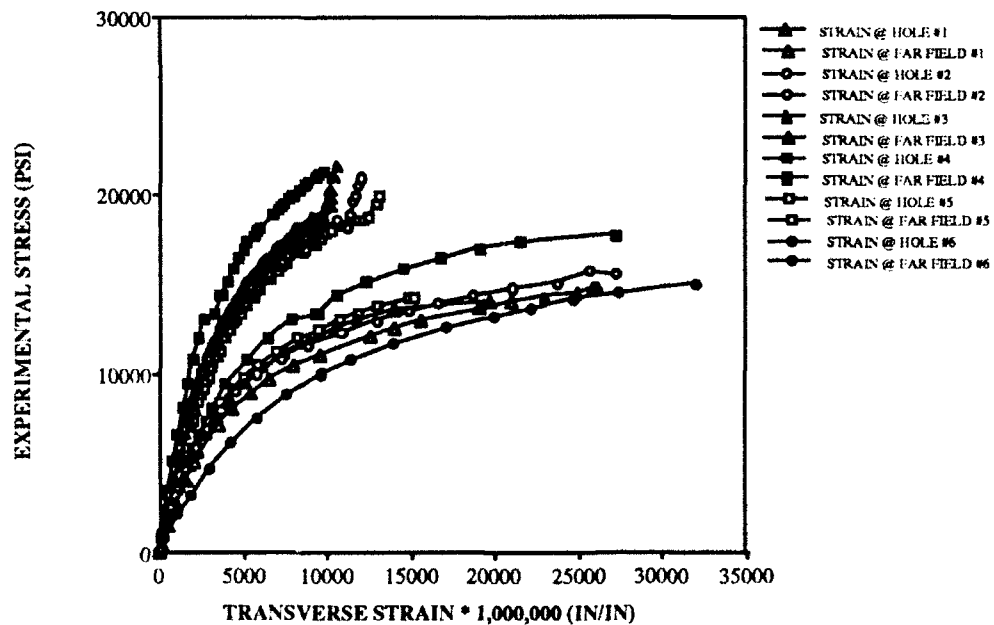
As mentioned before in the Material Properties Section of this chapter, the use of a stacked rosette may not be the most logical gage for the loading of a shear specimen. However, at the hole, it is necessary to approximate the strain at a point so it can be compared to the results of the finite element code. The hole almost closes as the composite is displaced. The large displacements also cause the gage not only to saturate but to separate at around 80% of the maximum recorded load. The far field gages, on the other hand, continue to record data until the maximum load is reached.

The shear specimens displayed an interesting phenomenon of symmetry between the transverse strain and the longitudinal strain. The results of the stress-strain data can be seen in Figure 5-14. The discontinuity in the graph of specimen #4 resulted from the switching of the load range during the testing and is not materials related, but could account for the reason it displays a stiffer behavior than the rest of the specimen.

HOLE AND FAR FIELD LONGITUDINAL STRAIN [±45]



HOLE AND FAR FIELD TRANSVERSE STRAIN [±45]



EXPERIMENTAL STRESS = LOAD / CROSS-SECTIONAL AREA

Figure 5-14: Graph of Far Field and Hole Strain for ±45°

Because these specimens did not fracture into two pieces, the failure surface could not be observed with the Scanning Electron Microscope, but was inspected with a conventional microscope and with an ultrasound investigation procedure.

The most notable feature of each of the failed shear specimens was the deformation of the hole. The hole was deformed from a circle of 0.5" diameter to an ellipse with a major axis, $2a$, of 0.5625" and a minor axis, $2b$, of 0.4375". The area of the hole seems to have changed from about 0.785 in² to 0.773 in². The width of the specimen increased by around 0.0625" at the mid plane of the ellipse. This dimensional change seems to be constant throughout the six specimens tested.

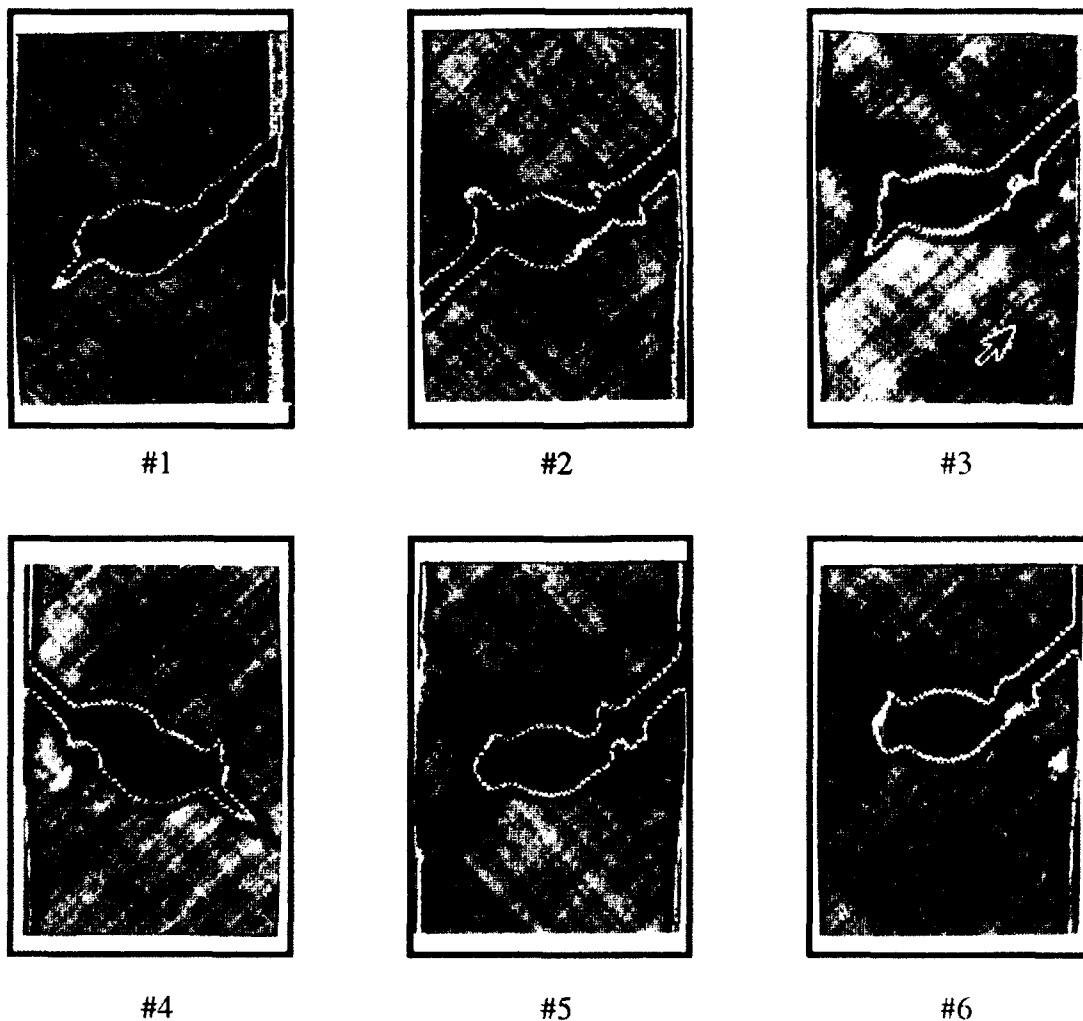


Figure 5-15: Ultrasonic Images of $\pm 45^\circ$

There was delamination visible at the mid-plane of the specimen where it appears that one half of the specimen was forced into the other half. The edges of the specimens developed a shear plane from the hole to the outer edge. The shear plane at the edge of the specimen displays little or no delamination, while the edges that do not have the shear plane display no damage. The tested specimens were subjected to an ultrasound inspection to determine if there were any internal flaws that were not visible on the surface. The results of these investigations are shown in Figure 5-15.

The images show that there was not much consistency in the direction of failure from one area to the next. The areas of the picture that are red indicate that the ultrasound signal was reflected directly back to the transducer and represent areas of extremely high density or openings in the specimen. As can be seen all the specimens suffered the same type of fracture. The failures in specimens # 1, 3, 5, and 6 occur at an angle that is 42° from the horizontal. Only the #2 specimen displayed cracks that started at the hole and progressed to both edges of the specimen. However specimens # 3, 4, and 5 show evidence of this crack forming and starting to progress towards the outer edge. A close observation of the pictures shows areas of substantial damage originating at angles of $\pm 45^{\circ}$ from the hole. If the specimen could have loaded until it fractured into two pieces, it is quite possible that all the specimens may have developed cracks that were $\pm 45^{\circ}$ and $\pm 135^{\circ}$ from the horizontal.

Another interesting occurrence on each of the specimens was the development of a large red area on the ultrasounds that was located on the major crack. This area appears to be a location where the composite material has bulged out caused by the pushing of one half into the other.

Specimen #2 was separated by hand and the failure surface was observed. A true analysis of the fiber surface could not have been performed by the SEM since some of the damage was introduced by the separation process. However, several gross area conclusions can be drawn from the surface. First, while there was delamination around

the edge of the hole there was no delamination or damage at the top or bottom of the hole. The delamination seemed to proceed from the holes edge for about 45° around the surface of the hole until it tapers off. The failure plane appears to be just one surface instead of the two observed in the crossply and is at a 45° angle towards the edge of the hole. Near the edge of the hole the surface appears to be matted down or crushed, while away from the hole the fibers were still standing. When the specimen was separated, there was much audible popping heard from the failure surface. This sound indicates that even though a shear plane had developed within the specimen many of the fibers had still not failed and were, to some degree, still supporting the imposed loaded.

The use of $\pm 45^{\circ}$ plies also contributed to the resistance of interlamina shear forces that can be generated when a composite is loaded in tension or compression. They will provide some assistance to the $[0^{\circ}/\pm 45^{\circ}/90^{\circ}]_{2S}$ specimens that were tested in compression.

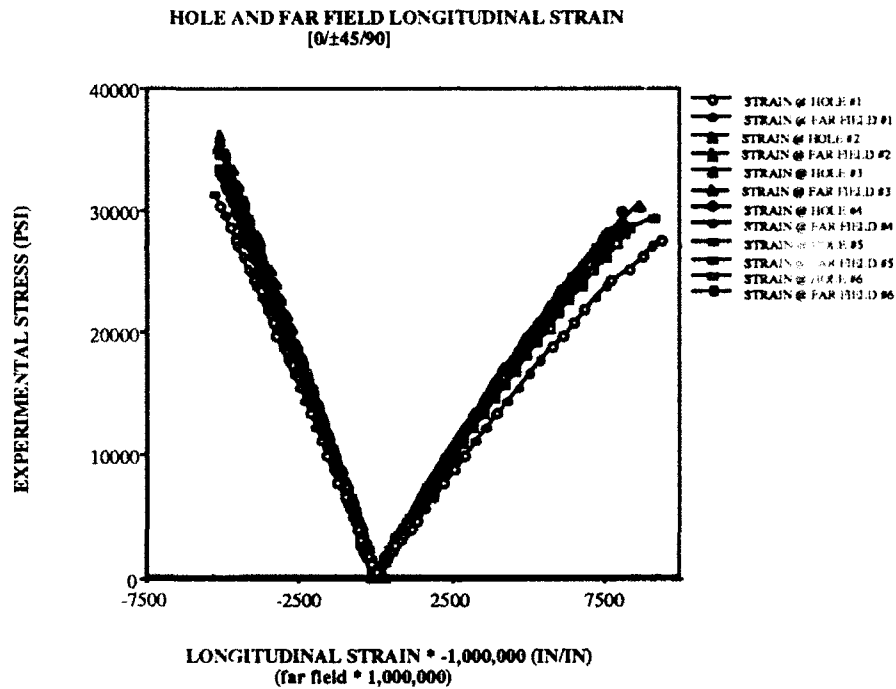
(e) $[0^{\circ}/\pm 45^{\circ}/90^{\circ}]_{2S}$ Quasi-isotropic Specimens

All six of these specimens exhibited a horizontal crack at the hole similar to the type of failure exhibited by most of the other specimens. As in the others, there was a large amount of deviation in the result from one specimen to the next. The first specimen exhibited a load that is much lower than the rest of the specimens as shown in Table 5-6. The quasi-isotropic specimens exhibited the same type of linear behavior that was shown by the crossply specimens. The discontinuity that was apparent in the crossply specimens at the first part of the loading cycle was present, but to a lesser degree. It seemed to occur around 300 lb. into the loading cycle and did not appear in the recorded data. The curves displayed some nonlinear behavior at approximately 100 lb. from the ultimate strength. In addition, after the failure occurred the load on the specimens dropped off immediately. The linearity of the data is clearly visible in Figure 5-16. The transverse strain at the hole exhibits the most nonlinearity with the curve changing drastically at the end of the

[0/±45/90]_{2S}

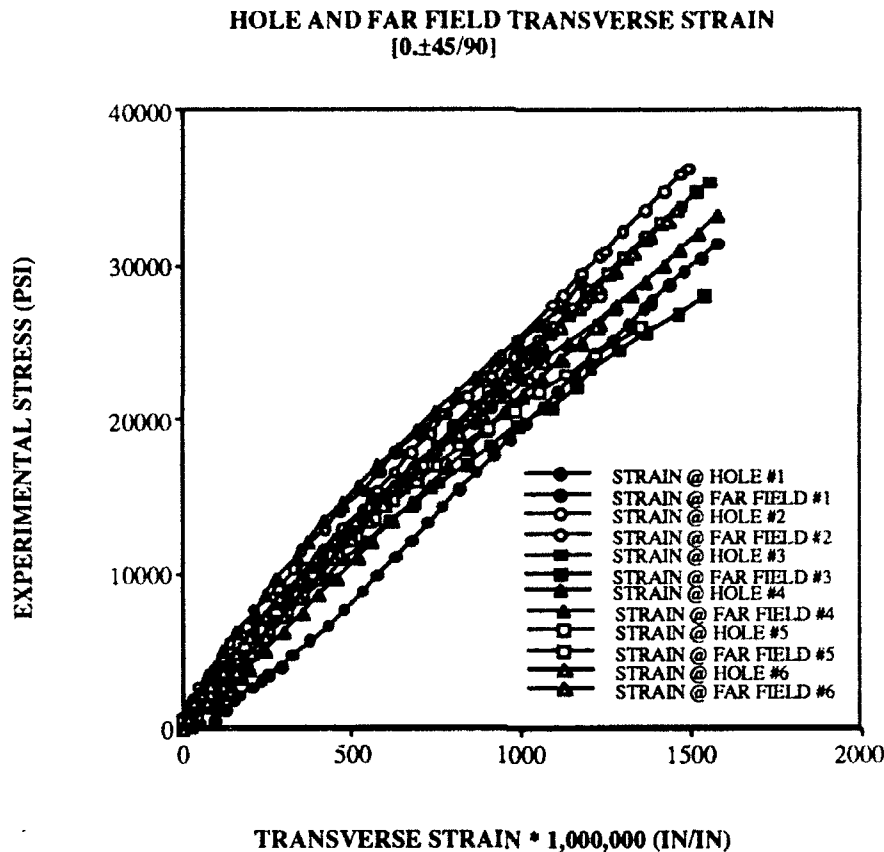
SPECIMEN #	LOAD (LB.)	EXPERIMENTAL STRESS (PSI)
1	3978.37	31325.75
2	4647.21	36165.06
3	4711.77	35286.23
4	4449.93	33060.40
5	4334.79	32567.92
6	4482.95	33859.14
AVERAGE	4434.17	33710.75
STD DEVIATION	261.81	1785.78

Table 5-6: Ultimate Strength of Quasi-isotropic Specimens



EXPERIMENTAL STRESS = LOAD / CROSS-SECTIONAL AREA

Figure 5-16: Graph of Far Field and Hole Strain for 0°/±45°/90°

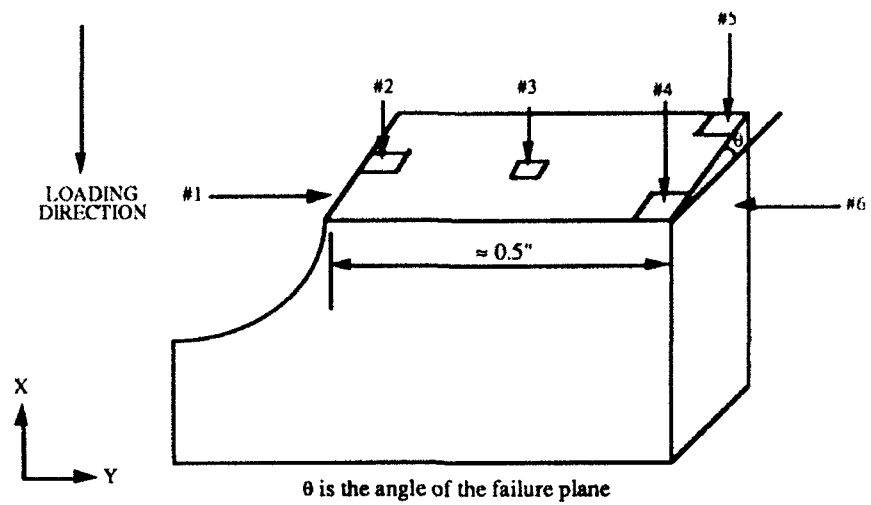


$$\text{EXPERIMENTAL STRESS} = \text{LOAD} / \text{CROSS-SECTIONAL AREA}$$

Figure 5-16: Graph of Far Field and Hole Strain for $0^\circ/\pm 45^\circ/90^\circ$ (cont)

loading cycle. The longitudinal strain at the hole also seemed to lose its continuity towards the end of the loading cycle because of the formation of the crack and the jamming of the two pieces together as the specimen fails. The amount of movement of the failed planes is not as much as in the other specimens, possibly because the $\pm 45^\circ$ fibers still support some of the load after the failure plane has developed.

Because of the nature of the failure of composites and because this particular layup contains four separate orientations of plies, the failure modes were not as clearly defined as the other layups. Figure 5-17 shows the location of the photographs.



Location of SEM Photographs

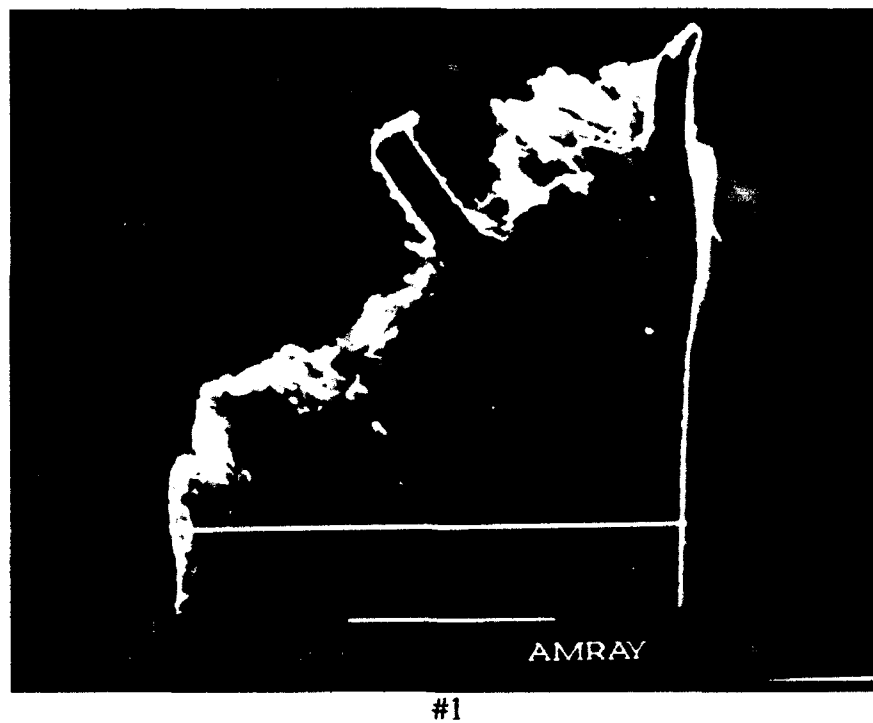
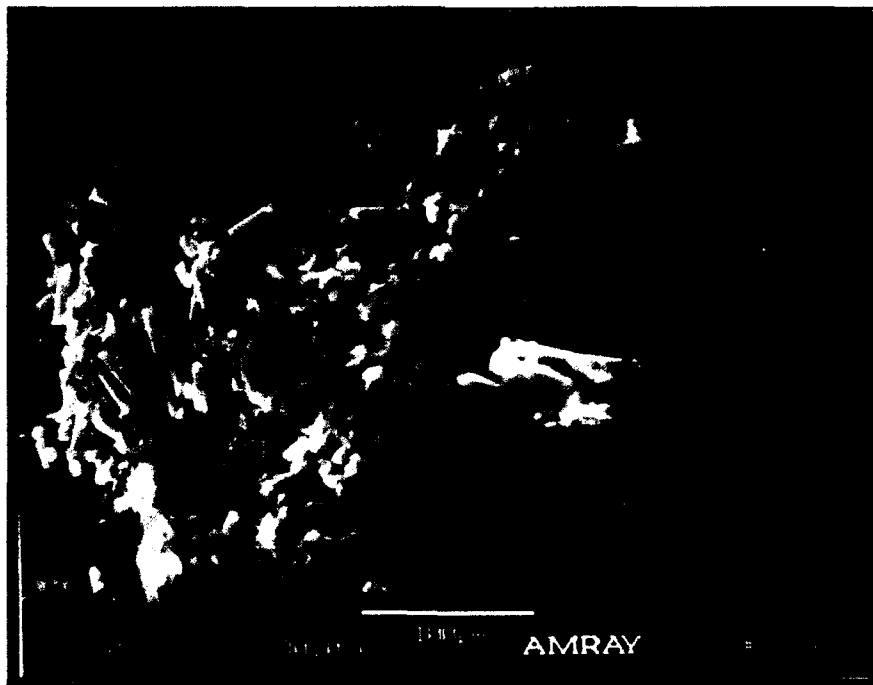


Figure 5-17: SEM Photographs of $0^\circ/\pm 45^\circ/90^\circ$



#2

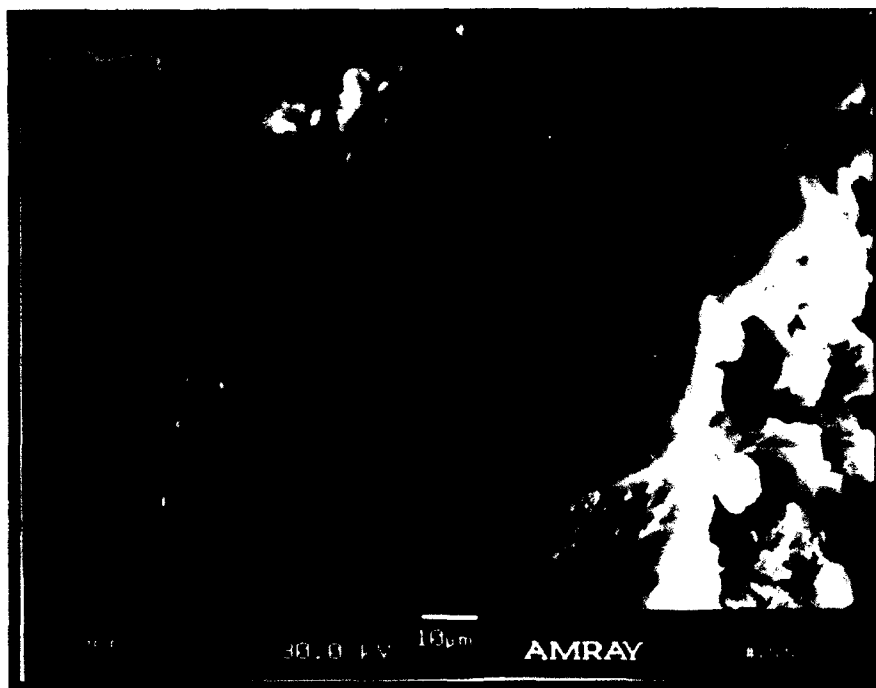


#3

Figure 5-17: SEM Photographs of $0^{\circ}/\pm 45^{\circ}/90^{\circ}$ (cont)

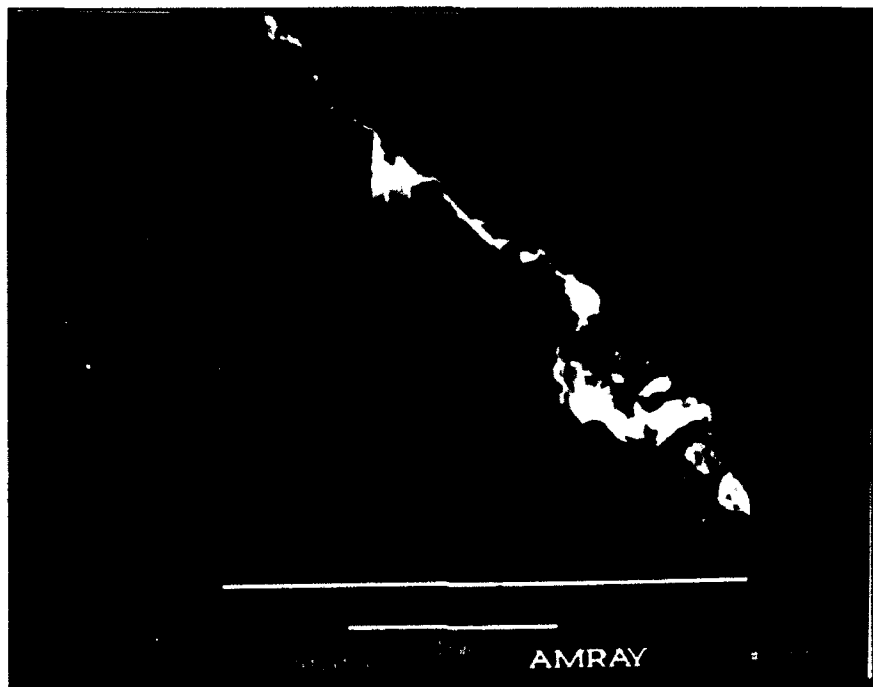


#4



#5

Figure 5-17: SEM Photographs of $0^\circ/\pm 45^\circ/90^\circ$ (cont)



#6

Figure 5-17: SEM Photographs of $0^\circ/\pm 45^\circ/90^\circ$ (cont)

The first photograph shows the end of the specimen facing the hole. Many failure modes exist in this section and clearly some delamination has occurred at the hole edge. The overall failure angle is measured at 49° from the loading direction. The mid-plane of the specimen consists of a portion of the two 90° laminates that seems to have separated from the rest of the laminate and is sticking up at an angle that is roughly normal to the shear plane. In addition, the 0° ply on the top outer edge still appears to be intact and has separated from the adjacent $+45^\circ$ ply.

A close-up of the hole edge is shown in photo #2. What can be distinguished from this jumble of fibers is that around the bottom of the hole's edge it seems that many of the plies have delaminated. It would appear that the failure may have originated at the top of the specimen and progressed down to the bottom of the specimen. The matrix still seems to adhere to the fibers indicating the strength of the fiber-matrix interface. Some crushing of the fibers is visible at the top between the two bundles of fibers towards the middle of the photo.

The crushing of the fibers is also visible in photo #3. This photo was taken at the mid-plane of the failure surface and is a good representation of the type of failure surface that was visible around the middle of the specimen. A bundle of fibers seems to have broken off. This crushing of the fiber is evidenced all over the specimen, but it seems to be the dominate feature in the middle of the specimen.

The other area that had a distinctive type of failures is the outer edge of the specimen. The crushed fibers are present all over the surface, but at the edge a bundle of fibers seems to have separated from the rest of the ply and may indicate the formation of a kink band that could have resulted in the failure of the composite. The kink band has been studied by many and is commonly defined as the horizontal or out-of-plane displacement of fibers that may result in failure of a composite structure. Crippling of the fibers is also visible at the top edge of the hole. Crippling of the fiber can be defined as the buckling of the fiber with the displacement of the failed ends in a direction normal to the loading. The layer that is visible is a 0° ply that has fractured at the top and has been displaced at the bottom of the picture.

The final picture, #6, displays clearly the shear plane that was found in the first photograph. The angle measured is still 49° from loading direction indicating that the plane remains somewhat constant throughout the length of the failure surface. The same delamination is also present but it is not as prominent as in the crossply, possibly due to the addition of the $\pm 45^{\circ}$ plies to assist in supporting the shear stresses that develop between the plies. In several areas the uniformity of the failure slope has been disrupted by the removal of material. This disruption may be the effect of the crushing of the fibers and the resulting loss of the material which may become loose after the failure occurs. When the specimens were removed from the Boeing fixture, many flakes and chunks of the composite came out with it.

In one area at the bottom of the failure surface, a ply appears to be bent over. This ply was inspected and appears to be a -45° ply that suffered shear failure along the fiber

plane and may have caught the upper failure surface and was bent. There is no indication that the fibers of the -45° ply were broken or crushed, just their direction was changed.

Of all the specimens examined the failure mechanisms of the quasi-isotropic specimens were the most difficult to distinguish. The predominate features of these specimens were the appearance of crushed fibers and the accompanying delamination. The delamination may be the result of the failure of the specimens and could be considered post failure damage. The failure modes of the shear specimens were rather difficult to distinguish since the specimens failed to fracture into two separate pieces. What was visible was the formation of $\pm 45^{\circ}$ fracture surfaces that have a 45° plane. The hole deformed to an elliptical shape. The stress-strain response seemed to be symmetric for both the transverse and longitudinal strain.

The crossply specimens had several distinctive failure modes including a tension-compression failure of the composite. They exhibited delamination as a result of the formation of two separate shear planes, each of 45° , again this may be a post failure damage. There is also an indication of "slow-ductile" failure towards the midplane of the specimen and of a faster type of matrix ductile failure near the hole. There was also some evidence of a fiber crippling, but no distinctive kink bands were located.

The two unidirectional specimens produced entirely different results. The 90° has a very distinctive failure surface that did not vary greatly from specimen to specimen. While there was some displacement or twisting of some of the plies there was no distinctive failure mode which indicates that such displacement was the result of post failure damage and not actual failure modes. Moreover, crushing of the fibers occur on a local scale. The failure surface was also around 24° from the loading direction and the surface on the whole was rather clean.

The 0° produced two distinctive failed specimens: a splitting failure at the hole and a horizontal cracking at the hole. The angle of the crack in the shear plane was approximately 65° from the loading direction. Also some compression-tension failure of

the specimen at the midplane of the specimen was present. There was a realignment of the fibers from 0° to an angle of 45° at the top of the specimen on the edge and some areas where the fibers were bent, but there was no distinguishable kink band formation. The vertical split occurred at a higher load than the horizontal cracks. When specimens were examined using ultrasound, there were cracks visible around the edges of the hole and more splits appeared to be in the process of forming before the loading was stopped. These failure modes were not distinctive in nature and were hard to quantify.

The results of these tests leads the author to believe that the progression of failure of a composite can be predicted using a finite element code rather than closed form methods, like those mentioned in Chapter 2

(3) Progression of Failure Testing in the Boeing Fixture

The progression of failure study was conducted after the testing of each of the ultimate strength ply layups. An average of all the ultimate compressive loads was determined and the standard deviation was checked. If there was a large amount of deviation of one specimen from the rest it was removed and a new average was computed. The average computed was multiplied by 0.9 and 0.95 respectively to obtain the level at which the loading would be stopped. The Instron Machine's strip chart was annotated to show the level at which the loading was stopped for each specimen.

In retrospect, what should have been done was to divide each ultimate strength specimen by its cross-sectional area and average the ultimate stresses. The 90% and 95% load could then be determined by multiplying the average ultimate stress by the individual specimen's cross-sectional area. This method would have removed the problems associated with the variations in thickness experienced by each specimen and eliminated some of the earlier failures that occurred in this testing.

Of the nineteen specimens used in this test, five failed before they reached the prescribed load: four of the five specimens were unidirectional, two 0° and two 90° . The fifth was a $0^\circ/90^\circ$ cross-ply specimen. These failures caused some concern on the part of the author who consulted with Dr. Edvins Demuts of Wright Laboratories Flight Dynamics Division. Dr. Demuts, who has worked extensively with Gr/PEEK, stated that it tends to show a large amount of deviation in the final failure loads and that a unidirectional layup may be more sensitive to loading than a multi-directional layup [35].

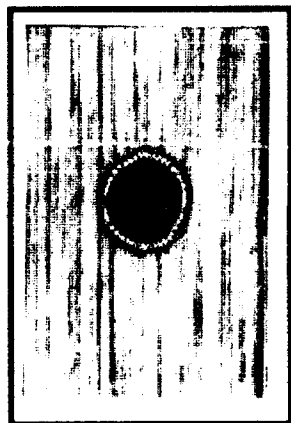
(a) $[0^\circ]_{16}$ Unidirectional Specimens

Referring to Table 4-1, for the 0° , specimens #7 and #10 failed before they could reach the prescribed load. The specimens that did not fail were unloaded and investigated using ultrasound. Specimen #8 was loaded to 6000 lb. and showed no visible damage when removed from the fixture. The results of these investigations are shown in Figure 5-18. Dark lines appear on the left edge of the hole running parallel to the fibers that could possibly indicate the formation of a longitudinal split. There is no visible indication of a horizontal crack.

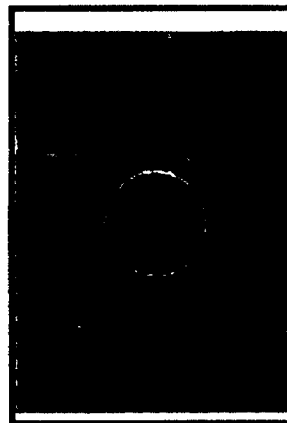
Two of the specimens, #9 and #11, were loaded to 6220 lb. or 95% of the computed ultimate load. Once again there is no visible damage present in these specimens; however, the ultrasound scans in Figure 5-18 show that there are several regions of damage. A vertical split appears to be forming on the right edge of the hole in specimen #9, as well as a split forming on the left edge at the hole in specimen #11. The absence of visible damage in these two specimens seems to indicate that the splitting failure is an instantaneous phenomenon. Each of the tested specimens would have failed from vertical splitting and not from horizontal cracking. The two specimens that failed both failed due to horizontal cracks. An ultrasound ply-by-ply image was taken of

specimen #10. The image was a grouped ply analysis that looked at a group of four plies at a time. This is shown in Figure 5-19.

90%

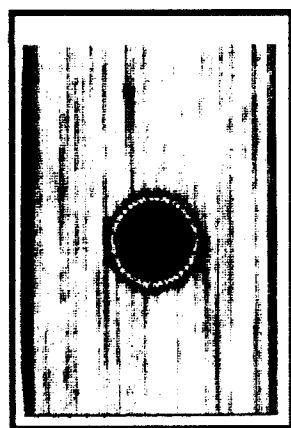


#7

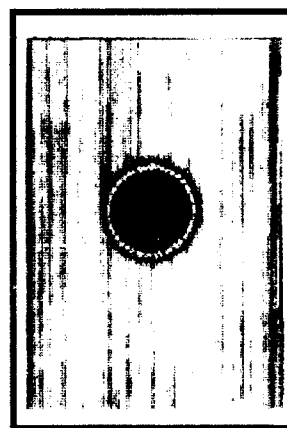


#5

95%



#9



#11

Figure 5-18: Ultrasonic Images of 0°

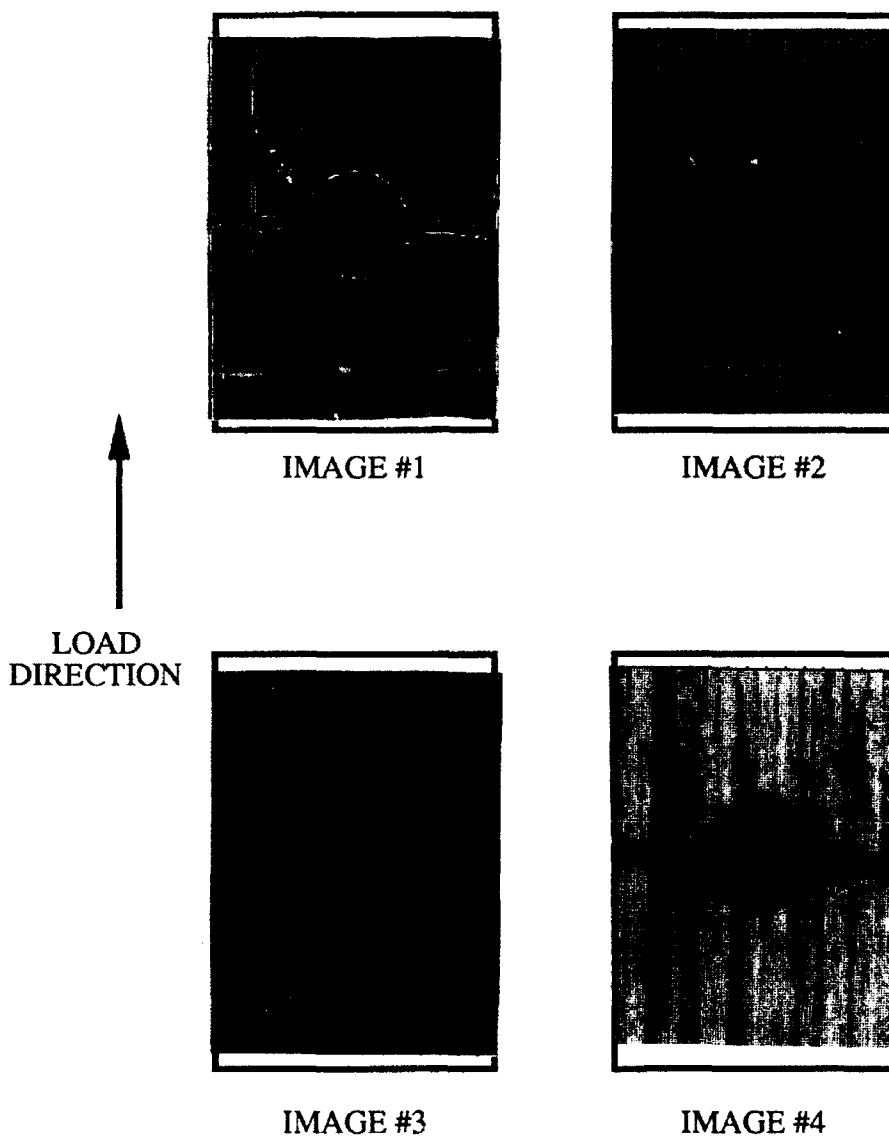


Figure 5-19: Ply-by-Ply Analysis of Specimen #10

Some vertical splitting is visible in this specimen, but it is not present in any of the other specimens that failed by cracking. At the top of image #2 there is some indication of delamination (white areas) within the plies at the top edge of the hole. (The area that is approximately at an angle of 135° for the cracked surface is a dust speck that landed on the specimen during the scanning.) There is no visible damage in the third group plies. The fourth group of plies shows some amount of vertical splitting as well as some other damage that may be post failure damage. The unidirectional specimens created the most erratic results of all the specimens tested.

(b) $[90^\circ]_{16}$ Unidirectional Specimen

Only three specimens were available for the 90° progression of failure study because of problems in the fabrication process. Of the three specimens used, two failed before reaching the 90% load of 2150 lb, thus failing considerably lower than the six ultimate strength specimens tested. The final specimen, #10, was stopped at 90% of load.

As can be seen from the ultrasound image in Figure 5-20 the specimen was probably within milliseconds of failing completely. The shear plane has already formed on the left side of the hole and the specimen had become two separate parts on the left

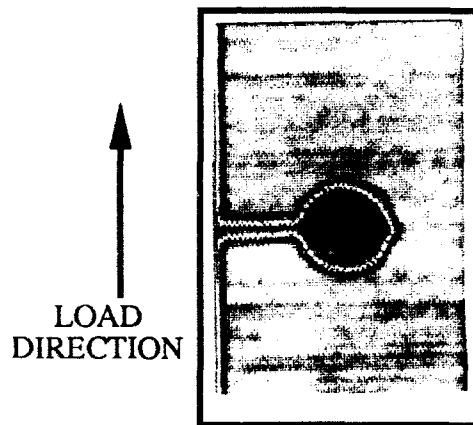


Figure 5-20: Ultrasonic Images of 90° Specimen

side of the hole. The right side of the hole shows areas where the horizontal crack was starting to form. This would seem to indicate that the unidirectional specimens tend to fail very quickly and are rather more sensitive to loading conditions.

(c) $[0^\circ/90^\circ]_{4S}$ Crossply Specimens

The next set of specimens tested was the $0^\circ/90^\circ$ layup. Only one specimen failed before the prescribed load was reached. Ultra sound was performed on the specimens and the results are shown in Figure 5-21. The most interesting failure feature of these

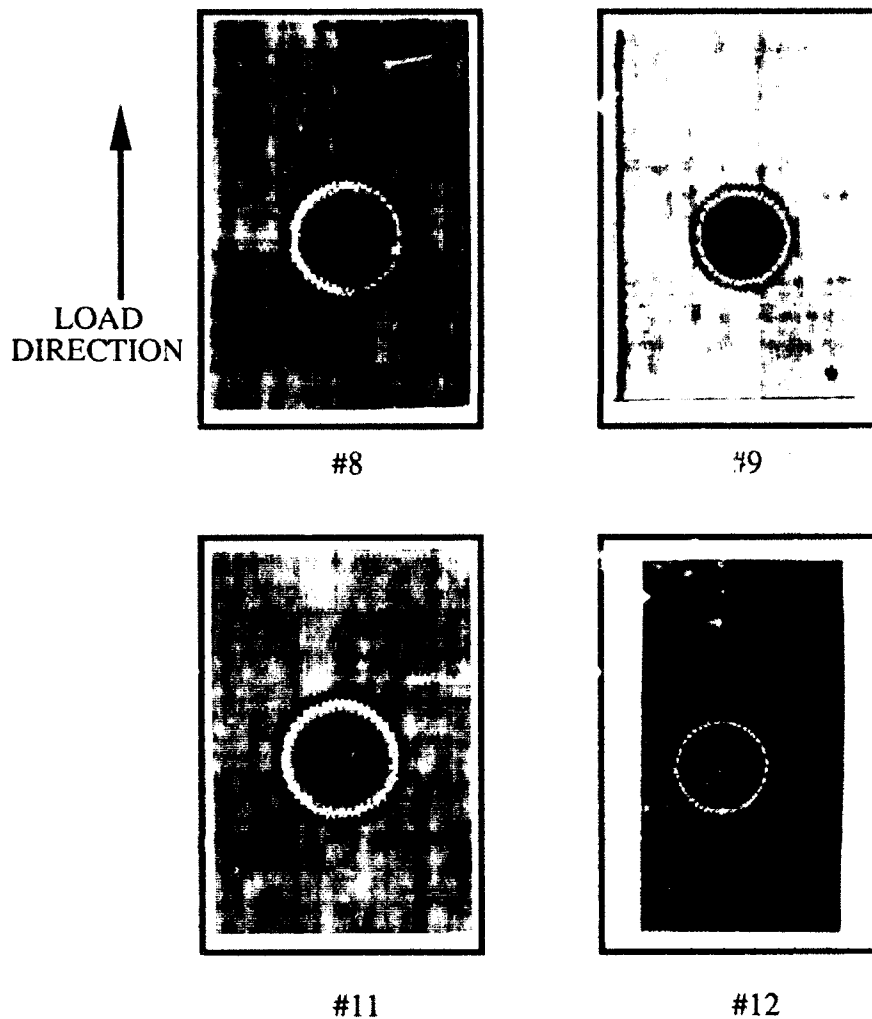


Figure 5-21: Ultrasonic Images of 0°/90° Specimen

specimens can not be seen in these images, but was observed in the ply-by-ply analysis that was conducted on specimen #12 which will be discussed subsequently. There seems to be no indication of any damage on specimens #9 or #8 occurring before the loading was stopped. A visual inspection of the specimens revealed that an extremely small crack was present on the surface of the hole on specimen #8. The crack is at the same angle as the shear plane that was formed on the surface of failed specimens. The pink ring around the hole is the electronic noise that has been generated by the hole and the crack may have been obscured by this noise.

In specimen #10 the ultrasound image reveals a damaged area at the hole and a dark line emanating from the hole towards the edge of the specimen. There was no visible damage at the edge, but cracking was present on the surface of the hole at the same shear plane angle. The ply-by-ply investigation of #10 is shown in Figure 5-22.

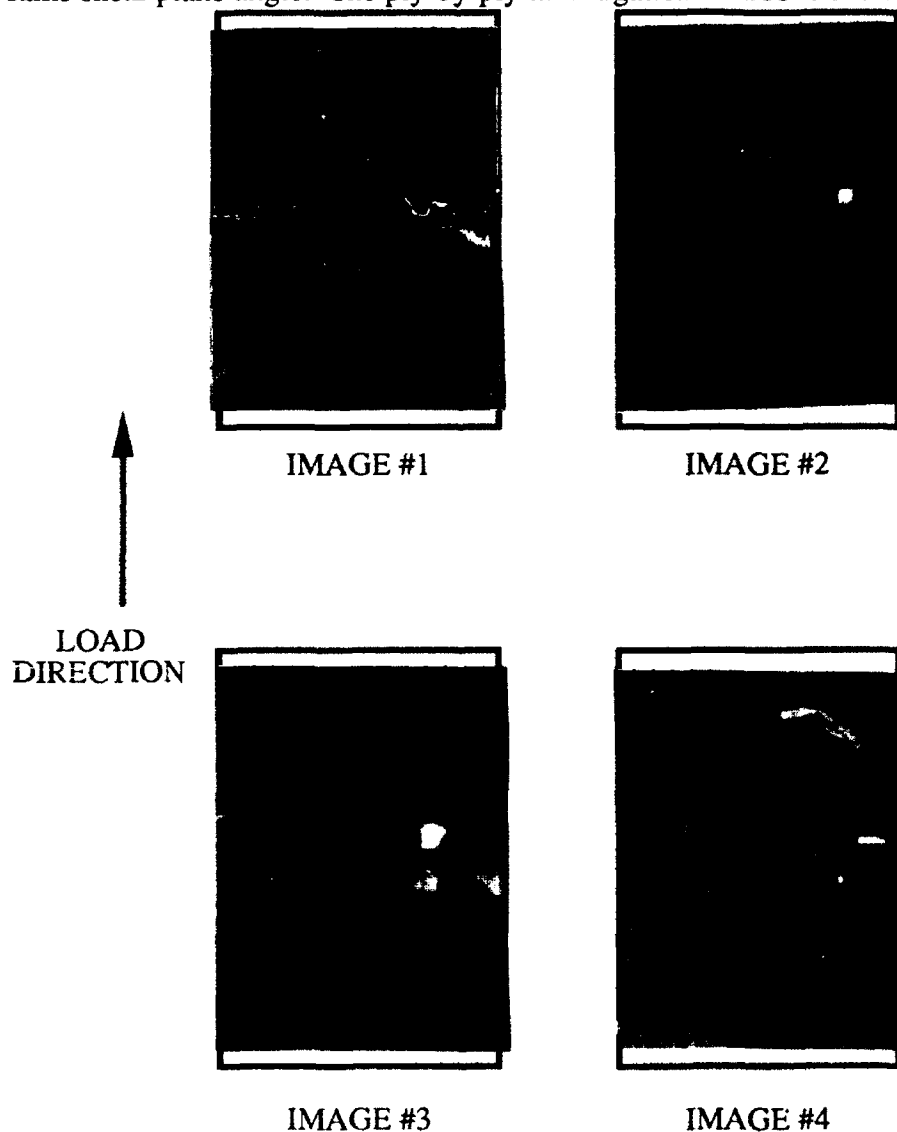


Figure 5-22: Ply-by-Ply Analysis of Specimen #10

The visible red lines are just surface imperfections present in this specimen and are not related to the specimen's failure. There is evidence of a crack on both the left and the right side of the hole shown in image #1. These cracks show up as small red areas at the edges that are perpendicular to the load. They are not clearly visible in image #2 or

#3, but can be seen on the left side of the fourth image. The white areas on the right side of the image are areas where delamination occurred. From the failure of specimen #10, it can be concluded that the crossply layup seems to be fairly sensitive with damage occurring near the very end of the loading.

(d) $[\pm 45^\circ]_{4S}$ Shear Specimen

After all the initial testing was conducted on the Boeing fixture to determine its limitations there was only one shear specimen left to test in the progression of failure study. The specimen, #10, was loaded to 2075 lb. or 90% of the maximum value obtained from the specimens.

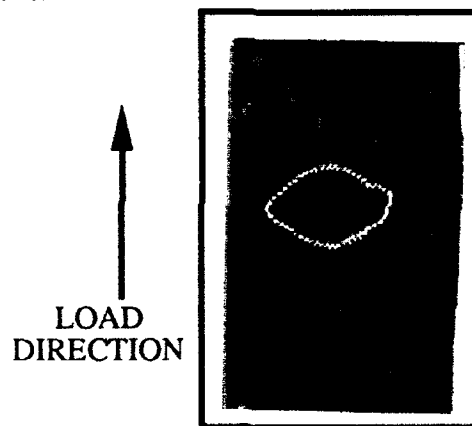


Figure 5-23: Ultrasonic Images of $\pm 45^\circ$ Specimen

There is evidence of damage at the "corners" of the hole and some indications of top part of the hole into the bottom. Had the testing been allowed to continue, it appears that the damage zone at the top right of the hole would have become the crack that was observed in all the ultimate strength specimens subjected to ultrasound in Figure 5-15. Specimen #10 shows more symmetry of damage than any of other $\pm 45^\circ$ specimens tested.

(e) $[0^\circ/\pm 45^\circ/90^\circ]_{2S}$ Quasi-isotropic Specimens

The last layup that was tested was the quasi-isotropic specimens. None of these specimens experienced failure. Specimens #8 and #9 were subjected to the 90% load of 3815 lb. and specimens #10, #11, and #12 were subjected to the 95% load of 4025 lb. One interesting point is the similarity of the cross-sectional areas of these specimens used in the progressive failure study, as seen in Table 4-1. This similarity could be the reason there was no failure of the specimens and gives credence to the use of the ultimate stress to determine the 90% and 95% loads.

The through-the-thickness ultrasound images showed no visible damage of any of the specimens and are not presented. Visibly, the 90% specimens showed the barest indication of a crack forming perpendicular to the loading direction, but was not detected by the ultrasound. This crack showed up only as a slightly discolored area in comparison to the rest of the material. This discoloration was located along the surface inside the hole. The 95% specimens show a little more indication of the crack forming. Each of the 95% specimens has an area where the material seems to be coming into the hole., This does not occur through the thickness of the specimen only on two separate plies. These plies seem to be 0° plies located toward the middle of the specimen. This could be initiation of failure at the hole as the 0° plies start to buckle or cripple into the hole. The outer edges of the specimen do not seem to be buckling into the hole but there are cracks visible on the surface of the specimen. This may indicate the possible points at which the ultimate failure is initiated. The cracks are located on the higher edge of the shear plane that is starting to develop.

A ply-by-ply analysis was completed on specimen #11 and is shown in Figure 5-24. This analysis verified the conclusions drawn in the preceding paragraphs.

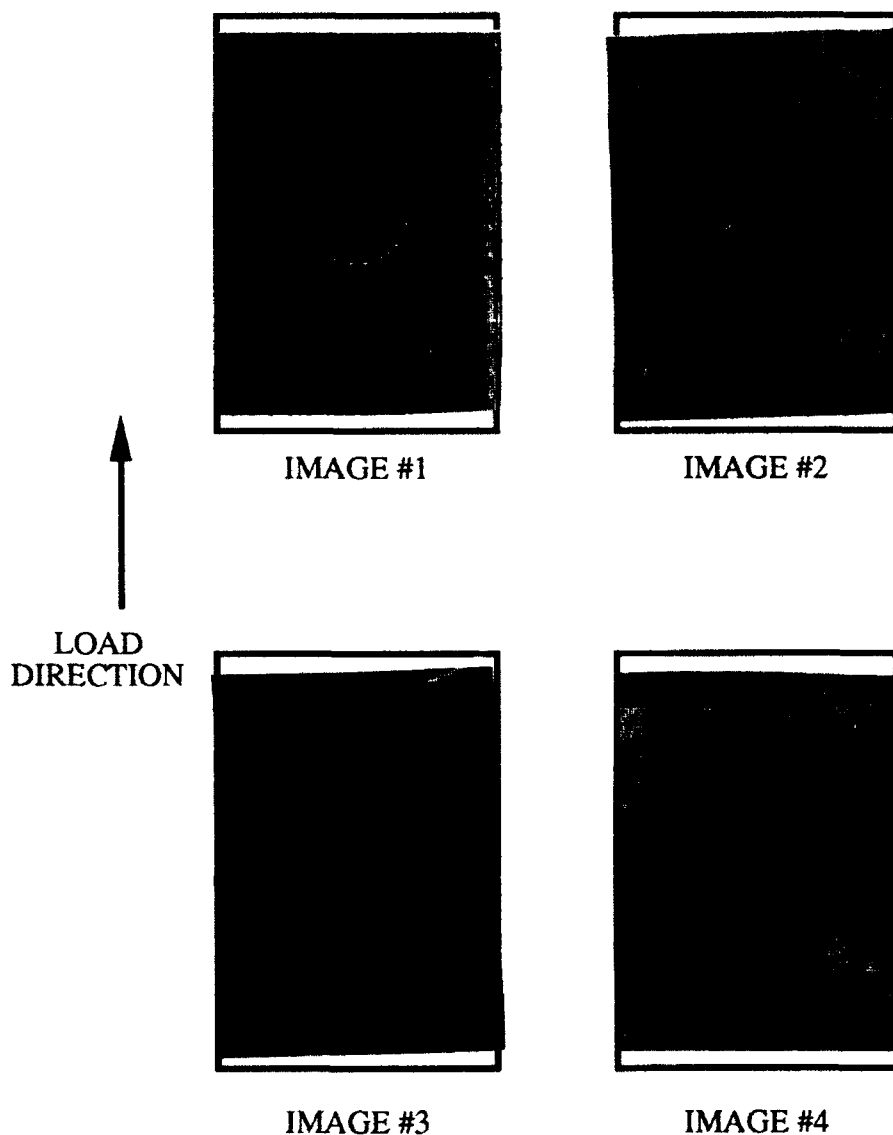


Figure 5-24: Ply-by-Ply Analysis of Specimen #11

The small white areas of the hole edges perpendicular to the load direction indicate some type of failure within the four ply group and can be attributed to the 0^0 ply which buckled into the hole. The second group shows slight indication of a straight crack at the left edge of the hole. The third group, while extremely difficult to interpret, reveals that the crack is at the edge of the hole. The final image, which is the outer edge of the specimen, shows the formation of the crack. The quasi-isotropic specimens give the best indication of the initiation of failure. They show that failure seems to manifest itself experimentally only towards the very end of the loading.

In many of the specimens that were investigated it was apparent that very little damage had occurred, even when the load was approximately 95% of the ultimate load. It is possible that a specimen first experienced a quasi-static failure, which manifested itself as a cracking within the specimen. There seems to exist a point at which the cracking changes from a quasi-static crack to a dynamic failure that results in the sudden, total failure of the specimen. This dynamic failure seems to be present in all failed specimens, but it was uncertain at which part of the progressive damage survey the quasi-static failure started. However, the ultrasound provided a good indication of the load levels at which damage actually started to appear. This dynamic failure can not be modeled by the finite element code.

Also, the progression of failure study gave a good indication of where the damage initiated and what the levels of damage were as the specimen approached its ultimate load. The ply-by-ply analysis shows that the failure seems to occur in one ply and proceed through-the-thickness. This thesis also allows for a good comparison with the analytical investigation of the specimens conducted by PLNRS.

C. Analytical Comparison

The previously discussed experimentation was performed in order to draw a comparison to the analytical method developed by Dr. Sandhu. The main goal of this thesis is to determine if the failure of a composite in compression can be modeled by Dr. Sandhu's energy method. This modeling is essential so that a composite structure can be designed to meet a specific loading condition without the expense of experimentation. The author believes that this method can best model the failure of the composite because it incorporates the actual material response in the form of material data.

This incorporation of the response includes any material nonlinearity as well as the ultimate stresses and strains from experimental tests. This data can be developed for

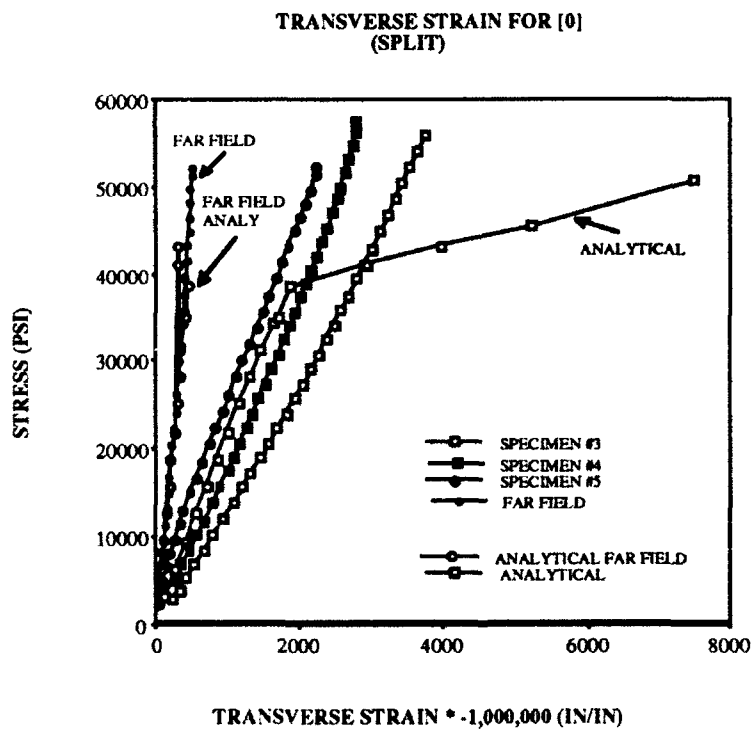
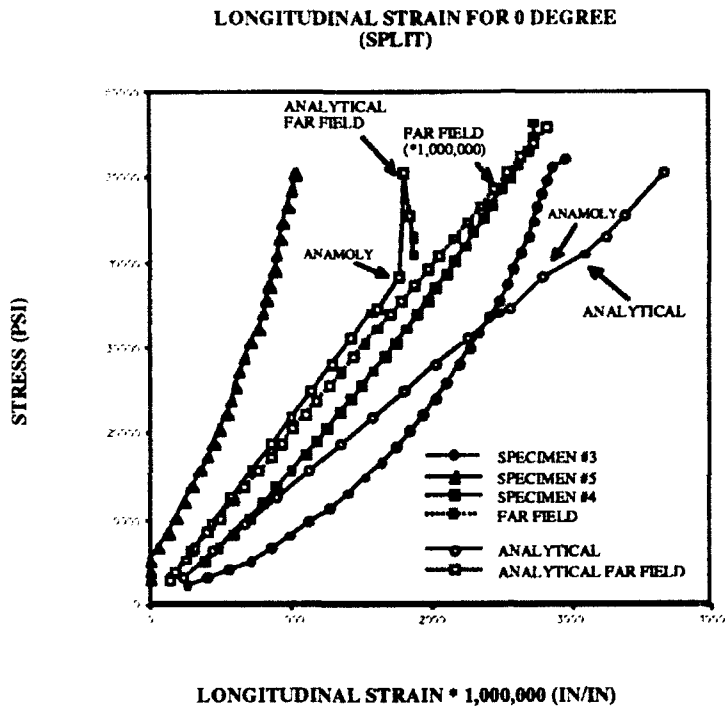
each composite system and can be used whenever the composite is modeled. This means that failure modes such as fiber buckling, material shear, fiber kinking and other possible micromechanical failure modes will be included in the data. This could eliminate the need for using closed form solutions to determine the ultimate stress of a composite.

This section will address each of the specimen layups and discuss the comparison of the analytical results to the experimental results. The analytical methods will then be compared to the experimental results in graphical form and discussed in depth. The validity of the modeling will be discussed in this section and all conclusions will be discussed in Chapter VI.

(1) $[0^0]_{16}$ Unidirectional Model

The first layup tested was the 0^0 unidirectional specimen. This created the most concern on the part of the author since the 0^0 layup produced two separate failure modes in experimentation. In the analytical portion of this study the 0^0 also experienced a rather sudden failure occurring at approximately 43,022 psi.

In comparing the analytical results to the experimental results it is immediately obvious that this particular specimen did not fail due to a horizontal crack. The ultimate load of the analytical specimen was 43,022 psi while the experimental specimens with the vertical split averaged 52,967 psi. There is a difference of 23.11% between the analytical and experimental results, and is a disparity which really cannot be accounted for by the author. Figure 5-25 shows a comparison of the analytical results to the three specimens that failed due to a vertical split. These graphs show both the longitudinal strain and the transverse strain.



EXPERIMENTAL STRESS = LOAD / CROSS-SECTIONAL AREA

ANALYTICAL STRESS IS TAKEN FROM UNIFORM STRESS FIELD

Figure 5-25: Comparison of Analytical and Experimental Data for 0° (Split)

The progression failure is shown in Figure 5-26. Only two increments are shown since only two increments showed any damage before the specimen failed. At the first, when the specimen begins to fail, there is some cracking along the edge of the hole. It also indicates that there is some failure at the top of the hole of a transverse nature. Immediately after this increment, the specimen experienced the failure of 396 elements, some in transverse tension and the rest in longitudinal compression. This type of catastrophic failure seems to be somewhat indicative of the longitudinal split. As will be discussed later in this section, the other specimens failed over a series of increments, not instantaneously like the 0°.

This possibility is reinforced by the plots of the contours, Figure 5-27, that were made of the strain data, which is continuous between the elements and a good indication of locations of high strain. The plots were made of strain instead of stress since for all multi-layered laminates the stresses would be different though the thickness of the specimen, while strain would be continuous. These areas of high strain are also areas of high stress while the composite is intact. The extremely high areas of strain are found around the hole and coincide with the locations of the vertical splits. The shear strain also shows an area of maximum shear strain occurring parallel to the hole and following the fiber direction. Once the failure of the model has occurred, the plots tend to lose some of their continuity. This could be the result of the unloading scheme and its effect on the strain of the unloaded elements. The shear contour gives a very good representation of how the shear strain and shear stress seem to "flow" around the hole. The transverse plot is shown and indicates the model experienced a substantial increase in the transverse strain after failure occurred. While the model did not show an exact representation of how a specimen might fail due to the vertical split, it does indicate that once the split occurs the model and the specimen are unable to support the applied load.

0 DEGREE FAILURE MESH

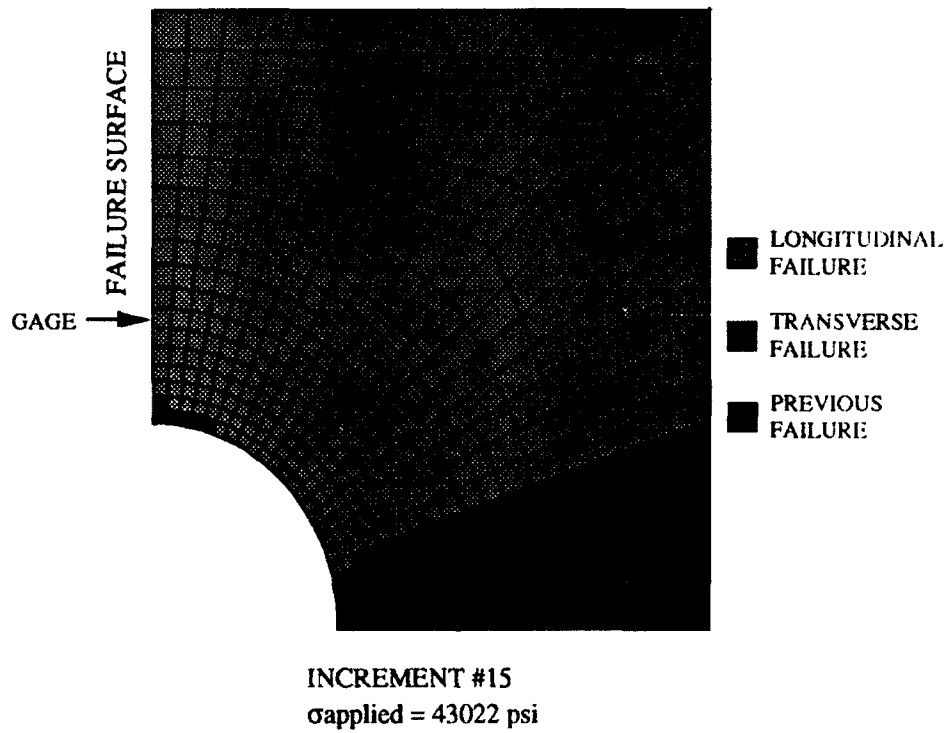
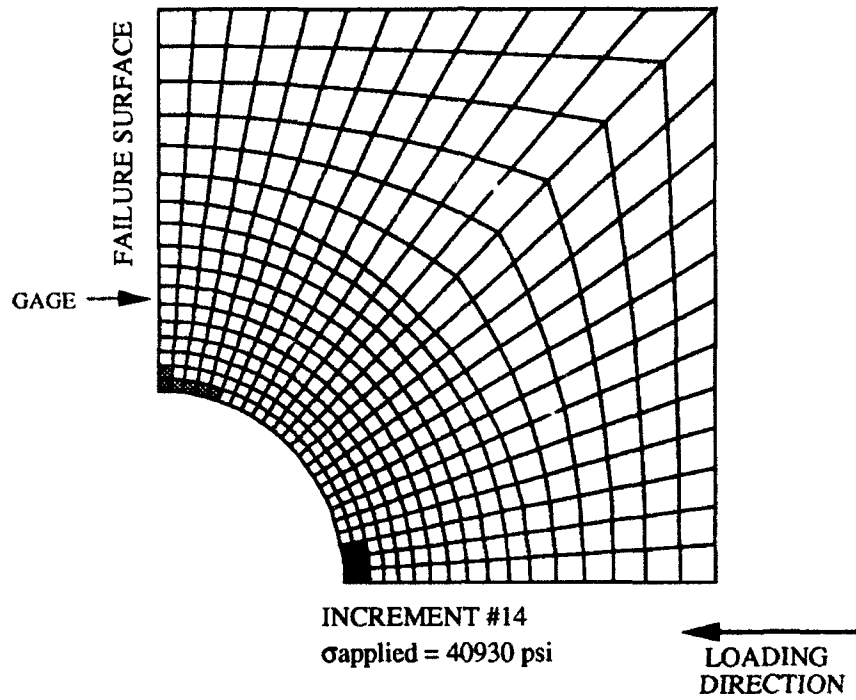
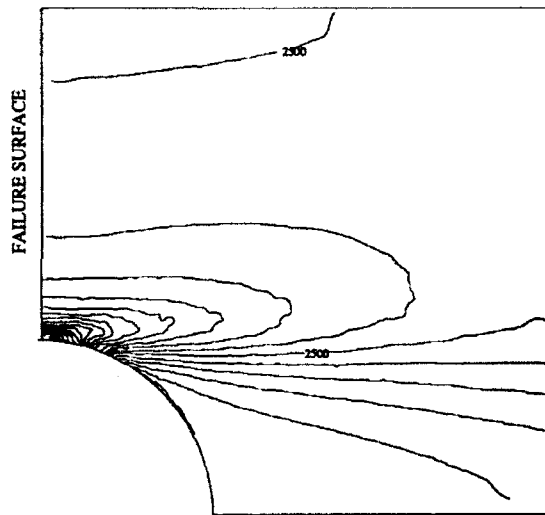
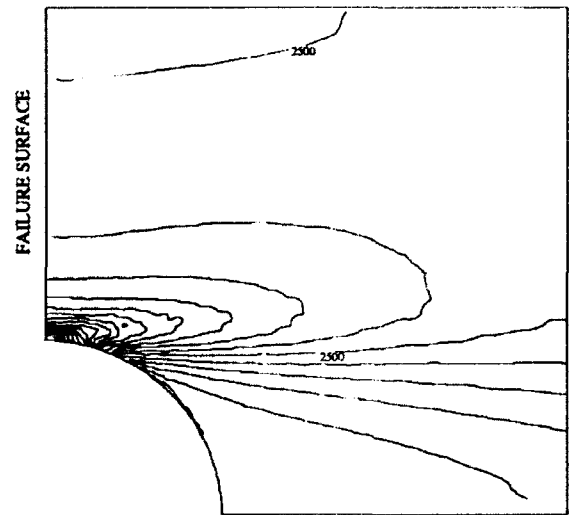


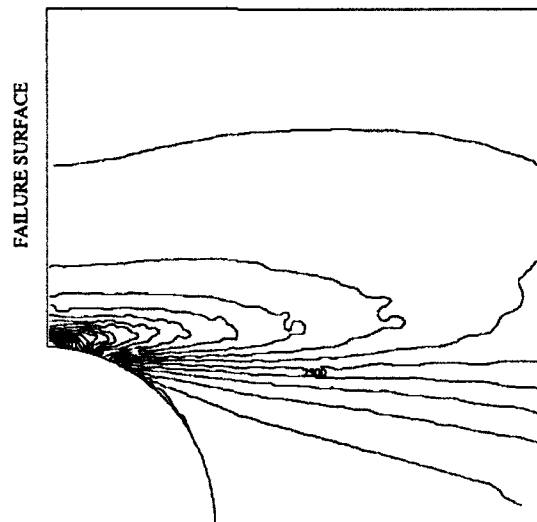
Figure 5-26. Progression of Failure for 0° Model



0 DEGREE INCREMENT #14 LONGITUDINAL
 $\sigma_{\text{applied}} = 40930 \text{ psi}$
 $U_x = 0.0123016 \text{ in}$

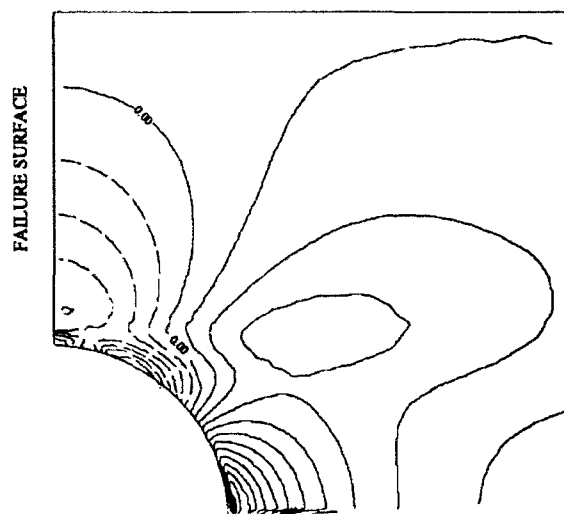


0 DEGREE INCREMENT #15 LONGITUDINAL
 $\sigma_{\text{applied}} = 43022 \text{ psi}$
 $U_x = 0.0123022 \text{ in}$



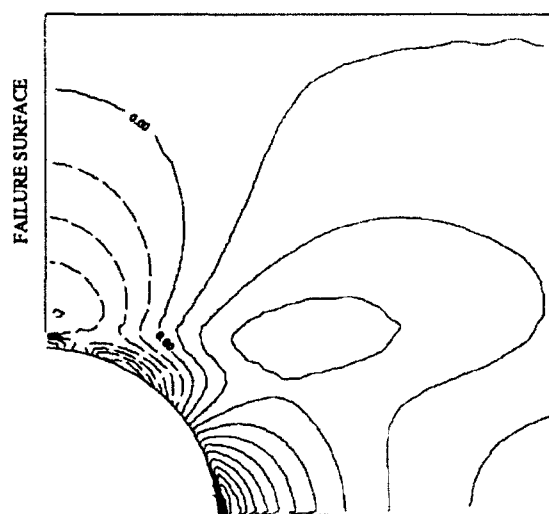
0 DEGREE INCREMENT #16 LONGITUDINAL
 $\sigma_{\text{applied}} = 45530 \text{ psi}$
 $U_x = 0.014022 \text{ in}$

Figure 5-27: Contour Plots of 0 degree Model



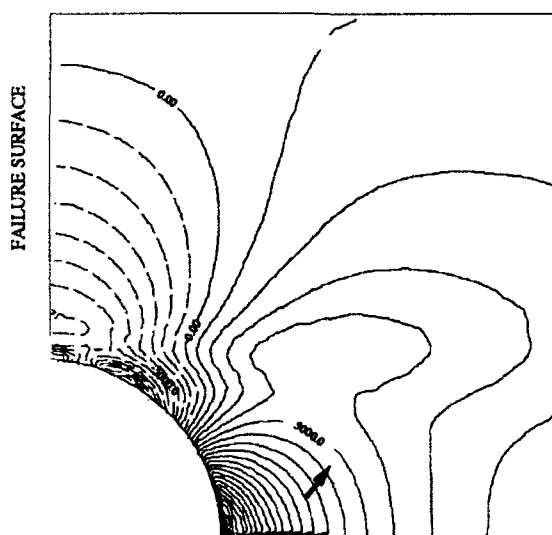
0 DEGREE INCREMENT #14 TRANSVERSE

$\sigma_{\text{applied}} = 40930 \text{ psi}$
 $U_x = 0.013016 \text{ in}$



0 DEGREE INCREMENT #15 TRANSVERSE

$\sigma_{\text{applied}} = 43022 \text{ psi}$
 $U_x = 0.013022 \text{ in}$

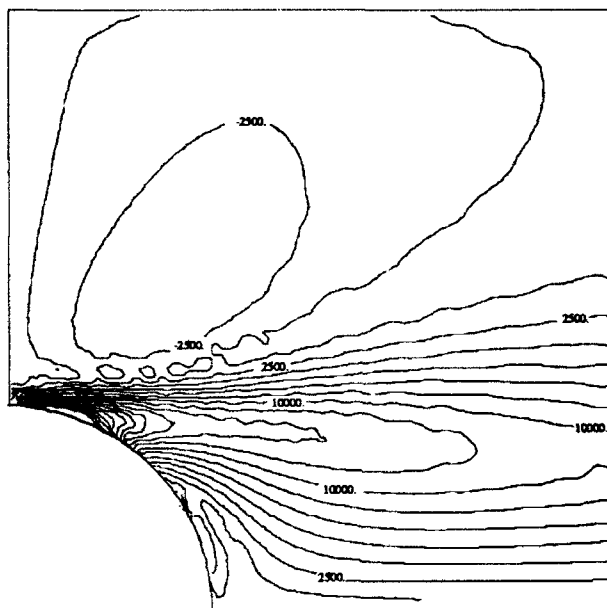


0 DEGREE INCREMENT #16 TRANSVERSE

$\sigma_{\text{applied}} = 45530 \text{ psi}$
 $U_x = 0.014022 \text{ in}$

Figure 5-27: Contour Plots of 0 degree Model (cont)

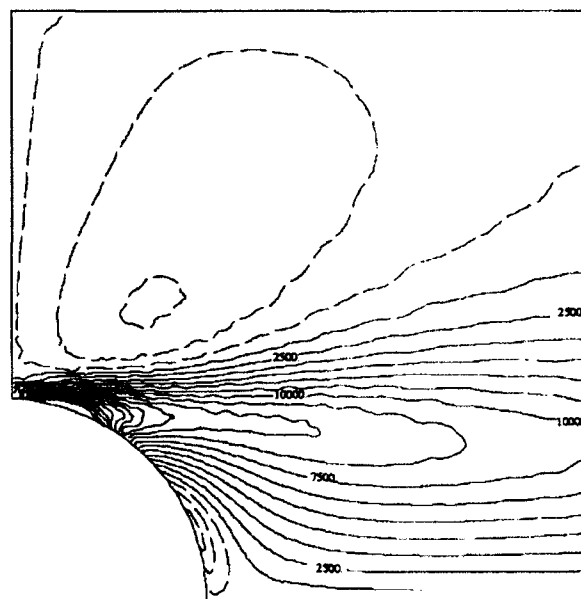
FAILURE SURFACE



0 DEGREE INCREMENT #14 SHEAR

$\sigma_{\text{applied}} = 40930 \text{ psi}$
 $U_x = 0.013016 \text{ in}$

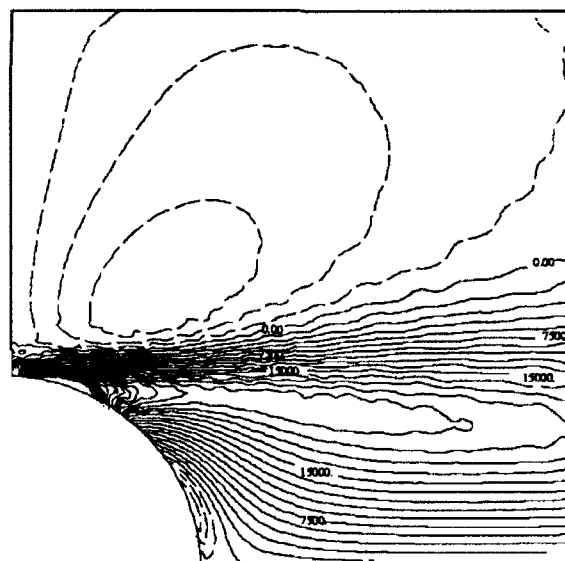
FAILURE SURFACE



0 DEGREE INCREMENT #15 SHEAR

$\sigma_{\text{applied}} = 43022 \text{ psi}$
 $U_x = 0.013022 \text{ in}$

FAILURE SURFACE



0 DEGREE INCREMENT #15 SHEAR

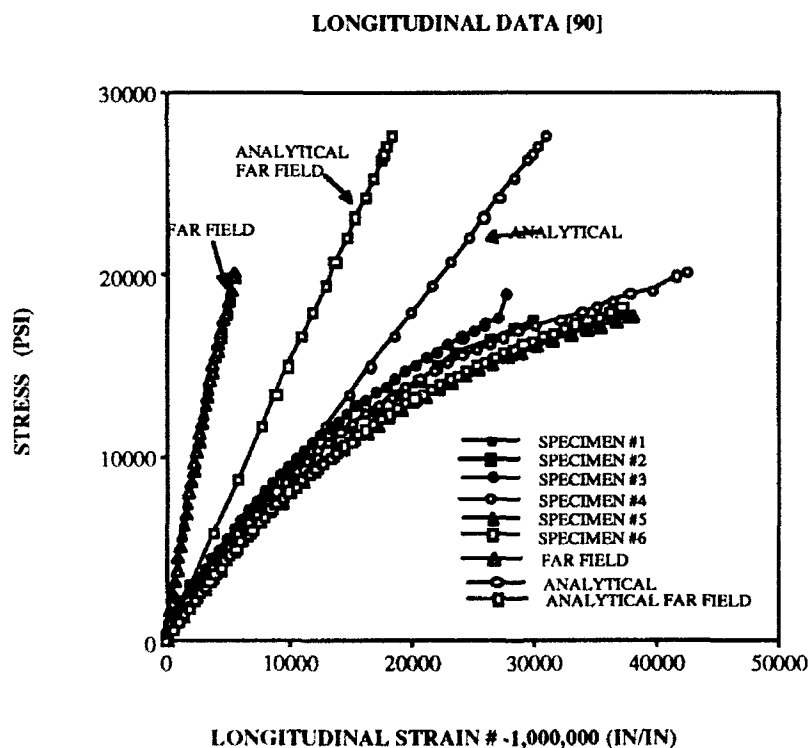
$\sigma_{\text{applied}} = 45530 \text{ psi}$
 $U_x = 0.014022 \text{ in}$

Figure 5-27: Contour Plots of 0 degree Model (cont)

The progression of failure was rather difficult in the analytical model due to the sudden nature of the failure. The split seems to be modeled initially by the failure of the first five elements around the edge of the hole. This is followed by the collapse of the entire specimen. The other unidirectional specimen was modeled more effectively by the analytical method than the 0°.

(2) $[90^\circ]_{16}$ Unidirectional Model

There seemed to be no obvious indications of where failure may have occurred in the 90° as there were in the 0°. The specimen experienced a large number, fourteen, of failed elements at 21,940 psi. This corresponds within 10% of the ultimate experimental stress. The comparison of the analytical stress-strain response is shown in Figure 5-28.



EXPERIMENTAL STRESS = LOAD / CROSS-SECTIONAL AREA

ANALYTICAL STRESS IS TAKEN FROM UNIFORM STRESS FIELD

Figure 5-28: Analytical-Experimental Comparison of 90°

The analytical curve does not model the nonlinear behavior of the composite that is present in the experimental curves. This may be a result of comparing a mathematically correct model to a structurally imperfect specimen. The experimental far field response appears to be stiffer than the analytical far field. This may be attributed to the fixture, which is bolted around the specimen and may impose some sort of constraint in the far field that is not present in the model. The bolts must be torqued so that the fixture is firmly fastened to the specimen so that it does not slip during the loading process. These applied constraints may be what produce a rather stiff, linear behavior of the far field, even though the strain at the hole displays some very nonlinear features.

In the experimentation, the 90° specimens all failed by a horizontal crack that originated from the hole edge and progressed to the outer edge of the specimens. It was more difficult to determine when the failure actually took place in the analytical portion. By the end of the fortieth increment, the specimen has been displaced by a total of -0.09655" at a load of 31,345 psi before it fails as seen in Figure 5-29. The experimental specimens failed at an average of 18,739.21 psi. The data was investigated and many different plots were made to try to determine if there was some indications that failure may have occurred during the loading. At the analytical far field there exists an area where the far field data experiences a disproportionate increase in strain as compared to the stress. This is the same type of behavior that the specimens experimentally experienced before they failed. In the experimental testing this was the point at which the specimen transitions from the quasi-static failure to the dynamic failure that resulted in the complete failure of the composite. In the analytical portion this change in the curve occurred at 28,750 psi.

Contour plots were made of the longitudinal strain and the shear strain at the region around the hole and are shown in Figure 5-30. The plots were made from the point at which the experimental failure occurred in increments until a crack propagated from the edge of the hole to the outer edge of the specimen. Areas of high negative

90 DEGREE FAILURE MESH

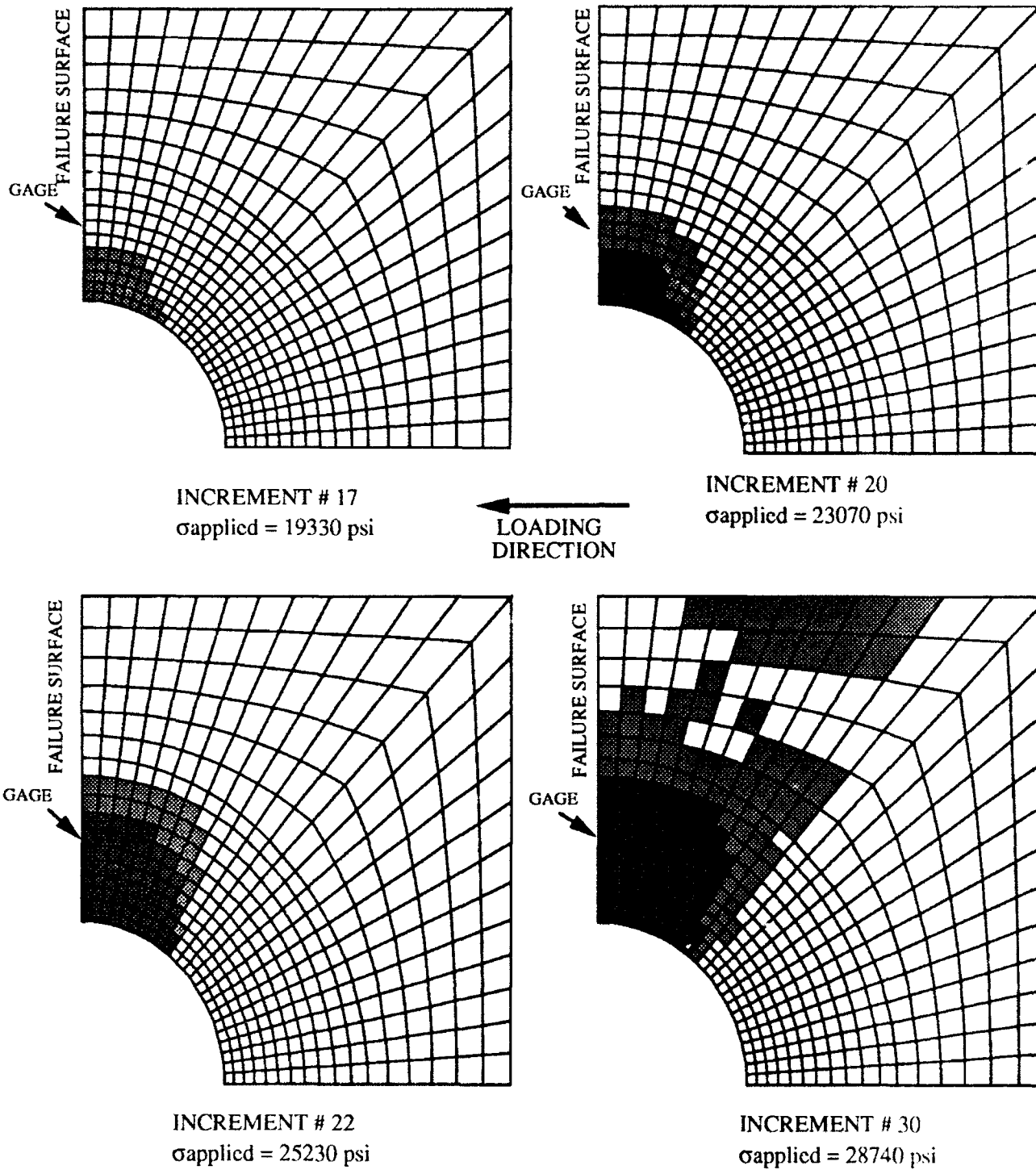
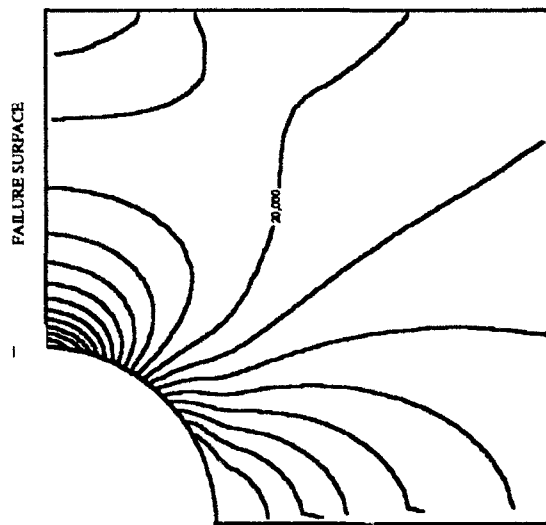
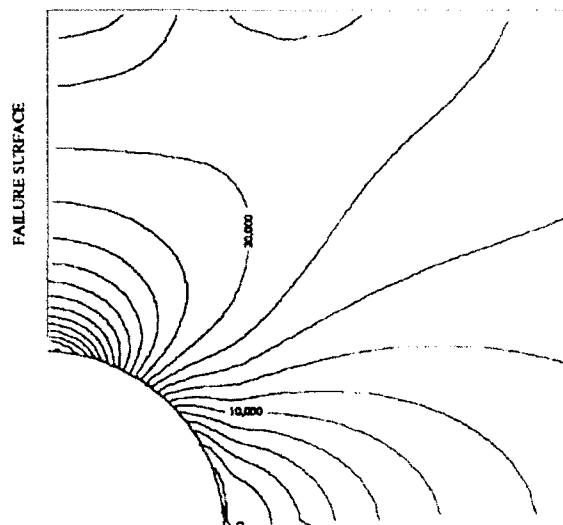


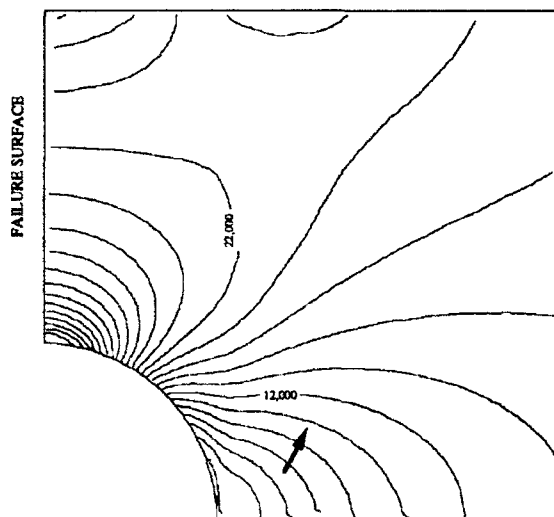
Figure 5-29: Progression of Failure for 90° Model



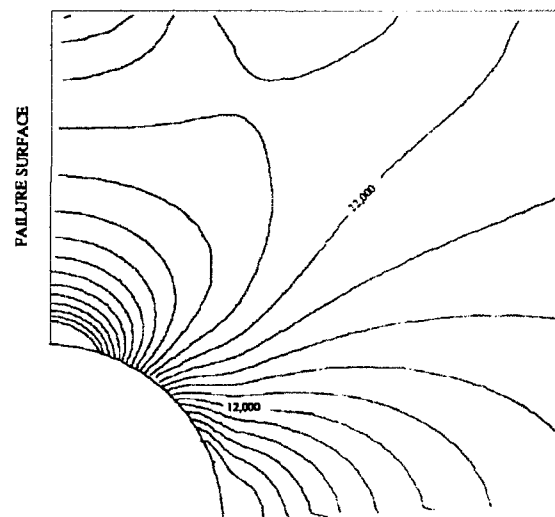
90 DEGREE INCREMENT #17 LONGITUDINAL
 $\sigma_{\text{applied}} = 19370$
 $U_x = 0.00832 \text{ in}$



90 DEGREE INCREMENT #20 LONGITUDINAL
 $\sigma_{\text{applied}} = 23070$
 $U_x = 0.00868 \text{ in}$



90 DEGREE INCREMENT #22 LONGITUDINAL
 $\sigma_{\text{applied}} = 25230$
 $U_x = 0.00876 \text{ in}$

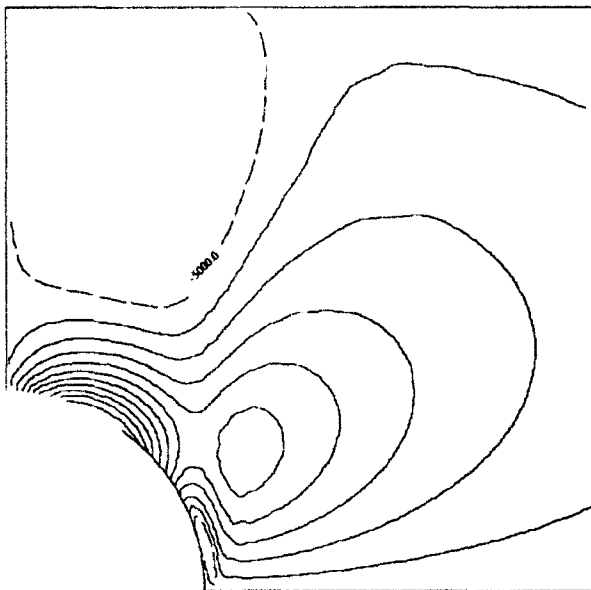


90 DEGREE INCREMENT #30 LONGITUDINAL
 $\sigma_{\text{applied}} = 28740 \text{ psi}$
 $U_x = 0.00893 \text{ in}$

← LOADING
 DIRECTION

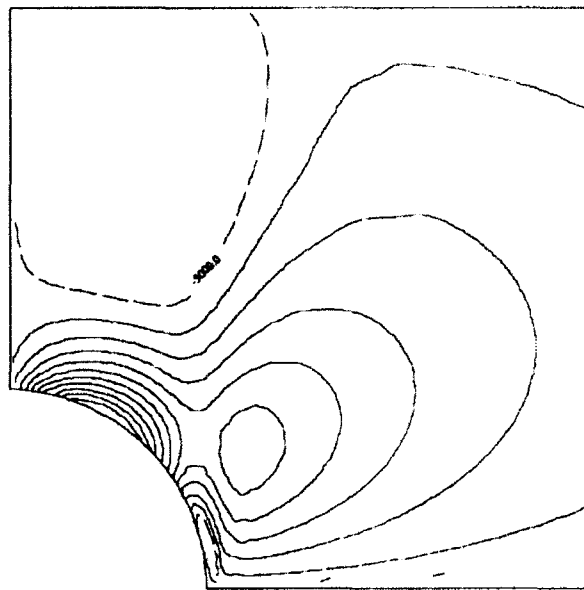
Figure 5-7: Contour Plots of 90 degree Model

FAILURE SURFACE



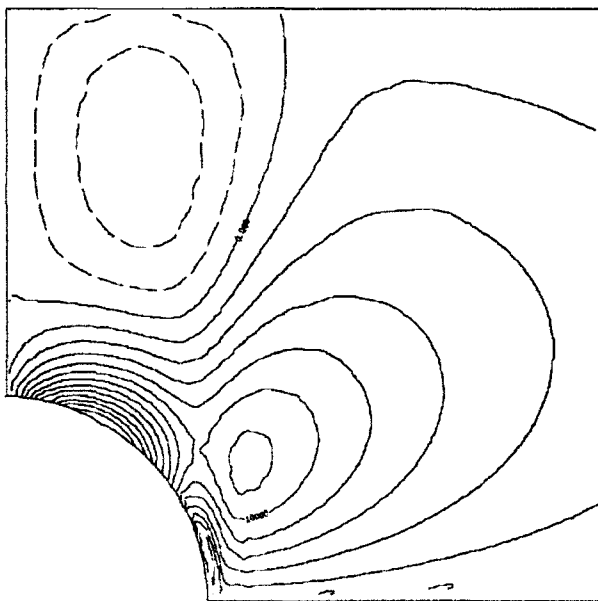
90 DEGREE INCREMENT #17 SHEAR
 $\sigma_{\text{applied}} = 19330 \text{ psi}$
 $U_x = -0.00847 \text{ in}$

FAILURE SURFACE



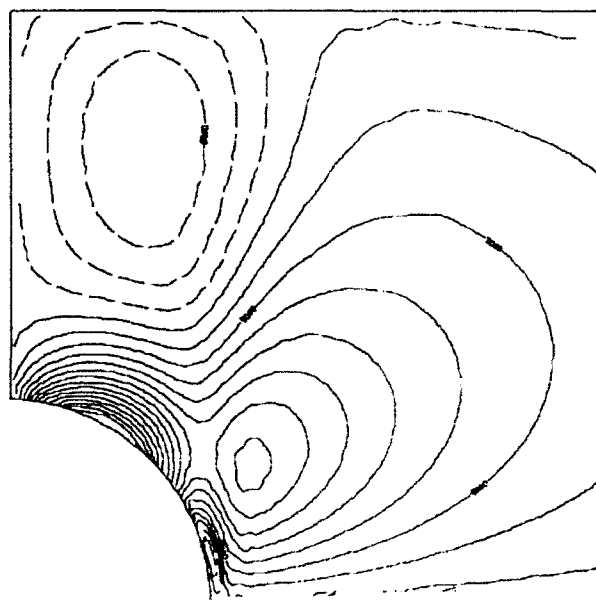
90 DEGREE INCREMENT #20 SHEAR
 $\sigma_{\text{applied}} = 23070 \text{ psi}$
 $U_x = -0.00868 \text{ in}$

FAILURE SURFACE



90 DEGREE INCREMENT #22 SHEAR
 $\sigma_{\text{applied}} = 25230 \text{ psi}$
 $U_x = -0.00876 \text{ in}$

FAILURE SURFACE



90 DEGREE INCREMENT #30 SHEAR
 $\sigma_{\text{applied}} = 28740 \text{ psi}$
 $U_x = -0.00893 \text{ in}$

← LOADING
DIRECTION

Figure 5-30: Contour Plots of 90 degree Model (cont)

longitudinal strain are located at the edge of the hole where failure occurs. This area coincides with the failure location found in the experimental specimens. There is also a small strain concentration at the top edge of the hole normal to the failure surface. This concentration is lower and did not result in the failure of any elements.

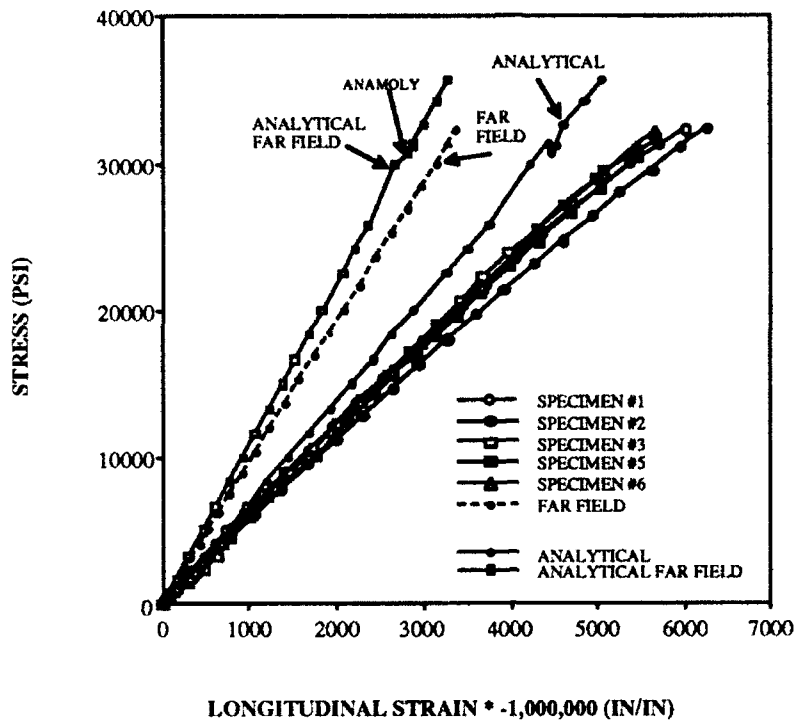
There exists a concentration of shear strain located at a 20° angle from the failure edge located on the shear strain contour plot and there is a rather severe gradient originating from the failure surface to this location. The shear strain is lower than the longitudinal strain because the matrix is the component resisting the load that is imposed on the specimen. The high shear strain is the result of a basic property of this type of compression. The center section, where the hole is located, is unable to resist the load due to the discontinuity. It must rely on the outer sections and the distribution of stresses around the hole to support the load. As a result, a large amount of shear stress/strains build up as the center section tries to compress and is resisted by the outer sections. While this phenomenon was most clearly seen in the 0° , with the vertical splits, it could also be a contributing factor to all the failures.

In the experimental work, the 90° was of a three dimensional failure. While the program can not model the three dimensional effects, it can model the progression of failure within the specimens. A combination of the results of the unidirectional specimens was seen in the $0^\circ/90^\circ$ crossply specimen.

(3) $[0^\circ/90^\circ]$ Crossply Model

In the experimental results the crossply failed similarly to the 90° , from a horizontal crack occurring at the edge of the hole normal to the load and the progressing to the outer edge of the specimen. The stress-strain response of the $0^\circ/90^\circ$ specimen is compared to the experimental in Figure 5-31. Both the analytical strain at

LONGITUDINAL DATA FOR [0/90]



EXPERIMENTAL STRESS = LOAD / CROSS-SECTIONAL AREA

ANALYTICAL STRESS IS TAKEN FROM UNIFORM STRESS FIELD

Figure 5-31: Analytical-Experimental Comparison of 0°/90°

the hole and the analytical strain at the far field are stiffer than the experimental. The stiffness of the experimental far field observed in the 90° specimens was not observed in the crossply specimens. There is a anomaly occurring at 31,300 psi where the longitudinal stress at the hole decreases while the strain increases. At the far field, there is a decrease in the slope which reflects an increase in strain without a corresponding change in stress that was present in the points before this. This also models the same effect that is present in the experimental specimen immediately prior to the final failure of the composite. The total energy of the system was checked three increments prior to and four increments after the discontinuity and the system remained conservative throughout

that time. However, the energy of the element being plotted was discovered to have decreased when this discontinuity occurred.

The progression of failure is shown in Figure 5-32. The progression of failure within this model seems to be very slow in comparison to the experimental results. There were no major cascades of failed elements until 55,575 psi were 14 elements failed. This is much higher than the experimental ultimate stress of 32,362 psi. For this reason, plots were made of higher values of stress even though the model may have failed analytically at a lower load. All the plots made were of the strain state after the anomaly within the stress-strain occurred.

Contour plots shown in Figure 5-33 were made of the longitudinal and shear strain and show there are areas of very high strain concentrations and very high strain gradients. To analyze the anomaly at 31,300 psi, a series of plots were generated for a region of the hole to see if the anomaly was manifested in the contour plots. There were no truly distinctive features present in the sequence from increment #16 to increment #23. The plots that are shown represent the build up in strains in the various areas. In the longitudinal plot there seems to be two small areas of very high longitudinal strain near the failure surface that coincide with the failure location, and the growth of the longitudinal strains coincide with the progression of failure.

The shear strain plots are similar to the 0° . As the load increases the shear strain increases at the edge of the hole parallel to the loading direction. There is a high shear stress concentration located at an angle of around 20° that coincides with the higher edge of the shear plane that was observed in the SEM work.

0/90 DEGREE FAILURE MESH

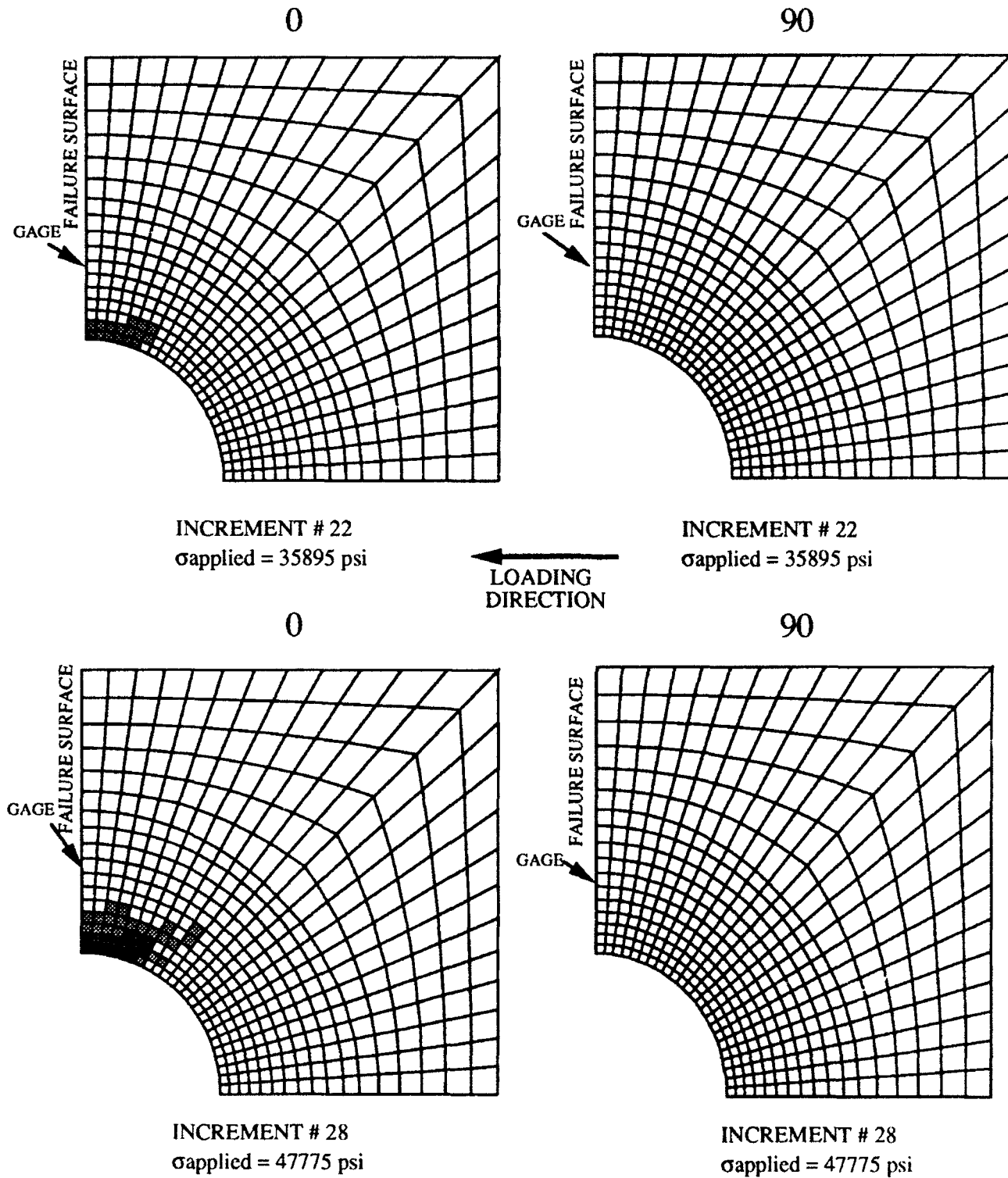


Figure 5-32: Progression of Failure for 0/90° Model

0/90 DEGREE FAILURE MESH

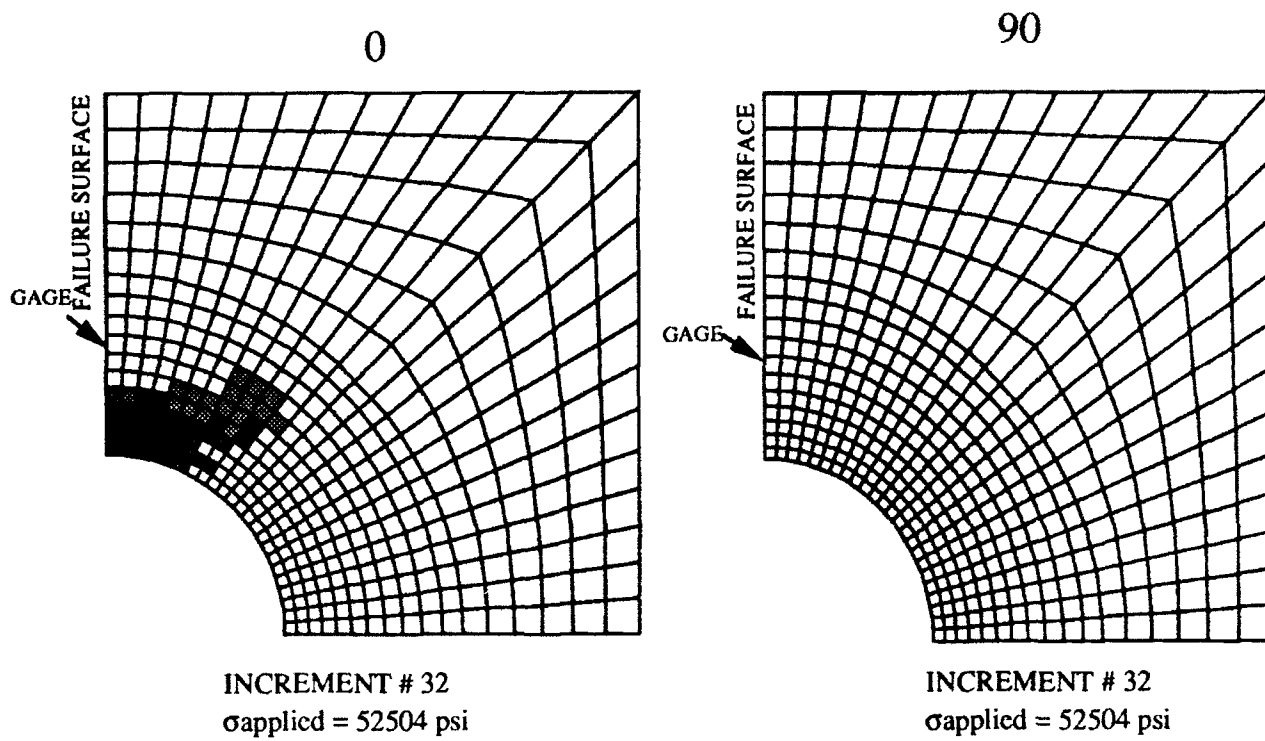
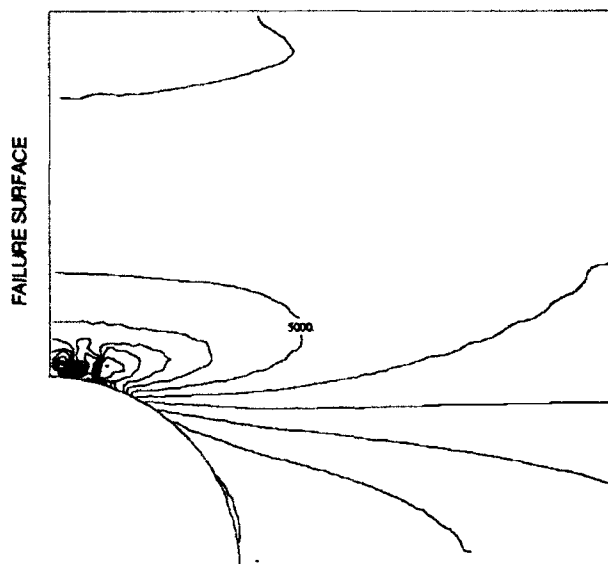
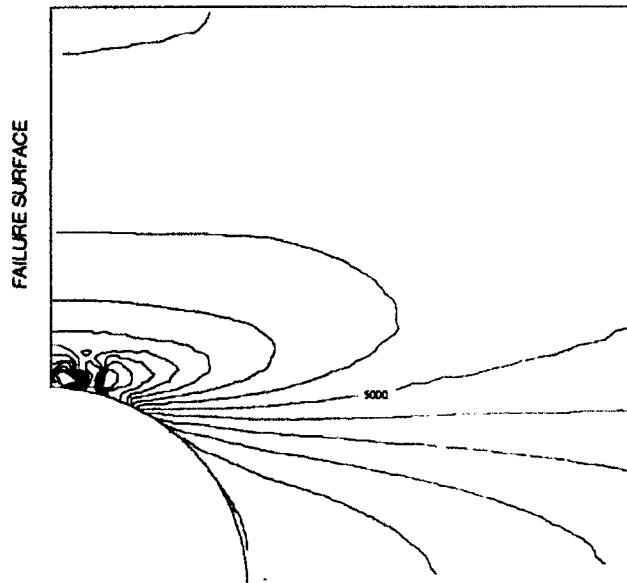


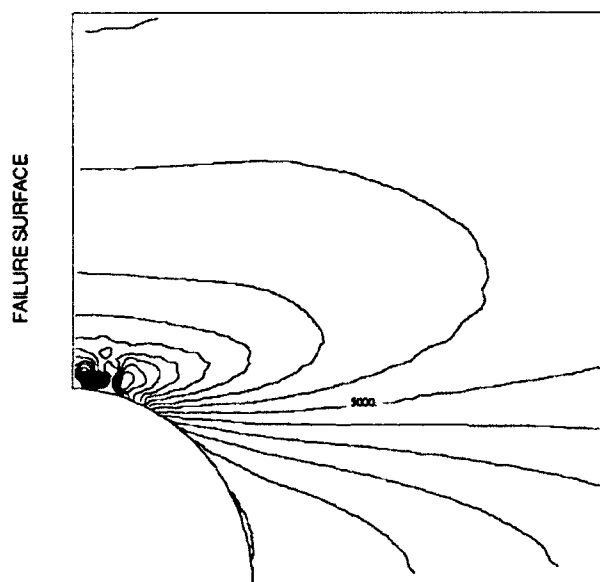
Figure 5-32: Progression of Failure for 0/90° Model (cont)



0/90 DEGREE INCREMENT #22 LONGITUDINAL
 $\sigma_{\text{applied}} = 35616 \text{ psi}$
 $U_x = 0.018718 \text{ in}$

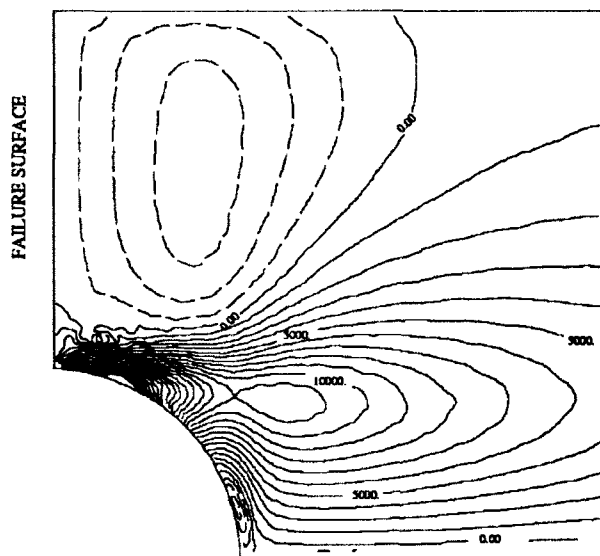


0/90 DEGREE INCREMENT #29 LONGITUDINAL
 $\sigma_{\text{applied}} = 47590 \text{ psi}$
 $U_x = 0.02309 \text{ in}$

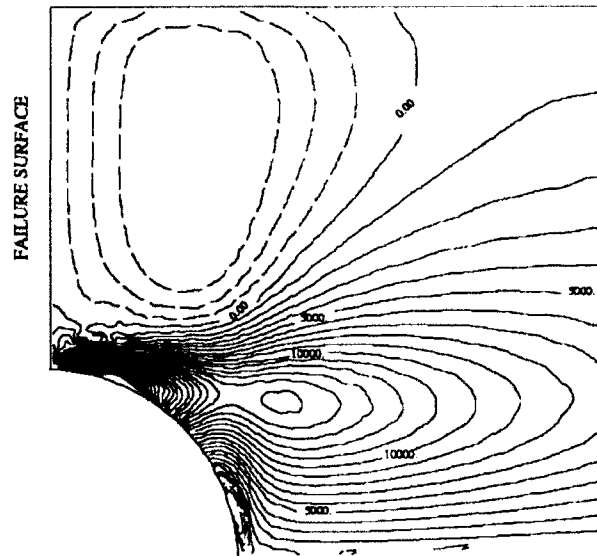


0/90 DEGREE INCREMENT #32 LONGITUDINAL
 $\sigma_{\text{applied}} = 51687 \text{ psi}$
 $U_x = 0.024651 \text{ in}$

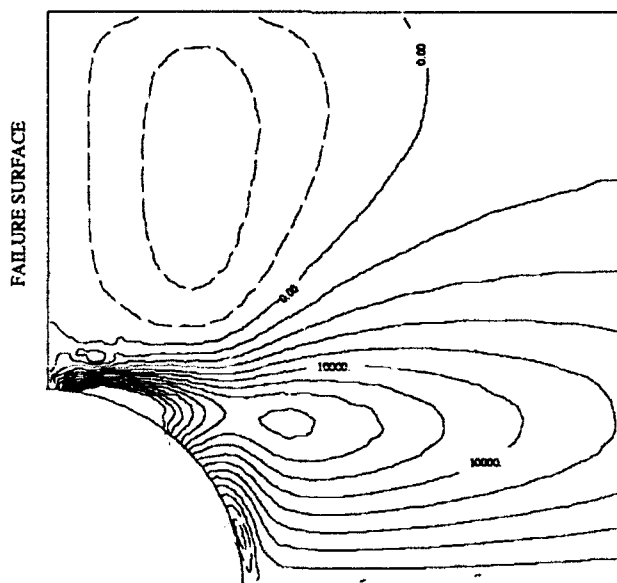
Figure 5-33: Contour Plots of 0/90 degree Model



0/90 DEGREE INCREMENT #22 SHEAR
 $\sigma_{\text{applied}} = 35616 \text{ psi}$
 $U_x = 0.018718 \text{ in}$



0/90 DEGREE INCREMENT #29 SHEAR
 $\sigma_{\text{applied}} = 47590 \text{ psi}$
 $U_x = 0.02309 \text{ in}$



0/90 DEGREE INCREMENT #32 SHEAR
 $\sigma_{\text{applied}} = 51687 \text{ psi}$
 $U_x = 0.024651 \text{ in}$

Figure 5-33: Contour Plots of 0/90 degree Model

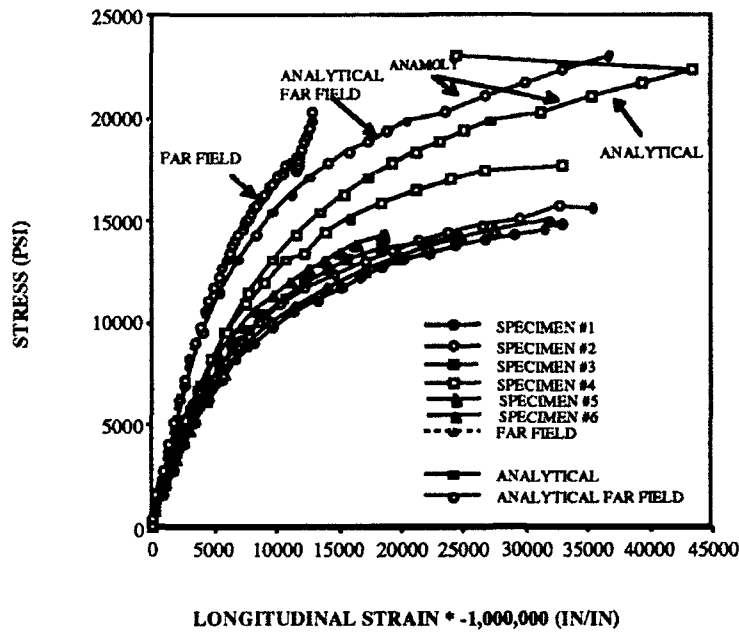
The $0^\circ/90^\circ$ specimens are a good indication when the failure may go from a quasi-static to a dynamic failure mode. The dynamic failure will not be modeled by the program, but its initiation may be tied to the anomaly that appears within the curve. This change in the slope of the curve is present in many of the models as the loading approaches ultimate load recorded in the experimental work. While this similarity is not proven it may be an indicator of when the failure transitions from a quasi-static failure to a dynamic failure.

(4) $[\pm 45^\circ]_{4S}$ Shear Model

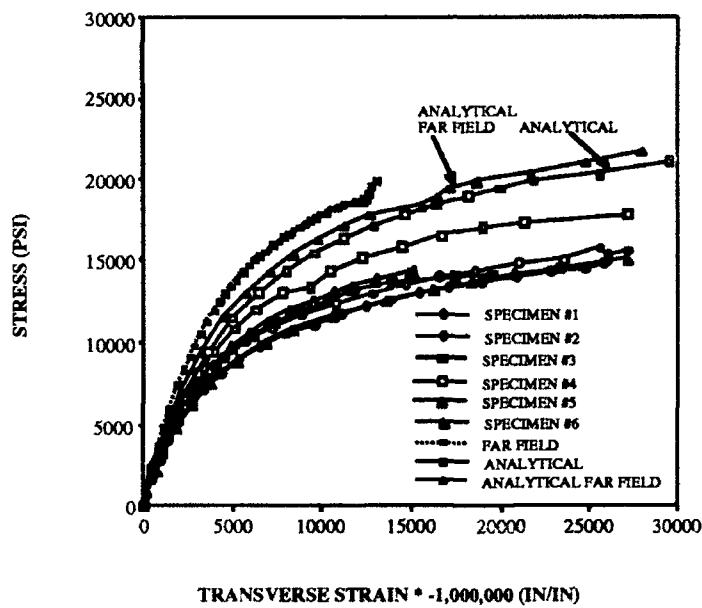
The $\pm 45^\circ$ model produced the best comparison of the experimental to the analytical. The model exhibits the nonlinear behavior of the $\pm 45^\circ$ specimens, both of which are shown in Figure 5-34. The analytical stress-strain curve was stiffer than the experimental portion. Part of the reason the analytical response was stiffer is that it does not model the scissoring of the plies that was present in the experimental results. There was also an area present where the far field experienced a sudden change in the slope of the far field curve without similar corresponding change in stress. This occurs at 20,237 psi. This concurs well within the average maximum experimental load of 20,625 psi. While it is uncertain when the failure of the $\pm 45^\circ$ specimens occurred experimentally, it can be assumed that failure of the specimens occurred at or about 20,000 psi.

There are two notable features present within the graph. The first is the sharp decrease in strain which occurs at increment #19. The element that is being tracked shed more than half of its longitudinal strain and approximately half of its total energy. There is no change in the loading, which continues to increase, but many of the elements near element #335 seem to also shed strain and the energy is absorbed by other elements in the region. The far field gage is also stiffer than the analytical, but may be the effect of

LONGITUDINAL STRAIN FOR ± 45 DEGREE



TRANSVERSE STRAIN FOR $[\pm 45]$



EXPERIMENTAL STRESS = LOAD / CROSS-SECTIONAL AREA

ANALYTICAL STRESS IS TAKEN FROM UNIFORM STRESS FIELD

Figure 5-34: Analytical-Experimental Comparison of $\pm 45^\circ$

scissoring of the fibers. The scissoring in the experimental curves seems to start at the point at which the experimental curve deviates from the analytical curve and starts to progress towards a state where strain increases without an increase in stress. Both the far field gage measurements demonstrate an increase in slope towards the end of the loading. This may be the effect of the fixture closing before the test was stopped. This feature was present in each of the far field response curves.

A progression of failure plot was made for the both the $+45^{\circ}$ and -45° layups, Figure 5-35, and the most interesting item present was the fact that the failure was not symmetric. A crack formed at the hole edge at an angle of 42° to the edge of the hole normal to the loading direction. The crack propagated through the model very quickly and reached the outer edge at 24,212 psi. The angle of the failure coincided well with experimental specimens where the angle of the failure appears to be at an angle of approximately 30° away from the hole edge. The fact that the cracking appears at 42° instead of 45° is attributed to the deformation of the specimen in the region of the hole.

The longitudinal strain was plotted as a contour plot in Figure 5-35. There is a shift of the graph from the smaller contours featured in increments #18 to areas of high strain concentrations in increments #20, #21, 22#. These areas also coincide with the failure lines that were observed in the ultrasonic analysis. The area of highest strain for the longitudinal strain shown on the contour plot is at an angle of 48° from the edge of the hole normal to the loading direction. This angle shows excellent correlation between experimental results and the progression of failure shown in Figure 5-36.

±45 DEGREE FAILURE MESH

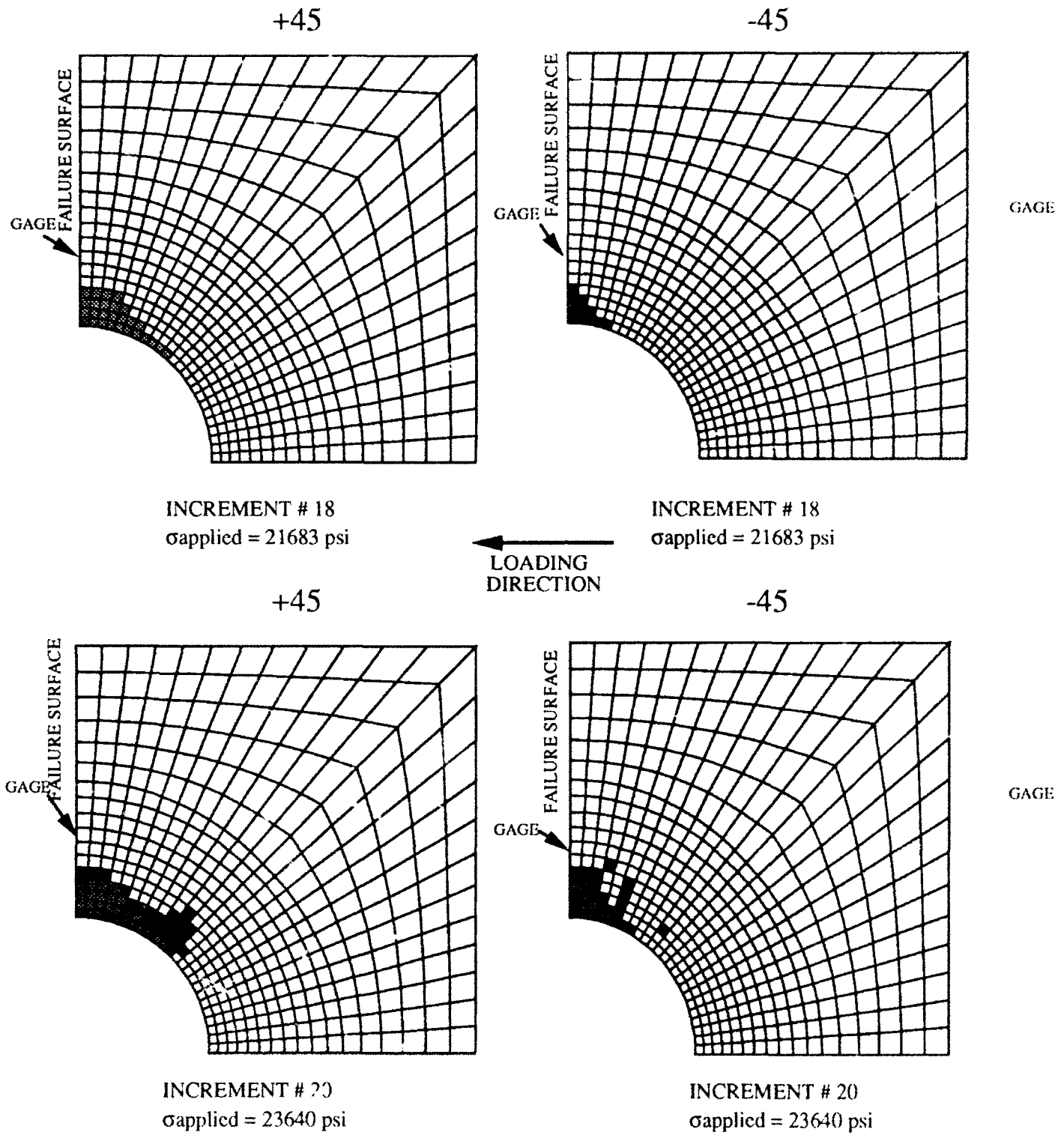


Figure 5-35: Progression of Failure for ±45° Model

± 45 DEGREE FAILURE MESH

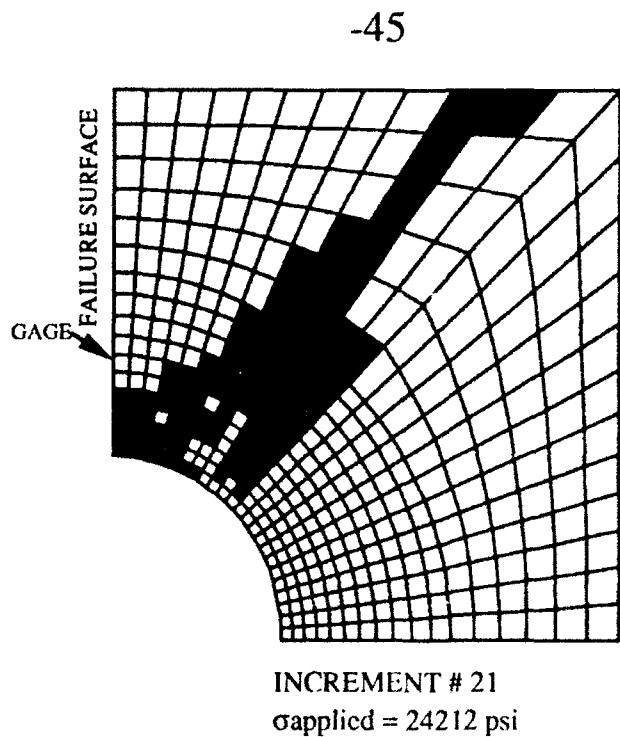
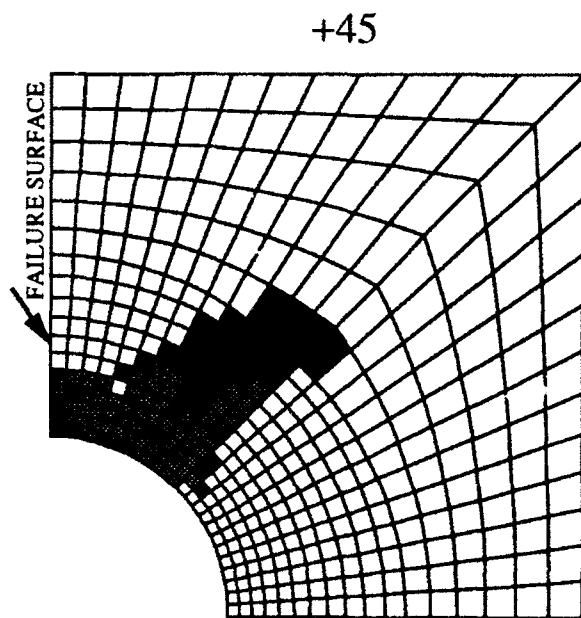
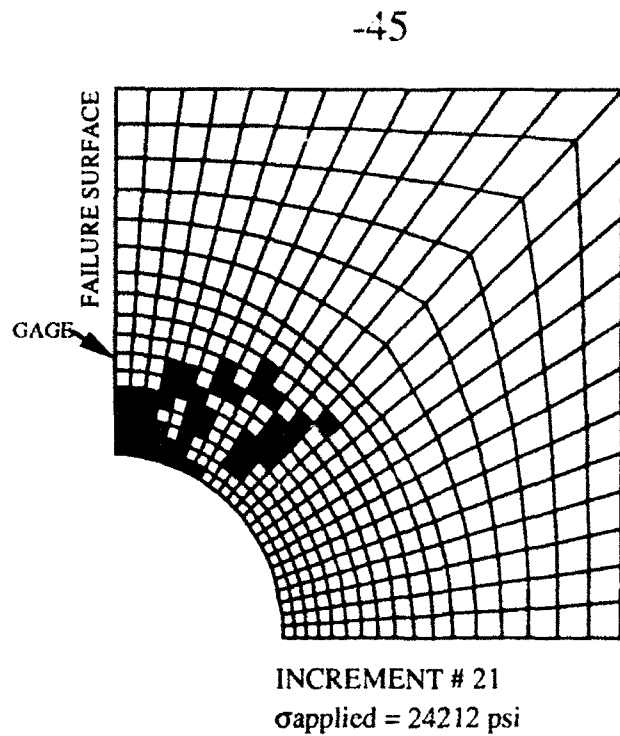
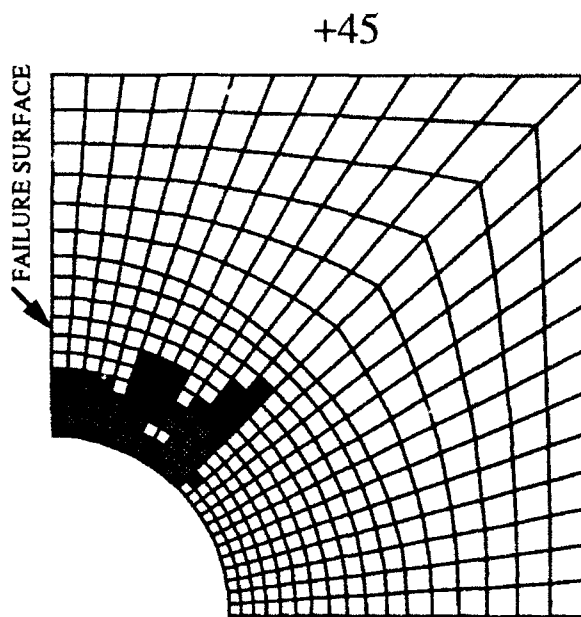
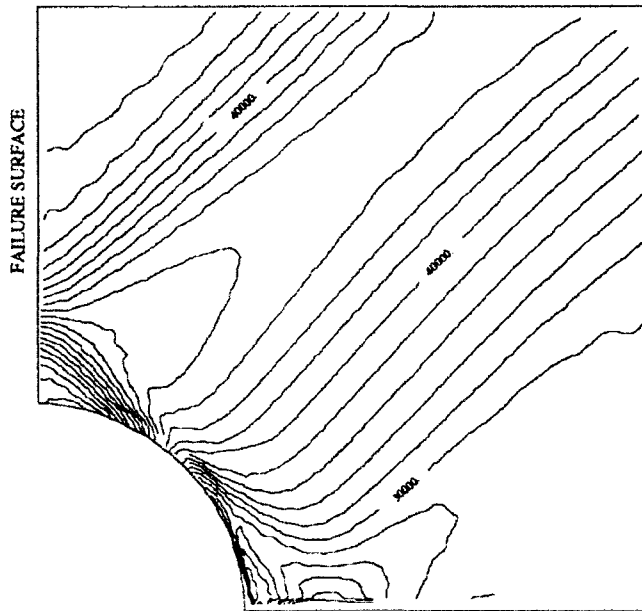
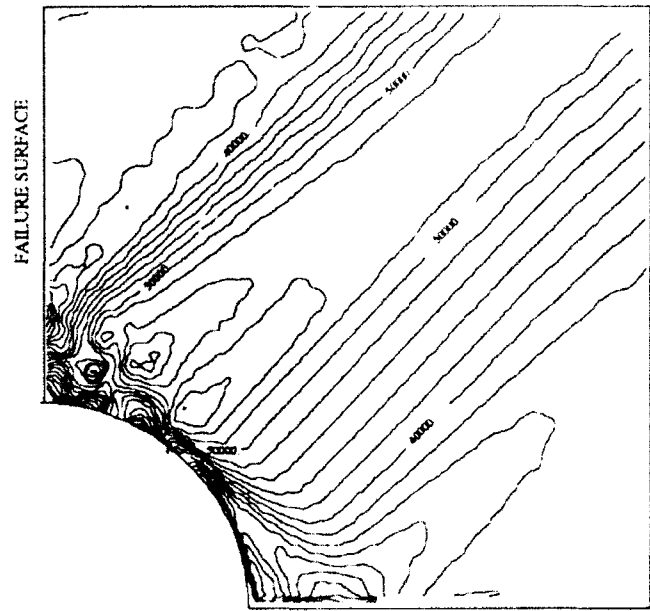


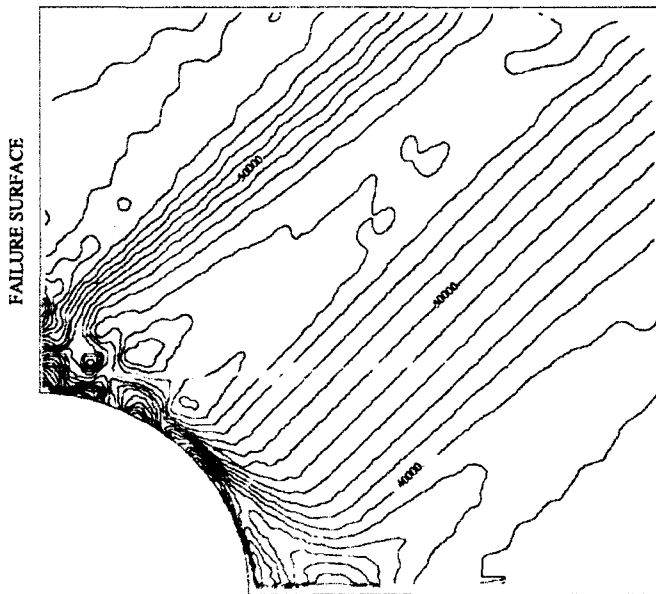
Figure 5-35: Progression of Failure for $\pm 45^\circ$ Model (cont)



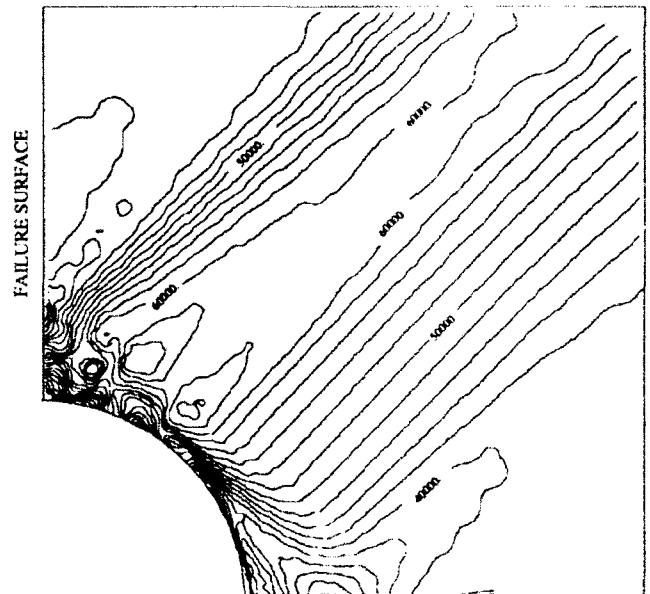
±45 DEGREE INCREMENT #18 LONGITUDINAL
 $\sigma_{\text{applied}} = 22332 \text{ psi}$
 $U_x = 0.15200 \text{ in}$



±45 DEGREE INCREMENT #20 LONGITUDINAL
 $\sigma_{\text{applied}} = 22332 \text{ psi}$
 $U_x = 0.16000 \text{ in}$



±45 DEGREE INCREMENT #21 LONGITUDINAL
 $\sigma_{\text{applied}} = 24212 \text{ psi}$
 $U_x = 0.16800 \text{ in}$



±45 DEGREE INCREMENT #22 LONGITUDINAL
 $\sigma_{\text{applied}} = 24625 \text{ psi}$
 $U_x = 0.17163 \text{ in}$

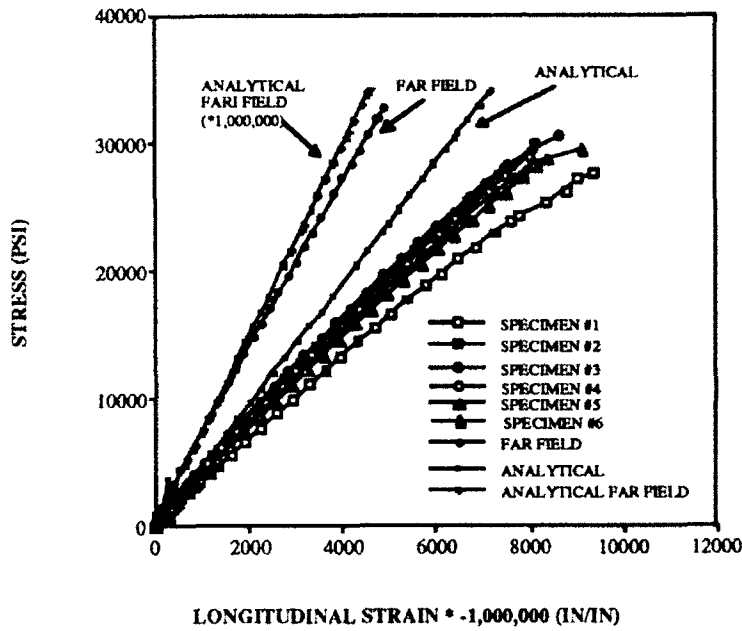
Figure 5-36: Contour Plots of ±45 degree Model

The response of the $\pm 45^\circ$ was extremely well behaved and the analytical method seems to model the stress strain response accurately. Since the actual failure of the specimen was not accurately determined one cannot compare the ultimate stress of the analytical to the experimental. The failure of the specimens seems to coincide with the experimental, however the transformation of the hole to an ellipse was not well modeled by the finite element method. The incorporation of $\pm 45^\circ$ plies into the a $0^\circ/\pm 45^\circ/90^\circ$ specimen has a very interesting effect. When three nonlinear plies are incorporated with a linear response ply, the resultant laminate is very linear in its longitudinal response.

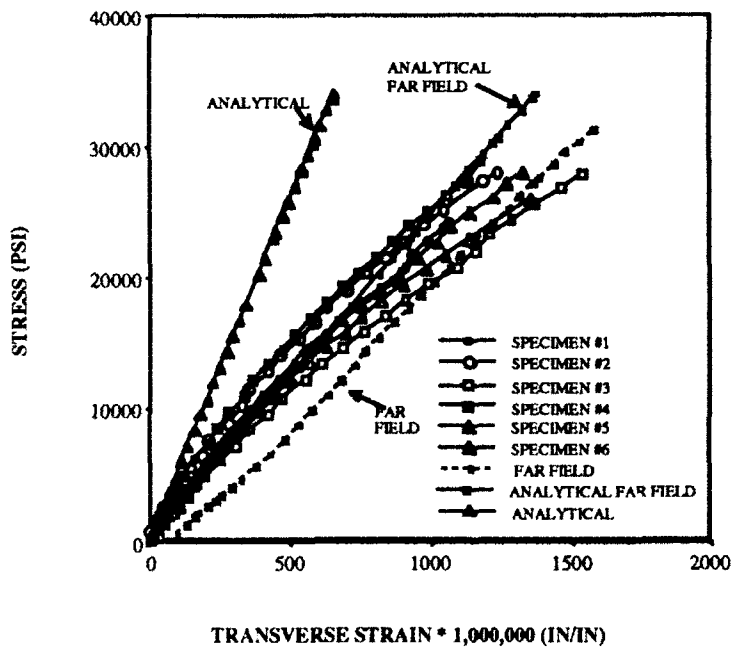
(5) $[0^\circ/\pm 45^\circ/90^\circ]_{2S}$ Quasi-isotropic Model

The quasi-isotropic model incorporates each of the plies that have been studied in the pervious four models. The modeled response of the laminate seems to incorporate some of the features displayed by the other specimen models. The graph of the stress-strain response, Figure 5-37, shows a very well behaved laminate. The graphs of the experimental data demonstrate a very linear behavior until the end of the load when the curves start to go nonlinear. The analytical graph shows the same kind of linear behavior, however the nonlinearity towards the end of the loading is not present. Like the other models, the loading of the finite element model continues well past the ultimate experimental loading of ultimate experimental strength of the $0^\circ/90^\circ$ and $\pm 45^\circ$ specimens. The difference between this model and the rest of the models is that the change in the slope of the strain, defined as the anomaly, did not vary throughout the loading.

LONGITUDINAL STRAIN FOR QUASI-ISOTROPIC



TRANSVERSE STRAIN FOR QUASI-ISOTROPIC



EXPERIMENTAL STRESS = LOAD / CROSS-SECTIONAL AREA

ANALYTICAL STRESS IS TAKEN FROM UNIFORM STRESS FIELD

Figure 5-37: Analytical-Experimental Comparison of $0^\circ/\pm 45^\circ/90^\circ$

The analytical longitudinal hole and far field strain are both stiffer than the experimental data, as seen in Figure 5-37. In the transverse data, the analytical hole strain was much stiffer than the far field analytical data. This may be the result of the incorporation of $\pm 45^\circ$ plies into the laminate. In the graphs of the $\pm 45^\circ$ in Figure 5-14, it is evident that the strain at the hole was on the same order of magnitude as the far field data. This seems to create the same effect within the quasi-isotropic meshes.

The progression of failure in Figure 5-38 shows that the zero laminates fail first before any of the laminates start to be effected by the load. The 90° ply does not suffer any failure throughout the loading process. There is a rather large cascade of failed elements, 26, at increment #16 at a load of 36,208 psi. If cascading is the event that signifies the failure of the composite then there is a favorable comparison with the experimental ultimate stress of 33,638 psi.

The progression also indicates that at increment #24 a crack progressed from the hole edge to the outer edge of the specimen. This crack occurred at a load of 46,860 psi. At this point the load would only be supported by the $\pm 45^\circ$ and 90° layers. Even with this crack passing through the specimen it is still able to complete 40 increments with a stress in excess of 60,000 psi.

The contour plots were made of the longitudinal and shear strains, and they have the characteristics of the contour plots seen in the plots of previous models. The longitudinal plots in Figure 5-39 show a concentration of very high strains at the edge of the hole normal to the load. There is also the appearance of a very high strain gradient starting at around 45° from the failure edge. At the higher increments the longitudinal strain seems to develop a region that is orienting itself approximately 42° from the loading surface. This is due to the effects generated by the $\pm 45^\circ$ plies within the model.

The shear contour plots shows a concentration of shear strain around the area of elements #73 and #77 or at an angle of about 20° from the failure surface. The direction

0/±45/90 DEGREE FAILURE MESH

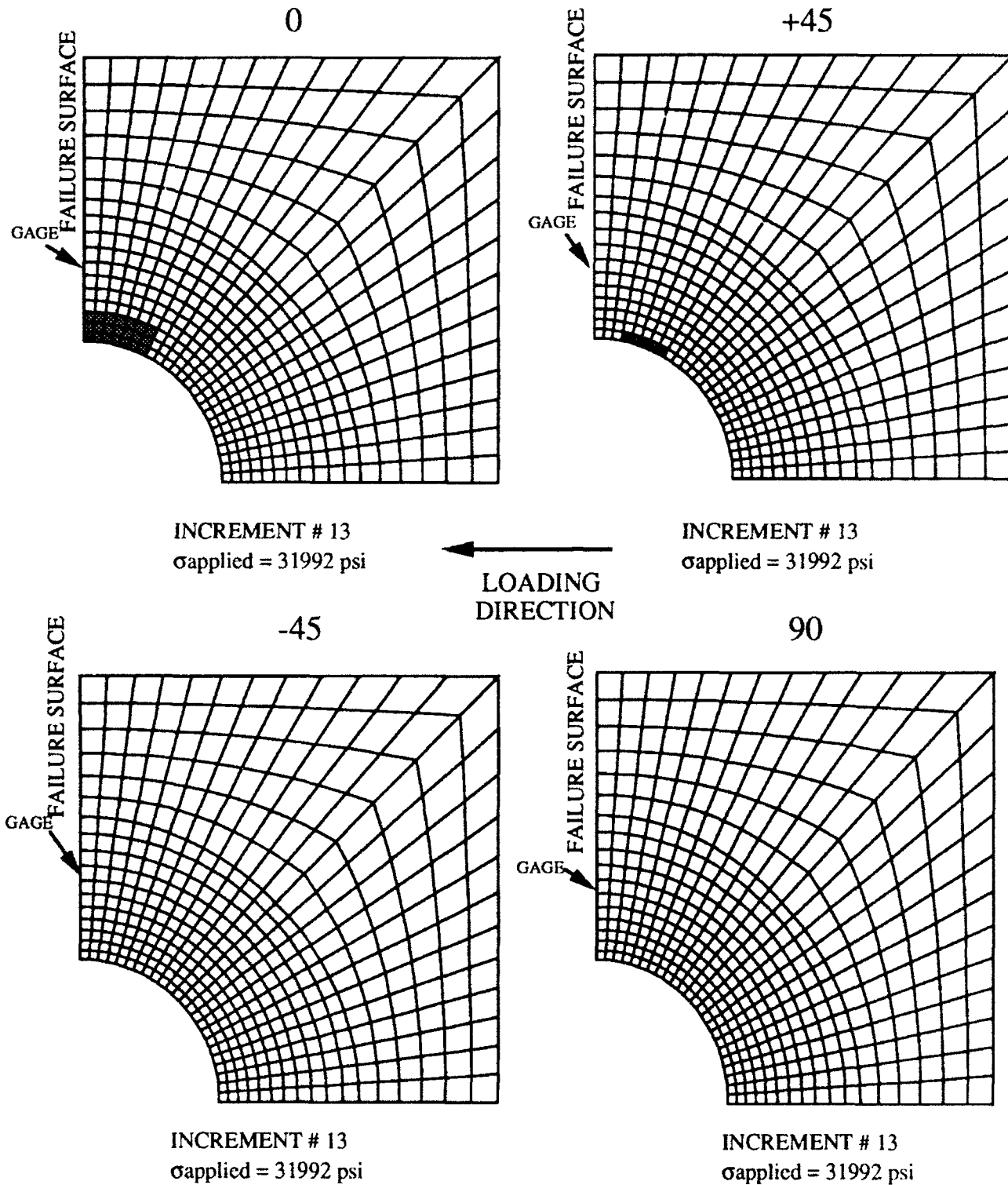
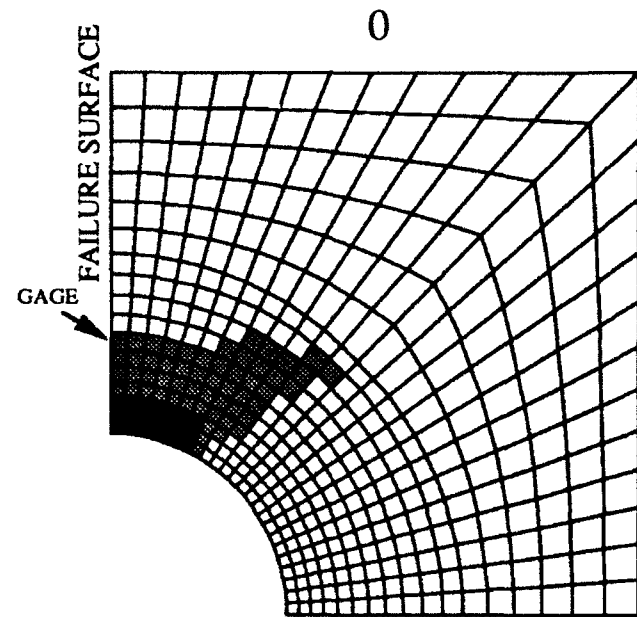
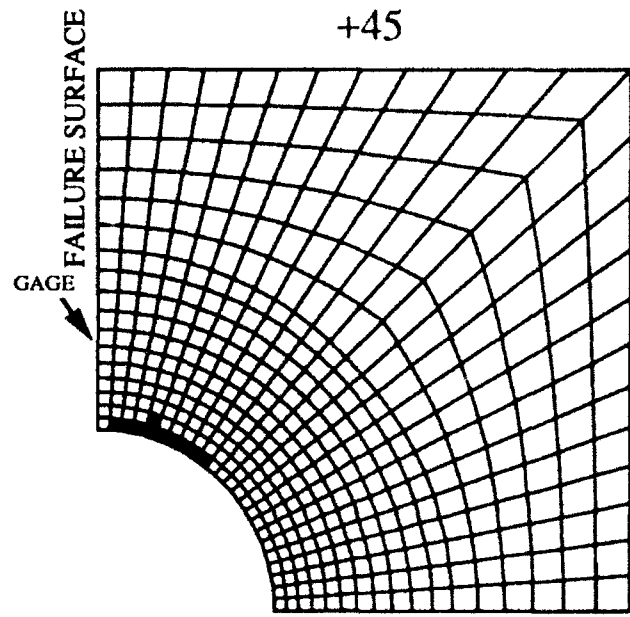


Figure 5-38: Progression of Failure for 0/±45/90 ° Model

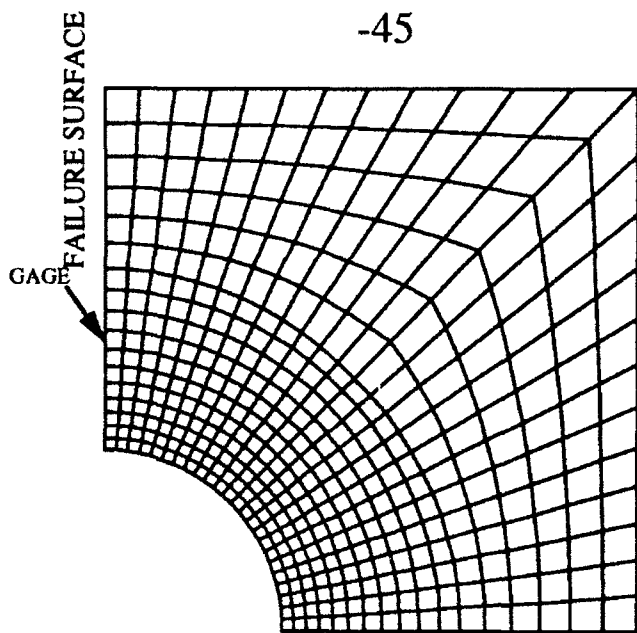
0/±45/90 DEGREE FAILURE MESH



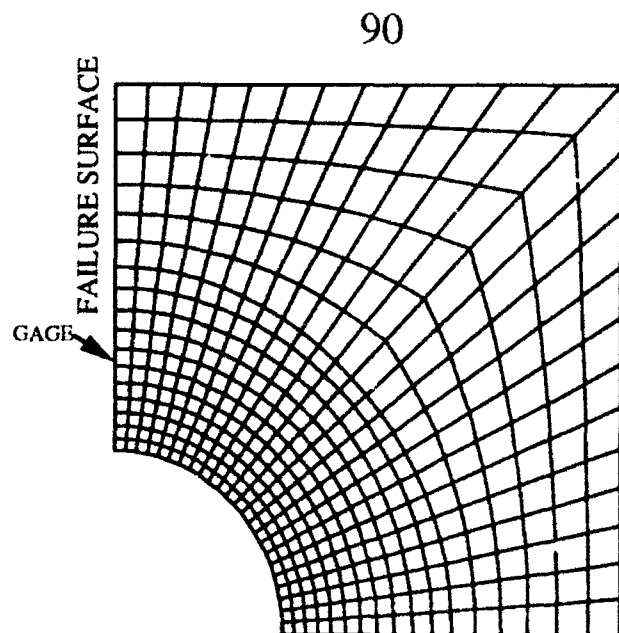
INCREMENT # 18
 $\sigma_{\text{applied}} = 39215 \text{ psi}$



INCREMENT # 18
 $\sigma_{\text{applied}} = 39215 \text{ psi}$



INCREMENT # 18
 $\sigma_{\text{applied}} = 39215 \text{ psi}$



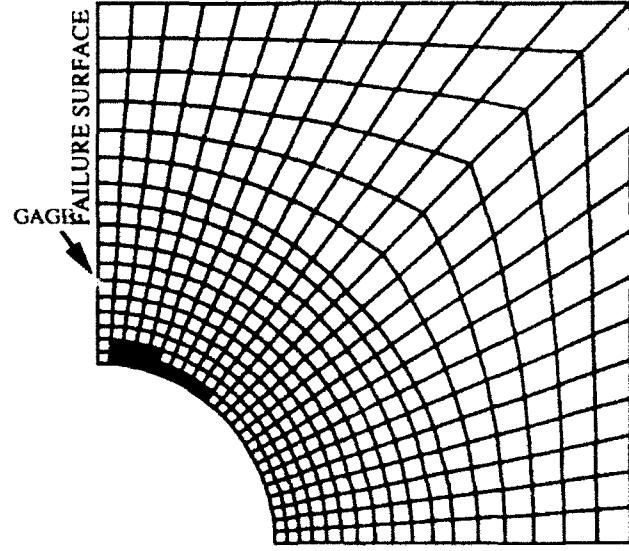
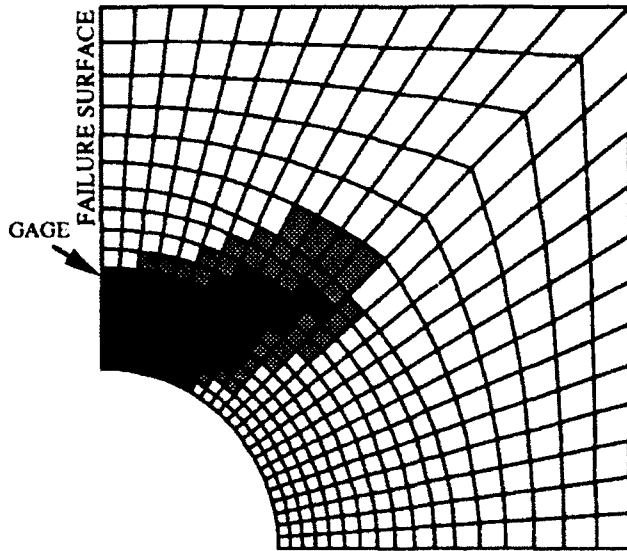
INCREMENT # 18
 $\sigma_{\text{applied}} = 39215 \text{ psi}$

Figure 5-38: Progression of Failure for 0/±45/90° Model (cont)

0/±45/90 DEGREE FAILURE MESH

0

+45



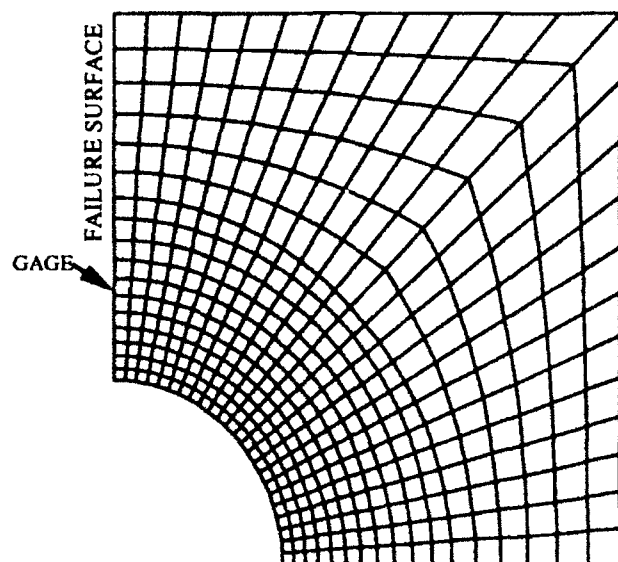
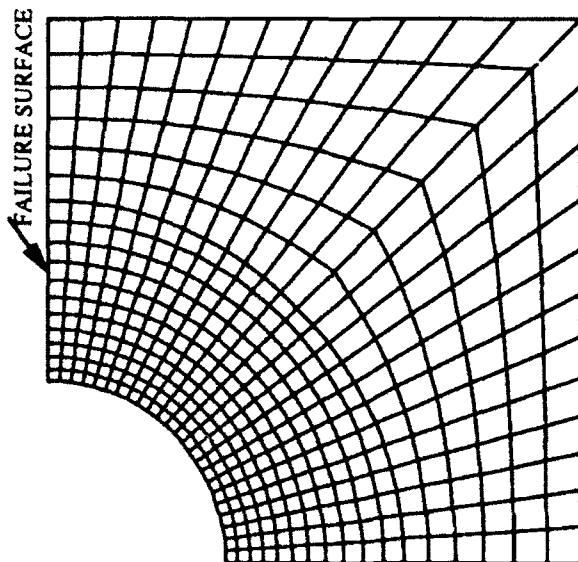
INCREMENT # 20
 $\sigma_{\text{applied}} = 41362 \text{ psi}$

INCREMENT # 20
 $\sigma_{\text{applied}} = 41362 \text{ psi}$

GAGE

-45

90



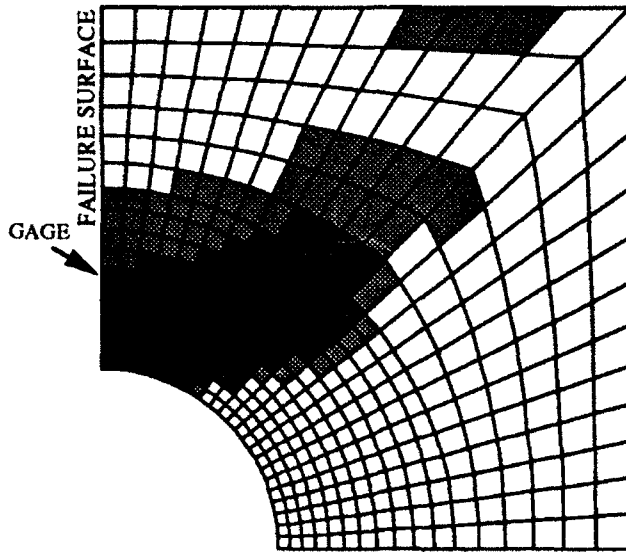
INCREMENT # 20
 $\sigma_{\text{applied}} = 41362 \text{ psi}$

INCREMENT # 20
 $\sigma_{\text{applied}} = 41362 \text{ psi}$

Figure 5-38: Progression of Failure for 0/±45/90 ° Model

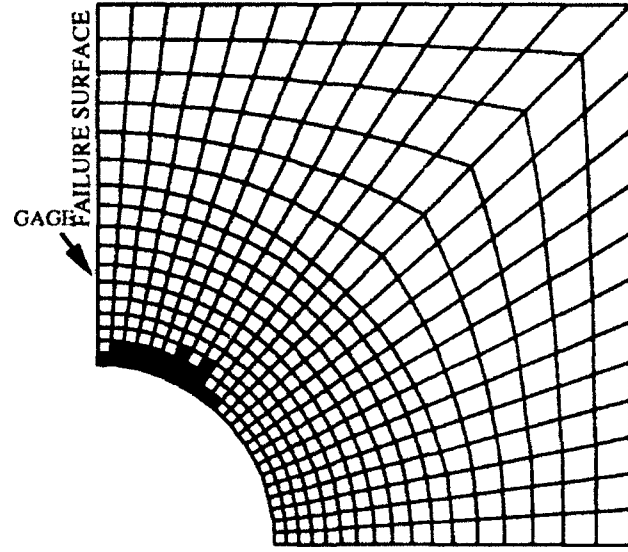
0/±45/90 DEGREE FAILURE MESH

0



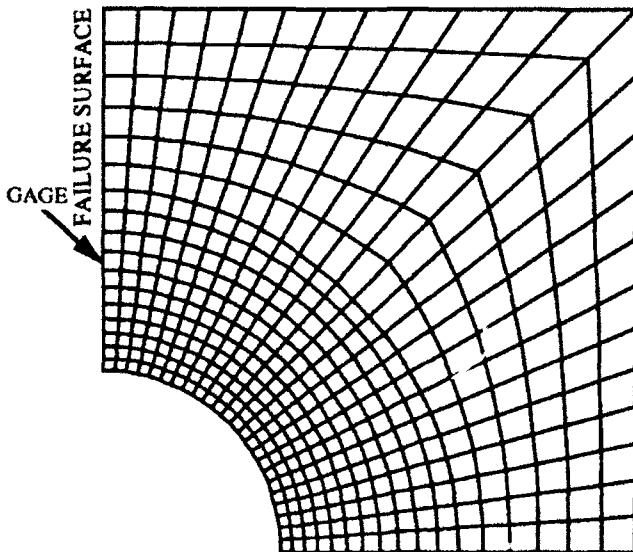
INCREMENT # 24
 $\sigma_{\text{applied}} = 45337 \text{ psi}$

+45



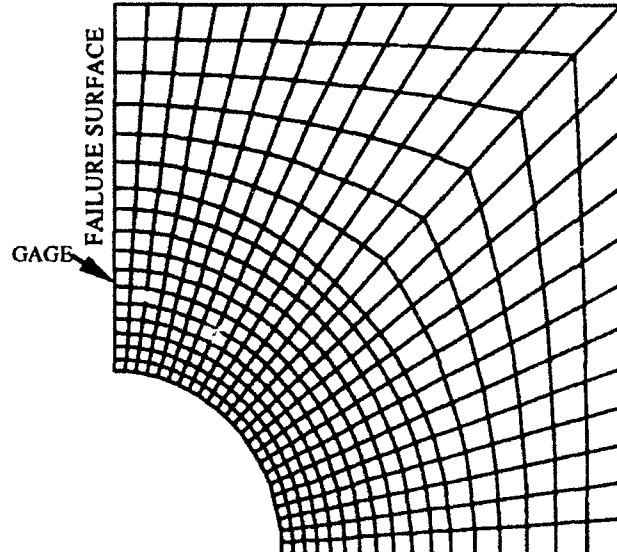
INCREMENT # 24
 $\sigma_{\text{applied}} = 45337 \text{ psi}$

-45



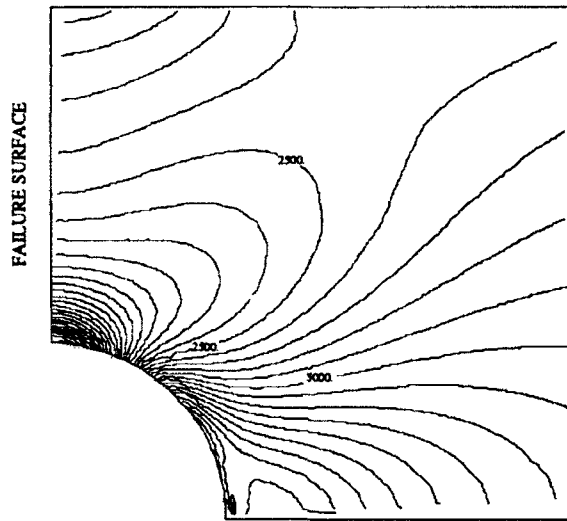
INCREMENT # 24
 $\sigma_{\text{applied}} = 45337 \text{ psi}$

90

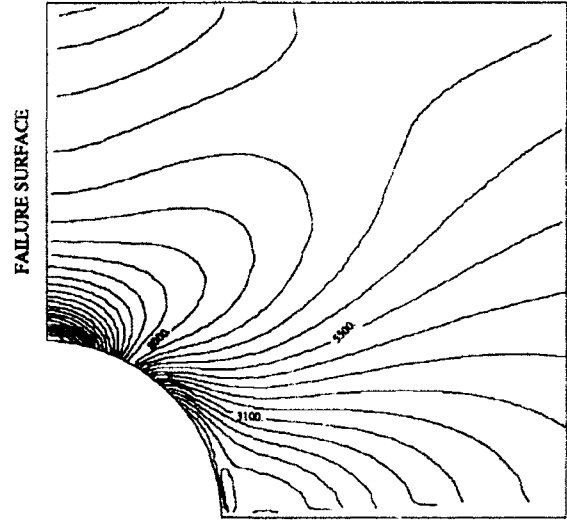


INCREMENT # 24
 $\sigma_{\text{applied}} = 45377 \text{ psi}$

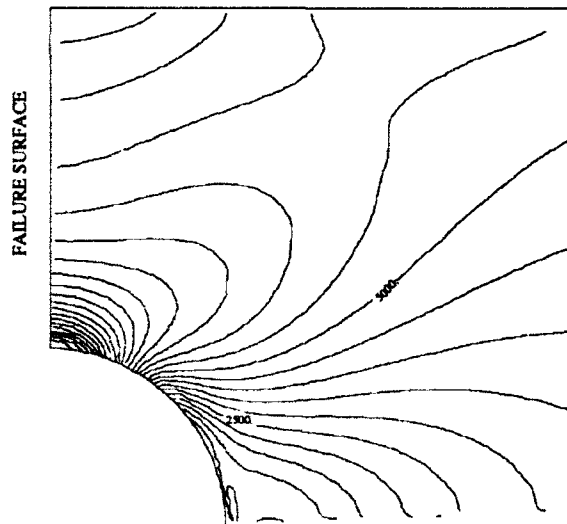
Figure 5-38: Progression of Failure for 0/±45/90° Model (cont)



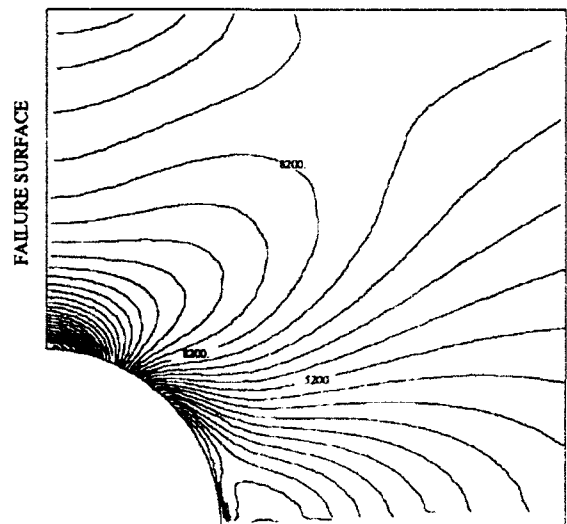
QUASI-ISOTROPIC INCREMENT #13 LONGITUDINAL
 $\sigma_{\text{applied}} = 31988 \text{ psi}$
 $U_x = 0.020559 \text{ in}$



QUASI-ISOTROPIC INCREMENT #18 LONGITUDINAL
 $\sigma_{\text{applied}} = 39210 \text{ psi}$
 $U_x = 0.023487 \text{ in}$

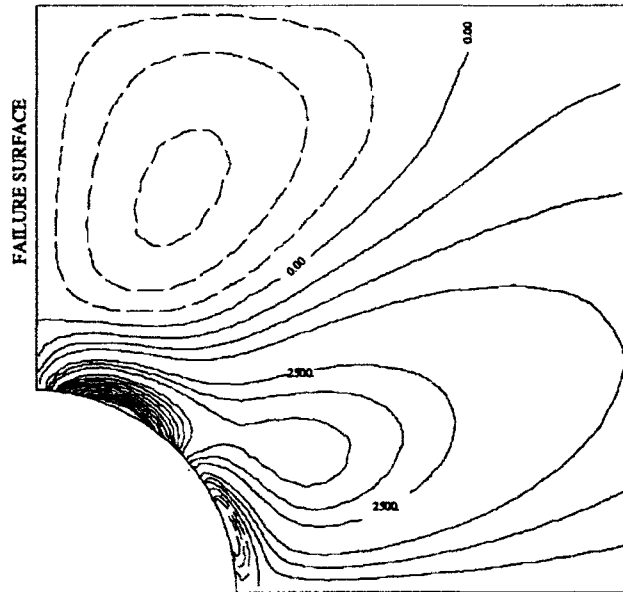


QUASI-ISOTROPIC INCREMENT #20 LONGITUDINAL
 $\sigma_{\text{applied}} = 41357 \text{ psi}$
 $U_x = 0.024542 \text{ in}$

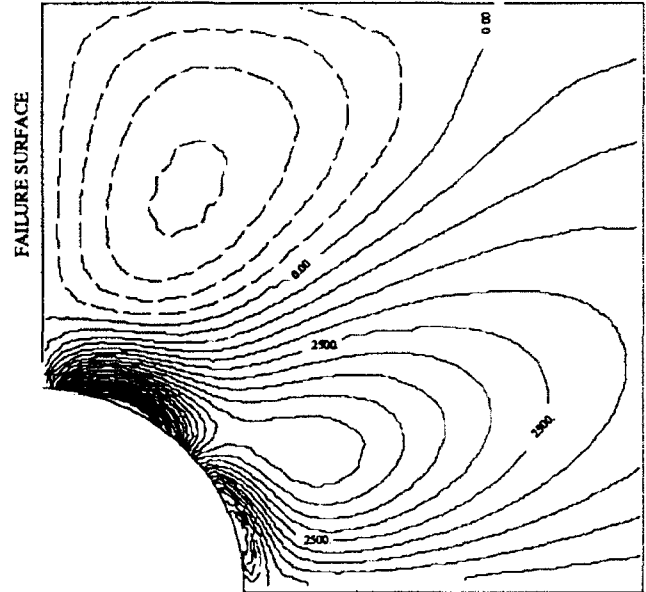


QUASI-ISOTROPIC INCREMENT #24 LONGITUDINAL
 $\sigma_{\text{applied}} = 46860 \text{ psi}$
 $U_x = 0.027295 \text{ in}$

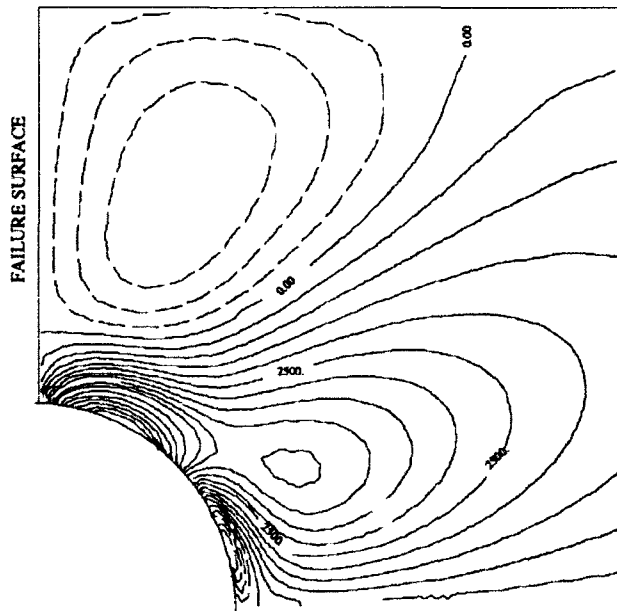
Figure 5-39: Contour Plots of 0/±45/90 degree Model



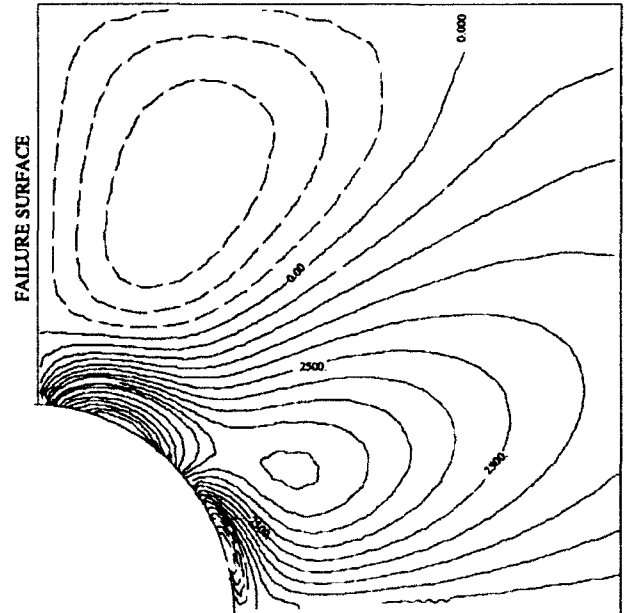
QUASI-ISOTROPIC INCREMENT #13 SHEAR
 $\sigma_{\text{applied}} = 31988 \text{ psi}$
 $U_x = 0.020559 \text{ in}$



QUASI-ISOTROPIC INCREMENT #18 SHEAR
 $\sigma_{\text{applied}} = 39210 \text{ psi}$
 $U_x = 0.023487 \text{ in}$



QUASI-ISOTROPIC INCREMENT #20 SHEAR
 $\sigma_{\text{applied}} = 41357 \text{ psi}$
 $U_x = 0.024542 \text{ in}$



QUASI-ISOTROPIC INCREMENT #24 SHEAR
 $\sigma_{\text{applied}} = 46860 \text{ psi}$
 $U_x = 0.027295 \text{ in}$

Figure 5-39: Contour Plots of 0/±45/90 degree Model

of the shear contours seems to reinforce the argument that the center section of the specimen is trying to displace and is generating a very high shear stress between the center segment and the two outer segments. This shear stress could be the mechanism that initiates the failure in all the specimens. The disparity of the shear stresses between the inner and outer segments combined with the longitudinal strain gradient at the edge appear to cause the failure of the composite.

What is seen with all the models that were analyzed using the PLNRS is there is no "smoking gun" that indicates the initiation of failure. Only the 0° degree exhibits a completely catastrophic failure in compression. While the failure of the 0° occurred at a much lower stress than obtained by the experimental results it was clearly a representation of a vertical split. Of the other four models tested, all demonstrated the initiation and propagation of a horizontal crack either normal to the failure surface or, in the case of the $\pm 45^{\circ}$ model, at an angle of 42° from the loading surface. Four of the five models exhibited some form of horizontal cracking that was present in the experimental specimens.

In the analysis, the progression of failure, failure was initiated loads comparable to those observed in the experimental portion. In most cases, when the crack within the model propagated to the outside edge of the model, the applied stress at the boundary of the model was almost twice the ultimate experimental stress. This suggests that the failure of the mesh occurs at a lower applied stress, and this results in a change of the failure from a quasi-static failure to a dynamic failure which can not be modeled directly by the program.

In both the $0^{\circ}/90^{\circ}$ degree and $0^{\circ}/\pm 45^{\circ}/90^{\circ}$ degree specimens there was some evidence of delamination at the edges of the specimen at the failure surface as well as the inner edges of the hole at the point of failure. This caused some concern on the part of the author as to whether the ultimate failure of the specimen may have been due to delamination within the specimen. To determine if delamination was the cause, two

methods were used. First, from a paper by T. Kevin O'Brien [37] we were able to determine the strain value at which delamination occurred within a Gr/PEEK composite. This value of σ_z was determined to be 23,300 psi based on the assumption that the material properties were the same in the Y and Z direction. From there, using the equilibrium equations (67) [15], the stresses in the Z direction, σ_{xz} , σ_{yz} , and σ_z , could be isolated and solved for individually as shown in equation (68). The location of Δx and Δy are shown in Figure 5-40. For all ply layups it was determined that the σ_z value at the initiation of failure at the hole was far less than the 23,300 psi determined by T.K. O'Brien indicating that delamination quite probably was not the cause of failure of the model.

$$\begin{aligned}\frac{\partial \sigma_x}{\partial x} + \frac{\partial \sigma_{xy}}{\partial y} + \frac{\partial \sigma_{xz}}{\partial z} &= 0 \\ \frac{\partial \sigma_{xy}}{\partial x} + \frac{\partial \sigma_y}{\partial y} + \frac{\partial \sigma_{yz}}{\partial z} &= 0 \\ \frac{\partial \sigma_{xz}}{\partial x} + \frac{\partial \sigma_{yz}}{\partial z} + \frac{\partial \sigma_z}{\partial z} &= 0\end{aligned}\quad (67)$$

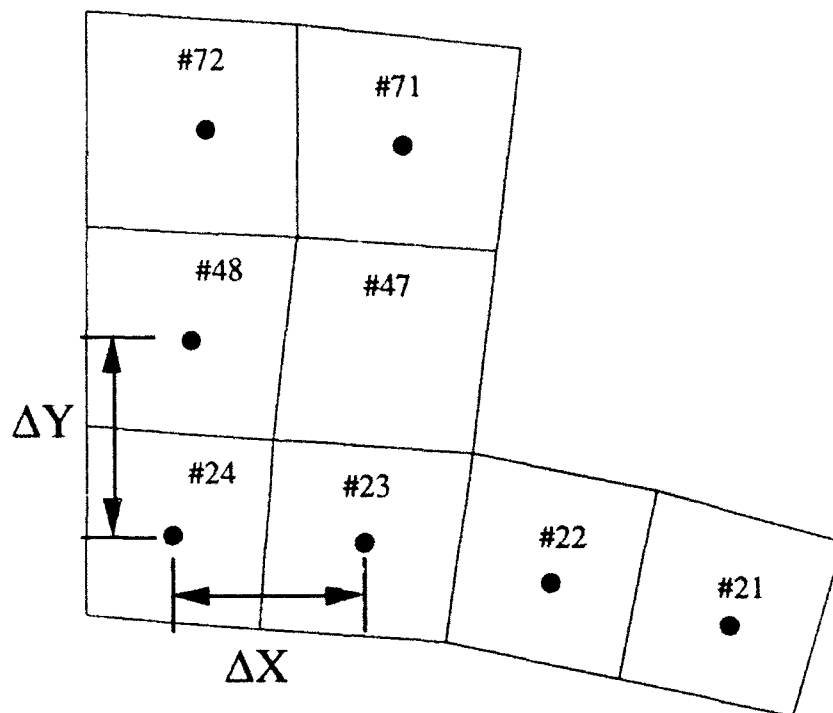
Using the finite differences we can rewrite the equations as:

$$\Delta \sigma_{xz} = \left(-\frac{\Delta \sigma_x}{\Delta x} - \frac{\Delta \sigma_{xy}}{\Delta y} \right) * t_{ply} \quad (68)$$

$$\Delta \sigma_{yz} = \left(-\frac{\Delta \sigma_{xy}}{\Delta x} - \frac{\Delta \sigma_y}{\Delta y} \right) * t_{ply}$$

$$\Delta \sigma_z = \left(-\frac{\Delta \sigma_{xz}}{\Delta x} - \frac{\Delta \sigma_{yz}}{\Delta y} \right) * t_{ply}$$

where t_{ply} = the thickness of the individual ply.



● CENTROID OF ELEMENT

Figure 5-40: Location of Elements for Delamination Check

This was verified by with the use of Dr. Sandhu and Dr. Sendekyj's Delamination Moment Coefficient technique which is detailed in [38]. What was determine was that the Delamination Moment Coefficient was much less for the laminates tested in this thesis than those laminates used by T.K. O'Brien. In addition, the moments determined for these laminates were much less that those determined to cause delamination. As a result of these calculations it was felt that the laminates tested did not failure due to delamination, but as a result of another or a combination of other failure modes. The delamination observed in the specimens was probably due to the post damage failure.

(6) Complex Variable Analysis

In addition to the use of the finite element code to analysis the composite layups a complex variable program was developed to perform an analysis. This code is based on the equations of G.N. Savin and written as the FORTRAN code which is included in Appendix B. The results are presented Table 5-7. The complex variable solutions were close to the FEM solutions for the 0° degree, 90° degree, and $0^\circ/\pm 45^\circ/90^\circ$ degree for σ_x ,

σ INFINITY (PSI)	SAVIN STRESS [$\sigma_x, \sigma_y, \tau_{xy}$] (PSI)	LAYUP 0° DEGREE	FINITE ELEM STRESS [$\sigma_x, \sigma_y, \tau_{xy}$] (PSI)	PERCENT DIFFERENCE (%)
-3102.24	-4230.00		-4646.00	-8.95
	-180.85		-317.70	
	397.59		18.48	
-15509.60	-21152.84		-23220.00	-8.90
	-904.00		-1583.00	
	1987.87		-92.73	
-31014.00	-42300.23		-46420.00	-8.87
	-1808.21		-3129.00	
	3975.00		-186.10	
-40932.22	-55827.76		-63610.00	-12.23
	-2386.47		-4055.00	
	5246.50		246.40	
		90° DEGREE		
-2429.76	-3215.60		-4109.00	-21.74
	-1822.66		-1036.00	
	2351.62		-8.21	
-10727.6	-14197.00		-19730.00	-28.04
	-8047.00		-5150.00	
	10382.00		-33.58	
-18690.85	-24735.00		-32680.00	-24.31
	-14026.00		-8455.00	
	16879.00		-59.23	
-23509.54	-31113.00		-39780.00	-21.79
	-17635.00		-102.80	
	22753.00		-73.19	

Table 5-7 Comparison of Complex Variable to FEM

σ INFINITY (PSI)	SAVIN STRESS $[\sigma_x, \sigma_y, \tau_{xy}]$	LAYUP	FINITE ELEM STRESS $[\sigma_x, \sigma_y, \tau_{xy}]$	PERCENT DIFFERENCE
		0°/90° DEGREE		
-1711	-2565.62.00		-4917.00	-47.82
	-56.00		-159.80	
	157.00		-8.55	
-8539.71	-12803.04		-24490.00	-47.72
	-282.74		-767.20	
	784.67		-43.61	
-17057.12	-25572.63		-48950.00	-47.76
	-564.00		-1505.00	
	1567.29		-87.44	
-26511.9	-39747.58		-76100.00	-47.76
	-877.75		-2324.00	
	2436.05		-136.10	
-32349	-49248.39		-93790.00	-47.49
	-1087.53		-2784.00	
	3018.33		-112.20	
-41197.12	-61764.19		-119400.00	-48.27
	-1363.98		-3533.00	
	3785.39		-158.00	
		±45° DEGREE		
-3659.37	-1498.56		-6791.00	-77.93
	-800.42		-2239.00	
	-949.05		3670.00	
-13027.84	-5335.00		-24560.00	-78.28
	-2849.00		-9276.00	
	-3378.00		13960.00	
-17745.92	-7267.00		-34290.00	-78.81
	-3881.00		-13550.00	
	-4602.87		19280.00	
-20262.39	-8297.73		-40650.00	-79.59
	-4431.99		-16480.00	
	-5255.02		22940.00	

Table 5-7 Comparison of Complex Variable to FEM (cont)

		0°/±45°/90° DEGREE		
-2390.352	-8299.30		-9546.00	-13.06
	-129.39		-94.27	
	370.71		-8.33	
-11943.91	-41469.08		-47770.00	-13.19
	-646.55		-452.03	
	1852.34		-41.71	
-26373.57	-91568.65		-114000.00	-19.68
	-1427.66		-1388.00	
	4090.18		-99.53	
-34346.09	-119249.10		-138700.00	-14.02
	-1359.24		-1726.00	
	5326.60		-121.30	
-41361.53	-143606.00		-167300.00	-14.16
	-2239.00		-2121.00	
	6416.60		-146.60	

Table 5-7 Comparison of Complex Variable to FEM (cont)

but it did not predict the σ_y and τ_{xy} with any degree of accuracy. The ply stresses are determined by taking the point stresses developed by the complex variable solution and calculating the point strains using the inverse of the A_{ij} matrix. From there the ply stresses are determined using the plies' \overline{Q}_{ij} matrix.

If the point stresses determined higher than the actual stresses at the point then the resulting strains and ply stresses will be much lower than the existing stresses and strains. That may be what is occurring within the $\pm 45^\circ$ degree and $0^\circ/90^\circ$ degree specimens. The predicted point strains and stresses are much lower than the values predicted by the finite element analysis. One other thing that may be a factor is that when Savin did his formulation he considered the plate to be of infinite dimensionality. Since all the models are of finite dimensionality then it is quite possible that this resulted in the differences between the point stress analysis and the FEM $\pm 45^\circ$ degree and $0^\circ/90^\circ$ degree models. In addition, since Gr/PEEK is a nonlinear material then the change in the material properties would not be modeled by Savin's technique.

Finally, as can be seen from Table 5-7, while the longitudinal point stresses showed some correlation between the two methods, many times the shear stresses and sometimes the transverse stresses were not well predicted by the point stress analysis. This may be the result of the finite dimensionality of the model as well as the nonlinearity of the finite element analysis. While the complex variable analysis seems to track the nonlinear analysis, evidenced by the small change in percentage from one increment to the next, this is not an indicator of the complex variable analysis tracking the nonlinearity. Instead, it is a combination of the application of the equations of an infinite dimensional plate to a finite specimen as well as the linearity of the program, which causes this effect. After completing the analysis it is shown that the finite element method is much better than the complex variable analysis in modeling the conditions and providing an accurate picture of stress and strain.

VI. Conclusions

This section summarizes the results obtained within the thesis and summarizes the conclusions as they relate to the objectives listed in Section A, Chapter 1. First, the conclusions from a comparison of the analytical and experimental results are presented. Second, conclusions will be drawn concerning the compression testing process as it relates to the Boeing Open Hole Compression fixture. Finally, general conclusion are given involving the use of the nonlinear finite element technique as well as the use of macromechanical failure methods verse micromechanical.

A. Experimental versus Analytical Failure Predictions.

(1) $[0^0]_{16}$ Unidirectional Laminates

The finite element method did a good job of predicting the stress-strain response of the composite. The failure load predicted was -21.96% less than the average ultimate stress recorded for a unidirectional composite that failed by a vertical split. In addition, the FEM did not predict the splitting of the specimen, rather it failed catastrophically. To complicate matters, there was a second failure mode, a horizontal cracking, that was present in half of the specimens tested. The Scanning Electron Microscope work showed no dominating failure mode within those specimens that failed due to a horizontal crack. It is clear however that the failure of the laminate was initiated at the hole by the collapse of material into the hole. The ultrasound imaging of specimens that failed by a vertical split did not show any evidence of the formation of a horizontal crack. From the experimentation and FEM it could be concluded that the primary mode of failure was due to vertical splitting.

(2) $[90^0]_{16}$ Unidirectional Laminates

The finite element code did a good job of predicting the response of the 90^0 laminate at low loads, but was unable to accurately model the material's nonlinear response at higher load levels. The analytical far field also displayed a less stiff response than the experimental far field, a condition that may have been induced by the Boeing fixture. A crack propagated through the model at 31,345 psi, well above the average experimental ultimate stress of 18,739.21. However, a increase in strain without a similar increase in stress was visible in the far field data at 28,750 lb.. This anomaly corresponded to the behavior of the experimental curve before failure and may signal the initiation of failure within the analytical model.

(3) $[0^0/90^0]_{4S}$ Crossply Laminates

PLNRS did an excellent job of modeling the stress-strain response of a $0^0/90^0$ specimen until the very end of the experimental loading. At 31,300 psi there was the same type of anomaly that was exhibited in the 90^0 analytical data. This anomaly coincided well with the experimental load's average experimental ultimate stress of 32,362 psi. However, the progression of failure study done on the experimental data showed that very few elements had failed at a load level of 35,895 psi. This coincides well with the experimental progression of failure study which showed that even at 95% of predicted ultimate strength very little damage had occurred within the composite.

(4) $[\pm 45^0]_{4S}$ Shear Laminates

The $\pm 45^0$ model showed excellent correlation with the experimental data. The nonlinear behavior and the stress-strain response of the experimental data very well modeled by the analysis. Like the pervious two laminates, the analytical strain at the hole was stiffer: i.e. the slope of the line was steeper: than the experimental strain. Towards the end of the loading the experimental seemed to less stiff, but this was an indication of

the analytical inability to model the scissoring effect of the fibers present in the experimental. The analytical progression of failure study showed that a crack propagated through the model in the -45° plies at 24,212 psi. However, once again the anomaly was present in the analytical data, this time occurring 20,327 psi. While the experimental specimens did not fracture into two separate pieces, ultrasonic images revealed that failure did occur within the specimens, probably occurring at or about 20,000 psi based on the reactions of the Instron Machines strip chart.

The angle of failure within the experimental failure was modeled well by the analytical model. The contour plots of analytical strain show very high concentrations of strain coinciding with the failure on the experimental. However, once again the far field experimental data was stiffer than the analytical data. This may also be a byproduct of the Boeing fixture or a result of the scissoring of the fibers placing stresses on the far field gages resulting in an incorrect reading.

(5) $[0^{\circ}/\pm 45^{\circ}/90^{\circ}]_{2S}$ Quasi-isotropic Laminates

The stress-strain of the quasi-isotropic was well modeled by PLNRS in the longitudinal direction, but not as well in the transverse direction. The nonlinear behavior of the specimens towards the end of the loading cycle at the hole in the transverse direction was not well modeled by the analytical. However, the anomaly which was present in the rest of the models was not present in this model. This cast some doubt on the fact that the failure of the model may occur at the anomaly. The analytical progression of failure study shows that a crack propagated through the specimen at 45,337 psi which is far greater than the average experimental ultimate stress of 33,710 psi. This does not coincide well with the experimental progression of failure study which revealed that at 95% of predicted ultimate failure very little internal damage had occurred before ultimate failure took place.

B. Compression Testing

The one main conclusion that can be drawn from this analysis is that tension and compression result in two entirely different types of responses in composite materials. This section will address the problems and concerns on the author's part in regards to the actual testing procedure.

The Boeing Open Hole Compression fixture has numerous disadvantages in its use for the testing of composites with open holes. First, the fixture requires large amounts of material for a single test, and with the cost of composite materials, this makes the testing of large quantities a rather large financial undertaking. Second, the fixture is extremely bulky and great care had to be taken when placing the specimen within the fixture so as not to damage the specimen or the gages. Twice the fixture slipped before it was securely fastened to a specimen and both times it "guillotined" the far field gage resulting in damage to the gage. Third, the fixture may have been responsible for the multiple failure modes observed in the 0° specimens. Since the fixture must be bolted onto the specimen to restrain out-of-plane buckling, it must induce, upon the far field area where it is bolted, a constraint on the material. While the constraint may not be great, it may still effect the results obtained from the far field gage. Finally, because of all the plates required to prevent out-of-plane buckling within the specimen there was no way for actual propagation of failure to be studied during the test. This problem requires the use of a progressive failure test by loading specimen to 90% and 95% of their predicted ultimate load. This is not the best way to test the actual progression of failure of the composite.

It is the recommendation of the author that a single compression fixture be designed and adopted for use in the testing of composite materials. The aforementioned disadvantages make the use of the Boeing Open Hole Compression fixture less than desirable, in the author's view, for the testing of composite materials in compression.

C. General Conclusions

(1) Nonlinear Finite Element Program (PLNRS)

The nonlinear finite element code, PLNRS, developed by Dr. Sandhu does a good job of modeling the stress-strain response of Gr/PEEK in compression. While there was no "smoking gun" within the testing to indicate where failure took place, the code did seem to model the point at which the experimental composites failed by showing a disproportional increase of strain to stress around the experimental ultimate failure load. The progression of failure study done on the experimental specimens reveals that there was a limited amount of damage taking place before the actual failure of the composite. This would seem to help validate the increase in strain feature as the failure point since the analytical progression of failure at the increase was similar to the amount observed in the experimental.

With the manufacturing of more powerful computational devices, this program could be used on more platforms than just the CRAY. Efforts could be made to adapt the program to the Sun workstations or to a DEC 5000. The entry of the data is easy, especially if a mesh generation program is used. The only drawback is the acquisition of the material properties data to model the response of the specimen. The data could be constructed for many of the material systems in existence from existing databases of information and could be constructed easily for new material systems. The use of curves to represent material response is much more accurate than the use of constant moduli. Overall the use of the code to model the response of a composite could be done easily with the existing computational capacity and material database.

(2) Macromechanical versus Micromechanical

One of the objectives of this thesis is to show how the use of a macromechanical failure prediction method is far superior to a micromechanical failure prediction. For this reason failed specimens were investigated using a Scanning Electron Microscope in order to discover if there existed a single micromechanical effect that would have initiated the failure of the composite. What was discovered was that there were numerous failure modes visible over the failed surfaces making it extremely difficult to determine which of these modes have been the one to initiate failure within the composite. In addition, many of the failures showed that the fiber and matrix failed as a unit and not as individual components as some micromechanical methods predict.

The appeal of micromechanical methods using close form solutions is that they are basically simple algebraic equations which can be solved given certain material properties. The problem is that many of the properties which are being entering into the equations are not constant, as in the case of the shear modulus, but change depending on the loading conditions and type of material. If the solution obtained is relied on for the design of a composite material then the resulting design may not accurate.

Through the use of this macromechanical approach not only the progression of failure can be determined, but many of the possible micromechanical failure modes will have been incorporated into the material properties curves. While the actual failure load was not clearly determined from this study there is an indication that the moment of failure that composites experience within the experimental is being modeled in analytical response. To validate this several tests should be conducted with different material systems and ply layups to see if the response does model the experimental failure. If it does hold true then this thesis has shown that there is excellent correlation between the experimental and analytical ultimate strengths.

(3) Closing

This thesis has raised many possible issues that could be undertaken to better understand the failure of Gr/PEEK in compression. Some of these issues include:

- a. The designing of a compression fixture that will accurately test the compressive strength of a composite without interfering with the testing.
- b. A study of the hole region during compression to determine if delamination is the mode of failure which may initiate the total failure of the specimen.
- c. The use of other techniques to determine the initiation and progression of experimental failure to include acoustic testing, high speed photography, and stereo x-ray imaging.
- d. A thorough study of the analytical data in comparison to the experimental data to determine if there does exist a point at which the failure of the model occurs. While there were many indications of possible failure point there was no criterion developed to actually determine that point.

This thesis has sought to undertake a detailed investigation in order to fulfill the objectives stated in Section A, Chapter 1. It has shown that the nonlinear material finite element program, PLNRS, does an excellent job of modeling the stress-strain response of the nonlinear material Gr/PEEK, and there does exist within the analysis a point which may indicate the failure of the composite specimen. While the author was unable to prove that this point represented the actual failure of the composite specimen, there is every indication that this may be true. It is hoped that this thesis will contribute to other research projects involving the use of nonlinear composite materials, such as Gr/PEEK.

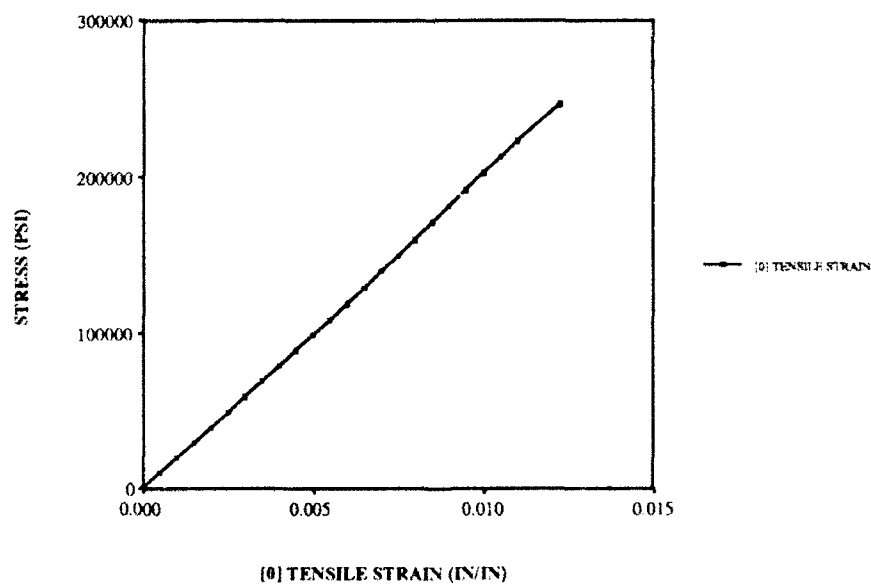
Appendix A. Material Properties Curves

Basic property tests were conducted to obtain the material properties for Gr/PEEK at room temperature. This data is listed in tabular form for future reference and shown graphically to demonstrate the nonlinear relationships between stress and strain for Gr/PEEK.

[0] TENSION STRESS-STRAIN DATA

0 TEN STRN (IN/IN)	0 TEN STRS (PSI)
0.0000	0.00
0.0005	9938.65
0.0010	19547.58
0.0015	29164.00
0.0020	38848.27
0.0025	48622.52
0.0030	58504.41
0.0035	68454.20
0.0040	78458.17
0.0045	88511.98
0.0050	98615.75
0.0055	108764.83
0.0060	118943.23
0.0065	129143.77
0.0070	139359.75
0.0075	149598.47
0.0080	159934.39
0.0085	170280.09
0.0090	180716.75
0.0095	191170.47
0.0100	201697.61
0.0105	212248.28
0.0110	222863.22
0.0122	245829.72

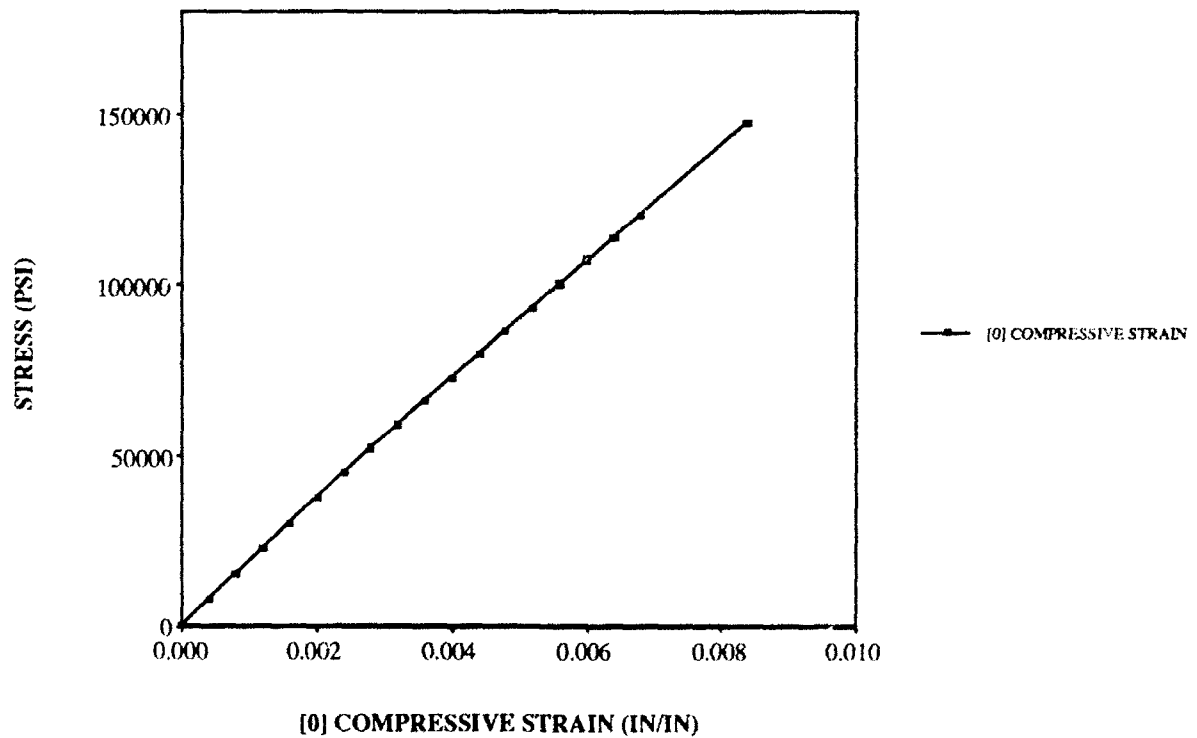
STRAIN FOR [0] TENSION



[0] COMPRESSION STRESS-STRAIN DATA

[0] COMPRESSION STRAIN (IN/IN)	[0] COMPRESSION STRESS (PSI)
0.0000	0.00
0.0004	7523.33
0.0008	15066.50
0.0012	22605.36
0.0016	30047.37
0.0020	37396.43
0.0024	44598.05
0.0028	51768.01
0.0032	58878.63
0.0036	65905.99
0.0040	72852.92
0.0044	79825.67
0.0048	86687.93
0.0052	93519.20
0.0056	100320.69
0.0060	106969.41
0.0064	113625.31
0.0068	120159.06
0.0084	147055.86

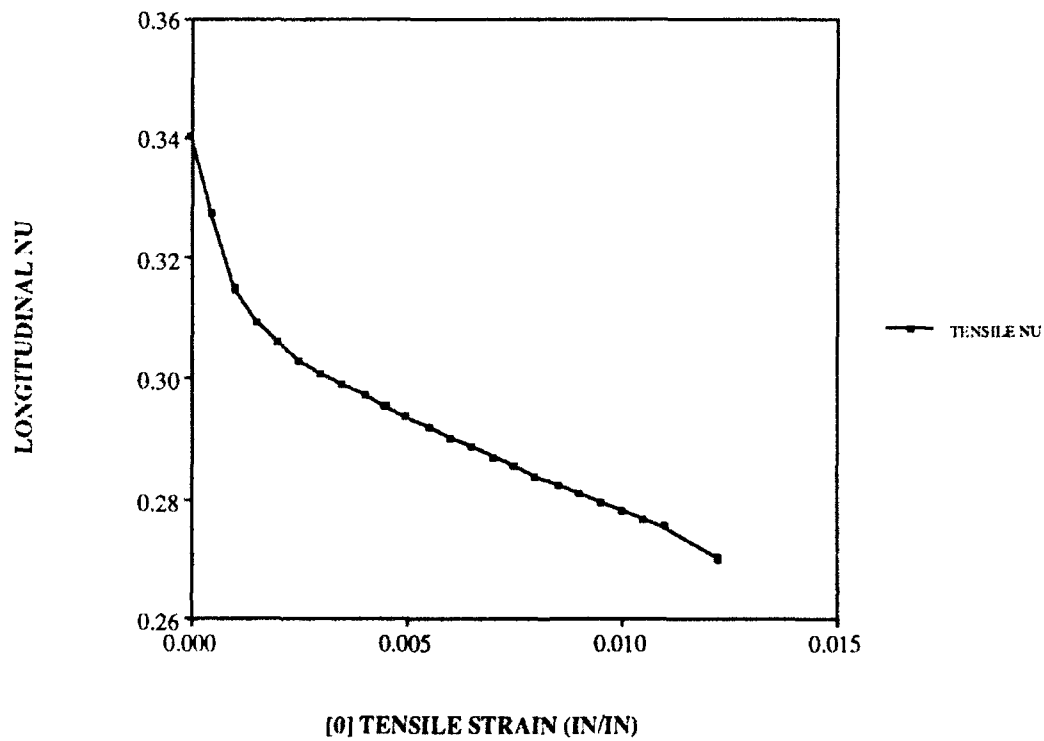
STRAIN FOR [0] COMPRESSION



[0] TENSION STRAIN-NU DATA

[0] TENSION STRAIN (IN/IN)	[0] TENSION NU
0.0000	0.340
0.0005	0.327
0.0010	0.315
0.0015	0.309
0.0020	0.306
0.0025	0.303
0.0030	0.301
0.0035	0.299
0.0040	0.297
0.0045	0.295
0.0050	0.293
0.0055	0.292
0.0060	0.290
0.0065	0.289
0.0070	0.287
0.0075	0.285
0.0080	0.284
0.0085	0.282
0.0090	0.281
0.0095	0.279
0.0100	0.278
0.0105	0.277
0.0110	0.275

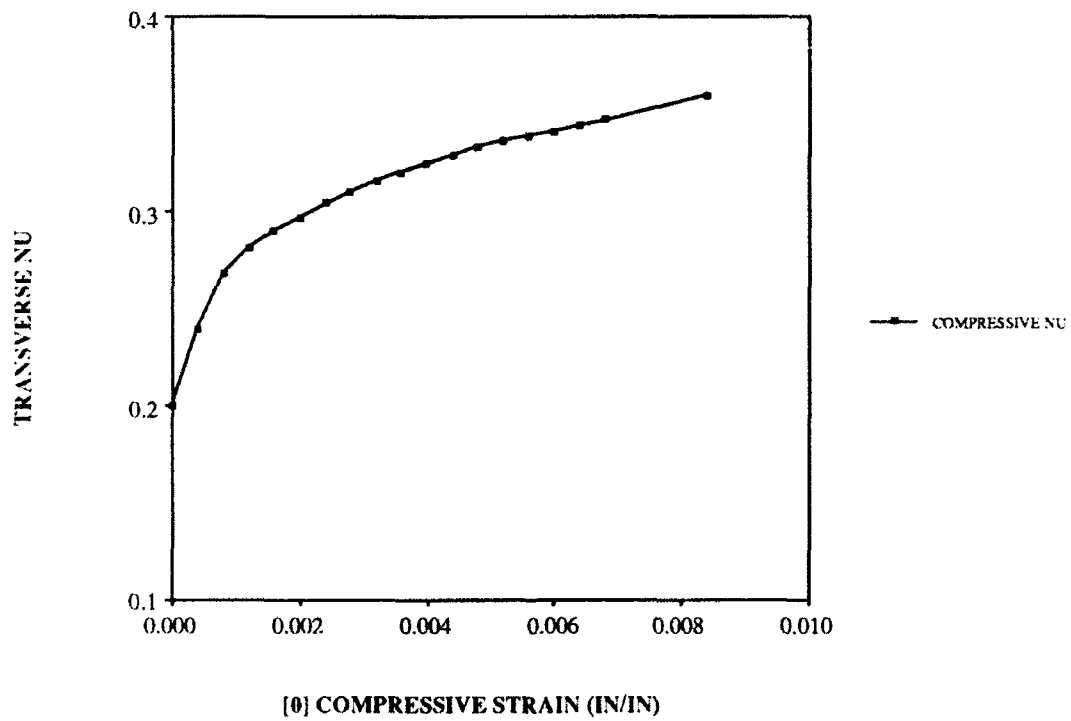
NU FOR [0] TENSION



[0] COMPRESSION STRAIN-NU DATA

[0] COMPRESSIVE (IN/IN)	[0] COMPRESSIVE NU
0.0000	0.200
0.0004	0.240
0.0008	0.268
0.0012	0.282
0.0016	0.290
0.0020	0.297
0.0024	0.304
0.0028	0.310
0.0032	0.315
0.0036	0.320
0.0040	0.325
0.0044	0.329
0.0048	0.333
0.0052	0.336
0.0056	0.339
0.0060	0.341
0.0064	0.344
0.0068	0.347
0.0084	0.360

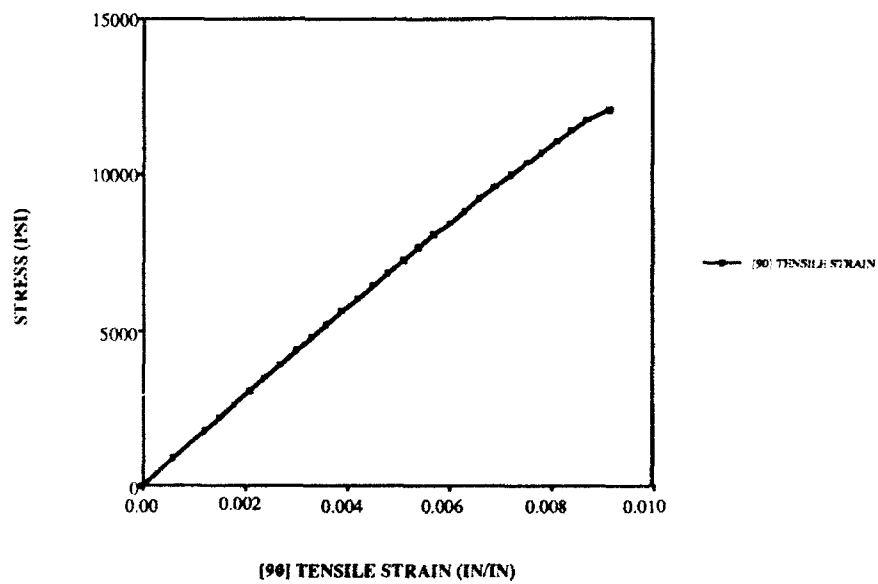
NU FOR [0] COMPRESSION



[90] TENSION STRESS-STRAIN DATA

[90] TENSION STRAIN (IN/IN)	[90] TENSION STRESS (PSI)
0.0000	0.000
0.0003	435.45
0.0006	898.96
0.0012	1780.95
0.0015	2215.18
0.0018	2641.42
0.0021	3084.15
0.0024	3515.53
0.0027	3939.77
0.0030	4367.89
0.0033	4788.01
0.0036	5214.22
0.0039	5630.01
0.0042	6038.98
0.0045	6452.16
0.0048	6853.30
0.0051	7258.20
0.0054	7656.59
0.0057	8051.64
0.0060	8446.71
0.0063	8833.58
0.0066	9212.64
0.0069	9589.33
0.0072	9954.61
0.0075	10322.76
0.0078	10683.32
0.0081	11031.28
0.0084	11375.40
0.0087	11695.78
0.0091	12015.00

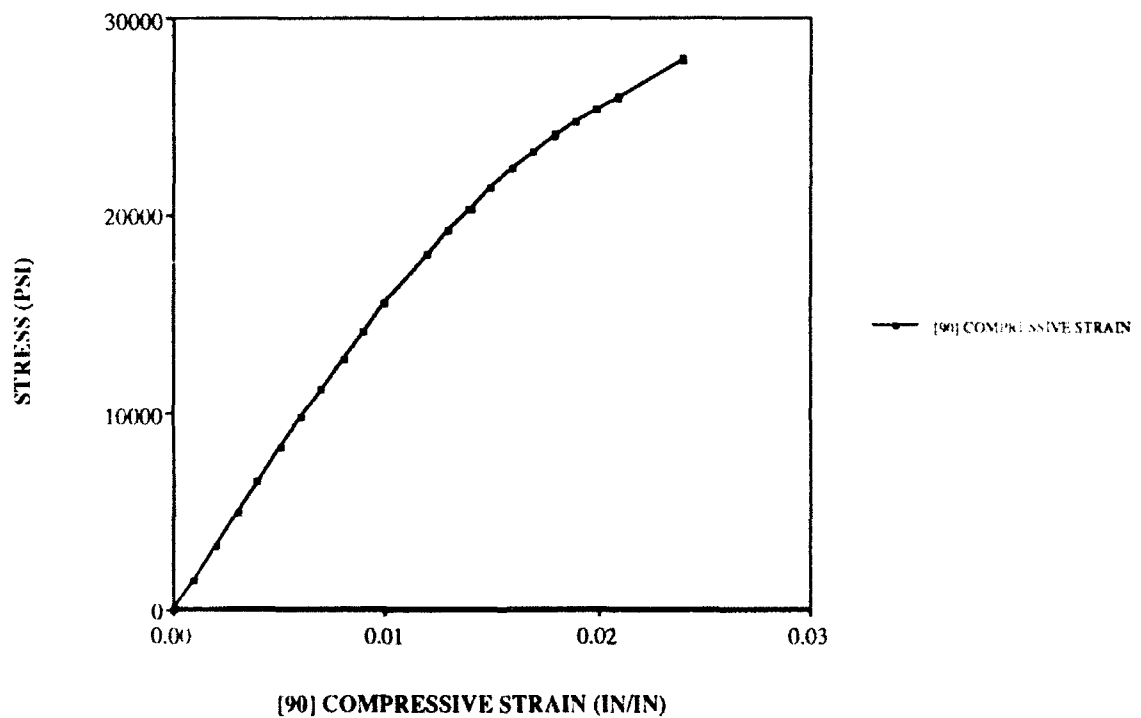
STRAIN FOR [90] TENSION



[90] COMPRESSION STRESS-STRAIN DATA

[90] COMPRESSIVE STRESS (IN/IN)	[90] COMPRESSIVE STRAIN (PSI)
0.000	0.00
0.001	1473.41
0.002	3237.05
0.003	4928.06
0.004	6607.35
0.005	8247.30
0.006	9789.12
0.007	11239.03
0.008	12749.96
0.009	14145.28
0.010	15504.37
0.012	18035.65
0.013	19201.81
0.014	20349.12
0.015	21370.73
0.016	22323.39
0.017	23203.96
0.018	24017.09
0.019	24729.55
0.020	25379.10
0.021	25969.66
0.024	27923.00

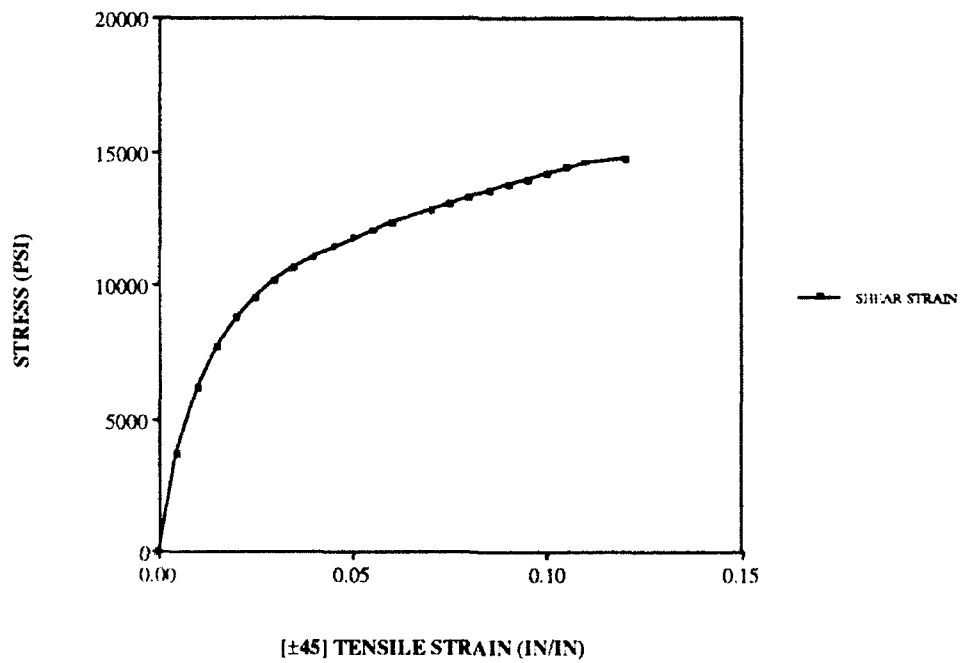
STRAIN FOR [90] COMPRESSION



SHEAR STRESS-STRAIN DATA

SHEAR STRAIN (IN/IN)	SHEAR STRESS (PSI)
0.000	0.000
0.005	3679.67
0.010	6185.00
0.015	7713.28
0.020	8764.49
0.025	9545.52
0.030	10158.39
0.035	10656.16
0.040	11064.73
0.045	11430.19
0.050	11741.46
0.055	12035.50
0.060	12302.89
0.070	12803.27
0.075	13038.60
0.080	13277.77
0.085	13502.60
0.090	13719.42
0.095	13936.90
0.100	14154.06
0.105	14378.16
0.110	14587.23
0.120	14740.21

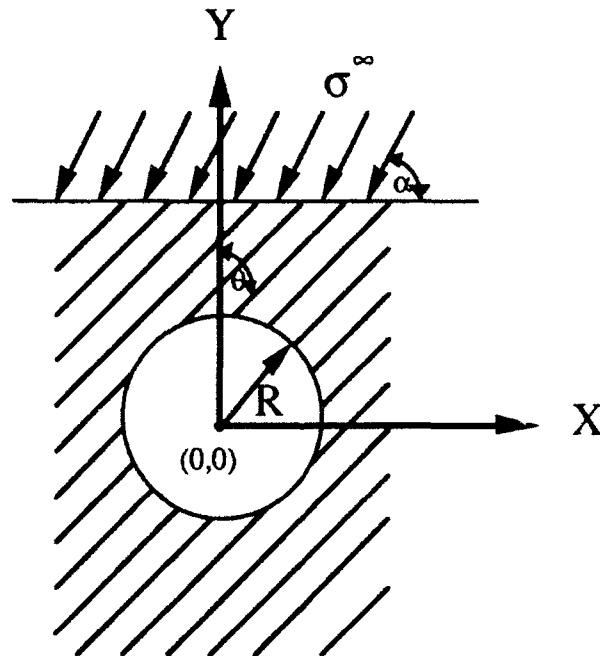
STRAIN FOR $\pm 45^\circ$ TENSION



Appendix B: Point Stress Analysis Code (SAVIN)

A point stress analysis FORTRAN code was developed to compare with the results of the PLNRS. The equations were discovered in an article by Gurdal and Haftka [25] and were incorporated into a FORTRAN code. The code is entitled SAVIN and is named after G.N. Savin of the Former Soviet Union, who developed the equations on which this code is based. [36]

These equations were developed to determine the stress components at coordinates loaded near the hole. These are based on a loading condition applied to a plate at a given orientation. The best way to depict the conditions that must be considered is represent then in a diagram, shown in Figure B-1.



θ = The ply orientation
 R = The radius of the circle
 α = The angle of the applied stress
 X, Y = The location of the point of interest

Figure B-1: Loading Conditions for Savin's Calculation

For the formulation of the point stresses, the A_{ij} matrix, from the composites properties, must first be formulated.

$$[A_{ij}] = \begin{bmatrix} \overline{Q}_{11} & \overline{Q}_{12} & \overline{Q}_{16} \\ \overline{Q}_{21} & \overline{Q}_{22} & \overline{Q}_{26} \\ \overline{Q}_{16} & \overline{Q}_{26} & \overline{Q}_{66} \end{bmatrix} * t_k$$

where t_k = the thickness of each ply considered

\overline{Q}_{ij} = The terms of the Reduced Stiffness Matrix, eq (13).

The terms of the A_{ij} matrix are then substituted the characteristic equation below.

$$a_{11}s^4 + 2a_{16}s^3 + (2a_{12} + a_{66})s^2 - 2a_{26}s + a_{22} = 0$$

Care must be taken to use only a symmetric laminate when determining the point stress.

A symmetric laminate will result in a characteristic equation where the a_{16} and a_{26} are equal to zero and the result roots can be determined as $s = (\pm a \pm 1)$. If an unsymmetric laminate is used the resulting answer will not be correct, because the quadratic equations will produce incorrect roots.

The roots, designated as s_1 and s_2 , will be substituted into the following equations:

$$z_1 = x + s_1 y \quad z_2 = x + s_2 y$$

where x, y = the locations of the stress components.

The values are then substituted into

$$\Phi_0'(z_1) = A_1(\sigma^\infty, \alpha) \left[1 - \frac{z_1}{\sqrt{z_1^2 - R^2(1 + s_1^2)}} \right]$$

$$\Psi_0'(z_2) = A_2(\sigma^\infty, \alpha) \left[1 - \frac{z_2}{\sqrt{z_2^2 - R^2(1 + s_2^2)}} \right]$$

where $A_1(\sigma^\infty, \alpha)$ and $A_2(\sigma^\infty, \alpha)$ are equal to:

$$A_1(\sigma^\infty, \alpha) = \frac{-i\sigma^\infty[(s_2 \sin 2\alpha + 2 \cos^2 \alpha) + i(2s_2 \sin^2 \alpha + \sin 2\alpha)]}{4(s_1 - s_2)(1 + s_1)}$$

$$A_2(\sigma^\infty, \alpha) = \frac{i\sigma^\infty[(s_1 \sin 2\alpha + 2 \cos^2 \alpha) + i(2s_1 \sin^2 \alpha + \sin 2\alpha)]}{4(s_1 - s_2) / (1 + s_2)}$$

The values of $\Phi_0'(z_1)$ and $\Psi_0'(z_2)$ are then substituted into

$$\sigma_x = \sigma^\infty \cos^2 \alpha + 2\text{Re} \left[s_1^2 \Phi_0'(z_1) + s_2^2 \Psi_0'(z_2) \right]$$

$$\sigma_y = \sigma^\infty \sin^2 \alpha + 2\text{Re} \left[\Phi_0'(z_1) + \Psi_0'(z_2) \right]$$

$$\tau_{xy} = \sigma^\infty \cos \alpha \sin \alpha - 2\text{Re} \left[s_1 \Phi_0'(z_1) + s_2 \Psi_0'(z_2) \right]$$

to determine the stress components. The stress components are then converted into global strain components by:

$$N_X = \sigma_X * \text{thickness}$$

$$N_Y = \sigma_Y * \text{thickness}$$

$$N_{XY} = \sigma_{XY} * \text{thickness}$$

$$[S_{ij}] = \begin{Bmatrix} \epsilon^0_X \\ \epsilon^0_Y \\ \epsilon^0_{XY} \end{Bmatrix} = \begin{bmatrix} \overline{S}_{11} & \overline{S}_{12} & \overline{S}_{16} \\ \overline{S}_{21} & \overline{S}_{22} & \overline{S}_{26} \\ \overline{S}_{16} & \overline{S}_{26} & \overline{S}_{66} \end{bmatrix} / t_k * \begin{Bmatrix} N_X \\ N_Y \\ N_{XY} \end{Bmatrix}$$

The stresses for the individual ply (k) can then be determined by

$$\begin{Bmatrix} \sigma_X \\ \sigma_Y \\ \sigma_{XY} \end{Bmatrix}_k = \begin{bmatrix} \overline{Q}_{11} & \overline{Q}_{12} & \overline{Q}_{16} \\ \overline{Q}_{21} & \overline{Q}_{22} & \overline{Q}_{26} \\ \overline{Q}_{16} & \overline{Q}_{26} & \overline{Q}_{66} \end{bmatrix}_k \begin{Bmatrix} \epsilon^0_X \\ \epsilon^0_Y \\ \epsilon^0_{XY} \end{Bmatrix}$$

and the answer are produced at the end of the program.

```

PROGRAM SAVIN
COMPLEX*16 AB1,AB2,SS1,SS2,SS3,SS4,D1,D2,DD1,DD2,AA1,
1      AA2,A1,A2,PHI,PSI,SIGX,SIGY,TAUXY,AL1,AL2,
1      AL3,Z1,Z2
      DIMENSION Q(3,3),A(3,3),T(3,3),W(3,3)
C
C*****
C
C      THIS PROGRAM IS DEVELOPED AS A COMPARISON TO A FINITE
C      ELEMENT ANALYSIS CONDUCTED BY CAPT. BENJAMIN WHAM,
C      GA93-M. IT IS BASED ON THE EQUATIONS IN A PAPER BY
C      ZAFER GURAL AND RAPHAEL T. HAFTKA ENTITLED "COMPRESSIVE
C      FAILURE MODEL FOR ANISOTROPIC PLATES WITH A CUTOUT."
C      AIAA JOURNAL, NOVEMBER 1987. VOL: 25 PP.1476-1481.
C      DUE TO THE NATURE OF THE FOURTH ORDER POLYNOMIAL SOLVER
C      THIS PROGRAM WILL ONLY WORK WITH SYMMETRIC LAMINATES
C      BECAUSE THE COEFFICIENTS X^3 AND X^1 ARE EQUAL TO
C      ZERO. THE EQUATION CAN BE FACTORED INTO TWO QUADRATICS
C      AND SOLVED BY USING THE QUADRATIC EQUATION.
C
C*****
C
C      PRINT*,'ENTER SIGMA INFINITY'
C      READ*,SIGIN
C      PRINT*,'ENTER RADIUS'
C      READ*,R
C
C      PRINT*,'ENTER E11,E22'
C      READ*,E11,E22
C
C      PRINT*,'ENTER G12,NU'
C      READ*,G12,PNU
C
C      PRINT*,'ENTER LOAD ANGLE'
C      READ*,ALPHA
C
C*****CALCULATE Q
C
C      10 DO 19 I=1,3
C         DO 9 J=1,3
C            A(I,J)=0.
C            Q(I,J)=0.
C         9 CONTINUE
C      19 CONTINUE
C      PRINT*,'ENTER NUMBER OF PLIES'
C      READ*,NUM
C
C      DO 99 I=1,NUM
C
C      PRINT*,'ENTER PLY ANGLE'
C      READ*,THETA
C
C      PRINT*,'ENTER THE INDIVIDIAL PLY THICKNESS'

```

```

C READ*,THICK
PI=3.1415926536
TD=THETA*PI/180.
AM=SIN(PI/2.-TD)
AP=SIN(TD)
PRINT*,'AM=',AM,'AP=',AP
S1=AM**4
S2=AM*AM*AP*AP
S3=(AM**3)*AP
S4=AP**4
S5=(AP**3)*AM
S6=AM*AM
S7=AP*AP
S8=AM*AP
UN=PNU*E22/E11
UNU=1./(1.-UN*PNU)
C11=E11*UNU
C12=E22*PNU*UNU
C22=E22*UNU
C66=G12
C16=0.
C26=0.
C61=0.
C62=0.
C21=C12

C
C C
C CALCULATING Q-BAR MATRIX
Q(1,1)=(S1*C11+2.*S2*C12+S4*C22+4.*S2*C66)*THICK*NUM
Q(1,2)=(S2*C11+(S1+S4)*C12+S2*C22-4.*S2*C66)*THICK*NUM
Q(1,3)=(S3*C11+(-S3+S5)*C12-S5*C22+2.*(-S3+S5)*C66)*THICK*NUM
Q(2,2)=(S4*C11+2.*S2*C12+S1*C22+4.*S2*C66)*THICK*NUM
Q(2,3)=(S5*C11+(-S5+S3)*C12-S3*C22+2.*(-S5+S3)*C66)*THICK*NUM
Q(3,3)=(S2*C11-2.*S2*C12+S2*C22+(S6-S7)**2*C66)*THICK*NUM
Q(2,1)=Q(1,2)
Q(3,1)=Q(1,3)
Q(3,2)=Q(2,3)
A(1,1)=Q(1,1)+A(1,1)
A(1,2)=Q(1,2)+A(1,2)
A(1,3)=Q(1,3)+A(1,3)
A(2,1)=Q(2,1)+A(2,1)
A(2,2)=Q(2,2)+A(2,2)
A(2,3)=Q(2,3)+A(2,3)
A(3,1)=Q(3,1)+A(3,1)
A(3,2)=Q(3,2)+A(3,2)
A(3,3)=Q(3,3)+A(3,3)
PRINT*,'Q11=',Q(1,1),'Q12=',Q(1,2),'Q13=',Q(1,3)
PRINT*,'Q21=',Q(2,1),'Q22=',Q(2,2),'Q23=',Q(2,3)
PRINT*,'Q31=',Q(3,1),'Q32=',Q(3,2),'Q33=',Q(3,3)
PRINT*,'A11=',A(1,1),'A12=',A(1,2),'A13=',A(1,3)
PRINT*,'A21=',A(2,1),'A22=',A(2,2),'A23=',A(2,3)
PRINT*,'A31=',A(3,1),'A32=',A(3,2),'A33=',A(3,3)
99 CONTINUE

```

```

DO 49 I=1,3
DO 59 J=1,3
IF(A(I,J).LT.100.) A(I,J)=0.
59 CONTINUE
49 CONTINUE
A9=A(1,1)
B8=2.*A(1,3)
B=B8/A9
F8=2*A(2,1)+A(3,3)
F=F8/A9
D8=-2.*A(2,3)
D=D8/A9
E8=A(2,2)
E=E8/A9
PRINT*,'S^4','+',B,' S^3','+',F,' S^2','+',D,'S','+',E
C
C***ROOTS ARE FOUND USING A ROOT SOLVING PROGRAM
AL1=(1,0)
AL2=F
AL3=E
AB1=(-AL2+(AL2**2.-4.*AL3)**.5)/2.
AB2=(-AL2-(AL2**2.-4.*AL3)**.5)/2.
SS1=(AB1)**.5
SS2=(AB2)**.5
SS3=-(AB1)**.5
SS4=-(AB2)**.5
PRINT*,'ROOTS OF THE QUARTIC ARE ','S1= ',SS1,'S2= ',
1 SS2,'S3= ',SS3,'S4= ',SS4
C
IF(ABS(THETA).EQ.45.AND.NUM.EQ.2) SS4=SS3
C*****
C COMPUTE A1 AND A2 OF SAVIN'S EQUATION
C*****
PRINT*,'ENTER X LOCATION'
READ*,X
C
PRINT*,'ENTER Y LOCATION'
READ*,Y
C
ALPHA=PI*ALPHA/180.
SN2=SIN(2*ALPHA)
SNSQ=SIN(ALPHA)**2.
CSSQ=COS(ALPHA)**2.
Z1=X+SS1*Y
Z2=X+SS4*Y
DD1=4*(SS1-SS4)*(1+(0,1)*SS1)
DD2=4*(SS1-SS4)/(1+(0,1)*SS4)
AA1=(0.,-1.)*SIGIN*((SS4*SN2+2.*CSSQ)+
1 (0.,1.)*(2.*SS4*SNSQ+SN2))
AA2=(0.,1.)*SIGIN*((SS1*SN2+2.*CSSQ)+(0.,1.)
1 *(2.*SS1*SNSQ+SN2))
D1=(Z1**2.-(R**2.*(1.+SS1**2.)))**.5
D2=(Z2**2.-(R**2.*(1.+SS4**2.)))**.5

```

```

A1=AA1/DD1
A2=AA2/DD2
PHI=A1*((1.,0)-(Z1/D1))
PSI=A2*((1.,0)-(Z2/D2))
SIGY=SIGIN*CSSQ+2*((SS1**2.)*PHI+(SS4**2.)*PSI)
SIGX=SIGIN*SNSQ+2.*(PHI+PSI)
TAUXY=SIGIN*SQRT(SNSQ*CSSQ)-2.*(SS1*PHI+SS4*PSI)
C
PRINT*,'SIGX NOMINAL= ',SIGX
C
PRINT*,'SIGY NOMINAL= ',SIGY
C
PRINT*,'TAUXY NOMINAL= ',TAUXY
C
SIGXX=SIGX
SIGYY=SIGY
TAUXYY=TAUXY
PRINT*,'SIGX= ',SIGXX
C
PRINT*,'SIGY= ',SIGYY
C
PRINT*,'TAUXY= ',TAUXYY
DO 29 I=1,3
DO 39 J=1,3
W(I,J)=0.
T(I,J)=0.
Q(I,J)=0.
39 CONTINUE
29 CONTINUE
DO 199 I=1,NUM
PRINT*,'RENTER PLY ANGLES'
READ*,THETA
TD=THETA*PI/180.
AM=COS(TD)
AP=SIN(TD)
S1=AM**4
S2=AM*AM*AP*AP
S3=(AM**3)*AP
S4=AP**4
S5=(AP**3)*AM
S6=AM*AM
S7=AP*AP
S8=AM*AP
UN=PNU*E22/E11
UNU=1./(1.-UN*PNU)
F11=1/E11
F12=-PNU/E11
F13=0.
F21=F12
F22=1/E22
F23=0.
F31=0.
F32=0.
F33=1/G12

```

```

T(1,1)=(S1*F11+2*F12*S2+F33*S2+F22*S4)
T(1,2)=(F12*(S1+S4)+(F11+F22-F33)*S2)
T(1,3)=((2*F11-2*F12-F33)*S3-(2*F22-2*F12-F33)*S5)
T(2,2)=(S4*F11+2*F12*S2+F33*S2+F22*S1)
T(2,3)=((2*F11-2*F12-F33)*S5-(2*F22-2*F12-F33)*S3)
T(3,3)=((4*F11+4*F22-8*F12-2*F33)*S2+F33*(S1+S4))
T(2,1)=T(1,2)
T(3,1)=T(1,3)
T(3,2)=T(2,3)
W(1,1)=T(1,1)+W(1,1)
W(1,2)=T(1,2)+W(1,2)
W(1,3)=T(1,3)+W(1,3)
W(2,1)=T(2,1)+W(2,1)
W(2,2)=T(2,2)+W(2,2)
W(2,3)=T(2,3)+W(2,3)
W(3,1)=T(3,1)+W(3,1)
W(3,2)=T(3,2)+W(3,2)
W(3,3)=T(3,3)+W(3,3)
PRINT*, 'T11=', T(1,1), 'T12=', T(1,2), 'T13=', T(1,3)
PRINT*, 'T21=', T(2,1), 'T22=', T(2,2), 'T23=', T(2,3)
PRINT*, 'T31=', T(3,1), 'T32=', T(3,2), 'T33=', T(3,3)
PRINT*, 'W11=', W(1,1), 'W12=', W(1,2), 'W13=', W(1,3)
PRINT*, 'W21=', W(2,1), 'W22=', W(2,2), 'W23=', W(2,3)
PRINT*, 'W31=', W(3,1), 'W32=', W(3,2), 'W33=', W(3,3)
199 CONTINUE
EPX=W(1,1)*SIGXX+W(1,2)*SIGYY+W(1,3)*TAUXYY
EPY=W(2,1)*SIGXX+W(2,2)*SIGYY+W(2,3)*TAUXYY
GAMXY=W(3,1)*SIGXX+W(3,2)*SIGYY+W(3,3)*TAUXYY
PRINT*, 'EPSILONX FOR PLY=', EPX
PRINT*, 'EPSILONY FOR PLY=', EPY
PRINT*, 'GAMMAXY FOR PLY=', GAMXY
PRINT*, 'ENTER THE ANGLE OF THE PLY YOU ARE INTERSTED IN.'
READ*, ETA
ZA=ETA*PI/180.
AR=COS(ZA)
AS=SIN(ZA)
R1=AR**4
R2=AR*AR*AS*AS
R3=(AR**3)*AS
R4=AS**4
R5=(AS**3)*AR
R6=AR*AR
R7=AS*AS
R8=AR*AS
UN=PNU*E22/E11
UNU=1./(1.-UN*PNU)
D11=E11*UNU
D12=E22*PNU*UNU
D22=E22*UNU
D66=G12
D16=0.
D26=0.
D61=0.
D62=0.

```

```

D21=D12
Q(1,1)=(R1*D11+2.*R2*D12+R4*D22+4.*R2*D66)
Q(1,2)=(R2*D11+(R1+R4)*D12+R2*D22-4.*R2*D66)
Q(1,3)=(R3*D11+(-R3+R5)*D12-R5*D22+2.*(-R3+R5)*D66)
Q(2,2)=(R4*D11+2.*R2*D12+R1*D22+4.*R2*D66)
Q(2,3)=(R5*D11+(-R5+R3)*D12-R3*D22+2.*(-R5+R3)*D66)
Q(3,3)=(R2*D11-2.*R2*D12+R2*D22+((R6-R7)**2)*D66)
Q(2,1)=Q(1,2)
Q(3,1)=Q(1,3)
Q(3,2)=Q(2,3)
PRINT*, 'Q11=', Q(1,1), 'Q12=', Q(1,2), 'Q13=', Q(1,3)
PRINT*, 'Q21=', Q(2,1), 'Q22=', Q(2,2), 'Q23=', Q(2,3)
PRINT*, 'Q31=', Q(3,1), 'Q32=', Q(3,2), 'Q33=', Q(3,3)
SIGMAX=(Q(1,1)*EPX)+(Q(1,2)*EPY)+(Q(1,3)*GAMXY)
SIGMAY=(Q(2,1)*EPX)+(Q(2,2)*EPY)+(Q(2,3)*GAMXY)
TAUUXY=(Q(3,1)*EPX)+(Q(3,2)*EPY)+(Q(3,3)*GAMXY)
C PRINT*, 'SIGX NOMINAL FOR PLY= ' SIGMAX*THICK*NUM
C PRINT*, 'SIGY NOMINAL FOR PLY= ', SIGMAY*THICK*NUM
C PRINT*, 'TAUXY NOMINAL FOR PLY= ', TAUUXY*THICK*NUM
C END

```


Appendix C

In order to ensure that these results can be reproducible, the stress strain data for each specimen is included in this appendix. This data is not the actual data, since some of these data files were in excess of 500 data points. Instead, the data have been thinned out so that it is a representative sample of the data that was included. This thinning process was accomplished in such a manner that all the physical features of the curve were kept intact and that all slope changes and discontinuities were present. The original data files are available from the author who can be contacted at his permanent address listed in the Vita.

[0]₁₆ Boeing Ultimate Strength Data

SPECIMEN #1 STRESS	SPECIMEN #1 TRAN @ HOLE	SPECIMEN #1 LONG @ HOLE	SPECIMEN #2 STRESS	SPECIMEN #2 TRAN @ HOLE	SPECIMEN #2 LONG @ HOLE	SPECIMEN #2 STRESS	SPECIMEN #3 STRESS	SPECIMEN #3 TRAN @ HOLE	SPECIMEN #3 LONG @ HOLE	SPECIMEN #4 STRESS	SPECIMEN #4 TRAN @ HOLE	SPECIMEN #4 LONG @ HOLE
520.38	10.42	46.68	1985.19	149.42	65.95	2854.26	233.34	0	233.34	4301.98	383.22	251.69
1079.95	-1.76	113.74	2643.61	138.00	157.75	3789.16	323.20	0	323.20	6536.11	490.42	352.30
1295.95	-4.96	140.03	3036.78	129.65	192.21	5101.91	427.25	0	427.25	8219.84	591.70	455.77
1551.22	-8.30	169.25	3931.08	129.47	272.67	6603.66	539.88	57.69	539.88	9952.77	698.68	565.35
1835.93	-6.04	201.42	4471.60	135.03	315.75	8264.46	666.91	120.58	666.91	11735.31	796.71	672.64
2031.20	-3.62	230.64	5041.58	137.81	361.72	10074.50	805.46	183.40	805.46	13517.85	900.47	773.91
2415.17	1.57	259.87	6486.25	199.64	459.35	11944.22	943.97	246.18	943.97	15399.60	1004.18	882.29
2886.44	14.90	306.68	7331.41	247.44	511.02	13625.01	1070.88	297.94	1070.88	17281.34	1101.82	994.26
3405.83	25.40	341.78	8176.57	295.15	562.69	15524.54	1215.14	351.99	1215.14	18915.47	1182.77	1033.24
4447.51	74.80	408.72	9070.88	345.84	611.50	17175.45	1330.49	400.81	1330.49	20593.80	1269.28	1172.21
5694.36	132.48	493.09	9955.42	399.20	663.16	18806.45	1448.73	446.68	1448.73	22322.93	1350.04	1251.16
7035.52	198.34	583.32	10849.72	446.66	717.69	20467.33	1564.03	492.41	1564.03	23867.06	1436.37	1347.22
8531.79	264.17	679.34	11753.87	497.13	772.22	22118.24	1685.12	538.28	1685.12	25500.79	1514.18	1426.13
9994.64	332.74	769.54	12658.02	547.50	826.72	23789.00	1806.13	572.85	1806.13	27184.52	1591.99	1522.16
11457.34	395.58	871.33	14436.79	636.77	932.86	25469.80	1924.25	607.40	1924.25	28868.25	1675.36	1605.31
12949.79	451.10	970.24	15331.10	681.46	984.48	27150.51	2042.45	630.29	2042.45	30502.38	1744.52	1591.31
14471.59	520.98	1069.12	17168.93	773.49	1090.54	28880.95	2270.15	667.21	2270.15	33869.44	1902.48	1654.67
16042.49	583.54	1170.92	18092.69	820.87	1142.15	30561.70	2365.28	709.22	2365.28	35503.17	1977.33	1934.90
17632.98	651.69	1272.70	19026.30	868.13	1196.60	32232.51	2474.65	765.46	2474.65	36988.88	2035.15	2000.79
19203.80	708.37	1377.39	19979.60	909.77	1251.05	33923.18	2581.15	802.50	2581.15	38623.01	2112.64	2078.12
20794.30	765.13	1479.12	20913.20	959.92	1302.64	35584.06	2687.62	828.13	2687.62	40256.74	2175.91	2155.45
22424.14	824.62	1580.83	22800.11	1040.29	1408.62	37254.90	2794.18	845.16	2794.18	41890.87	2247.59	2232.76
24044.06	878.40	1685.45	23743.56	1087.64	1457.32	39164.38	3018.45	884.53	3018.45	43525.00	2313.66	2304.34
25693.50	926.19	1790.13	28500.19	1289.52	1720.79	40845.09	3136.22	898.80	3136.22	45159.12	2377.03	2375.90
27352.69	976.95	1894.70	29473.10	1322.47	1775.18	42784.46	3236.71	918.51	3236.71	45793.25	2440.16	2444.59
29041.39	1019.01	1996.46	30426.39	1355.37	1826.71	44664.06	3328.47	918.25	3328.47	48476.58	2517.80	2513.27
30739.92	1069.49	2101.06	31379.69	1393.88	1878.24	46553.70	3423.22	940.98	3423.22	49813.49	2567.18	2573.36
32458.05	1111.46	2202.77	32323.14	1429.68	1929.76	48433.30	3532.24	983.40	3532.24	51398.01	2633.08	2636.30
34176.18	1150.50	2307.32	34239.50	1486.83	2032.78	50303.02	3655.68	1008.87	3655.68	53032.14	2699.09	2693.51
35904.07	1189.47	2408.99	35222.25	1522.43	2084.29	52162.78	3769.71	986.11	3769.71	54616.66	2739.53	2750.72
37632.04	1222.83	2507.78	36175.55	1549.56	2132.91	54002.62		1034.11		56201.19	2740.23	2793.62
39360.00	1255.86	2606.54	37138.69	1579.55	2184.40	55822.52				57488.40		2810.75
41087.97	1283.36	2705.21	39035.44	1630.92	2287.39							
42805.10	1313.79	2757.81	39998.50	1658.00	2338.87							
44052.95		2798.00	40932.10	1679.48	2387.50							
45553.12		2818.83	41875.56	1706.54	2433.25							
47125.82			44932.03	1770.34	2593.34							
			45875.43	1786.05	2639.07							
			46985.98									

[0]₁₆ Boeing Ultimate Strength Data

SPECIMEN #5 STRESS	SPECIMEN #5 LONG @ HOLE	SPECIMEN #5 TRAN @ HOLE	SPECIMEN #6 STRESS	SPECIMEN #6 LONG @ HOLE	SPECIMEN #6 TRAN @ HOLE	FAR FIELD STRESS	FAR FIELD STRAIN
0.00	0.00	0.00	0.00	0.00	0.00	0.00	0.00
2167.80	259.70	48.15	2484.05	394.48	17.155	2167.80	10.13
2933.46	403.34	59.84	2840.32	468.22	14.245	2933.46	14.65
3858.24	552.03	80.20	3246.08	555.02	11.365	3858.24	19.93
5021.75	717.70	97.67	3711.25	632.05	11.365	5021.75	25.78
6384.05	857.06	150.10	4770.23	807.19	20.665	6384.05	33.96
7895.53	996.36	199.64	5403.61	917.45	28.730	7895.53	41.55
9486.53	1135.55	257.85	6907.93	1123.14	63.525	9486.53	49.64
11147.25	1283.30	318.98	7719.45	1215.67	86.745	11147.25	58.14
12927.17	1410.74	391.70	8590.30	1308.29	115.71	12927.17	67.86
14727.09	1532.47	473.15	9490.97	1406.79	147.63	14727.09	76.98
16546.77	1645.51	557.48	10401.39	1502.43	173.72	16546.77	86.93
18396.41	1752.52	647.62	12370.87	1652.88	257.77	18396.41	95.27
20265.89	1856.83	737.70	13380.36	1734.18	298.33	20265.89	105.59
22145.24	1946.69	833.57	14340.36	1812.34	347.58	22145.24	114.88
24024.70	2036.57	923.61	16418.65	1943.10	446.07	24024.70	124.58
25963.82	2125.99	1022.34	17517.21	2004.14	498.18	25963.82	134.99
27873.06	2201.55	1118.15	19506.44	2111.99	602.42	27873.06	144.15
29772.35	2279.82	1213.95	20416.94	2161.89	648.73	29772.35	154.78
31691.55	2352.52	1303.92	21317.53	2200.32	695.07	31691.55	164.63
33590.83	2425.09	1399.72	23168.20	2288.88	793.45	33590.83	174.22
35470.27	2486.21	1492.58	24108.37	2324.51	845.52	35470.27	184.61
37379.52	2544.81	1582.54	25038.70	2365.90	894.71	37379.52	194.21
39278.80	2597.18	1675.39	26909.12	2434.23	995.92	39278.80	204.10
41148.28	2649.99	1765.31	27869.11	2475.54	1042.25	41148.28	214.02
43067.49	2699.76	1852.30	29828.68	2543.67	1154.97	43067.49	224.34
44698.24	2733.05	1927.75	30758.93	2559.21	1207.00	44698.24	232.50
46349.00	2769.06	2006.02	31718.93	2586.17	1256.12	46349.00	241.265
47949.96	2796.77	2078.53	33619.09	2637.20	1360.18	47949.96	249.37
49570.83	2844.25	2148.14	34559.34	2664.29	1406.42	49570.83	258.49
51171.79	2882.96	2214.83	35499.50	2688.46	1458.42	51171.79	266.18
52066.77	2968.45	2232.25	37409.58	2733.74	1562.43	52066.77	271.35
			38349.75	2760.82	1608.64		
			40249.91	2797.61	1712.64		
			41209.90	2821.58	1761.71		
			43179.30	2864.09	1862.78		
			44178.88	2882.47	1911.86		
			46039.46	2919.20	2012.87		
			46494.71	2932.65	2038.85		

COMMENTS

Specimen #5: Back gage @ hole, Leg C was not functional.
Specimen #6: Back gage @ hole, Leg C was not functional

[90]₁₆ Boeing Ultimate Strength Data

SPECIMEN #1		SPECIMEN #1		SPECIMEN #1		SPECIMEN #2		SPECIMEN #2		SPECIMEN #2		SPECIMEN #3		SPECIMEN #3		SPECIMEN #3		SPECIMEN #4		SPECIMEN #4		SPECIMEN #4	
STRESS		LONG @ HOLE		TRAN @ HOLE		STRESS		LONG @ HOLE		TRAN @ HOLE		STRESS		LONG @ HOLE		TRAN @ HOLE		STRESS		LONG @ HOLE		TRAN @ HOLE	
0.00	0.00	0.00	0.00	0.00	0.00	0.00	0.00	0.00	0.00	0.00	0.00	0.00	0.00	0.00	0.00	0.00	0.00	0.00	0.00	0.00	0.00	0.00	
1659.19	1602.51	11.51	1063.87	678.64	11.51	1030.70	195.65	-0.14	195.65	329.21	47.51	33.31	33.31	33.31	33.31	33.31	33.31	33.31	33.31	33.31	33.31	33.31	
2198.35	2224.42	11.51	2242.25	2034.44	11.51	1348.20	563.71	-11.65	563.71	1071.09	653.23	39.00	39.00	39.00	39.00	39.00	39.00	39.00	39.00	39.00	39.00	39.00	
2774.67	2903.43	11.51	3225.03	3262.01	23.01	1909.94	1287.92	-0.14	1287.92	1577.19	1218.54	50.11	50.11	50.11	50.11	50.11	50.11	50.11	50.11	50.11	50.11	50.11	
3067.48	3248.65	0.00	4308.05	4350.65	46.02	1909.94	1287.92	-0.14	1287.92	2078.33	1788.93	55.79	55.79	55.79	55.79	55.79	55.79	55.79	55.79	55.79	55.79	55.79	
3662.38	3949.96	11.51	5491.24	5552.14	103.55	2080.92	1310.84	-0.14	1310.84	2648.27	2399.84	78.26	78.26	78.26	78.26	78.26	78.26	78.26	78.26	78.26	78.26	78.26	
3959.79	4317.74	0.00	6679.15	7014.84	126.56	2481.45	1712.91	-0.14	1712.91	3252.62	3067.48	95.04	95.04	95.04	95.04	95.04	95.04	95.04	95.04	95.04	95.04	95.04	
4545.41	5018.32	23.01	7819.39	8623.16	172.57	2940.56	2252.60	-0.14	2252.60	3871.68	3740.67	112.09	112.09	112.09	112.09	112.09	112.09	112.09	112.09	112.09	112.09	112.09	
5140.31	5787.18	11.51	8825.97	10103.32	218.57	3429.04	2734.54	-0.14	2734.54	4490.83	4470.60	123.91	123.91	123.91	123.91	123.91	123.91	123.91	123.91	123.91	123.91	123.91	
5433.12	6142.91	11.51	9827.82	11694.65	253.07	3922.44	3273.47	0.00	3273.47	5085.33	5165.68	117.51	117.51	117.51	117.51	117.51	117.51	117.51	117.51	117.51	117.51	117.51	
6014.12	6933.77	11.51	10753.39	13316.77	310.57	4445.13	3812.12	23.01	3812.12	5679.84	5882.85	123.19	123.19	123.19	123.19	123.19	123.19	123.19	123.19	123.19	123.19	123.19	
6302.24	7323.33	11.51	11669.43	15105.84	356.57	4977.51	4407.80	23.01	4407.80	6279.23	6645.83	151.34	151.34	151.34	151.34	151.34	151.34	151.34	151.34	151.34	151.34	151.34	
6887.86	8147.59	11.51	12580.65	16992.56	425.55	5509.96	4980.18	34.52	4980.18	6863.97	7373.66	156.76	156.76	156.76	156.76	156.76	156.76	156.76	156.76	156.76	156.76	156.76	
7189.95	8605.20	11.51	13358.23	18774.18	471.53	6037.49	5575.07	45.02	5575.07	7443.75	8129.65	179.23	179.23	179.23	179.23	179.23	179.23	179.23	179.23	179.23	179.23	179.23	
7775.56	9473.95	23.01	14121.61	20697.92	540.50	6569.94	6169.75	34.52	6169.75	8028.42	8941.92	179.23	179.23	179.23	179.23	179.23	179.23	179.23	179.23	179.23	179.23	179.23	
8063.69	9930.91	23.01	14923.07	22162.42	643.92	7087.71	6797.98	57.67	6797.98	8588.52	9747.99	207.37	207.37	207.37	207.37	207.37	207.37	207.37	207.37	207.37	207.37	207.37	
8635.40	10867.09	23.01	15676.84	23561.10	735.84	7561.51	7357.67	69.17	7357.67	9163.35	10604.51	229.84	229.84	229.84	229.84	229.84	229.84	229.84	229.84	229.84	229.84	229.84	
9188.47	11802.18	34.52	16368.67	26479.40	793.28	8064.67	8042.38	69.17	8042.38	9703.85	11448.88	249.93	249.93	249.93	249.93	249.93	249.93	249.93	249.93	249.93	249.93	249.93	
9750.82	12816.07	34.52	16979.33	28473.30	896.65	8523.86	8669.67	69.17	8669.67	10244.35	12349.49	263.40	263.40	263.40	263.40	263.40	263.40	263.40	263.40	263.40	263.40	263.40	
10029.65	13305.59	34.52	17423.01	29877.61	977.04	9417.71	9945.88	69.03	9945.88	10774.94	1289.07	280.18	280.18	280.18	280.18	280.18	280.18	280.18	280.18	280.18	280.18	280.18	
10564.13	14317.68	57.53	17985.92			9852.46	10617.06	92.18	10617.06	11315.44	14210.65	302.64	302.64	302.64	302.64	302.64	302.64	302.64	302.64	302.64	302.64	302.64	
11047.49	15294.74	57.53				10287.20	11265.35	92.18	11265.35	11826.42	15205.19	315.42	315.42	315.42	315.42	315.42	315.42	315.42	315.42	315.42	315.42	315.42	
11512.26	16304.65	69.03				10717.10	11958.70	92.18	11958.70	12327.56	16232.58	336.20	336.20	336.20	336.20	336.20	336.20	336.20	336.20	336.20	336.20	336.20	
11972.43	17358.95	69.03				11552.37	13332.08	115.33	13332.08	12823.82	17298.48	358.65	358.65	358.65	358.65	358.65	358.65	358.65	358.65	358.65	358.65	358.65	
12395.36	18412.08	69.03				11957.82	14046.61	115.33	14046.61	13305.36	18391.32	398.16	398.16	398.16	398.16	398.16	398.16	398.16	398.16	398.16	398.16	398.16	
12915.87	19621.85	92.04				12348.59	14794.24	126.97	14794.24	13781.94	19517.23	426.03	426.03	426.03	426.03	426.03	426.03	426.03	426.03	426.03	426.03	426.03	
13427.10	20965.51	103.54				12739.36	15552.99	115.33	15552.99	14253.64	20703.56	448.48	448.48	448.48	448.48	448.48	448.48	448.48	448.48	448.48	448.48	448.48	
13659.48	21664.92	103.54				13115.44	16321.72	138.47	16321.72	14695.82	21854.92	470.67	470.67	470.67	470.67	470.67	470.67	470.67	470.67	470.67	470.67	470.67	
14170.78	23073.07	115.04				13491.60	17158.10	138.47	17158.10	15128.16	23078.28	487.17	487.17	487.17	487.17	487.17	487.17	487.17	487.17	487.17	487.17	487.17	
14403.17	23770.28	138.05				14199.88	18658.54	185.05	18658.54	15491.77	24204.12	454.17	454.17	454.17	454.17	454.17	454.17	454.17	454.17	454.17	454.17	454.17	
14881.84	25220.12	138.05				14610.17	19503.92	196.69	19503.92	15840.59	25294.69												
15100.33	25949.45	149.55				15000.94	20359.03	231.48	20359.03	16174.76	26429.09												
15523.19	27265.32	195.56				15382.02	21258.69	254.62	21258.69	16518.62	27595.65												
15903.96	28599.06	218.56				15767.87	22157.69	266.26	22157.69	16842.95	28794.49												
16104.19	29337.38	230.06				16534.80	24154.07	324.17	24154.07	17201.61	30115.49												
16430.68	30703.95	264.56				16891.35	25139.66	347.31	25139.66	17525.85	32215.35												
16651.94	31425.12	287.55				17252.83	26124.19	370.45	26124.19	17874.75	33967.12												
17024.45	32876.80	310.55				17614.31	27107.92	382.09	27107.92	18203.89	35098.21												
17353.70	34381.03	310.55				18669.72	27733.57	370.86	27733.57	18533.10	36387.17												
17530.93	35075.77	322.04				18908.77				18533.10	36387.17												
18111.99	35798.72	357.98				19450.99				19552.48	37818.52												
18135.57	35985.72	379.47				20066.47				19552.48	37818.52												
										19552.48	37818.52												
										19552.48	37818.52												
										19552.48	37818.52												
										19552.48	37818.52												
										19552.48	37818.52												
										19552.48	37818.52												
										19552.48	37818.52												
										19552.48	37818.52												
										19552.48	37818.52												
										19552.48	37818.52												
										19552.48	37818.52												
										19552.48	37818.52												
										19552.48	37818.52												
										19552.48	3												

[90]₁₆ Boeing Ultimate Strength Data

SPECIMEN#5 STRESS	SPECIMEN#5 LONG @ HOLE	SPECIMEN#5 TRAN @ HOLE	SPECIMEN#6 STRESS	SPECIMEN#6 LONG @ HOLE	SPECIMEN#6 TRAN @ HOLE	FAR FIELD STRESS	FAR FIELD LONG	FAR FIELD TRANSVERSE
0.00	0.00	0.00	0.00	0.00	0.00	0.00	0.00	0.00
687.98	518.90	0.00	552.10	582.85	11.51	329.21	22.36	5.68
1338.02	1291.20	0.00	1036.91	1108.69	11.51	1071.09	167.65	0.00
1840.95	1878.71	11.51	1776.21	1919.74	11.51	1577.19	284.95	0.00
2334.37	2454.33	34.52	2165.04	2365.28	23.01	2078.33	391.07	5.68
2837.30	3040.92	46.02	2534.72	2787.39	34.52	2648.27	519.48	5.68
3363.95	3684.68	46.02	3235.56	3596.43	34.52	3252.62	664.62	5.68
3657.37	4281.80	46.02	3586.02	4017.71	46.02	3871.68	804.12	5.68
4350.87	4890.27	57.53	3922.09	4450.35	34.52	4490.83	960.32	11.36
4853.80	5532.63	46.02	4598.94	5247.51	57.53	5085.33	1094.15	5.68
5351.93	6151.60	69.03	5275.86	6112.02	80.54	5679.84	1244.67	11.36
5888.09	6861.70	92.04	5991.16	7066.88	92.04	6279.23	1389.58	17.04
6429.03	7628.68	80.54	6332.00	7532.48	103.55	6863.97	1534.43	11.36
6955.68	8394.76	103.55	6691.99	8043.93	92.04	7443.75	1679.25	11.36
7525.05	9263.11	115.05	7032.84	8531.72	115.05	8028.42	1824.03	5.68
8084.92	10141.88	138.06	7359.30	9019.72	115.05	8588.52	1974.34	11.36
8635.29	11042.68	161.06	8986.70	11646.89	149.56	9163.35	2124.65	5.68
9176.16	11976.77	184.07	9308.31	12223.93	161.06	9703.85	2269.27	11.36
9626.93	12773.31	207.07	9615.55	12767.64	161.06	10244.35	2408.26	11.36
10053.90	13580.44	230.07	10230.02	13912.27	172.56	10774.94	2552.79	11.36
10499.89	14443.84	241.57	11127.74	15728.07	218.57	11315.44	2702.82	11.36
10907.93	15294.47	299.07	11420.60	16347.38	230.07	11826.42	2841.69	11.36
11368.20	16303.78	299.07	11722.99	16954.74	253.07	12327.56	2980.47	5.68
11766.75	17232.42	310.57	12299.08	18258.11	276.07	1283.82	3119.25	5.68
12170.00	18159.64	345.07	12855.57	19604.32	299.07	13305.36	3257.99	11.36
12559.11	19154.48	368.06	13143.97	20276.37	322.06	13781.94	3396.72	17.04
12948.15	20147.38	391.06	13676.84	21675.55	336.55	14253.64	3540.94	17.04
13318.25	21127.79	437.04	13940.86	22379.63	379.55	14695.82	3674.06	17.04
13678.85	22186.39	460.03	14444.97	23830.73	425.54	15128.16	3812.63	22.72
14044.17	23254.62	494.52	14704.15	24566.87	437.04	15491.77	3929.02	22.72
14399.98	24343.52	529.00	15198.65	26058.06	494.51	15840.59	4045.39	28.40
14746.37	25442.26	574.98	15899.95	28355.56	551.98	16174.76	4156.17	22.72
15078.54	26595.94	609.45	16110.74	29174.67	574.96	16518.62	4272.48	22.72
15415.34	27747.21	666.90	16336.38	30014.94	597.95	16842.95	4388.75	17.04
15728.50	28942.16	712.86	16998.85	32550.46	655.41	17201.61	4510.52	28.40
16041.65	30191.42	747.33	17219.72	33463.78	655.41	17525.86	4632.29	28.40
16354.82	31494.61	793.28	17834.19	36180.15	724.34	17874.75	4754.00	34.08
16648.93	32915.33	839.23	18040.61	37063.31	735.82	18203.89	4866.73	39.76
16882.20	33059.59	839.23	18160.58	37200.06	770.29	18533.10	5008.40	34.08
16947.92	34355.47	896.65	18169.42		781.78	18852.48	5135.53	34.08
17213.55	35490.64	965.56	18323.85		735.62	19152.25	5257.13	34.08
17465.07	36768.73	1011.49	18352.61			19393.24	5367.62	39.76
17659.62	37837.13	1045.93	18376.61			20110.29	5367.62	39.76
17692.77	37979.45	1068.89	18386.22					

COMMENTS

Specimen #4: Back gage @ hole, Leg C was not functional.
Specimen #5: Front gage @ Far Field was not functional
Specimen #6: Front gage and back gage @ Far Field were not functional

[0/90]_{4s} Boeing Ultimate Strength Data

SPECIMEN#1 STRESS	SPECIMEN#1 LONG @ HOLE	SPECIMEN#1 TRAN @ HOLE	SPECIMEN#2 STRESS	SPECIMEN#2 LONG @ HOLE	SPECIMEN#2 TRAN @ HOLE	SPECIMEN#2 STRESS	SPECIMEN#3 STRESS	SPECIMEN#3 LONG @ HOLE	SPECIMEN#3 TRAN @ HOLE	SPECIMEN#4 STRESS	SPECIMEN#4 LONG @ HOLE	SPECIMEN#4 TRAN @ HOLE
1785.16	0.00	0.00	0.00	0.00	0.00	0.00	0.00	0.00	0.00	0.00	0.00	0.00
2214.27	276.38	34.24	486.48	90.64	-34.52	838.57	150.40	46.31	46.31	537.70	185.20	0.00
2293.02	333.88	45.75	1156.04	171.47	-34.52	1483.33	289.42	46.31	46.31	1484.51	448.65	46.30
3139.31	334.02	57.12	1478.74	206.26	-34.52	1628.69	300.92	46.31	46.31	1922.29	603.47	46.30
4093.92	472.02	68.62	2008.58	310.48	-23.02	1657.80	312.41	46.31	46.31	2264.88	734.64	69.59
5097.71	598.62	91.50	3198.33	519.06	-11.51	2418.80	486.03	57.95	57.95	2583.61	803.99	92.60
6185.13	771.18	102.86	4580.79	785.21	0.00	3218.63	613.34	80.96	80.96	3335.39	989.07	92.60
7459.62	943.67	137.24	6136.60	1062.93	23.01	4464.44	786.76	103.98	103.98	4344.09	1158.49	138.90
8881.67	1162.10	160.10	7817.69	1375.28	45.02	5831.39	995.04	138.63	138.63	5300.02	1732.45	208.21
10426.69	1403.31	171.61	9469.85	1675.77	57.53	7314.72	1214.88	173.00	173.00	7451.15	2262.46	277.51
12030.84	1679.01	205.98	11136.52	1999.26	69.03	8894.95	1469.12	207.65	207.65	9078.41	2815.30	323.81
13615.27	2218.60	251.84	14517.91	2299.65	92.04	10538.16	1746.36	242.30	242.30	10719.93	3391.14	393.10
15224.30	2539.84	263.34	16218.22	2645.99	103.54	12195.96	2012.01	288.30	288.30	12361.52	3920.60	462.38
16828.37	2838.10	286.20	17937.88	3280.63	115.04	13877.99	2289.08	311.31	311.31	14045.87	4564.94	508.66
18437.40	3124.73	297.70	19614.11	3603.53	138.04	15535.79	2600.51	322.94	322.94	15692.11	5163.41	554.95
20046.43	3422.67	320.69	21285.56	3926.45	149.54	17193.59	2854.38	368.94	368.94	17376.53	5738.43	624.22
21650.57	3720.62	343.55	22990.73	4283.59	161.04	18861.10	3153.92	403.58	403.58	19022.77	6359.21	647.50
23559.70	4075.61	366.54	24613.96	4606.12	172.54	20509.20	3441.90	426.57	426.57	20678.62	6956.97	716.77
25149.10	4373.32	389.40	26309.48	4951.61	184.03	22133.07	3683.70	484.19	484.19	22343.91	7577.23	763.04
26753.17	4705.24	412.26	27899.00	5273.98	184.03	23761.83	3994.76	518.54	518.54	23952.12	8174.72	786.03
28357.31	5037.05	435.12	29503.02	5642.30	207.03	25424.45	4317.24	564.53	564.53	25569.93	8771.81	855.28
29917.15	5379.76	515.42	31116.69	5975.81	218.52	27019.20	4605.14	610.50	610.50	27206.65	9368.52	901.55
31226.01	5722.28	629.92	32378.65	6273.55	241.51	28875.78	4985.65	736.22	736.22	28776.83	10033.27	971.09
32165.79	6018.57		33370.90		344.94	29379.93	5077.85	793.53	793.53	30361.26	10743.00	1040.61
32387.22			32778.50			31561.21	5698.68			31864.83	11429.43	1179.37
32456.11			32874.78							33544.45	12852.61	1638.48
			32619.50							33944.12	13490.05	1937.81
			32672.50							34182.06	13955.27	
			32792.92									
			32783.28									

[0/90]_{4s} Boeing Ultimate Strength Data

SPECIMEN #5 STRESS	SPECIMEN #5 LONG @ HOLE	SPECIMEN #5 TRAN @ HOLE	SPECIMEN #5 STRESS	SPECIMEN #6 LONG @ HOLE	SPECIMEN #6 TRAN @ HOLE	FAR FIELD STRESS	FAR FIELD LONG	FAR FIELD TRANSVERSE
0.00	0.00	0.00	0.00	0.00	0.00	0.00	0.00	0.00
560.88	68.41	12.41	326.36	0.00	0.00	1786.16	175.69	-5.62
1444.86	241.50	36.45	1196.59	138.76	22.88	2214.27	215.33	-28.02
1924.91	345.87	36.45	1641.14	254.36	34.24	2293.02	226.66	-61.63
2295.65	426.80	36.45	1939.09	300.51	34.24	3139.31	323.00	-72.83
3198.74	553.67	60.50	2326.89	358.43	45.75	4093.92	424.96	-72.83
4591.31	773.18	96.19	2937.05	451.12	57.12	5097.71	521.27	-72.83
6107.49	1027.25	120.23	4251.82	659.04	79.99	6185.13	628.87	-11.21
7785.25	1328.67	143.52	6082.20	959.41	114.23	7459.62	753.09	72.82
10085.70	1767.51	191.60	7988.18	1282.50	148.60	8881.67	900.59	151.21
12462.19	2138.23	214.89	9908.33	1594.12	182.83	10426.69	1070.31	229.59
14196.97	2450.60	226.53	11866.36	1928.43	217.20	12030.84	1234.33	313.56
15532.53	2669.57	262.21	13814.92	2273.97	240.07	13615.27	1403.93	397.50
16958.43	2935.88	273.84	15777.73	2630.99	251.43	15224.30	1573.47	481.45
18189.42	3155.69	285.48	17707.35	2964.75	285.79	16828.37	1742.94	570.96
19458.45	3387.32	297.12	19670.08	3332.81	297.29	18437.40	1918.03	654.87
21169.56	3676.71	320.39	21628.11	3666.51	331.52	20046.43	2087.38	738.75
22894.82	4012.83	332.03	23581.44	4034.38	354.38	21650.57	2262.34	828.21
24620.16	4335.46	356.06	25468.48	4356.13	377.23	23559.70	2459.75	912.08
26583.12	4716.21	379.33	27379.24	4712.34	411.45	25149.10	2634.57	1001.50
28237.14	5048.63	404.88	29252.12	5079.64	422.81	26753.17	2803.71	1079.74
30409.19	5484.89	465.33	31082.42	5458.93	514.08	28357.31	2978.40	1169.14
30204.82			32118.18	5666.02	571.00	29917.15	3147.38	1213.83
30475.78			32364.17			31226.01	3282.51	
30684.87						32165.79	3383.84	
30827.50						32387.22		
						32456.11		

Comments

Specimen #1: Front gage @ hole, B Leg was not functional.
Specimen #2: Front gage @ hole, A Leg was not functional.

[±45]_{4s} Boeing Ultimate Strength Data

SPECIMEN #1 STRESS	SPECIMEN #1 TRAN @ HOLE	SPECIMEN #1 LONG @ HOLE	SPECIMEN #2 STRESS	SPECIMEN #2 TRAN @ HOLE	SPECIMEN #2 LONG @ HOLE	SPECIMEN #2 STRESS	SPECIMEN #3 STRESS	SPECIMEN #3 TRAN @ HOLE	SPECIMEN #3 LONG @ HOLE	SPECIMEN #3 STRESS	SPECIMEN #4 STRESS	SPECIMEN #4 TRAN @ HOLE	SPECIMEN #4 LONG @ HOLE
0.00	0.00	0.00	0.00	0.00	0.00	0.00	0.00	0.00	0.00	0.00	0.00	0.00	0.00
372.96	104.99	208.96	1058.11	116.48	197.02	3680.73	1133.49	2030.45	810.94	144.38	247.51	144.38	247.51
1533.34	513.38	940.42	2552.99	652.66	1170.30	4214.83	1385.65	2443.49	2201.52	505.33	883.60	505.33	883.60
2757.22	956.99	1730.24	3213.09	885.97	1564.58	4869.18	1683.99	2925.65	3533.58	973.64	1626.80	973.64	1626.80
4017.87	1482.65	2613.49	3591.73	1037.68	1819.76	5715.98	2108.80	3591.66	5156.39	1610.31	2641.46	1610.31	2641.46
5098.99	2032.29	3485.95	4669.21	1504.79	2597.19	6683.05	2648.99	4407.43	6662.16	2303.03	3689.16	2303.03	3689.16
7152.79	3438.10	5571.72	5848.64	2101.01	3538.06	7654.97	3293.36	5350.22	8110.33	3060.63	4778.76	3060.63	4778.76
8092.36	4319.27	6798.52	6994.13	2803.40	4596.40	8636.53	4065.53	6432.15	9443.32	3938.80	6000.27	3938.80	6000.27
8951.59	5331.46	8144.55	8071.62	3624.16	5772.92	9555.46	5012.22	7688.45	10833.90	5122.01	7549.48	5122.01	7549.48
9725.90	6523.33	9681.63	9066.62	4599.19	7103.45	10411.91	6099.77	9096.88	11934.66	6334.51	9093.36	6334.51	9093.36
10448.24	7930.97	11388.31	9993.70	5764.76	8612.75	11191.38	7387.13	10670.57	13035.42	7776.07	10843.19	7776.07	10843.19
11095.13	9521.09	13300.27	10843.03	7145.89	10348.67	11908.28	8783.22	12283.70	14367.49	9380.76	12316.18	9380.76	12316.18
12152.12	12490.09	16717.39	11624.52	8815.63	12338.31	12562.63	10359.13	14122.71	15120.83	10503.73	13901.50	10503.73	13901.50
12615.35	13951.40	18488.61	12323.44	10800.85	14654.47	13096.65	11668.73	15570.02	15815.66	14481.33	18380.31	14481.33	18380.31
13016.70	15465.24	20185.76	12949.53	12854.43	17038.45	13597.04	13930.58	18335.41	16511.41	16805.99	21172.89	16805.99	21172.89
13710.73	19005.53	24447.73	13498.04	14784.41	19297.52	14092.64	19654.49	24493.28	16974.94	19093.49	23972.76	19093.49	23972.76
14003.43	20925.02	26824.70	13973.64	16626.07	21469.17	14463.13			17322.35	21451.77	26775.09	21451.77	26775.09
14277.27	22888.56	29234.16	14371.65	18632.64	23816.04	14804.77			17686.04	27188.82	33090.59	27188.82	33090.59
14518.08	24800.38	31591.38	14735.67	21073.96	26664.08	15103.05			17889.96				
14754.08	25822.22	33036.14	15041.47	23637.38	29600.29	15637.15			18107.84				
14905.16			15560.80	27192.16	35412.37	16099.04			18858.53				
15330.08			15720.94	25654.44	32698.37	16325.13			19187.68				
15528.39			15968.55			16926.57			19340.62				
15721.96			16400.49			17123.88			19498.24				
16293.23			17123.69			17840.71			19822.69				
16463.23			17618.74			18033.17			19966.34				
16803.15			18506.99			18201.64			20267.60				
17124.23			18875.82			18625.04			20550.29				
17440.57			18050.77			18754.94			20703.30				
18016.57			18749.69			18788.57			20953.51				
18021.23			19579.65			18745.29			21092.55				
17662.46			19943.66			18499.92			21236.27				
17379.15			20569.75			19308.24							
17870.22			20894.94			20977.78							
18474.53						21632.14							
19329.03													
19824.84													
20278.07													

[±45]_{4S} Boeing Ultimate Strength Data

SPECIMEN #5 STRESS	SPECIMEN #5 TRAN @ HOLE	SPECIMEN #5 LONG @ HOLE	SPECIMEN #5 STRESS	SPECIMEN #6 TRAN @ HOLE	SPECIMEN #6 LONG @ HOLE	SPECIMEN #6 STRESS	FAR FIELD STRESS	FAR FIELD STRAIN
0.00	0.00	0.00	0.00	0.00	0.00	0.00	0.00	0.00
2067.64	468.00	721.09	866.27	149.61	242.07	372.96	372.96	34.12
2939.69	792.42	1160.51	2170.22	644.79	1083.89	1553.34	1553.34	358.12
3713.30	1058.70	1564.77	3222.76	1082.82	1799.15	2757.22	2757.22	829.54
4861.93	1539.99	2321.97	4745.67	1844.58	2965.02	4017.87	4017.87	1294.79
5973.15	2074.38	3132.13	6170.82	2711.67	4247.54	5098.99	5098.99	1714.27
7370.33	2889.11	4337.35	7498.06	3754.25	5693.85	7152.79	7152.79	2557.77
8383.04	3648.10	5348.83	8867.31	5194.41	7560.77	8092.36	8092.36	2981.78
9151.92	4338.77	6291.89	9989.70	6825.59	9549.38	8951.59	8951.59	3399.77
9766.10	4901.75	7061.30	10772.09	8356.93	11357.45	9725.90	9725.90	3868.20
10563.16	5866.51	8301.08	11675.60	10669.01	13934.98	10448.24	10448.24	4251.59
11285.16	6958.63	9645.05	12546.49	13583.73	17080.44	11095.13	11095.13	4634.67
11941.56	8173.74	11134.74	13198.51	16206.55	19842.35	12162.12	12162.12	5315.55
12504.19	9489.85	12449.86	13710.75	18341.42	22092.32	12615.35	12615.35	5635.96
12991.76	10636.90	13733.85	14143.88	20726.17	24673.30	13016.70	13016.70	5933.69
13441.91	11782.23	15038.27	14511.79	23182.80	27429.56	13710.73	13710.73	6489.32
13831.05	13035.21	16381.03	15014.78	27123.02	31922.31	14003.43	14003.43	6730.44
14234.23	14860.56	18497.14	15275.60			14277.27	14277.27	6988.26
14285.78	15116.27	18659.81	15513.13			14518.08	14518.08	7223.54
14712.49			15722.69			14754.08	14754.08	7441.90
15270.38			16220.97			14905.16	14905.16	7587.42
15729.85			16458.51			15330.08	15330.08	8034.89
15940.84			16863.66			15528.39	15528.39	8230.52
16170.61			17087.24			15721.96	15721.96	8481.94
16798.83			17436.57			16293.23	16293.23	9134.98
16976.99			17594.85			16463.23	16463.23	9341.30
17169.26			17948.81			16803.15	16803.15	9775.98
17572.45			18125.82			17124.23	17124.23	10193.54
17755.26			18433.13			17440.57	17440.57	10655.21
17924.10			18554.25			18016.57	18016.57	11538.38
18266.35			18535.60			18021.23	18021.23	11682.63
18561.71			18027.99			17662.46	17662.46	11715.92
18575.77			18489.03			17379.15	17379.15	11677.09
18725.82			19155.00			17870.22	17870.22	11799.11
19518.14						18474.53	18474.53	12115.14
19855.74						19329.03	19329.03	12597.08
						19824.84	19824.84	12962.36
						20278.07	20278.07	12962.36

COMMENT

Specimen #5: Back gage @ hole, Leg B and Leg C were not functional.

$[0/\pm 45/90]_{2S}$

SPECIMEN #1 STRESS	SPECIMEN #1 TRAN @ HOLE	SPECIMEN #1 LONG @ HOLE	SPECIMEN #1 STRESS	SPECIMEN #2 TRAN @ HOLE	SPECIMEN #2 LONG @ HOLE	SPECIMEN #2 STRESS	SPECIMEN #3 TRAN @ HOLE	SPECIMEN #3 LONG @ HOLE	SPECIMEN #3 STRESS	SPECIMEN #4 TRAN @ HOLE	SPECIMEN #4 STRESS	SPECIMEN #4 TRAN @ HOLE	SPECIMEN #4 LONG @ HOLE
465.23	0.00	80.54	601.89	0.00	23.01	94.28	23.01	92.04	0.00	0.00	0.00	0.00	0.00
1197.63	11.51	287.62	1551.22	23.29	277.66	164.98	34.52	287.62	482.51	11.51	482.51	11.51	103.69
1781.65	34.52	471.66	2608.16	46.59	566.63	1871.01	69.05	391.17	147.62	34.52	147.62	34.52	322.84
2078.58	46.03	563.67	3655.30	93.18	821.32	2257.50	69.05	460.18	1781.73	34.52	1781.73	34.52	368.99
2553.73	57.54	690.17	4521.45	116.48	1029.42	3167.10	115.08	644.22	2125.05	46.03	2125.05	46.03	461.28
3083.27	80.55	862.65	5456.07	139.78	1237.19	3944.73	161.12	828.24	2640.12	69.05	2640.12	69.05	576.45
3434.59	92.06	966.14	6464.07	186.38	1503.13	4840.17	195.65	1046.72	3271.11	69.05	3271.11	69.05	691.72
3964.14	126.59	1161.59	7643.41	209.69	1780.32	6032.54	253.21	1334.16	3809.36	92.06	3809.36	92.06	853.14
4527.34	161.12	1380.00	8886.25	279.60	2138.38	7177.73	310.78	1598.58	4964.70	115.08	4964.70	115.08	1118.27
5513.17	195.66	1644.33	10173.21	326.22	2473.44	8374.82	356.84	1897.40	6147.91	161.12	6147.91	161.12	1429.33
6547.54	230.19	1943.07	11479.78	349.53	2796.46	9604.93	425.93	2219.19	7345.02	207.17	7345.02	207.17	1751.96
7641.26	276.24	2264.74	12766.67	419.46	3142.66	10839.69	472.00	2517.86	8532.84	241.71	8532.84	241.71	2051.52
8749.86	322.30	2597.80	14039.00	466.09	3488.82	12050.93	552.64	2851.06	9697.40	276.25	9697.40	276.25	2373.97
9868.30	368.35	2942.25	15316.16	536.05	3846.74	13309.28	610.24	3184.09	10899.19	333.81	10899.19	333.81	2696.26
10976.90	414.42	3275.16	16554.17	582.69	4181.25	14562.91	690.89	3540.08	12100.90	368.36	12100.90	368.36	3018.54
12100.38	472.00	3642.43	17806.82	629.33	4504.21	15807.10	760.04	3861.58	13302.62	414.43	13302.62	414.43	3340.78
13208.90	518.07	3975.15	19059.54	699.31	4873.49	17032.49	840.72	4194.50	14495.12	472.02	14495.12	472.02	3674.47
14322.46	575.67	4342.24	20292.66	769.30	5253.87	18290.84	909.89	4561.73	15678.25	518.10	15678.25	518.10	3996.56
15431.07	633.28	4697.78	21506.16	839.30	5588.48	19525.60	990.60	4894.57	16870.75	575.70	16870.75	575.70	4353.16
16539.59	679.37	5064.61	22734.45	909.30	5980.25	20769.79	1094.39	5273.32	18044.68	633.31	18044.68	633.31	4675.14
17613.55	736.99	5419.97	23938.15	979.32	6337.61	22013.98	1163.60	5640.29	19209.31	690.93	19209.31	690.93	5020.09
18667.68	806.14	5786.77	25156.64	1049.35	6694.75	23253.53	1209.76	6006.94	20373.87	748.55	20373.87	748.55	5376.41
19711.97	863.77	6141.93	27387.95	1189.44	7397.38	24450.62	1290.53	6385.27	21533.89	806.18	21533.89	806.18	5709.61
20736.42	909.88	6485.51	27984.94	1236.14	7593.23	25619.40	1371.31	6740.65	22703.13	863.82	22703.13	863.82	6077.09
21780.63	932.94	6874.45	29384.42			26797.61	1463.65	7107.45	23858.48	921.46	23858.48	921.46	6421.57
22785.24	990.59	7240.74	30583.29			27952.31	1544.45	7462.68	24999.93	990.64	24999.93	990.64	6788.96
23824.57	1048.24	7618.34	30774.17			28131.37		7552.44	26136.69	1059.83	26136.69	1059.83	7144.68
24146.29		7767.04	32119.80			29300.15		8064.21	27259.56	1129.04	27259.56	1129.04	7523.33
25160.82		8355.79	33450.81			30445.42		8633.89	28772.13	1175.18	28772.13	1175.18	8039.12
26160.48		8791.35	34752.40			31567.09			29843.94		29843.94		8096.01
27140.45		9055.05	35760.47			32688.77			30934.34		30934.34		
27140.45		9387.37	36161.68			33735.03			31955.17		31955.17		
27476.97						35285.59			33068.68		33068.68		
27630.40													
28610.29													
29525.87													
30377.06													
31317.35													

[0/±45/90]_{2S} Boeing Ultimate Strength Data

SPECIMEN #5 STRESS	SPECIMEN #5 TRAN @ HOLE	SPECIMEN #5 LONG @ HOLE	SPECIMEN #5 STRESS	SPECIMEN #6 TRAN @ HOLE	SPECIMEN #6 LONG @ HOLE	SPECIMEN #6 STRESS	SPECIMEN #6 TRAN @ HOLE	SPECIMEN #6 LONG @ HOLE	FAR FIELD STRESS	FAR FIELD STRAIN
0.00	0.00	0.00	0.00	0.00	0.00	0.00	0.00	0.00	0.00	0.00
544.45	11.65	46.30	624.48	11.51	115.33	544.45	11.51	115.33	544.45	5.65
1417.32	34.80	311.75	1728.88	34.52	403.64	1417.32	34.52	403.64	1417.32	124.83
2111.90	81.11	508.14	2125.00	57.54	518.94	2111.90	57.54	518.94	2111.90	238.29
2599.99	104.27	658.22	2740.15	80.55	692.02	2599.99	80.55	692.02	2599.99	306.35
3336.86	127.43	854.27	3672.16	115.08	934.35	3336.86	115.08	934.35	3336.86	414.12
4270.83	162.10	1096.56	4730.00	161.12	1245.61	4270.83	161.12	1245.61	4270.83	550.17
5157.83	185.26	1304.02	5932.31	195.65	1545.43	5157.83	195.65	1545.43	5157.83	686.20
6223.13	231.59	1580.73	7167.24	241.70	1891.15	6223.13	241.70	1891.15	6223.13	833.51
7391.75	277.92	1880.49	8406.79	287.75	2225.29	7391.75	287.75	2225.29	7391.75	1014.75
8593.20	335.77	2203.19	9688.36	345.32	2582.34	8593.20	345.32	2582.34	8593.20	1190.23
9841.61	382.11	2525.76	10923.28	391.38	2904.84	9841.61	391.38	2904.84	9841.61	1377.03
11094.68	439.97	2859.92	12134.93	448.96	3261.72	11094.68	448.96	3261.72	11094.68	1558.07
12296.13	497.84	3182.38	13318.58	506.55	3595.70	12296.13	506.55	3595.70	12296.13	1744.72
13492.85	567.38	3539.40	14492.91	552.63	3906.48	13492.85	552.63	3906.48	13492.85	1919.93
14694.30	625.26	3873.18	15662.61	621.75	4274.64	14694.30	621.75	4274.64	14694.30	2106.44
15876.97	694.82	4195.65	16832.31	679.36	4596.80	15876.97	679.36	4596.80	15876.97	2275.90
17045.59	752.72	4540.75	18020.60	748.50	4953.34	17045.59	748.50	4953.34	17045.59	2462.21
18232.99	822.29	4874.54	19185.67	817.65	5321.24	18232.99	817.65	5321.24	18232.99	2642.83
19415.65	903.41	5231.22	20341.34	886.82	5700.53	19415.65	886.82	5700.53	19415.65	2829.06
20593.66	984.53	5599.46	21497.01	955.99	6033.80	20593.66	955.99	6033.80	20593.66	3003.87
21757.55	1054.14	5944.46	22652.76	1025.17	6390.03	21757.55	1025.17	6390.03	21757.55	3178.68
22907.38	1135.29	6289.51	23794.48	1071.30	6757.44	22907.38	1071.30	6757.44	22907.38	3359.03
24052.48	1216.46	6668.80	24945.52	1140.50	7136.37	24052.48	1140.50	7136.37	24052.48	3544.91
25972.02	1355.75	7289.58	26082.61	1221.24	7526.76	25972.02	1221.24	7526.76	25972.02	3843.37
27107.80		7689.74	27210.37	1267.39	7893.87	27107.80	1267.39	7893.87	27107.80	4023.47
28234.11		8079.91	27983.88	1325.08	8169.32	28234.11	1325.08	8169.32	28234.11	4203.50
29318.28		9141.72	28529.18		8363.73	29318.28		8363.73	29318.28	4372.21
30407.10			29600.97			30407.10			30407.10	4552.10
31655.43			30700.75			31655.43			31655.43	4754.41
31833.81			31786.57			31833.81			31833.81	4799.35
32570.61			32825.75			32570.61			32570.61	4917.28
			33426.94							
			28412.61							

COMMENT

Specimen #2: Back gage @ hole, Leg A was not functional

Appendix D: Thesis Test Plan

When the author first started this effort he was unable to locate any information concerning how to write a Test Plan for the experiemental portion of the thesis. It is his hope the plan presented here can act as a sample for any research being conducted in the future.

STUDY OF GRAPHITE PEEK WITH CONCENTRIC HOLES UNDER COMPRESSION.

1. PROGRAM INFORMATION

a. Organization	WL/FIBCA
b. Project Number	24010366
c. Project Title	"An Investigation of Graphite PEEK with Concentric Holes Under Compression "
d. Security Classification	Unclassified
e. Project Engineer	Capt Benjamin Wham II
f. Project Advisor	Dr. Anthony Palazotto
g. Project Sponsor	Dr. R.S. Sandhu
h. Instrumentation Engineer	Designated by FIBT
i. USAF Fabrication Engineer	Designated by Comp. Facility
j. Test Location	Structures Test Facility, Bldg. 65, Area B, WPAFB

2. PROJECT OBJECTIVES

The objectives of this program are to correlate the analytical and the experimental responses of Graphite Polyetheretherketone (PEEK) with a central hole under compression loading.

3. TECHNICAL DESCRIPTIONS

The following paragraphs provide technical details to fabricate specimens required to conduct the investigation .

3.1 Materials

The specimens required for this program will be fabricated from panels of the following material:

3.1.1 APC-2: AS4 Graphite Fibers in a Polyetheretherketone (PEEK) matrix.

3.2 Stacking Sequences of Specimens

Specimens (of sizes that will be specified in paragraph 3.4) will be cut from panels of the material system of paragraph 3.1.1. and will conform to the following stacking sequences:

<u>Panel Designation</u>	<u>Panel Stacking Sequence</u>	<u>Number of Plies</u>
A	[0°] ₁₆	16
B	[±45°] _{2S} (SH)	8
C	[0°] ₁₆	16
D	[90°] ₁₆	16
E	[±45°] _{4S}	16
F	[0° / 90°] _{4S}	16
G	[0° / ±45 ° / 90 °] _{2S} (QI)	16

3.3 Panels

The panels are supplied to the fabrication engineer in the following sizes and quantities:

<u>Panel Designation</u>	<u>Size Before Trimming</u>	<u>Size After Trimming</u>	<u>Quantity</u>
A	16.0" x 14.0"	15.0" x 13.0"	1
B	12.0" x 8.5"	9.0" x 7.0"	1
C	22.0" x 14.0"	21.5" x 12.0"	1
D	22.0" x 14.0"	21.5" x 12.0"	1
E	22.0" x 14.0"	21.5" x 12.0"	1
F	22.0" x 14.0"	21.5" x 12.0"	1
G	22.0" x 14.0"	21.5" x 13.0"	1

3.3.1 Void Content and Thickness

The void content will not be in excess of one per cent. The thickness will be .00525±.0003" and will be measured on each panel in accordance with Figure 1.

3.3.2 Determination of Flaws

All untrimmed panels will be subjected to C-scan to determine flaws before being cut into specimens. The final acceptance or rejection of the panels will be made by the project engineer.

3.3.3 Resin Content

Samples will be taken at suitable locations to determine resin content, fiber volume, and

void fraction for all the panels. These results will be compared with optical observations and thickness per ply.

3.4 Specimens

Specimens of the following types will be cut from the panels of paragraphs 3.2 and 3.1.1.

- | | | |
|----|------------|---|
| a. | 0T | 0.5 inch wide tension specimen with standard tapered tabs (Fig. 5&2) |
| b. | 0C | 0.75 inch wide compression specimen with square ended tabs (Fig. 5&3) |
| c. | 90T | 1.0 inch wide tension specimen with standard tapered tabs (Fig. 5&2) |
| d. | 90C | 0.75 inch wide compression specimen with square ended tabs (Fig. 5&3) |
| e. | ± 45 T | 1.0 inch wide tension specimen with standard tapered tabs (Fig. 6&2) |
| f. | 0CT | 1.5 inch wide compression specimen with hole for Boeing device without tabs cut from panel C (Fig. 7&4). |
| g. | 90CT | 1.5 inch wide compression specimen with hole for Boeing device without tabs cut from panel D. (Fig. 8&4) |
| h. | SHCT | 1.5 inch wide compression specimen with hole for Boeing device without tabs cut from panel E. (Fig. 9&4) |
| i. | (0/90)CT | 1.5 inch wide compression specimen with hole for Boeing Device without tabs cut from panel F. (Fig. 10&4) |
| j. | QICT | 1.5 inch wide compression specimen with hole for Boeing device without tabs cut from panel G. (Fig 11&4) |

The specimens will conform to the dimensions shown in Figures 2 thru 4. These specimens will be designated as follows:

XX - ZZ - NN

where

XX: Specimen type

ZZ: Panel designation (A, B, C, D, E, F, G)

NN: Specimen number

3.5 Tabbing Specimens

Tabs when required for the specimens identified in paragraph 3.4 will be cut from fiber glass fabric 1/16 inch thick (approximately) and bonded to the specimens using standard procedures.

3.6 Instrumentation

The specimens will be instrumented using the appropriate gages etc. as indicated in the following paragraphs:

a. A pair of strain gage rosettes CEA-03-125UR-350 will be bonded at the center and opposite faces of specimens 3.4a through 3.4e. Exact location of the gage will be provided at a later date.

a A pair of strain gage rosettes, WA-03-030UR-120 will be bonded at the center of the specimen and opposite faces of specimen. In addition, a far field strain gage rosette, CEA-03-125UR-350, will be bonded at the midpoint between the hole and the end of the specimen on both sides of 3.4f through 3.4j. Exact location of the gage will be provided at a later date.

3.7 Testing

The testing to be accomplished in this program will consist of the three phases:

- (1) Test for material properties.
- (2) Test for the ultimate strength.
- (3) Test to 90% and 95% of ultimate load.

3.7.1 Test for Basic Properties

To determine the basic property data, specimens corresponding to 3.4a through 3.4e will be tested under static loading.

3.7.2 Test for Ultimate Compressive Strength

To determine the ultimate compressive strength of specimens with the 0.5-inch diameter hole all specimens will be instrumented with strain gage rosettes near the hole and with far field strain gages and tested under compression. At least three specimens of each type will be tested. The specimens will be placed within the Boeing Apparatus to conduct the test.

3.7.3 Test for Progression of Ply Failure Near Ultimate Strength

To determine the growth of ply failure in specimens with the 0.5-inch diameter hole, specimens of each type will be loaded to 90% and 95% of Ultimate Compressive Strength. The specimen will then be removed from the loading device and investigated using a scanning electron microscope and ultrasonic techniques.

3.7.4 Loading Rate and Sampling Rates

All specimens will be loaded at the crosshead speed of 0.05 inches per minute. Sampling rate as follows:

<u>Ply layup</u>	<u>Sample Rate</u>
0T	1 sample/sec

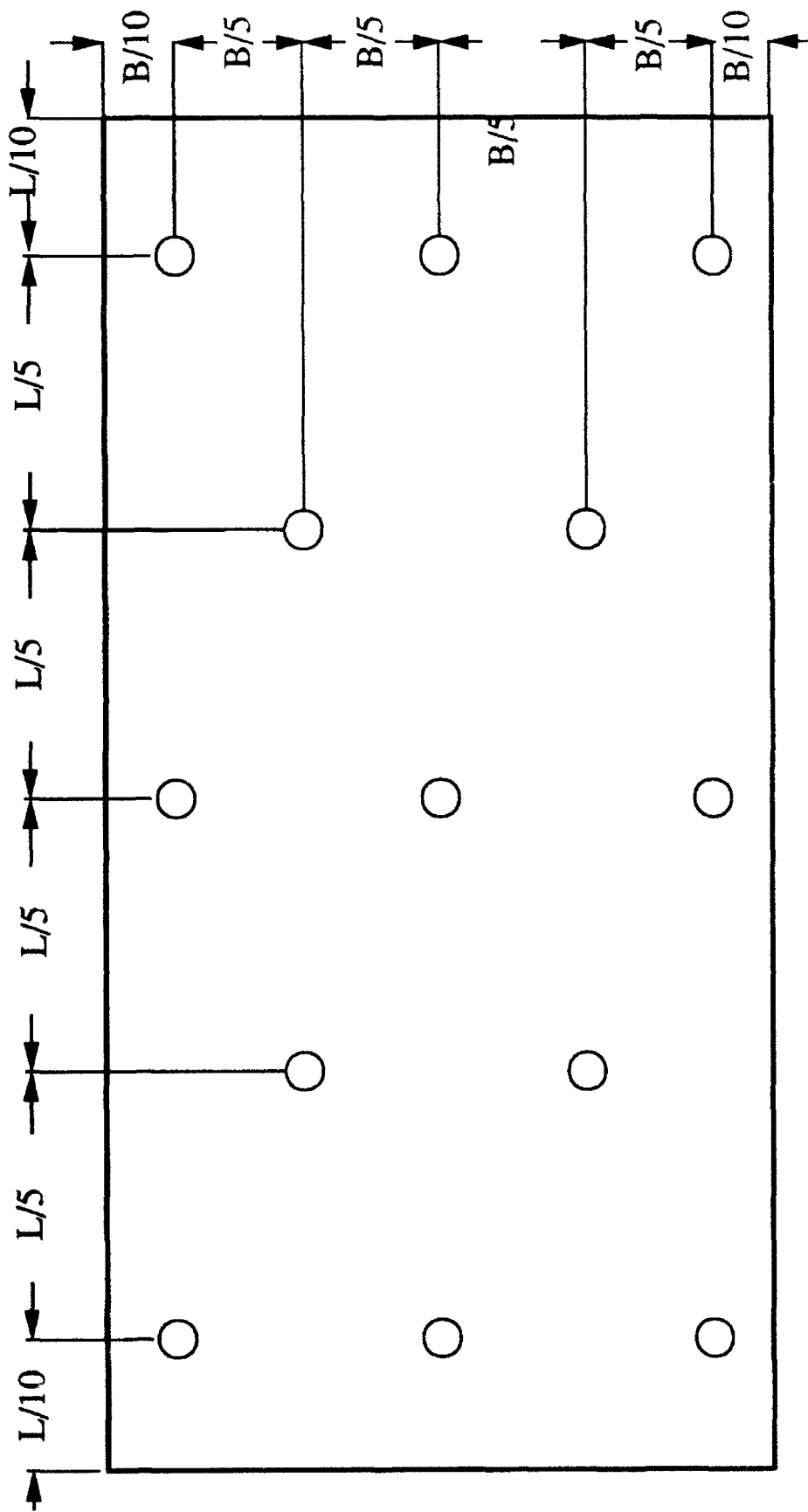
0C	1 sample/sec
90C	2 samples/sec
90T	4 samples/sec
±45T	1 sample/sec
0CT	2 samples/sec
90CT	4 samples/sec
SHCT	2 samples/sec
0/90CT	2 samples/sec
QICT	2 samples/sec

3.8 Scrap

The scrap will be saved and identified.

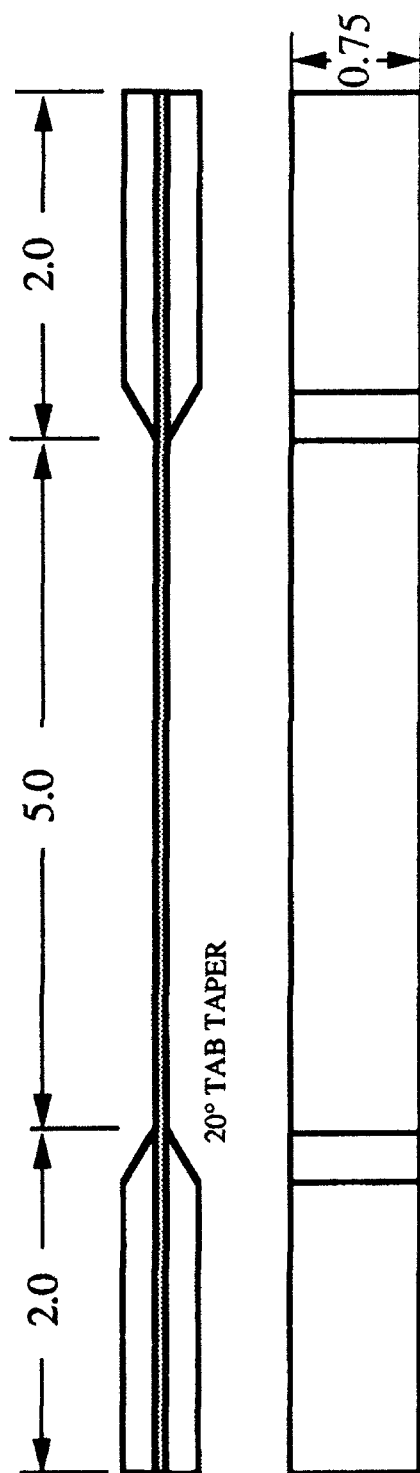
3.9 Report

The results of this study will be compared and contrasted to an analytical study. The final results and discussion will be incorporated into a graduate thesis for the project engineer.

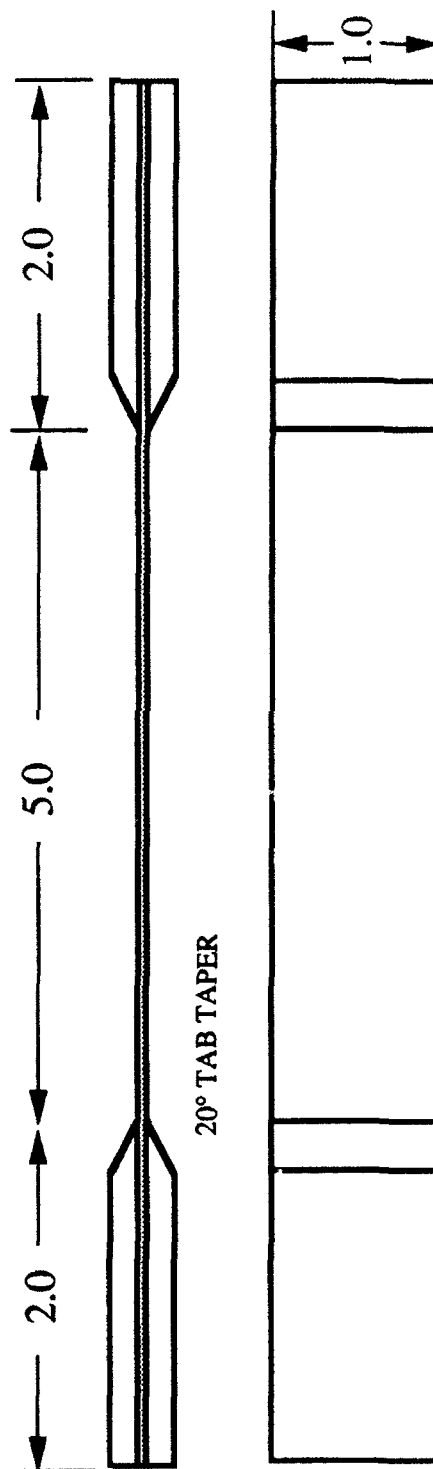


○ Location for Thickness Measure

Figure 1. Thickness Measurement



a. Specimen 0T



b. Specimen 90T, & (±45)T

Figure 2: Tensile Specimens

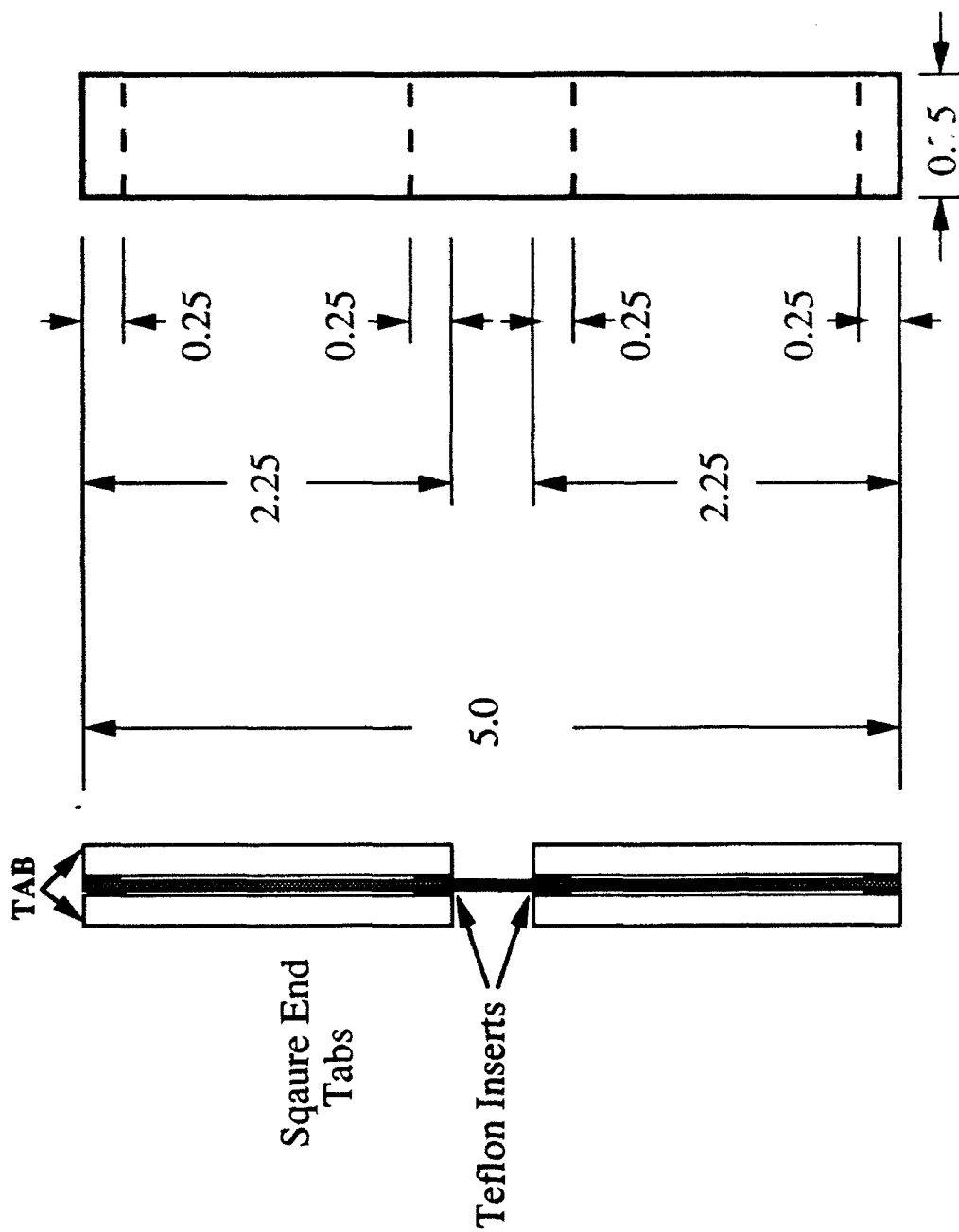
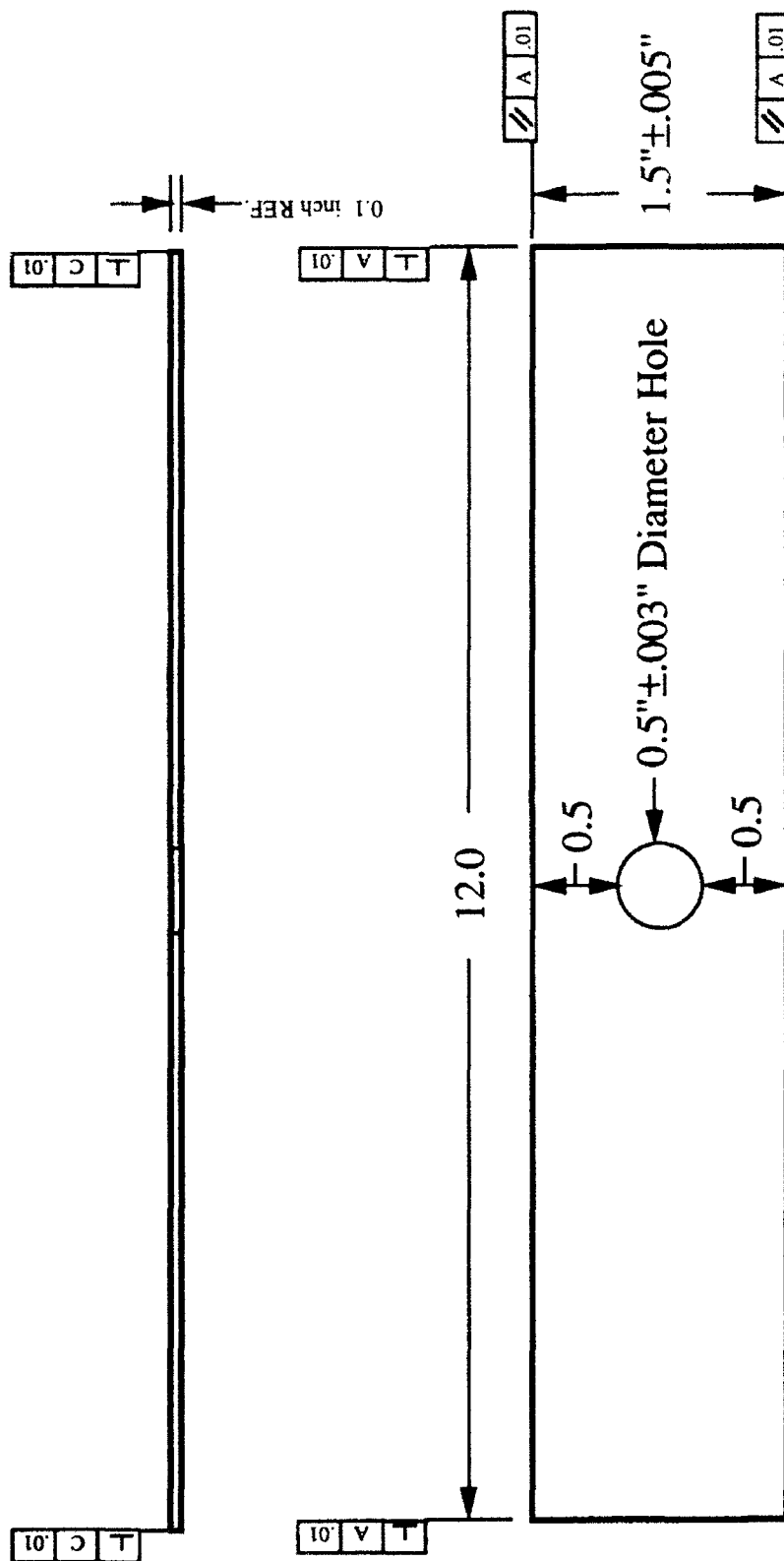


Figure 3. Compression Specimens



c. Specimen 0CT, 90CT, SHCT, (0/90)CT, & QICT

Figure 4. Boeing Apparatus Tension Specimens

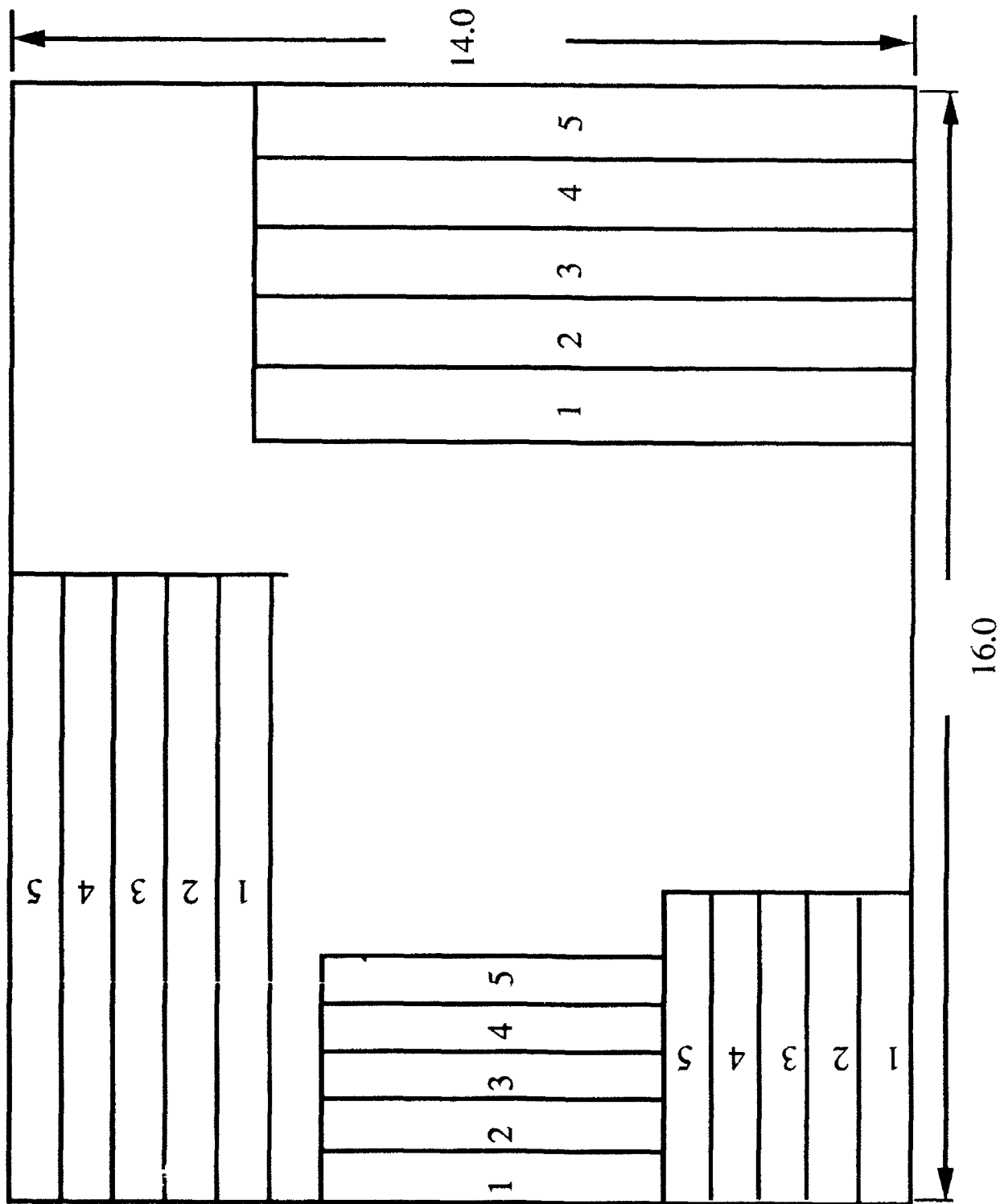


Figure 5: Panel A

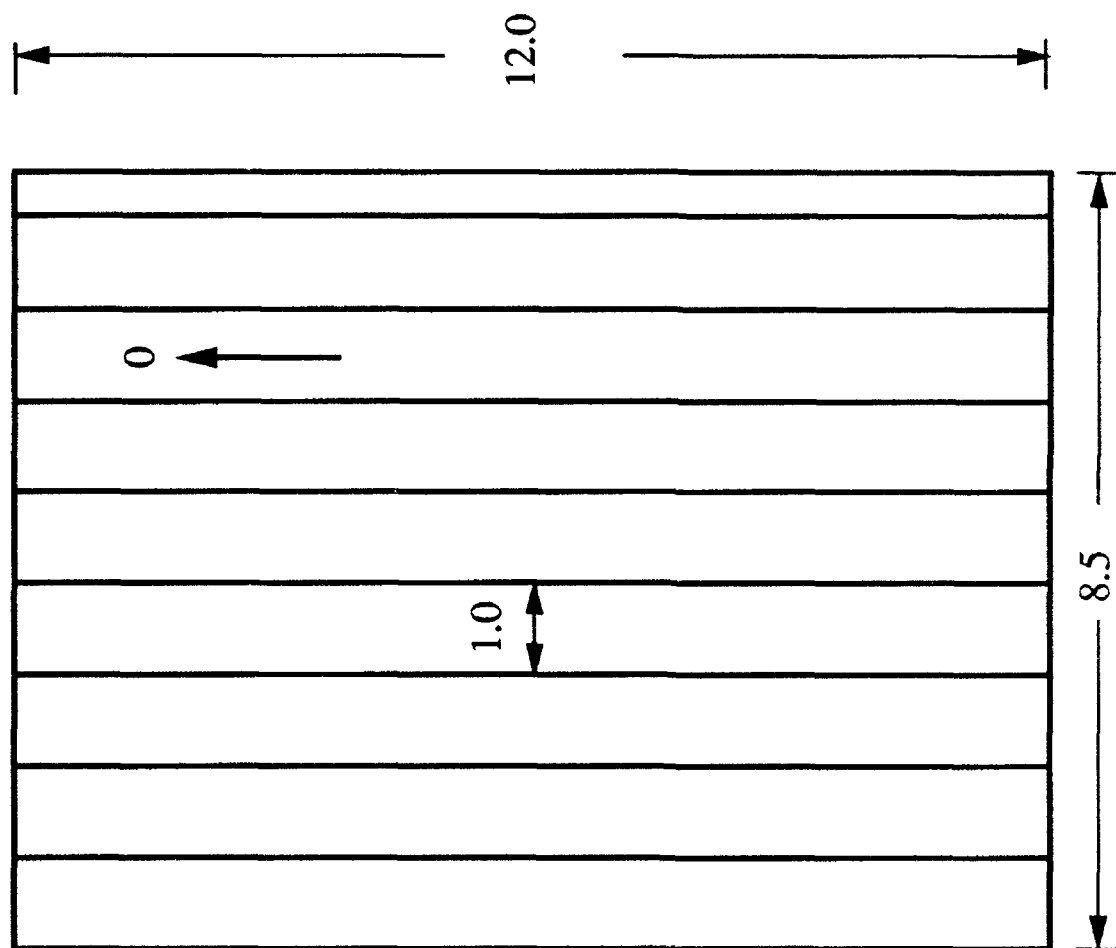


Figure 6: Panel B for (± 45)T Specimens (See Fig. 2)

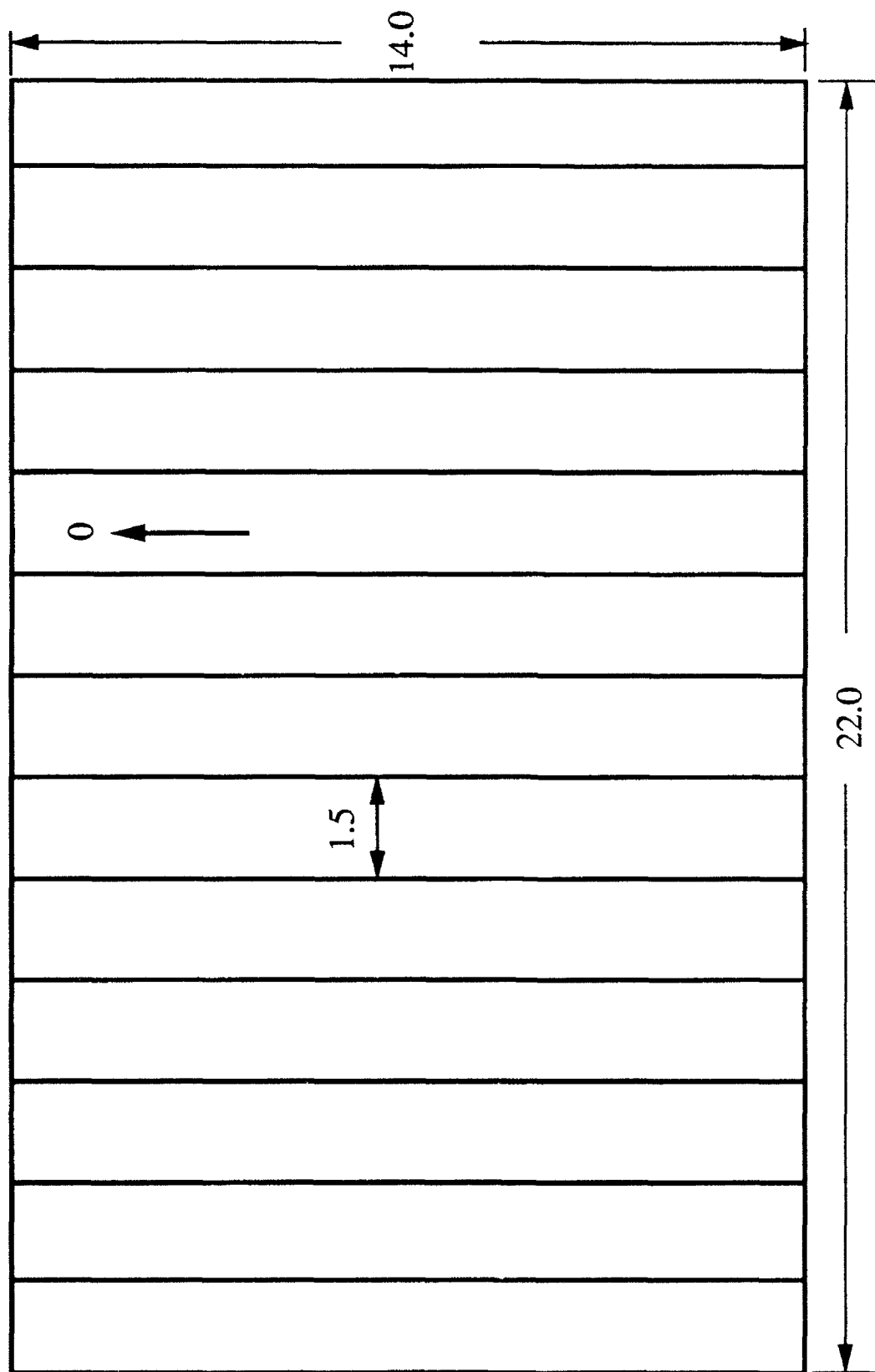


Figure 7: Panel C for OCT Specimens (See Fig. 4)

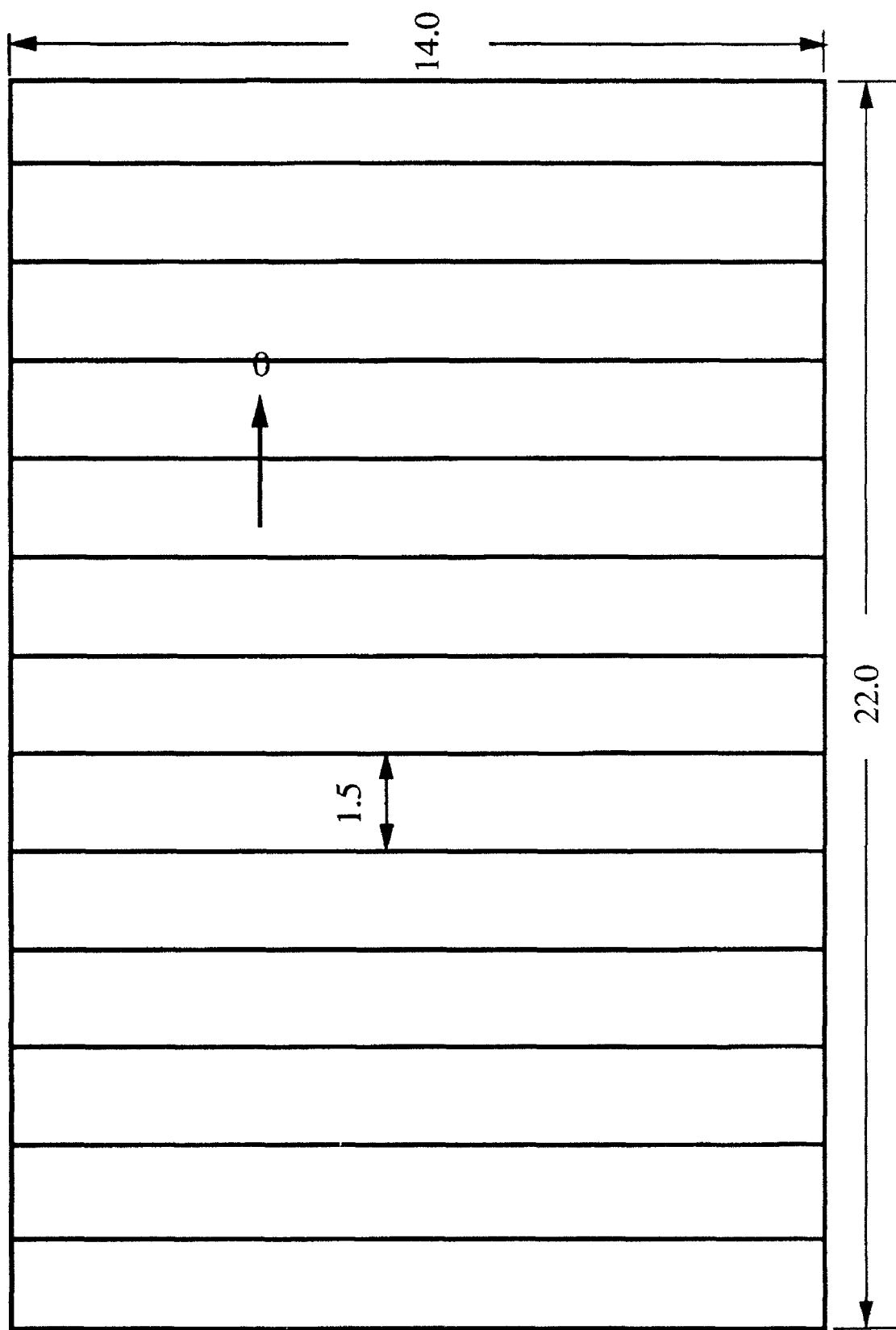


Figure 8: Panel D for Specimen 90CT (See Fig. 4)

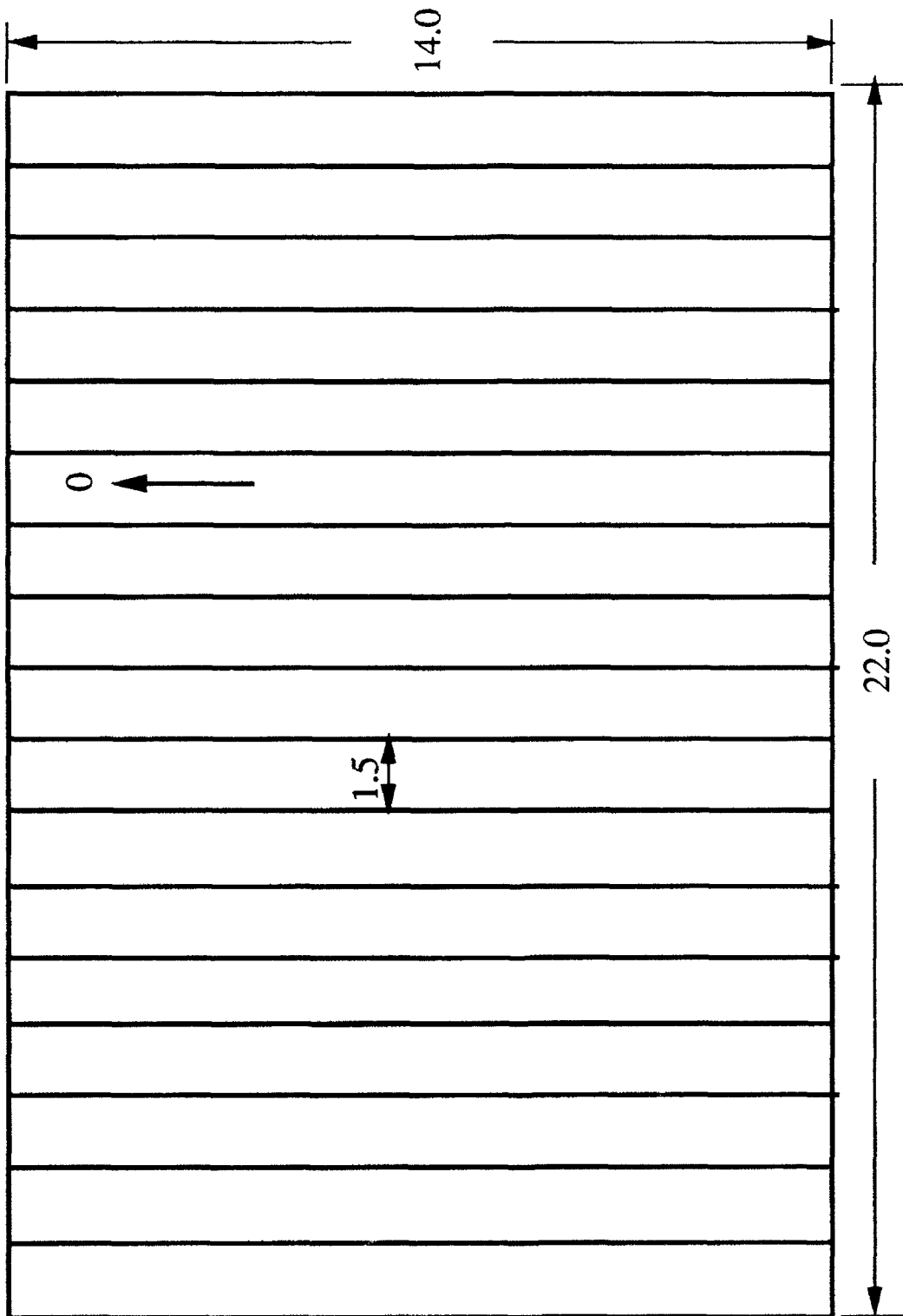


Figure 9: Panel E for ± 45 CT Specimens (See Fig. 4)

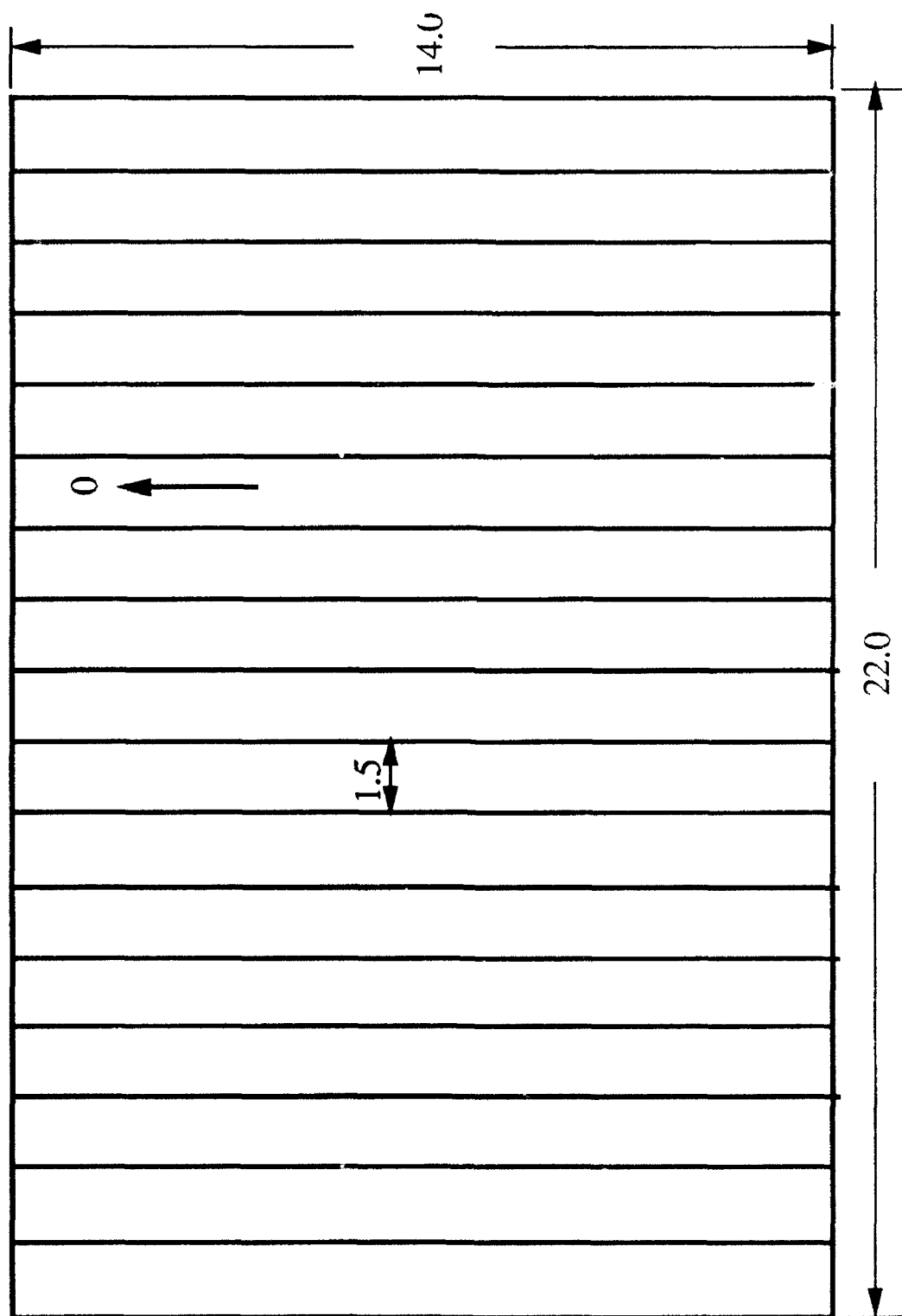


Figure 10: Panel F for Specimens (0/90)CT (See Fig. 4)

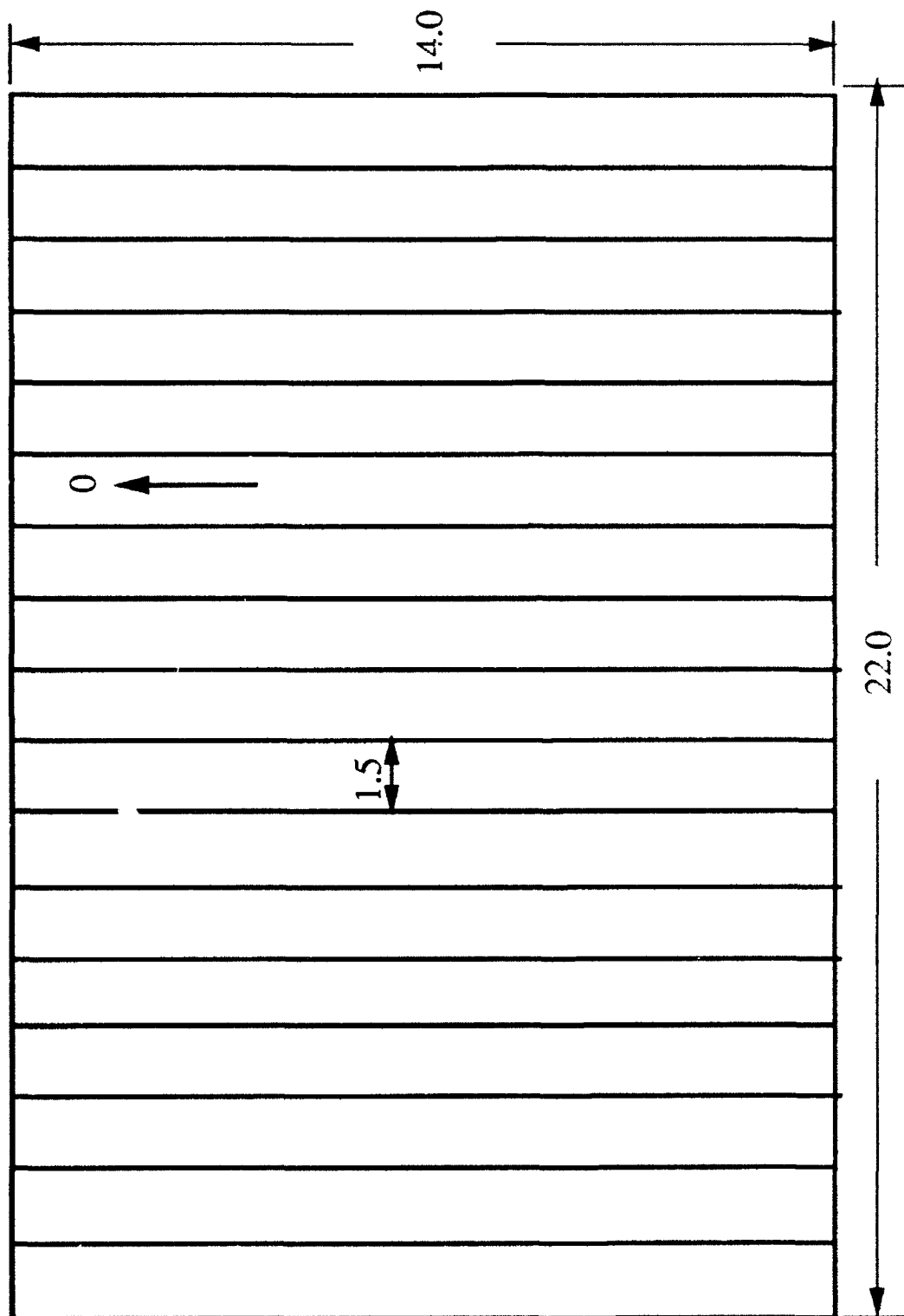


Figure 11: Panel G for QICT Specimens (See Fig. 4)

Bibliography

1. ICI Composites Inc. Thermoplastic Composite Materials Handbook, Tempe, AZ: Fiberite Composite Materials, January 1992.
2. Martin, J. A Study of Failure Characteristics in Thermoplastic Composite Materials, MS Thesis, AFIT/GA/AA/88M-2. School of Engineering, Air Force Institute of Technology (AU), Wright Patterson AFB, OH. March 1988
3. Cox, J.T. "How the Station Will Operated", Aerospace America, Vol 24, (September 1988), pp 20-27.
4. McConnell, V. P. "Composites in Sports: Going for the Gold", Advanced Composites, Vol 7, (Sept-Oct 1992) pp. 37-47.
5. Cook, R.D. Concepts and Applications of Finite Element Analysis, New York: John Wiley & Sons, Third Ed., 1989.
6. Awerbuch, J. and M.S. Madhukar. "Notched Strength of Composite Laminates: Predictions and Experiments--A Review", Journal of Reinforced Plastics and Composites, Vol. 4, (January 1985).
7. Sandhu, R.S. "Nonlinear Behavior of Unidirectional and Angle Ply Laminates", Journal of Aircraft, Vol. 13, (February 1976), pp. 104-111.
8. Sandhu, R.S. "Ultimate Strength Analysis of Symmetric Laminates", Technical Report AFFDL-TR-72-71, AD 756889, Air Force Flight Dynamics Laboratory, Wright-Patterson AFB, OH, February 1974.
9. Dato, M.H. Mechanics of Fibrous Composites, New York: Elsevier Applied Science LTD, 1991.
10. Lustiger, A. "Fiber-Matrix Interface", International Encyclopedia of Composites, Ed. Stuart M. Lee. Vol. 4 New York: VCH Publishers, 1991 p. 168.
11. Fan, T.C. and Janet Knapp, "Properties of Composites", SAMPE Quarterly, Vol 18, (July 1987), pp 16-19.
12. Nahas, M.N. "Survey of Failure and Post-Failure Theories of Laminated Fiber-Reinforced Composites", Journal of Composites Technology and Research, Vol. 8, (Winter 1986), pp. 138-153.
13. Hahn, H.T. and Tsai, S.W. "Nonlinear Elastic Behavior of Unidirectional Composite Laminates", Journal of Composite Materials, Vol 7, (January 1973) pp. 102-118.
14. Daniels, J.A. A Study of Failure Characteristics in Thermoplastic Laminates Due To an Eccentric Circular Discontinuity, MS Thesis, AFIT/GAE/ENY/89D-06. School of Engineering, Air Force Institute of Technology (AU), Wright Patterson AFB, OH. December 89.

15. Saada, A.S. Elasticity: Theory and Applications, Malabar, Florida: Robert E. Krieger Publishing Company, 1989.
16. Woolstencroft, D.H., A.R. Curtis, and R.I. Haresceugh. "A Comparison of Test Techniques Used for the Evaluation of the Unidirectional Compressive Strength of Carbon Fibre-Reinforced Plastic", Composites, Vol 12, (October 1981) pp. 275-280.
17. Scobbo, J.J. and Nakajima, N. "Effect of Gage Length on Compressive Properties of Unidirectional Fiber Composites", Journal of Thermoplastic Composite Materials, Vol. 3 (July 1990), pp. 190-201.
18. Nuismer, R.J. and Labor, J.D. "Applications of Average Stress Failure Criterion: Part II-Compression", Journal of Composite Materials, Vol. 13, (January 1979) pp. 49-60.
19. Tan, S.C. "Tensile and Compressive Notched Strength of PEEK Matrix Composite Laminates", Journal of Reinforced Plastics and Composites, Vol. 6 (January 1985). pp. 253-267.
20. Frost, S.R., "Compressive Behaviour of Long-Fibre Unidirectional Composites", Journal of Composite Materials, Vol. 26, (August 92), pp. 1151-1172.
21. Hahn, H.T. and Williams, J.G., "Compression Failure Mechanisms in Unidirectional Composites", Composite Materials: Testing and Design (Seventh Conference), ASTM STP 893, J.M. Whitney, Ed., American Society for Testing and Materials, Philadelphia, 1986, pp. 115-139.
22. Lessard, L.B. 1989. "Compression Failure in Laminated Composites Containing an Open Hole". Thesis Dissertation, Stanford University.
23. Chang, F.K. and Lessard, L.B. "Damage Tolerance of Laminate Composites Containing an Open Hole and Subjected to Compressive Loadings: Part I-Analysis", Journal of Composite Materials, Vol. 25, (January 91), pp. 2-43.
24. Chang, F.K. and Lessard, L.B. "Damage Tolerance of Laminate Composites Containing an Open Hole and Subjected to Compressive Loadings: Part II-Experiment", Journal of Composite Materials, Vol. 25, (January 91), pp. 44-63.
25. Gurdal, Z and Haftka, R.T. "Compressive Failure Model for Anisotropic Plates with a Cutout", AIAA Journal, Vol 25, (November 87), pp. 1476-1481.
26. Cook, R.D., D.S. Malkus, and M.E. Plesha Concepts and Applications of Finite Element Analysis, (Third Edition) New York: John Wiley and Sons, 1989
27. Sandhu, R.S. Wright Laboratory, Wright Patterson AFB, OH Personal Notes. 1 November, 1992.
28. Fisher, J.M. A Study of Failure Characteristics in a Thermoplastic Composite Material at High Temperature, MS Thesis, AFTT/GAE/AA/88D-15. School of Engineering, Air Force Institute of Technology (AU), Wright Patterson AFB, OH December 1988.

29. Peterson, R. E. Stress Concentration Factors, New York: John Wiley and Sons, 1974, p. 150.
30. Whitney, J.M., Daniel, I.M. and Pipes, R.B. Experimental Mechanics of Fiber Reinforced Composite Materials, Brookfield Center, Connecticut: The Society for Experimental Stress Analysis, 1982.
31. Zambora, Ronald. Boeing Corporation, Seattle, WA. Telephone Interview. November 15, 1992.
32. SAMCA SMR 3-88. Open Hole Compression Properties of Oriented Fiber-Resin Composites, Association Brochure. Cleveland: Suppliers of Advanced Composite Materials Association, 1988.
33. Purslow, D. "Fractography of Fiber-reinforced Thermoplastics, Part 3. Tensile, Compressive and Flexural Failures", Composites, Vol. 19, (September 1988), pp. 358-366.
34. Purslow, D. "Fractography of Fiber-reinforced Thermoplastics, Part 2. Shear Failures", Composites, Vol. 19, (March 1988), pp. 115-126.
35. DeMutts, Edward. Wright Laboratories, WPAFB, OH. Personal Interview. January 28, 1993.
36. Savin, G.N. "Stress Distribution Around Holes" NASA Technical Translation NASA TT F-607, November 1970.
37. O'Brien, T.K. "Fatigue Delamination Behaviour of PEEK Thermoplastic Composite Laminates," in Delamination in Advanced Composites, Ed. Newaz, Golam M. Lancaster, PA: Technomic Publishing Co, 1991.
38. Sandhu, R.S. and Sendekyj, G. P., On Delamination of $(\pm\theta_m/\theta_n/2)_s$ Laminates Subjected to Tensile Loading, Air Force Wright Aeronautical Laboratories Technical Report, AFFDL-TR-87-3058, July 1987.
39. Fisher, J.M., Palazotto, A.N., and Sandhu, R.S., "A Study of the Failure Characteristics in Thermoplastic Composite Material at 250° F," Journal of Composites Technology & Research, Vol. 13, No. 3, Fall 1991, pp. 152-160.
40. Daniels, J.A., Palazotto, A.N., and Sandhu, R.S., "Failure Characteristics in Thermoplastic Composite Laminates Due to an Eccentric Circular Discontinuity," AIAA Journal, Vol. 29, No. 5, May 1991, Pages 830-937.

Vita

Capt. Benjamin Wham II was born on 12 May 1964 in Powell, Wyoming. He graduated in 1982 from Auburn High School in Auburn, Alabama. In 1982 he attended The Citadel in Charleston, South Carolina on a Four year Air Force Scholarship. He graduated in 1986 and was assigned to Wilford Hall (USAF) Medical Center as the Chief of Plans and Programs Section of the Facilities Management Branch. In 1988 he was assigned to Torrejon AB, Spain where he first served as the Chief of Engineering Design and then as the Chief of Readiness from April 1990 till April 1991. He is currently assigned to the Aeronautical Systems Center in the EMY office. He is married to the former Ellen Mary O'Connell and has a daughter, Jennifer.

Permanent Address: 4643 Burchdale St.
Kettering, OH 45440

OMP No. 2794 OIRB

[illegible]

NSN 7540-01-280-5500